Deciphering Maturation and β-Adrenergic Dynamics in HiPSC-Derived Cardiomyocytes via Integrated Transcriptomic and Functional Profiling

Camille Charrière

Lady Margaret Hall

Medical Sciences Division, Cardiovascular Medicine

University of Oxford

A thesis submitted for the degree of Doctor of Philosophy

Hilary Term 2025

Science is for everyone.

— Stand Up for Science

Je dédie ce travail à la communauté scientifique internationale, présente et future. Ensemble, assurons-nous que la production scientifique œuvre toujours dans l'intérêt réel de la population mondiale, dans toute sa diversité.

.....

I dedicate this work to the international scientific community, both present and future. Together, let us ensure that scientific production always serves the best interests of the world's population, in all its diversity.

Abstract

Human iPSC-derived cardiomyocytes (hiPSC-CMs) are a convenient cell source of human cardiomyocytes (CMs), valuable for modelling cardiac disease, drug testing, and regenerative research. However, they remain immature, limiting use in adult-onset diseases. Despite many maturation efforts since the 2010s, full maturity hasn't been achieved. Recent work points to the β-adrenergic pathway's role, but cAMP nanodomain formation and regulation are still unclear. Therefore this thesis aimed to explore the dynamics between maturation and organisation of the cAMP signalling pathway in hiPSC-CMs.

Specifically, this thesis explored how hiPSC-CM metabolic maturation and left ventricular lineage specification affect cAMP signalling. Single nucleus transcriptomics was used to assess RNA level maturity and cell types produced by differentiations. Functional measurements of action potentials, calcium transients and contractility were correlated with transcriptomic changes. Additionally, β-adrenergic-induced alteration of cellular function was investigated, in relation to changes in activity of PDE3 and PDE4 observed using FRET-based cAMP sensors.

This work found that the proportion of proliferative CMs was reduced with maturation. Transcriptomics showed a high proximity between hiPSC-CM groups, while functional analysis revealed that both protocols produced more mature hiPSC-CMs. Additionally, the left ventricular lineage specification robustly reduced hiPSC-CM functional heterogeneity. An increased reliance on human adult isoform PDE3 was observed in hiPSC-CM from both maturation protocols, and was associated with robust functional responses to β-adrenergic stimulation.

These findings advance our understanding of β-adrenergic signalling in hiPSC-CM maturation. Mapping cAMP nanodomains, and the corresponding enhancement of chronotropic and inotropic responses in hiPSC-CMs, will help establish clear molecular and functional benchmarks of β-adrenergic maturation, that will serve both as a sensitive readout and a driver of hiPSC-CM maturity.

Declaration

I declare that, unless otherwise indicated, all work presented in this thesis is entirely my own. The contents of this work are original and have not been submitted for consideration for another degree or qualification.

Acknowledgements

First of all, I want to express my deep gratitude to both of my supervisors, Christopher Toepfer and Manuela Zaccolo for their incredible guidance and unwavering support over the past 4 years. Chris, Manuela, your mentorship has truly made a world of difference in my journey towards becoming an independent researcher, and I am so thankful for all that you have done for me.

I want to give a huge shout-out to Yiangos Psaras who has been a wonderfull and dedicated Jedi Master in regard to wet lab research and taught me a great deal about live fluorescence microscopy and bioinformatics image analysis. I would also like to give a very special thank to Charlotte Hooper, our eminent molecular biology Wizard who was always there to help me out whenever I had a problem or a question! Yiangos, Charlotte, I just wanted to let you know how much your friendship and kindness mean to me. A big thank you to both of you!

A huge shout-out to my amazing friends Daan Paget and Manuel Schmid for bringing so much happiness and laughter into our lives. Thank you both for your incredible friendship!

I am truly grateful to Andreas Koschinski and Violetta Steeples for their invaluable advice and assistance. And of course, a big thank you to all the other wonderful members of both the Toepfer group at the Radcliffe Department of Medicine and the Zaccolo group at the Department of Physiology, Anatomy and Genetics!

I would like to express my sincere gratitude to our collaborators, Joshua Gorham and Seong-Won Kim from Harvard, for their assistance with the RNA sequencing. Additionally, I extend my thanks to Siwei Deng and Ying-Jie Wang from the University of Oxford for their support in the RNA sequencing analysis, as well as to Alfonso Bueno-Orovio for providing the simulated

adult cardiomyocyte physiology data.
I would like to express my gratitude to Carolyn Carr, Ming Lei, Julia Gorelik, and Charles Redwood for their valuable feedback as assessors during my Transfer and Confirmation of Status processes.
I am also thankful to David Greaves, Nicola Smart and Kim Dora for their guidance as directors of graduate studies for the British Heart Foundation 4-year DPhil program.
I would like to express my thanks to the British Heart Foundation, cohort Wilson-Olegario for funding my work.
I am very fortunate to have been part of the Lady Margaret Hall, a place not only filled with a vibrant community but also boasting the most exquisite grounds where I have found solace and tranquillity. Thank you, LMH, for being a sanctuary for my heart and mind.

Finally, I want to express my deepest gratitude to my beloved family for their unwavering love and support. *À mon incroyable mère Valérie Dunant, dont la volonté et la résilience hors du commun sont toujours une source d'admiration. À mon gigantesque petit frère Claudius Charriere, ma bouillonnante grande sœur Jennifer Onida, ainsi qu'à mes figures paternelles André Charriere et Stéphane Sieger. Merci du fond du cœur d'être des soutiens pleins d'amour et d'encouragements.*

To my eternal love and most recently wife, Sarah François: *Tes conseils avisés et ton soutien infaillible m'ont portée à travers les moments les plus sombres de mon parcours. Sans toi à mes côtés, cette thèse n'aurait jamais pu voir le jour. Aucun obstacle ne me paraît insurmontable lorsque tu m'accompagnes. Ta présence douce et encourageante, nos discussions stimulantes interminables et nos valeurs communes sont le pilier fondamental de mon existence. Tu es mon inspiration, ma joie, mon bonheur. Merci d'être toi. Je t'aime infiniment.*

Contents

Acronyms and abbreviations **xvi**

1 Introduction **2**

1.1 The cardiac function in health and disease 2

1.1.1 The excitation-contraction coupling 2

1.1.1.1 Cardiac action potentials 2

1.1.1.2 Calcium cycling 5

1.1.1.3 Sarcomeres, the contractile unit 6

1.1.2 The β-adrenergic pathway 8

1.1.2.1 Role of the β-adrenergic stimulation on cardiac function 8

1.1.2.2 cAMP compartmentalisation 10

1.1.3 The β-adrenergic pathway in disease and during cardiac development 14

1.2 The use of hiPSC-derived cardiomyocytes (hiPSC) in cardiovascular disease modelling 16

1.2.1 hiPSC-CM differentiation 16

1.2.2 hiPSC-CM characteristics 18

1.2.3 Maturation of iPSC-derived cardiomyocytes (iPSC) . . . 22

1.2.4 Overview of hiPSC-CM maturation protocols used in this thesis 24

1.3 Thesis aims 25

2 Material and Methods **28**

2.1 Definitions 28

2.2 General 28

2.2.1 Stem cell culture 28
2.2.2 Regular cardiomyocyte differentiation 29
2.2.3 Metabolic maturation 29
2.2.4 Left ventricle-like differentiation 30
2.2.5 hiPSC-CM replating for live imaging 31
2.2.6 Imaging buffer recipe 31
2.2.7 Adeno-associated viral vector generation 32
2.2.8 Cell pellet preparation and storage for snRNA-seq and western blots 34
2.2.9 Western blots 34
2.3 Specific to chapter 3 36
2.3.1 Single nucleus RNA sequencing 36
2.4 Specific to chapter 4 38
2.4.1 adeno-associated virus (AAV) transduction of FRET-based cyclic adenosine monophosphate (cAMP) indicators . . . 38
2.4.2 Immunofluorescent staining and imaging 38
2.4.3 Live fluorescent microscopy for cAMP measurements . . 39
2.4.4 Targeting of Cx43 with FluoSTEP sensors 40
2.4.4.1 PCR and gel electrophoresis 40
2.5 Specific to chapter 5 41
2.5.1 Sample preparation for live fluorescent microscopy . . . 41
2.5.2 Live fluorescent microscopy for calcium, contractility and voltage measurements 42
2.5.3 Statistical analyses 44
2.6 Reagents list 44

3 Using unbiased single nucleus RNA sequencing to compare the effects of two hiPSC-derived cardiomyocytes maturation protocols 48

3.1 Introduction 48
3.2 Results 50
3.2.1 Single nucleus RNA sequencing 50

3.2.1.1 Investigating cell types found in hiPSC-CM samples . . . 50
3.2.1.2 Comparison between the different protocols . . 54
3.2.1.3 Comparison to adult ventricular cardiomyocyte 61
3.2.1.4 Expression of genes of interest 66
3.2.2 Western Blots 66
3.3 Discussion and perspectives 72
3.3.1 Limitations 73

4 Using FRET-based cAMP sensors to explore the impact of maturation on β-adrenergic pathway in hiPSC-derived cardiomyocytes 82
4.1 Introduction 82
4.2 Results 85
4.2.1 EPAC-S^{H187} 87
4.2.1.1 Specific phosphodiesterase inhibition 87
4.2.1.2 β-adrenergic stimulation 92
4.2.1.3 Non-selective PDE inhibition 94
4.2.1.4 Adenylyl cyclase direct activation 96
4.2.2 Targeted sensors 97
4.2.2.1 CUTie sensors 97
4.2.2.2 FluoSTEP sensors 99
4.3 Discussion and perspectives 103
4.3.1 Limitations 104

5 Investigating maturation-induced physiological changes in hiPSC-derived CMs 106
5.1 Introduction 106
5.2 Results 108
5.2.1 Calcium handling 108
5.2.1.1 Basal conditions 108
5.2.1.2 β-adrenergic stimulation 111
5.2.2 Contractility 113

5.2.2.1 Basal conditions 113
5.2.2.2 β-adrenergic stimulation 115
5.2.3 Action potentials 117
5.2.3.1 Basal conditions 117
5.2.3.2 β-adrenergic stimulation 120
5.3 Discussion and perspectives 123
5.3.1 Limitations 127

6 Discussion **129**
6.1 The predictive power of snRNA-seq on hiPSC-CM function . . . 131
6.2 The replication of maturation protocols 139
6.3 How far are we still from adult CMs ? 143

References **147**

A Supplementary figures **166**

B Supplementary tables **174**

List of Figures

Figure 1.1 Schematic of excitation-contraction coupling in cardiomyocytes. 3
Figure 1.2 Schematic of excitation-contraction coupling adaptation to β-adrenergic stimulation in cardiomyocytes. 9
Figure 1.3 Schematic of several cAMP nanodomains and signalosomes in cardiomyocytes. 12
Figure 1.4 Features of immature and mature cardiomyocytes. 19
Figure 3.1 GO analysis of top 100 most expressed genes shows only cardiomyocytes. 52

Figure 3.2 The differentiation gives rise to two groups of hiPSC-CM, separated by their expression of cardiac genes. 53
Figure 3.3 New clustering reveals a subpopulation of proliferative cardiomyocytes. 55
Figure 3.4 The proportion of proliferative cardiomyocytes is decreased with maturation protocols. 56
Figure 3.5 Aerobic respiration is the main driver of the separation of LV from C and MM hiPSC-CM. 57
Figure 3.6 Metabolism in MM and synaptic organisation in C are the main drivers of the separation between these groups. . . 58
Figure 3.7 Decreased aerobic respiration in LV hiPSC-CM mainly drives their separation from C. 59
Figure 3.8 Decreased aerobic respiration and increased axon development make LV hiPSC-CM separate from MM. 60
Figure 3.9 MM and LV protocols do not bring hiPSC-CMs expression profile significantly closer to adult vCMs. 61
Figure 3.10 MM cells display signs of cardiac maturation and increased metabolism. 62
Figure 3.11 LV display signs of cardiac maturation and increased transcriptomic activity. 64
Figure 3.12 MM and LV hiPSC-CM still differ from adult left vCM mainly because of reduced cellular respiration. 65
Figure 3.13 MM and LV hiPSC-CMs are still much closer to C hiPSC-CMs than adult left vCMs. 67
Figure 3.14 PDE3B and LTCC show no band at the expected size. . . 69
Figure 3.15 A sarcomeric maturation is induced by both the metabolic maturation (MM) and left ventricle-like differentiation (LV) protocols. 70
Figure 3.16 Adult vCM donor D3 shows reduced cardiac activity-related gene expression, in favour of pro-inflammatory genes. 74

Figure 3.17 UMAP distances are not robust, a small change in data filtering can completely separate a cluster in two. 78

Figure 3.18 Most 'hiPSC-CM low' clusters are solely LV hiPSC-CM, with C and MM nuclei appearing in only one cluster. 81

Figure 4.1 Schematic presenting the different FRET-based cAMP sensors used. 86

Figure 4.2 Schematic presenting the principles of the FRET experiments, with the example of the cAMP sensor, EPAC-S^{H187}. 88

Figure 4.3 Example of ROIs drawn over hiPSC-CM transduced with EPAC-S^{H187} AAV. 88

Figure 4.4 PDE4 remains the main regulator of β-AR stimulation in hiPSC-CM. 89

Figure 4.5 Traces of individual biological replicates show the diversity of responses to the successive treatments. 91

Figure 4.6 An increased reliance on PDE3 is seen in some MM and LV hiPSC-CM in basal conditions. 92

Figure 4.7 The response to low ISO dose is mainly restricted by PDE4, with an increased importance of PDE3 in matured hiPSC-CM. 93

Figure 4.8 An increased reliance on PDE3 over PDE4 for cAMP regulation in the context of β-adrenergic stimulation is observed in hiPSC-CM from maturation protocols. 95

Figure 4.9 Maturation protocols induce an enhanced β-AR activity in response to isoproterenol (ISO). 97

Figure 4.10 AKAP79- and AKAP18-associated signalosomes in human cardiomyocytes. 98

Figure 4.11 Immunofluorescence confirms AKAP79- and AKAP18-CUTie sensors correct targeting in hiPSC-CM. 99

Figure 4.12 Targeted CUTie signal analysis faces important obstacles. 100

Figure 4.13 FluoSTEP sensors can be used to target endogenous proteins. 102

Figure 5.1 The maturation protocols tested do not induce a calcium handling maturation in basal conditions. 109
Figure 5.2 The LV protocol gives rise to more homogeneous hiPSC-CM populations in terms of calcium handling. 110
Figure 5.3 β-adrenergic stimulation induces a shortening of calcium transient decay time in control but a shortening of time to peak in ”matured” hiPSC-CM. 112
Figure 5.4 MM and LV maturation protocols have mixed effects on contractility. 113
Figure 5.5 Maturation protocols mainly impact sarcomere length. . . 114
Figure 5.6 β-adrenergic stimulation induces a shortening of contraction times in MM and LV hiPSC-CMs. 116
Figure 5.7 LV action potentials are shorter and more rectangular. . . 118
Figure 5.8 LV hiPSC-CMs electrophysiology is much closer to adult ventricular electrophysiology. 119
Figure 5.9 The proportion of ventricular-like action potentials is elevated in MM and further increased in LV hiPSC-CMs. . . . 121
Figure 5.10 MM hiPSC-CM react to ISO with a dose-dependant shortening of action potentials duration. 122

Figure 6.1 Comparison of the expression of genes involved in calcium cycling. 132
Figure 6.2 Comparison of the expression of genes involved in action potential. 133
Figure 6.3 Comparison of the expression of genes involved in β-adrenergic pathway. 134
Figure 6.4 Marker gene expression shows no difference in ventricular versus atrial hiPSC-CM proportions across protocols. . . . 137
Figure 6.5 The variability between differentiation batches is the main driver of global variability. 138
Figure 6.6 Differentiation variability creates functionally distinct subpopulations. 139

Figure A.1 Regular hiPSC-CM differentiation protocol and metabolic maturation. 166
Figure A.2 Left-ventricle like hiPSC-CM differentiation protocol. . . . 166
Figure A.3 Insertion of the GFP11 fragment at the C-terminus of Cx43 using Cas9 genome editing. 167
Figure A.4 Immunostaining confirmed pluripotency of edited Cx43-GFP cells. 168
Figure A.5 The relative expression of early and late cardiac genes by clusters reveals clusters with either high or low expression 169
Figure A.6 Average traces of cAMP sensor individual channels. . . . 170
Figure A.7 β-adrenergic stimulation have no robust effect on hiPSC-CM calcium transient. 171
Figure A.8 β-adrenergic stimulation induces a shortening of contraction times in MM and LV hiPSC-CMs. 172
Figure A.9 β-adrenergic stimulation induces a prolongation of action potentials in control cells but not in cells from the maturation protocols. 173

List of Tables

Table 2.1 41
Table 3.1 Example of discrepancies in GO annotations between well-known genes of similar functions. 75
Table 6.1 Summary of the relative efficiency of MM and LV protocols on hiPSC-CMs. 140
Table B.1 Statistical comparison of protein expression 174
Table B.2 Statistical comparison of calcium transient parameters . . . 175

Table B.3 Statistical comparison of calcium transient parameters in response to β-adrenergic stimulation 176
Table B.4 Statistical comparison of contraction parameters 180
Table B.5 Statistical comparison of contraction parameters in response to β-adrenergic stimulation 181
Table B.6 Statistical comparison of action potential parameters 184
Table B.7 Statistical comparison of action potential parameters in response to β-adrenergic stimulation 185

Acronyms and abbreviations

β-AR . . . . . β-adrenergic receptor

AAV . . . . . adeno-associated virus
AC . . . . . adenylyl cyclase
AKAP . . . . . A kinase-anchoring protein
ATP . . . . . adenosine triphosphate

C . . . . . control
cAMP . . . . . cyclic adenosine monophosphate
CFP . . . . . cyan fluorescent protein
CILO . . . . . cilostamide
CM . . . . . cardiomyocyte
cTnI . . . . . cardiac troponin I
Cx43 . . . . . connexin 43

DMSO . . . . . dimethyl sulfoxide
DPBS . . . . . Dulbecco's Phosphate buffered saline

EPAC . . . . . exchange protein directly activated by cAMP

FRET . . . . . fluorescence resonance energy transfer
FSK . . . . . forskolin

hiPSC . . . . . human induced pluripotent stem cell
hiPSC-CM . . . . . hiPSC-derived cardiomyocytes

IBMX 3-isobutyl-1-methylxanthine
iPSC . . . . . induced pluripotent stem cell
iPSC-CM . . . . . iPSC-derived cardiomyocytes
IQR . . . . . interquartile range

ISO . . . . . isoproterenol

LTCC . . . . . L-type calcium channel, $Ca_V1.2$

LV . . . . . left ventricle-like differentiation

MLC2a . . . . . atrial myosin light chain 2

MLC2v . . . . . ventricular myosin light chain 2

MM . . . . . metabolic maturation

MOI . . . . . multiplicity of infection

PDE . . . . . phosphodiesterase

PKA . . . . . protein kinase A

PLN . . . . . phospholamban

PP . . . . . phosphatase

R_{max} . . . . . maximum absolute R/R_0

R/R_0 . . . . . percentage of change in fluorescent ratio normalised to baseline

RNA . . . . . ribonucleic acid

ROLI . . . . . rolipram

RyR . . . . . ryanodine receptor channel

SERCA . . . . . sarco-endoplasmic reticulum calcium-ATPase

SL . . . . . sarcomere length

snRNA-seq . . . . . single nucleus RNA sequencing

SR . . . . . sarcoplasmic reticulum

ssTnI . . . . . slow skeletal troponin I

TBS . . . . . Tris buffered saline

T-tubules . . . . . transverse tubules

vCM . . . . . ventricular cardiomyocyte

YFP . . . . . yellow fluorescent protein

Chapter 1

Introduction

1.1 The cardiac function in health and disease

The human heart is an organ of central importance for the rest of the organism. It acts as a mechanical pump with regular contractions and relaxations, to ensure the circulation of blood through the entire body, thereby enabling the continuous delivery of oxygen, nutrients, and hormones to tissues while facilitating the removal of metabolic wastes. Given its importance, any dysfunction in cardiac activity can have profound consequences on overall health, making the heart a central focus of biomedical research. A comprehensive understanding of cardiac physiology and pathology is crucial for advancing the prevention, diagnosis, and treatment of cardiovascular diseases, which remain among the leading causes of death worldwide.

1.1.1 The excitation-contraction coupling

The coupling of excitation and contraction in cardiomyocyte (CM) is crucial in cardiac physiology, enabling the heart to function efficiently as a pump. This process integrates electrical signals with mechanical contraction through a finely tuned interplay of ionic fluxes, intracellular signalling, and molecular machinery (see Figure 1.1).

1.1.1.1 Cardiac action potentials

Spontaneous cardiac electrical activity arises from a subpopulation of CMs located in the right atrium, the sinus nodal CMs, which are distinguished

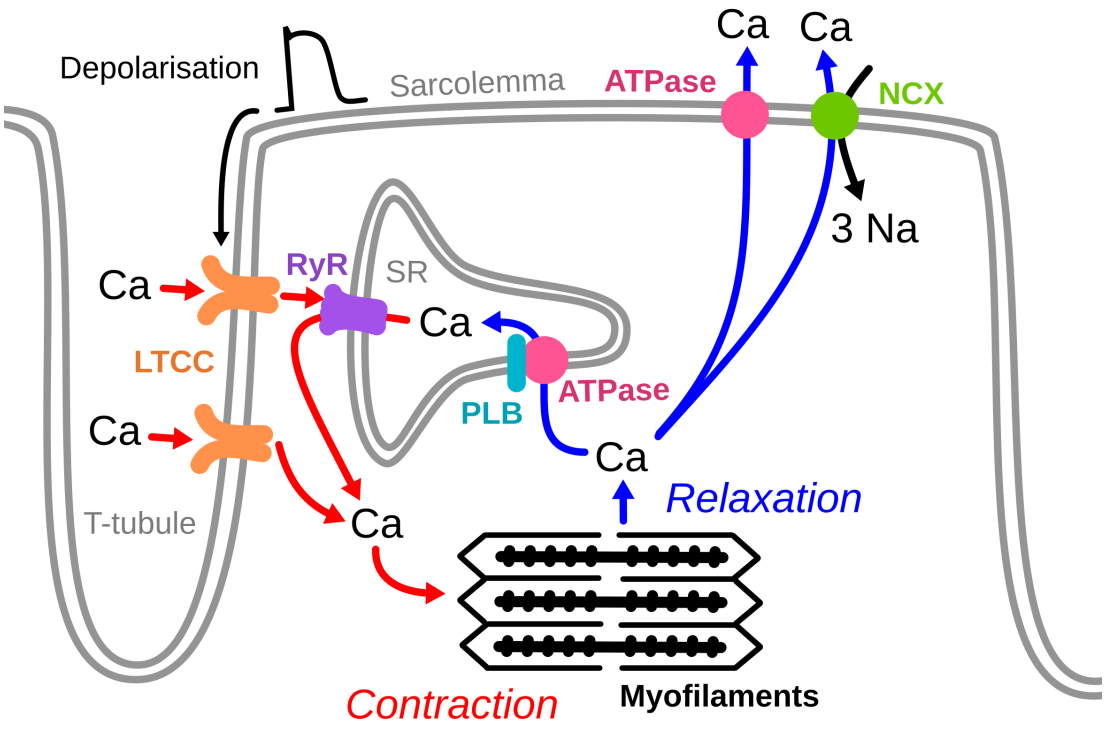

Figure 1.1: Schematic of excitation-contraction coupling in cardiomyocytes. *Representation of the link between intracellular calcium fluxes and CM contraction/relaxation. Red arrows show calcium entry and release from the SR that induce myofilaments to contract. Blue arrows illustrate calcium re-uptake and extrusion that allow relaxation. NCX = sodium-calcium exchanger, PLB = phospholamban, Ca = calcium ion, RyR = ryanodine receptor, LTCC = L-type Ca channel.*

by their pacemaker ability. Unlike other CMs, pacemaker cells display an unstable resting membrane potential with spontaneous depolarisation. This is due, on one hand, to the specific expression of hyperpolarisation-activated cyclic nucleotide–gated channels, a peculiar type of voltage-gated channels which, unlike most voltage-gated ion channels, activate at low voltages (below −50mV). They induce a mixed sodium/potassium influx during the hyperpolarisation of sinus nodal CMs (called the 'funny current'), which starts a slow depolarisation. In addition, localised spontaneous calcium leak from the sarcoplasmic reticulum (SR) through ryanodine receptor channels (RyRs), called calcium sparks, activate the sodium-calcium exchanger at the membrane, which increases the sodium influx, and therefore the depolarisation [1], [2]. When the membrane potential reaches about −50mV, it triggers a the successive opening of T-type and L-type calcium channels, which induces a fast depolarisation with a large influx of extracellular calcium ions. Progressively, because of the depolarisation, the calcium channels close and potassium channels open, leading to the repolarisation by efflux of potassium ions. This cyclic spontaneous depolarisation of pacemaker cells then propagates synchronously to all CMs through the atria first, then the signal converges to the atrioventricular node, and from there propagates to the ventricles through the bundle of His and Purkinje fibers. The crucial temporal and spatial coordination of action potentials across the myocardium is regulated by gap junctions, primarily composed of connexin 43, which enable rapid intercellular electrical communication [3]. In non-pacemaker CMs the propagation of an action potential across the sarcolemma is initiated by this transmitted depolarisation. The membrane potential rises from −90mV to −70mV and this triggers the rapid depolarisation phase (less than 2ms) to around +50mV, with the influx of sodium ions through activation of the voltage-gated sodium channels ($Na_V1.5$), followed by a plateau phase driven by the balance between calcium influx via L-type calcium channel, $Ca_V1.2$ (LTCC) and potassium efflux through delayed rectifier channels ($K_V11.1$, $K_V7.1$). This prolonged depolarization ensures

a sustained contraction necessary for efficient cardiac ejection. Finally, calcium channels progressively close, allowing the fast repolarisation of the CM. When the membrane potential returns below −70mV, the inward-rectifier potassium channel (K_{IR}) take over and participate to the ion fluxes equilibrium maintaining the membrane potential at its resting value of −90mV [4].

1.1.1.2 Calcium cycling

Calcium ions serve as the central link from electrical excitation to mechanical contraction. Following the depolarization of the sarcolemma, calcium enters the cytoplasm through LTCCs during the plateau phase of the action potential. LTCC are located predominantly within the transverse tubules (T-tubules), profound invaginations of the sarcolemma, required for an efficient and synchronous excitation-contraction coupling [5]. T-tubules associate with SR to form a functional dyad where LTCC and RyRs are kept in close proximity. This is crucial as the initial modest calcium influx through LTCC triggers a much larger release of calcium from the SR via RyRs, in a process termed calcium-induced calcium release (CICR). The resultant rise in cytosolic calcium concentration facilitates the binding of calcium ions to troponin C on the actin filaments of sarcomeres, inducing a conformational change in the troponins complex thereby promoting actin-myosin cross-bridge formation and muscle contraction. The initiation of relaxation necessitate the removal of calcium ions from the cytosol to allow its dissociation from troponin C. This is primarily achieved by the reuptake of calcium into the SR via the sarco-endoplasmic reticulum calcium-ATPase (SERCA) pump, which thereby restores the SR calcium stocks for the next contraction. SERCA activity is tightly modulated by the regulatory protein phospholamban, which undergoes phosphorylation to relieve its inhibitory effect on the pump. The SR calcium-buffering capacity is increased by luminal calcium-binding proteins such as calsequestrin. In addition to the SR reuptake, the sodium-calcium exchanger and the plasma membrane calcium-ATPase also extrude calcium ions from the cell, to restore diastolic

calcium levels.

1.1.1.3 Sarcomeres, the contractile unit

The sarcomere, the fundamental contractile unit of striated muscles, plays a pivotal role in the contraction of the cardiac muscle by translating biochemical signals into mechanical force. Its highly organized structure, composed of repeating units of actin and myosin filaments, ensures the efficient conversion of chemical signal into mechanical work. The sarcomere is built in mirror and delimited by Z-discs, which anchor the thin actin filaments. Within the sarcomere, thick myosin filaments are intercalated between thin filaments, with their heads projecting outwards to interact with actin. Thick filaments are formed by myosin heavy chains (MHCs) and associated light chains (MLCs). Each myosin molecule contains a globular head with actin-binding and ATPase activity, enabling force generation through cross-bridge cycling. Myosin-binding protein C interacts with both actin and myosin, modulating filament alignment and contraction kinetics. The giant protein Titin extends from the Z-disk to the middle of the sarcomere (the M-band) and runs along the thick filaments to bind them. It also acts as a molecular spring to maintain sarcomeric integrity and elasticity during contraction and relaxation cycles [6]. The actin-myosin interaction is regulated by the troponin-tropomyosin complex, which is embedded in the actin filaments. The troponin complex comprises three subunits: troponin C, the calcium-binding component ; troponin I, the inhibitory subunit that prevents actin-myosin interaction in the absence of calcium ; and troponin T, the subunit anchoring the complex to tropomyosin. Tropomyosin, is a filamentous protein which lies within the grooves of the actin helix, blocking the myosin-binding sites under resting conditions. Sarcomeres associate longitudinally at Z-disks to form myofibrils, which are anchored to the sarcolemmal cytoskeleton by desmin filaments. Myofibrils are organised in parallel bundles to ensure efficient unidirectional contraction [7].

The initiation of cardiac contraction is tightly regulated by intracellular calcium transients. During excitation-contraction coupling, calcium released from the SR binds to troponin C, inducing a conformational change in the troponin-tropomyosin complex. This shift exposes myosin-binding sites on actin, allowing cross-bridge formation. Adenosine triphosphate (ATP) is indispensable for the energy-intensive process of cross-bridge cycling. Myosin heads bind ATP, which is hydrolysed to adenosine diphosphate (ADP) and inorganic phosphate (P_i), priming the myosin for interaction with actin. Upon binding, P_i is released, which triggers a conformational change wherein the myosin head pivots, pulling the actin filament. This generalised phenomenon induces a global sliding of the actin filaments relative to the myosin filaments, and towards the M-band, on both sides of the mirrored sarcomere. This bi-directional sliding results in the overall contraction of the sarmomere, and through this, the contraction of the whole CM. ADP is subsequently released, and ATP binding to myosin detaches the cross-bridge, allowing the cycle to repeat. This cyclical process, driven by the hydrolysis of ATP, ensures continuous sarcomeric contraction as long as calcium levels remain elevated.

The force developed is dependent on calcium concentration, actin filaments' calcium sensitivity and initial sarcomere length. The relationship between cytoplasmic calcium concentration and force development is sigmoidal, characterized by a threshold, steep activation phase, and saturation plateau. Importantly, this relationship is modulated by cooperative interactions within the thin filament, whereby binding of calcium to one troponin complex enhances the likelihood of neighbouring complexes binding calcium [8]. At submaximal calcium levels, calcium sensitivity plays a key role in thin filament activation, which critically determines the force produced. Factors such as post-translational modifications of sarcomeric proteins (e.g. phosphorylation of troponin I) and changes in the isoform composition of troponin and tropomyosin can significantly alter calcium sensitivity. Additionally, sarcomere length (SL) profoundly influences the force-generating capacity of muscle through two primary mechanisms: the

length-tension relationship and length-dependent activation. The length-tension relationship delineates an optimal SL (2.0-2.2 µm in human striated muscle) at which maximal overlap between actin and myosin filaments occurs, allowing for optimal cross-bridge formation. Deviations from this optimal length reduce force production due to suboptimal filament overlap (at shorter lengths) or diminished cross-bridge binding potential (at longer lengths) [9]. Length-dependent activation refers to the increase in thin filament calcium sensitivity and therefore force generation with increasing SL. This phenomenon is attributed to changes in the lattice spacing between actin and myosin filaments, which influence the probability of cross-bridge interactions. At longer SLs, reduced lattice spacing enhances the proximity and alignment of myosin heads with actin-binding sites, thereby increasing the likelihood of force-generating cross-bridges. Additionally, length-dependent structural changes in the thin filament may enhance the cooperative activation of troponin-tropomyosin complexes, further augmenting calcium sensitivity [10].

Relaxation of the sarcomere occurs when cytosolic calcium levels decline through reuptake in the SR and extrusion to the extracellular space. As calcium dissociates from troponin C, tropomyosin re-blocks the myosin-binding sites on actin, terminating cross-bridge cycling and allowing the sarcomere to return to its resting state.

1.1.2 The β-adrenergic pathway

1.1.2.1 Role of the β-adrenergic stimulation on cardiac function

β-adrenergic stimulation is a key regulatory mechanism in cardiac physiology, enabling the heart to adapt to increased peripheral metabolic demands through enhanced force development (inotropy), heart rate (chronotropy), and relaxation (lusitropy) (see Figure 1.2).

Adrenergic receptors are responsible for the signal transduction from the sympathetic system to effector cells and in particular CMs. The most

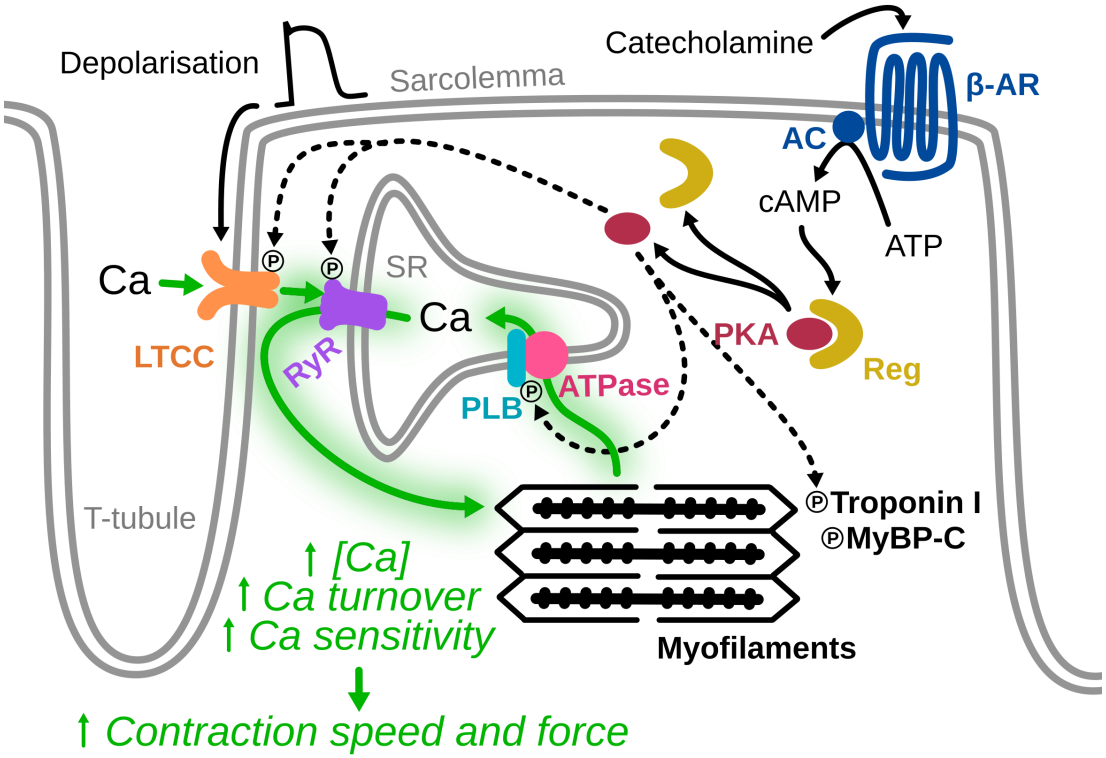

Figure 1.2: Schematic of excitation-contraction coupling adaptation to β-adrenergic stimulation in cardiomyocytes. *Representation of changes in mature CM function induced by catecholamine activation of the β-adrenergic pathway. Green arrows represent increased calcium entry and release from the SR inducing faster and stronger contraction, and faster relaxation through calcium re-uptake. β-AR = β-adrenergic receptor, AC = adenylyl cyclase, PKA = protein kinase A catalytic subunit, Reg = PKA regulatory subunit, PLB = phospholamban, Ca = calcium ion, RyR = ryanodine receptor, LTCC = L-type Ca channel.*

expressed isoform in human CMs is the β-adrenergic receptor (β-AR). Upon catecholamine binding, β-ARs activate the stimulatory G protein (Gs), leading to an increase in adenylyl cyclase (AC) activity and subsequent cAMP production. cAMP serves as an intracellular second messenger, activating protein kinase A (PKA), the central effector of β-adrenergic signalling. PKA is a serine/threonine kinase and orchestrates a cascade of phosphorylation events targeting key proteins in cardiac excitation-contraction coupling [11]. In particular, PKA phosphorylates LTCCs, RyR, phospholamban and troponin I, with the following effects:

Phosphorylation of the α1C subunit of LTCCs increases calcium influx from extracellular space during depolarization, augmenting CICR from SR. PKA-mediated phosphorylation of RyR2 directly promotes calcium release from the SR, increasing the amplitude of calcium transients ; and, together with phosphorylation of LTCCs, enhances contractility (inotropy). In its unphosphorylated state, phospholamban inhibits the SERCA. PKA phosphorylation relieves this inhibition, accelerating calcium reuptake into the SR and improving relaxation (lusitropy). Phosphorylation of troponin I reduces calcium sensitivity of the thin filament, facilitating faster dissociation of calcium from troponin C during diastole (chronotropy). These modifications collectively enhance both systolic contraction and diastolic relaxation, thereby increasing cardiac output.

1.1.2.2 cAMP compartmentalisation

cAMP is a ubiquitous second messenger that orchestrates - through the activation of PKA - a myriad of cellular processes, including gene expression, metabolism, and excitation-contraction coupling, particularly in CMs. However, it has been shown since the late 1970's that distinct effects could be obtained through the activation of different G protein-coupled receptors, despite a similar increase in global cAMP and PKA activity [12]. The coordination of the multiplicity of cAMP/PKA dependent effects is achieved via spatial and temporal confinement of PKA, but more

importantly cAMP, within the cytoplasm [13]. These functional localised gradients of cAMP are called nanodomains, as their size has been measured to be in the range of 30-60 nm [14], [15]. Current evidence suggests that four phenomena may contribute to generate these cAMP gradients: localized cAMP production, localised breakdown by phosphodiesterases (PDEs), restricted diffusion and buffering of cAMP.

One of the main actors of this confinement are A kinase-anchoring protein (AKAP), scaffold proteins that bind together β-AR, AC, PKA, PKA phosphorylation targets, phosphatases (PPs) and PDEs. Individual AKAPs preferentially bind specific isoforms of β-AR, AC, PDE as well as specific target proteins. This leads to the formation of various functional combinations called signalosomes. For obvious reasons, these signalosomes are mainly studied in rodents but there are discrepancies in many signalosomes components, and the role of specific PDE isoforms can be different in humans compared to what is seen in rodents, which is thought to be one of the main reasons for recurring unsuccessful clinical translation of promising findings [16]. In humans and rodents, AKAP18 links PKA to the SERCA, phospholamban (PLN), and PDE3A [17]. In rodents, AKAP79 tethers PKA to β2-AR, AC5/6, LTCC and PDE4D [18]. While this has not been directly confirmed to be the case in human hearts, indirect evidence suggests a similar complex [19] (see Figure 1.3).

The adrenergic pathway is highly responsive through the localised production of cAMP, and the close proximity of PKA to its targets. However, to ensure specificity of its effects, cAMP diffusion must be strictly controlled, as evidenced by experiments using fluorescence resonance energy transfer (FRET)-based cAMP sensors [20]. cAMP diffusion is thought to be shaped by PDEs, which act as ”sinks” by degrading cAMP from specific locations [21]. However some studies suggest that PDEs degradation capacity is not sufficient to prevent all diffusion of cAMP out of the nanodomains so there are likely other mechanisms involved [22], [23]. Recently, it was shown that the regulatory subunit of PKA undergoes liquid-liquid phase separation,

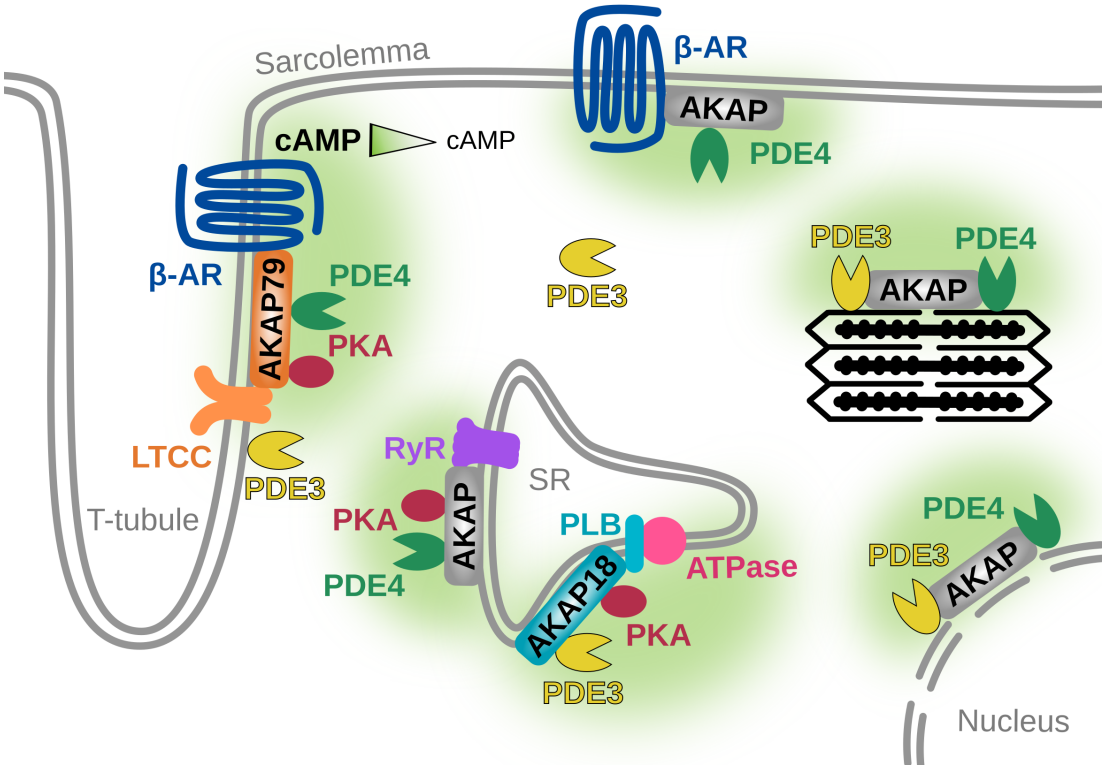

Figure 1.3: Schematic of several cAMP nanodomains and signalosomes in cardiomyocytes. *Representation of the main cAMP nanodomains and respective signalosomes in adult CMs. Shaded green areas represent the limits of each nanodomain, with color intensity showing variations of cAMP concentration. β-AR = β-adrenergic receptor, PDE = phosphodiesterase, PKA = protein kinase A catalytic subunit, AKAP = A kinase anchoring protein, PLB = phospholamban, Ca = calcium ion, RyR = ryanodine receptor, LTCC = L-type Ca channel.*

forming aggregates in the cytosol. These aggregates can capture cAMP, thereby limiting its diffusion [24]. Nonetheless, cAMP degradation by PDEs remains a key process in the β-adrenergic pathway regulation.

Among the 9 PDE isoforms expressed in human cardiac tissues, PDE3 and PDE4 have emerged as central regulators of the β-adrenergic pathway and excitation-contraction coupling in CMs [16]. PDE3 enzymes hydrolyze both cAMP and cyclic guanosine monophosphate, though they exhibit a markedly higher affinity for cAMP. The two isoforms of the PDE3 family, PDE3A and PDE3B, are expressed in the heart, with PDE3A being more predominant in CMs [25]. PDE3B is expressed in T-tubules, while PDE3A localizes to distinct subcellular domains, including the SR, where it modulates PLN phosphorylation and SERCA activity, and the sarcolemma, where it influences LTCC activity. Through these mechanisms, PDE3 regulates intracellular calcium handling, thereby exerting a profound effect on contractility and relaxation. PDE4 enzymes however, specifically hydrolyse cAMP. 3 isoforms of the PDE4 family are expressed in the heart: PDE4A, PDE4B and PDE4D [26], [27]. PDE4D is the most abundant isoform and is restricted to cAMP nanodomains via interactions with AKAPs and other scaffolding proteins. At the plasma membrane, specific PDE4D variants modulate β1- and β2-adrenergic receptor signalling, influencing receptor desensitization and alternative signalling. PDE4B, associates with LTCCs and inhibits β-AR stimulation of L-type calcium currents. Within the sarcoplasmic reticulum, PDE4D localizes to the RyR2 and interacts with the SERCA2–phospholamban complex, regulating calcium handling. Though PDE4 is expressed in both rodent and human hearts, its overall contribution to cAMP degradation is smaller in humans. Despite its localisation at the SR and β-ARs, inhibition of PDE4 by selective agents like rolipram has been shown not to affect catecholamine-induced inotropic and lusitropic responses. However, it was shown to potentiate the inotropic responses of cardiac tissue to PDE3 inhibition, suggesting a more critical role when cAMP levels are increased [26].

1.1.3 The β-adrenergic pathway in disease and during cardiac development

In the context of cardiovascular diseases, and particularly heart failure (HF), β-adrenergic signalling and cAMP nanodomains are profoundly dysregulated. Chronic HF is associated with extensive cardiomyocyte remodelling, including loss of T-tubule structure, which causes β_2-ARs to redistribute throughout the cell, losing their confinement to T-tubules. This redistribution leads to a more diffuse cAMP signal, a mechanism linked to arrhythmias [28]. In failing hearts, the proper association of PKA with AKAPs is markedly reduced [29], including diminished interaction between PKA and AKAP1 [30] and down-regulation of AKAP79 [31]. Despite elevated sympathetic activity, HF is paradoxically associated with reduced intracellular cAMP content and decreased phosphorylation of PKA substrates, thereby impairing cardiac contractility. Specifically, phosphorylation of PLN, cTnI, and myosin-binding protein C (MyBP-C) is diminished in human HF [32], [33]. Altered regulation of PDEs also contributes to disease progression: levels of PDE3A and PDE4D are decreased, which can provoke sarcoplasmic reticulum Ca^{2+} leak and cardiomyocyte apoptosis through PKA-dependent hyperphosphorylation of the RyR2 [34], [35], although some discrepancies remain between studies about these PDEs expression and activity. Conversely, PDE1 and PDE2 expression is upregulated in HF [36], [37]. The redistribution of PDEs, caused by T-tubule and AKAP loss, likely explains the impaired function, beyond changes in PDE expression [38]. Numerous PDE inhibitors have undergone clinical evaluation for their potential cardioprotective effects, due to chronic elevated sympathetic activity. However, despite promising preclinical data, these trials have showed mixed results, especially in long-term treatments [16]. Several factors likely contribute to the discrepancies between preclinical success and clinical outcomes. Key challenges lie in interspecies differences in PDE expression and localisation patterns, but also the complex interplay between the differential effect of specific isoforms. Moreover, even isoform-selective

inhibitors may not solve the problem if the targeted PDE is in different subcellular compartments with opposing physiological roles. This highlights the need for further research on the matter, drug screening and disease modelling to find new strategies against cardiovascular diseases.

Beyond HF, related pathologies also involve impaired cAMP/PKA signalling: in hypertrophic cardiomyopathy (HCM), PKA-dependent phosphorylation of myofilament proteins is reduced, while PLN phosphorylation remains unaffected [39]. And in diabetic cardiomyopathy, insulin resistance drives a PDE4D-mediated decline in total PKA activity [40]. Moreover, sustained catecholamine stimulation not only accelerates HF progression but also promotes insulin resistance in cardiomyocytes, where chronic β_2-AR overstimulation inhibits insulin-induced GLUT4 translocation to the plasma membrane, thereby reducing glucose uptake in a PKA-dependent manner [41].

The structural changes observed during disease remind what is seen in immature CMs. However, very few studies have focused on the β-adrenergic pathway evolution during cardiac development *in vivo*. In neonatal rat cardiomyocytes, adrenergic stimulation increases the calcium entry through LTCC [42]. Additionally, adrenergic stimulation induces phospholamban phosphorylation. However, calcium transients are not systematically altered, reflecting the immature functional state of the SR [43]. Moreover, a decrease in β-AR/AC sensitivity is observed between foetal and neonatal rat hearts, associated with a reduction in β-AR expression and also suggests uncoupling from AC [44]. Expression of β_2-AR is almost divided by two between human fetal hearts and adult human hearts, while β_1-AR is increased two-fold in adult vCMs compared to fetal CMs [45].

As functional measurements from *in vivo* models are limited, *in vitro* approaches using differentiating hiPSC-CMs represent an unprecedented opportunity to study the establishment of the β-adrenergic pathway [38], [46].

1.2 The use of hiPSC-CM in cardiovascular disease modelling

1.2.1 hiPSC-CM differentiation

Induced pluripotent stem cell (iPSC) originate from differentiated somatic cells that have been reprogrammed using specific transcription factors. Takahashi and Yamanaka were the first to identify 4 transcription factors necessary to de-differentiate cells: OCT3/4, SOX2, KLF4 and c-MYC [47]. iPSCs have the same advantages as embryonic stem cells as they self-renew and can then be re-differentiated into any cell type they have the advantage of raising fewer ethical problems. Therefore, they represent an easy way to obtain large quantities of human cells without the sourcing difficulties associated with some human primary samples, like cardiac cells. Moreover, human induced pluripotent stem cell (hiPSC) provide a true revolution in biology as they can be generated directly from patient cells, which is advantageous for medical applications as they possess the unique advantage of reflecting the genetic background of individual patients, thereby improving cardiovascular diseases modelling and facilitating personalized medicine approaches [48], [49]. For that reason, hiPSCs are an extensive and powerful tool to study developmental processes, for drug discovery, disease modelling, and regenerative medicine [50]. In particular, hiPSC-CM have been successfully used to model different life-threatening cardiac diseases such as hypertrophic [51] and dilated cardiomyopathy [52], and long QT [53] and Brugada syndrome [54]. hiCMs are more relevant than rodent CMs when studying human cardiac pathophysiology because there are important species differences in terms of ion channel abundance, protein isoforms, and electrophysiological properties between rodent and human that can confound and slow down clinical translation [55].

Efficient differentiation into CMs is required to ensure robustness and applicability of this promising research model. Several methods exist to

generate hiPSC-CMs and differentiation protocols have rapidly evolved to increase the CM yield (purity), and simplify the process. CM differentiation from iPSCs uses modulation of signalling pathways involved in cardiac development during normal embryogenesis [56]. There have been two main strategies to generate functional CMs from iPSCs, the differentiation of embryoid bodies and two-dimensional (monolayer) culture. Embryoid bodies are floating cell aggregates of pluripotent cells that have the ability to spontaneously produce derivative cells of all the three germ layers [57]. Originally, uncontrolled embryoid bodies differentiation was used to generate CMs from pluripotent cells. However, this procedure relying on the presence of serum suffered from low reproducibility and inter-line variability [58].

During embryonic development in vivo, pluripotent cells go through several steps to give rise to CMs: A mesoderm induction followed by early cardiac induction gives rise to cardiac progenitors, which in term fully differentiate into CMs. The in vitro differentiation protocols now use a directed specification of pluripotent cells, using this knowledge. Growth factors such as activin A, FGF2, and BMP4 were transitorily added to the culture medium to induce cardiac differentiation, in both embryoid bodies and monolayers, with a much higher efficiency [59], [60]. The stage-specific roles of these factors were subsequently examined, and highlighted the need for carefully optimized timings and concentrations for each cell line, through monitoring of cardiac differentiation, especially in the early stages [61]. The yield of cardiomyocytes was further enhanced, and the overall differentiation process became more consistent. A cross-talk between the BMP4/activin A and Wnt/β-catenin pathways was then identified as central for cardiac differentiation and new protocols explored this finding, using various combinations of activators and inhibitors of these pathways.

The cost of growth factors being comparatively expensive, and often less efficient in terms of variability and efficiency (CM yield), a transitory activation of the sole Wnt pathway using CHIR99021, followed by inhibitors

such as IWR, IWP2 or IWP4 have emerged as standard procedure [62]. However, these directed differentiation protocols did not selectively control CM lineage generation, leading to heterogeneous populations predominantly composed of ventricular CMs. Research on new procedures to generate specific CM lineages (mainly atrial and nodal) highlighted the predominant role for the activin A pathway, and more specifically the retinoic acid, in generation of atrial CMs [63]. With timings and concentration adjustments of this small molecule strategy, the differentiation efficiency is now around 90-95%. And with new protocols to generate specific CM lineages, hiPSC-CMs have emerged as a powerful tool in cardiovascular research [64].

1.2.2 hiPSC-CM characteristics

No model is perfect, and the main limitation of hiPSC-CMs is their relative developmental immaturity when compared to adult primary CMs. Indeed, hiPSC-CMs show more similarities with foetal CMs than adult CMs in some characteristics of their function and shape [65] (see Figure 1.4).

In terms of morphology, adult CMs display a rod-like shape with deep tubular invaginations of the sarcolemma called T-tubules. T-tubules are crucial in the normal physiology of CMs and the heart. They cluster ion channels such as LTCC which are integral to excitation-contraction coupling, and are rich in β2-adrenergic receptors, which are activated on sympathetic stimulation. T-tubular disruption is associated with pathological mechanisms that can lead to heart failure and increase the risk of life-threatening arrhythmogenic events [68]. In addition, adult CMs have highly organised sarcomeres and they display abundant tightly packed mitochondria, which are well aligned with the cardiac sarcomeres. In contrast, hiPSC-CMs are much smaller, with underdeveloped and disorganised sarcomeres, no T-tubular network, and fewer mitochondria. Moreover, an isoform switch occurs early on during development/maturation from foetal to adult sarcomeric proteins. For example, the cardiac troponin I (cTnI) replaces the slow skeletal troponin I (ssTnI), and a clear chamber specification occurs

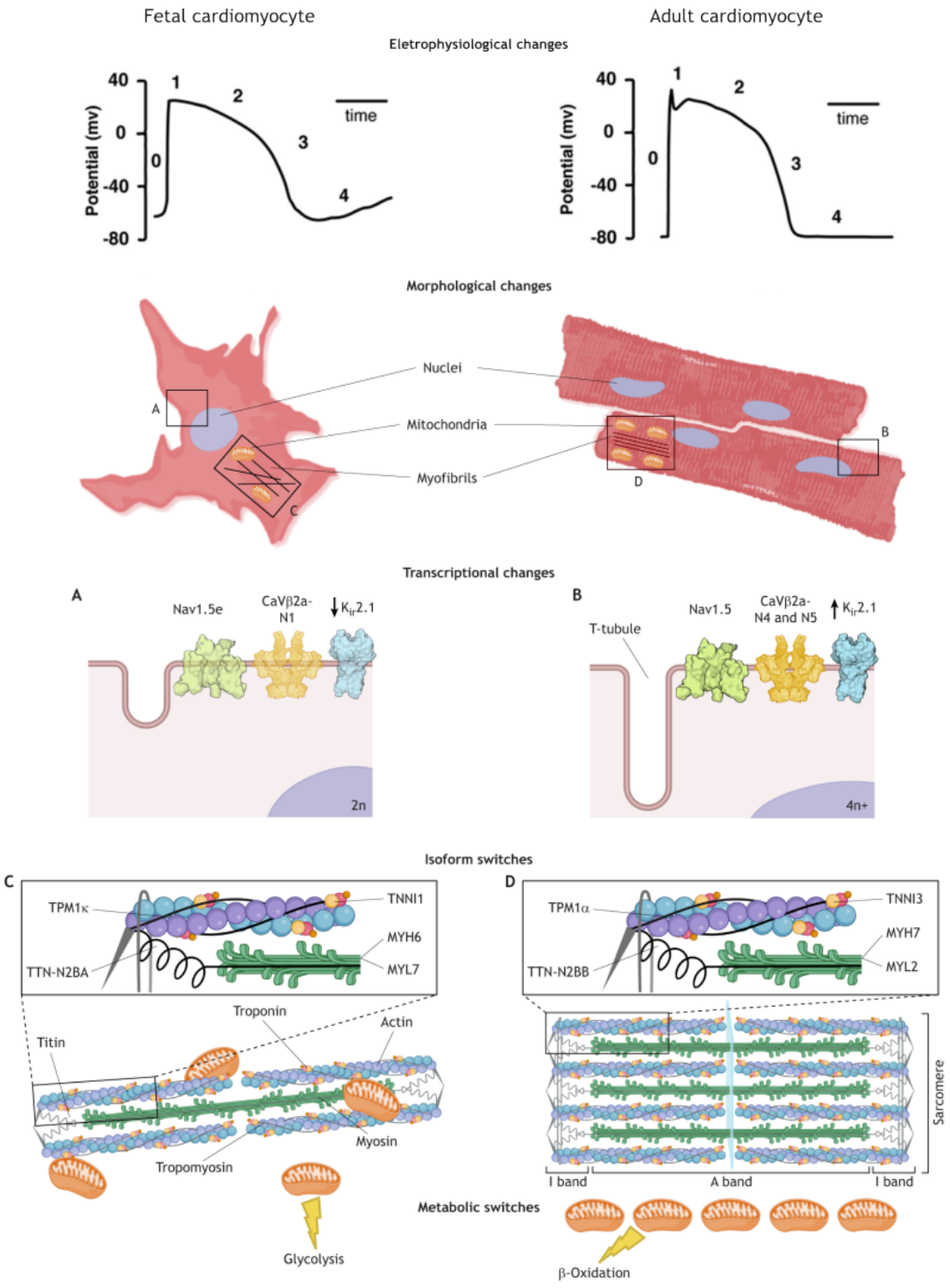

Figure 1.4: Features of immature and mature cardiomyocytes. *Adapted from Karakikes et al., Circulation Research (2015), Figure 3A [66] and Ottaviani et al., Development (2023), Figure 1 [67]. Cardiomyocyte maturation from fetal (left) to adult (right), with electrophysiological, morphological, transcriptional, ultrastructural and metabolic changes.* ***Top****: Schematic of ventricular APs. Phases 0 to 4 are the rapid upstroke, early repolarization, plateau, late repolarization, and diastole, respectively.* ***A,B****: Characteristic ion channels expressed at the plasma membrane of (A) immature versus (B) mature cardiomyocytes.* ***C,D****: Characteristics and structure of muscle fibres in cardiomyocytes, including magnifications of the sarcomeres in fetal cardiomyocytes (C) versus adult cardiomyocytes (D).*

between the atria and the ventricles with atrial myosin light chain 2 (MLC2a) and ventricular myosin light chain 2 (MLC2v) respectively, whereas only MLC2a is expressed in foetal and immature CMs [69]. These switches are associated with a change in CMs contractility due to their different properties [70].

The contractile function of CMs is also intrinsically linked to calcium dynamics. In hiPSC-CM, the immature calcium handling properties, additionally to the under development and disorganisation of sarcomeres, translate to reduced contractile force as compared to adult CMs. In native human CMs, the contraction is initiated during the plateau phase of the action potential, where calcium enters the cell via LTCC. This influx triggers the opening of RyR2 channels on the SR, leading to a substantial release of calcium into the cytoplasm. This allows myofilament contraction. Subsequently, relaxation occurs as calcium is re-sequestered into the SR through SERCA2 reuptake, or extruded from the cell via the sodium/calcium exchanger NCX1. In hiPSC-CM, while the fundamental components of calcium handling are present, there are notable differences compared to adult CMs. As immature hiPSC-CM lack a well-developed T-tubule system, there is a spatial separation between LTCCs and RYR2 channels. This structural disparity leads to a reduced and slower calcium release from the SR, making hiPSC-CM more reliant on transsarcolemmal calcium influx for contraction. Additionally, a larger fraction of cytosolic calcium is removed via NCX1 rather than reuptake into the SR, contributing to prolonged calcium transients and slower relaxation times [71].

The electrophysiological properties of hiPSC-CM are foundational to their function as cardiac cells. These cells exhibit spontaneous action potentials, regardless for their specific lineage differentiation, whereas only a specific subset of adult cardiac cells are pace-makers [72]. This phenomenon is due to the presence of pacemaker currents, primarily mediated by hyperpolarisation-activated cyclic nucleotide-gated channels. The action potentials in hiPSC-CM are characterized by a more depolarized resting

membrane potential, reduced upstroke velocity, and prolonged duration compared to adult CMs. These differences are attributed to the distinct profiles of ionic currents, including lower densities of inward rectifier potassium currents (I_{K1}) and variations in sodium (I_{Na}) and calcium (I_{Ca}) currents [66].

Adult CMs are characterised by a high energy production and consumption to support the constant contraction-relaxation cycles of the heart, which increases dramatically during physical activity. Mitochondria are therefore numerous and well organised, in close proximity to sarcomeres in adult CMs. During cardiac development, additionally to increasing density and organisation of mitochondria, substrate utilisation changes from glucose and lactate in the fetal heart primarily to fatty acids in the adult heart [73]. On this matter again, hiPSC-CMs display embryonic to fetal CMs characteristics [74].

Fetal CMs show chronotropic responses (increased beating frequency) in response to beta-adrenergic stimulation (norepinephrine) early in development [75]. In hiPSC-CM, β-ARs are present and functional, but their responsiveness varies with the maturation state of the cells. Younger hiPSC-CM predominantly express β_2-adrenergic receptors, while the expression of β_1-adrenergic receptors increases with maturation [46]. The effects of β-adrenergic stimulation on contractile force and relaxation rate vary greatly with the age of hiPSC-CM culture, but they are not as robust as in adult CMs [76].

Such physiological properties reflect the immature state of hiPSC-CM, and question the ability of this model to fully recapitulate adult disease phenotypes. Additionally, current differentiation protocols often give rise to heterogeneous populations of CMs and are characterised by excessive variability [77]. These problems limit the applicability of hiPSC-CMs in cardiovascular research and translational medicine, and underscore the need for strategies aimed at promoting their maturation to achieve adult-like cardiac physiology.

1.2.3 Maturation of iPSC-CM

In order to improve the applicability of hiPSC-CMs as a research model, focus incline toward generation of a highly mature and homogeneous CM population through new differentiation methodologies and technical modifications of current hiPSC-CM culture methods.

Prolonged time in culture, beyond 80 days, have proven to increase maturity of hiPSC-CMs. It happened through the development of key current densities implicated in cardiac action potentials, in relation to increased corresponding ion channels expression. Calcium transient velocities and sarcomere development were also reported [78]–[80]. However, in addition to the substantial cost of this strategy, there are inconsistencies between the different studies, and the variability within the hiPSC-CM cultures was persistent [81].

Other approaches used to induce maturation in vitro target specific pathways and processes underpinning CM physiology that are altered in hiPSC-CMs using biophysical, biochemical and mechanical properties of the native heart. 3-dimensional (3D) culture, long-term electrical stimulation, increased mechanical strain and fatty acid enrichment have all aided, separately, to produce more mature hiPSC-CMs [67].

Recently, several studies have focused on the influence of cardiac non-myocytes on hiPSC-CMs maturity. Giacomelli and collaborators co-cultured iPSC-derived cardiac fibroblasts (CFs), endothelial cells (ECs) and CMs, in 3D microtissues [82]. After 21 days, the CMs from these microtissues show an enhanced maturity when compared to CMs cultured alone in 2D or in the presence of only ECs or CFs. Their results suggest that cAMP and the downstream β-adrenergic pathway could be involved in CM maturation. The suggested mechanism of maturation in the co-cultured system is a close coupling between CFs and CMs from these microtissues, involving Connexin 43 gap-junctions, which can act as a bridge to allow the diffusion of cyclic guanosine monophosphate (cGMP) from the CFs to the CMs in co-culture.

There, cGMP is thought to enhance cAMP levels via the inhibitory effects of cGMP on PDE 3 that degrade cAMP. In other terms, PDE3-specific inhibition could be used to further mature hiPSC-CM, even in 2D monolayer.
PDE3 and PDE4 are the main regulators of the cAMP-PKA pathway in human CMs, although their relative predominance varies during cardiac development and in disease. PDE4 is the primary isoform responsible for regulating cAMP-PKA signalling in immature CMs, whilst PDE3 supplant PDE4 in adult CMs. In disease, such as heart failure, both isoforms are downregulated. It is important to highlight that PDE3 activity is associated with various downstream effects, depending on the nanodomain it is involved in [25]. With maturation, the cAMP-PKA pathway develops in hiPSC-CM. Maturation is associated with a significant increase in β-AR and ACs expression resulting in an increased cAMP production following isoproterenol treatment, and increased PKA-mediated phosphorylation of Troponin I and Phospholamban in hiPSC-CMs. Moreover, while no specificity of β-AR subtype for activation of downstream mediators was shown in early hiPSC-CMs, caveolar nanodomains develop, allowing β_2-AR compartmentation in more mature hiPSC-CMs [46].

Some techniques are more efficient than others at maturing hiPSC-CMs, but there is still no protocol that generates fully matured adult CMs from iPSCs. Research is now focusing on combining these techniques and defining the mechanisms and pathways that progress CM maturity when differentiating from iPSCs.

Combining methods has proven by far to give the best results in terms of global maturity. In an experiment combining 3D culture with electrical and physiological stimulation, the different types of stimulation potentiated the effects on maturation and gave rise to cardiac cells with a high comprehensive degree of maturity [83]. Another study combined fatty acid enrichment, nanopatterning and electrostimulation, demonstrating that although electrical stimulation contributed most to changes in maturity, combination of the techniques achieved the highest level of maturity [84].

However, integrating multiple techniques necessitates additional expertise, materials, and costs. Therefore, gaining a deeper understanding of the mechanisms underlying CM maturation could enhance robustness and facilitate the development of more streamlined protocols.

1.2.4 Overview of hiPSC-CM maturation protocols used in this thesis

In this thesis, the relative efficiency of two protocols designed to increase hiPSC-CM maturity, on several features of CMs physiology are explored. The first paper, published by Feyen and colleagues [85] established a culture medium based on adult CM metabolic needs. Their maturation medium is designed to increase utilisation of FAO in hiPSC-CMs and reduce reliance on glycolysis as an energy source, pushing hiPSC-CMs towards the metabolic switch CMs undergo during maturation. The MM medium differs from routinely used media such as RPMI+B27 by an increased calcium concentration to aid CM contractility; lower glucose levels to promote FAO; and supplementation with creatine, L-carnitine, and taurine to support CM energetics, as used in the culture of adult CMs. When cultured with MM medium, hiPSC-CMs show an increase in FAO, but they also display more global maturation. This includes a more mature ultrastructure with highly aligned sarcomeres and more abundant mitochondria, localised closer to the nucleus and sarcomeres. MM medium also induces maturational effects in cellular electrophysiology, increasing I_{K1} density to the level observed in adult CMs, inducing a more negative diastolic membrane potential, and increases reliance on sodium channels for the cardiac action potential upstroke, as expected in mature CMs. MM treatment also increases calcium cycling proteins activity, therefore increasing SR calcium release and re-uptake, which occurs alongside increased maximal contractile force. This suggests that metabolism, and in particular FAO, might be directly linked to different maturation events in CMs including electrophysiology and contractile proteins.

The second paper, published by Dark and colleagues [86] proposed a new differentiation protocol, designed to specifically give rise to left ventricle-like CMs. With this specification, hiPSC-CMs generated are more homogeneous and exhibit an increased overall maturation when compared with iPSCs differentiated with traditional small molecules-based differentiations. The LV relies on a reduced concentration of the Wnt pathway activator CHIR, combined with Activin A and BMP4, activators of the eponymous pathway, involved in cardiac ventricular specification alongside Wnt. Additionally, the retinoic acid pathway is continuously inhibited to prevent the undesirable emergence of atrial CMs. When differentiated with LV protocol, hiPSC-CMs exhibited an increased and fast sarcomere development, with adult-like sarcomere length and higher levels of MLC2v and cTnI, two adult ventricular sarcomeric protein isoforms. At the metabolic level, hiPSC-CMs from the LV protocol displayed a higher cellular respiration and ATP production. Electrophysiology was also significantly improved, with prolonged, more rectangular and homogeneous action potentials, and increased I_{K1}-associated channel expression. Similarly, calcium transients were closer to adult CM calcium transients, with increased amplitude and time to peak, and significant increase in calcium cytoplasmic entry, through both LTCC and RYR2. At the transcriptomics level, cells clustered closely to adult ventricular CMs, preforming better than age-matched hiPSC-CMs differentiated with standard protocols, even those cultured with MM medium.

1.3 Thesis aims

HiPSC-CMs are valuable for cardiac research, disease modelling, drug testing, and regeneration, but remain immature compared to adult cells. While cAMP signalling influences maturation, the mechanisms regulating cAMP nanodomains in hiPSC-CMs are unknown. Additionally, maturation protocols are very rarely directly compared for efficiency, leaving unclear whether they produce uniform maturity across all cardiac functions. Un-

derstanding these processes could enhance our understanding of hiPSC-CM maturation and open new avenues to improve their application in cardiovascular therapies.

This thesis hypothesises that maturation protocols do not achieve homogeneous maturation across all cardiac functions and that it impacts the development of the β-adrenergic pathway.

Using two previously published protocols that have been shown to enhance maturation of hiPSC-CMs, their relative impact on the organisation of the cAMP signalling pathway will be explored in this thesis. The first protocol, designed by Feyen and collaborators, involves a specific culture medium formulated to promote a metabolic switch from glycolysis to fatty acid oxidation in hiPSC-CMs. This switch naturally occurs during cardiac development but hiPSC-CMs usually still rely mainly on glucose for ATP synthesis at the end of conventional differentiation protocols. Enforcing this metabolic switch in hiPSC-CMs is associated with a more global maturation [85]. The second protocol, designed by Dark and collaborators, is a differentiation protocol designed to specifically give rise to left ventricle-like hiPSC-CMs, and is associated with an enhanced overall maturation, as compared to traditional non-specific CM differentiation protocols [86]. There is little understanding of how enforced metabolic switch toward fatty acid oxidation, or a more directed left ventricular like differentiation may impact cAMP signalling and indeed how it alters the make-up of the cells that are produced during the differentiation protocols.

Therefore the aims of this thesis are:

1. Establish how differentiation and maturation protocols influence the proportion and maturity of CMs produced in 2D culture, using transcriptomics to gain an in-depth understanding of RNA level maturity and cell types produced by differentiations, protein gels to assess mature protein isoform abundances that are associated with CM maturation, and functional measurements of action potentials, calcium transients

and contractility to correlate transcriptomic and protein level changes with CM functional changes.

2. Assess the relative activity of specific phosphodiesterases in hiPSC-CMs matured metabolically or pushed towards a more confined left ventricular lineage using live cell FRET-based cAMP imaging.
3. Assess the maturity of the cAMP signalling pathway in metabolically matured and left ventricular like CMs by assaying how β-adrenergic stimulation alters cellular function, and how this correlates with changes in PDE3 and PDE4 activity.

Chapter 2

Material and Methods

2.1 Definitions

Throughout this thesis, the terms *differentiation batch* was used to refer to all hiPSC-CMs that originated from the same hiPSC culture passage and were differentiated at the same time, with the same protocol. The differentiation batches were different for each chapter.

Unless otherwise stated, the terms *control cells*, *control group* or *control (C)* refer to hiPSC-CMs differentiated with the regular protocol that were not subjected to any maturation process. Not to be confused with *DMSO control* or *control treatment*.

2.2 General

2.2.1 Stem cell culture

The hiPSC line PGP1 was retrieved from vapour phase nitrogen storage. Cells were rapidly thawed and mixed with >5 mL of warm mTeSR1 medium containing 10 µM of Y-27632 (ROCK inhibitor). They were then centrifuged at 200 relative centrifugal force (rcf) for 3 min. The supernatant was discarded and the pellet resuspended in 2 mL of the same medium. 1 mL of the cell suspension was then transferred in 2 wells of a Matrigel-coated 12-well plate. The plate was then incubated at 37°C, 5% CO_2 for 24 h. Medium changes were carried out daily, without the addition of ROCK inhibitor as soon as the confluence was >20%.

Passaging was performed when the confluence reached >75%. The medium was removed and the cells were dissociated with 0.5 mL of Dulbecco's Phosphate buffered saline (DPBS) with 0.5 mM of EDTA, for 7 min at 37°C, 5% CO_2. DPBS was then removed and the cells were resuspended in 1 mL of warm passaging medium (mTeSR1 medium containing 10 µM of ROCK inhibitor). The 2 stock wells were then diluted at 1:6 for a total of 13.5 mL of passaging medium and distributed in a 12-well plate (propagating plate), with the remaining volume topped-up with passaging medium to 2 mL (approximately 1:12 final dilution) and then distributed evenly in 2 wells of a 12-well plate (stock plate). The cells were then incubated at 37°C, 5% CO_2, and medium changes were performed daily with plain mTeSR1.

2.2.2 Regular cardiomyocyte differentiation

Once the propagating hiPSCs confluence reached >85%, the culture medium was replaced with 1 mL of 10 µM CHIR99021 (CHIR) in RPMI1640 medium supplemented with B27 minus insulin (RPMI+B27$^-$). This was day 0 of differentiation. After a 24 h incubation, the medium containing CHIR was diluted with 0.5 mL of RPMI+B27$^-$ per well and incubated for a further 24 h. On day 2, the medium was entirely replaced with RPMI+B27$^-$. On day 3, the medium was replaced with 5 µM of IWP2 in RPMI+B27$^-$ and incubated for 48 h. Subsequent medium changes were performed every 48 h. On day 5, the medium was replaced with RPMI+B27$^-$. On day 7, it was switched to RPMI supplemented with B27 plus insulin (RPMI+B27$^+$). On day 11, metabolic selection with glucose-free RPMI+B27$^+$ and 4 mM L-lactic acid was performed to eliminate a maximum of non-cardiomyocytes that have arisen from the differentiation. From day 13, the medium was replaced with regular RPMI+B27$^+$ (See supplementary figure A.1).

2.2.3 Metabolic maturation

From day 20 of differentiation, half of the culture dishes or wells were assigned to the MM medium. This medium was designed to shift metabolic

processes to fatty acid oxidation instead of glycolysis to achieve maturation of the hiPSC-CMs [85]. The medium recipe remained unchanged from the original paper : ”DMEM without glucose (Thermo Fisher Scientific, 11966025) supplemented with 3 mM glucose (Sigma Aldrich, G7021), 10 mM L-lactate (Sigma Aldrich, 71718), 5mg/ml Vitamin B12 (Sigma Aldrich, V6629), 0.82 mM Biotin (Sigma Aldrich, B4639), 5 mM Creatine monohydrate (Sigma Aldrich, C3630), 2 mM Taurine (Sigma Aldrich, T0625), 2 mM L-carnitine (Sigma Aldrich, C0283), 0.5 mM Ascorbic acid (Sigma Aldrich, A8960), 1x NEAA (Thermo Fisher Scientific, 11140), 0.5% (w/v) Albumax (Thermo Fisher Scientific, 11020021), 1x B27 and 1% KOSR (Thermo Fisher Scientific, 10828028).”

The cells were kept in this medium for 3 weeks and were either harvested for transcriptomics/proteomics experiments, or used in live fluorescent imaging for physiological measurements (See supplementary figure A.1).

2.2.4 Left ventricle-like differentiation

The ventricular specification differentiation protocol was adapted from the published work of the Bernardo Laboratory [86]. Briefly, differentiation was started by replacing the iPSC medium with RPMI+B27$^-$ containing 100 nM of the retinoic-acid receptor inhibitor AGN193109 (AGN), 5 ng/mL Activin A, 3 ng/mL BMP4 and 3 µM CHIR. This was day 0. Our optimisation protocol eliminated FGF2 as the PGP1 iPSC line showed a better success rate of the differentiations without it. BMP4 and CHIR concentrations were optimised for the PGP1 iPSC line, to give rise to the highest proportion of mature ventricle-like cardiomyocytes, as evaluated by their expression of HAND1, MLC2v and cTnI proteins on day 20. 24 h later, the medium was replaced with RPMI+B27$^-$ containing 100 nM AGN. On day 2, the medium was changed to RPMI+B27$^-$ with 100 nM AGN, 65 µg/mL L-ascorbic acid and 5 µM IWP2. From then on, medium changes were performed every 48 h. On day 4 and 6 the medium was replaced with 100 nM AGN and 65 µg/mL L-ascorbic acid in RPMI+B27$^-$. From day 8 the medium was

changed to RPMI+B27$^+$ minus vitamin A with 65 µg/mL L-ascorbic acid, except on day 10. On day 10, the cells were subjected to metabolic selection with glucose-free RPMI supplemented with B27$^+$ minus vitamin A and 65 µg/mL L-ascorbic acid. Cells were replated on day 18 for imaging, as described above. On day 40-45 the cells were either harvested for transcriptomics/proteomics experiments, or used in live fluorescent imaging for physiological measurements (See supplementary figure A.2).

2.2.5 hiPSC-CM replating for live imaging

On day 18-20, hiPSC-CM were dissociated by removing the medium and adding 300 µL of 10X TrypLE Select per well. Cells were incubated at 37°C, 5% CO_2 for 8-10 min until sufficient dissociation was observed under the microscope at 10x magnification. Dissociation was neutralised with 1 mL of cardiomyocyte passaging medium (RPMI+B27$^+$ with 10% KOSR and 2 µM Thiazovivin) and the cells were resuspended by gently pipetting 6 times. The cell suspension was then transferred to a 15 mL tube and diluted with an additional 4 mL/well of passaging medium. The cells were centrifuged at 200 rcf for 3 min and the supernatant was discarded. Cells were resuspended with 2 mL/well of passaging medium and passed through a 100 µM cell strainer to remove cell clumps and facilitate cell counting. Cells were counted with the automatic cell counter Countess II and 150k cells were seeded per 35 mM Ibidi imaging dishes (polymer coverslips imaging surface), by pipetting 400 µL of cell suspension in the micro-well. After 24 h at 37°C, 5% CO_2, 1.5 mL of hiPSC-CM medium was added to each well. Medium changes with 1.5 mL/dish were performed every 48-72 h.

2.2.6 Imaging buffer recipe

The imaging buffer was used for calcium, contractility, membrane potential and cAMP measurements. It was a modified Tyrodes-HEPES buffer (136.5 mM NaCl, 5.4 mM KCl, 1 mM $MgSO_4$, 1.8 mM $CaCl_2$, 5.5 mM D-Glucose, 4.2 mM $NaHCO_3$, 0.3 mM NaH_2PO_4, 10 mM HEPES). The pH was

adjusted to 7.4 at 37°C with NaOH. The buffer was filter-sterilised and stored at 4°C.

2.2.7 Adeno-associated viral vector generation

Amplification and purification Ad293 cells were plated in a T25 flask and cultured in Dulbecco's Modified Eagle's Medium +10% foetal bovine serum +1% Penicillin-Streptomycin. On the day of plating, the cells were transfected with the adenovirus DNA plasmid with Lipofectamine according to manufacturer's protocol. The culture medium was changed every 2-3 days. Around 2 weeks after transfection, when most cells displayed strong viral expression under fluorescent microscope, the cells were resuspended by scraping in culture medium and split into 3 T75 flasks. The cells were maintained as described above and the flasks were split into 12 T175 flasks, and finally 50 T175 flasks. Then, the cells were resuspended by scraping in culture medium, centrifuged at 200 rcf for 3 min, and resuspended in 10 mL hypotonic VSB solution. They were lysed by freezing in liquid nitrogen for a couple of minutes, rapidly thawed in water bath at 37°C and vortexed thoroughly. This sequence was repeated 3 more times. The suspension was centrifuged at 3000 rcf for 5 min and the supernatent was transferred to a new tube and centrifuged again. The supernatent was transferred to another tube and 1.55 g of solid CsCl was added to the 10.5 mL of virus suspension. 1 mL of 1.4M CsCl was pipetted into 4 polyallomer ultracentrifuge tubes, then 1.5 mL of 1.3 M CsCl, followed by 2.5 mL of viral suspension were carefully pipetted on top to create a gradient. The tubes were weighed individually, and an additional volume of 1.1 M CsCl was finally added to the tubes, calculated to precisely balance the tubes. They were then put in an ultracentrifuge at 4°C, 45000 rpm, overnight. On the next day, a white band was visible in the CsCl gradient, corresponding to the purified virus. With an 18 gauge needle mounted on a 2 mL syringe, the tubes were pierced and the white band was aspirated. The viral suspension was transferred to regular tubes and mixed with an equal volume of storage

buffer. Viruses were aliquoted into small volumes to avoid freeze-thaw cycles and stored at −80°C.

Titration To ensure consistent expression across different virus batches, an endpoint dilution assay was performed. To do so, a serial tenfold dilution of viral suspension ranging from 10^{-1} to 10^{-7} was distributed in a 96-well plate, at 100 µL/well, with 5 replicates per dilution. Untreated medium was used as a control. 100k competent cells resuspended in 100 µL were added to each well. The plate was then incubated at 37°C, 5%CO_2 and the cells were cultured as usual. Counting was performed when a strong viral expression in the wells with the lowest dilution was visible under fluorescent microscope, usually after 48 h. Wells with cells expressing the virus, however low in number or expression, were counted as positive. The proportion of positive wells were calculated for each dilution. The medium tissue culture infectious dose ($TCID_{50}$) was calculated with the improved Kärber method [87]:

$$Log_{10}(TCID_{50}) = L - d(s - 0.5)$$

where L = $\log_{10}$(viral dilution giving highest response), d = $\log_{10}$(dilution factor), s = $\sum$ (proportions of positive wells of each dilution).
The titer per millilitre ($TCID_{50}$/mL), was calculated as:

$$TCID_{50}/mL = \frac{1}{10^{Log_{10}(TCID_{50})+v}}$$

where v = $\log_{10}$(viral volume conversion to mL). In our protocol, v = $\log_{10}(0.1) = -1$.
multiplicity of infection (MOI) was calculated approximately as:

$$MOI \approx \frac{0.7 \times TCID_{50}/mL}{n_{cells}}$$

where n_{cells} = number of cells seeded.

2.2.8 Cell pellet preparation and storage for snRNA-seq and western blots

hiPSC-CM were washed 3 times with DPBS on ice and then scraped off in 0.5 mL of DPBS per well. 2 wells of a 12-well plate (approximately 4 million cells) were combined and transferred in a single 1.5 mL tube. Tubes were kept on ice until centrifuged at 4°C and maximum speed for 1 min, and the supernatant was then discarded. The cell pellets were immediately frozen and stored at -80°C.

2.2.9 Western blots

Cell pellets were retrieved from storage at -80°C. Protein extraction was performed on ice by gently resuspending the cell pellet in 200 µL of RIPA buffer supplemented with protease and phosphatase inhibitors ($RIPA^+$) to the pellet. The tube was centrifuged at max speed for 10 min at 4°C, the supernatant was transferred to a clean tube and the pellet was discarded. Protein quantification was performed using a BCA protein assay kit. A 1:1 $RIPA^+$ buffer diluted in ddH_2O (0.5X $RIPA^+$) was used to prepwere a serial dilution of a BSA solution, ranging from 2 mg/mL to 0.125 mg/mL, by factor 2 dilutions. Pure 0.5X $RIPA^+$ was used for 0 mg/mL. These known protein dilutions were used to build a standard curve which was used to quantify the samples. 60 µL of each sample diluted at 1:10 in 0.5X $RIPA^+$ was then prepared. 25 µL of each BSA standard value was pipetted in duplicates in a flat-bottom 96-well plate, alongside each diluted sample in duplicates. 200 µL of the kit's working reagent (reagent A + 1:50 reagent B) was added to each well, then the plate was covered with Parafilm and incubated at 37°C for 30 min. The absorbance of each sample and standard was measured at 562 nm with an Omega MARS plate reader and each sample protein concentration was calculated using the standard curve. Samples were then diluted to a concentration of 1 µg/µL in $RIPA^+$ buffer and prepared with 1X NuPAGE LDS Sample buffer and 1X NuPAGE Reducing agent so that 8 µg of protein were loaded per sample. The samples were heated at 95°C

for 10 min and then spun to collect any condensation droplets. Samples were loaded in a Stain-Free 4–15% precast polyacrylamide gel alongside pre-stained 10–250 kDa protein standards. The gel was then run in 1X Tris-Glycine SDS-PAGE running buffer at 150 V. The stain-free dye of the gel was then activated by UV light for 1 min to show the relative total protein amount loaded per well and allow normalisation. A dry transfer was then performed on nitrocellulose membrane using the BioRad iBlot transfer system at 20 V for 7 min. The membrane was blocked with 5% milk in DPBS+0.1% Tween20 for 1 h at room temperature on a rocker. The membrane was then incubated overnight at 4°C on a rocker with primary antibodies at the dilution indicated below:

Antibody target	**Dilution**	**Antibody target**	**Dilution**
β_2-AR	1:500	SERCA2	1:1000
MLC2a	1:2000	MLC2v	1:1000
ssTnI	1:1000	cTnI	1:500
PDE4D	1:200	HAND1	1:200
PDE3B	1:100	$Ca_V1.2$	1:1000

The membrane was washed with Tris buffered saline (TBS)+0.1% Tween20 on a rocker, 3 times 10 min. The membrane was incubated at room temperature on a rocker with horseradish peroxidase conjugated secondary antibodies for 1 h, diluted at 1:5000 for anti-goat, 1:20000 for anti-mouse, or 1:50000 for anti-rabbit. The membrane was washed with TBS+0.1% Tween20 on a rocker, 3 times 10 min. Then the membrane was incubated with 1.5 mL of Western Blotting ECL substrate for 2 min and imaged with a Bio-Rad ChemiDoc imaging system. For myosin light chain and troponin I, the adult ventricular isoform was blotted for first, and the membrane was stripped for 10 min on a rocker at room temperature. Subsequently, the membrane was washed twice, then blocked and incubated again, as described above, with the foetal isoform.

Analysis The bands intensity volumes were determined using *Image Lab* (v5.1, Bio-Rad) and divided by the corresponding whole lane intensity volumes from the gels stain-free total protein imaging. The corrected values were then divided by the median corrected value of the control group. The statistical analysis was performed using R (v4.4.1). A Shapiro-Wilk normality test followed if needed by a Levene's test, were performed using the *Rstatix* (v0.7.2) package. According to the results, either an ANOVA followed by Tukey post-hoc pairwise comparisons if significant, or a Kruskal-Wallis test followed by Dunn's test for post-hoc pairwise comparisons if significant, were done. Data were presented as median±interquartile range (IQR).

2.3 Specific to chapter 3

2.3.1 Single nucleus RNA sequencing

Sample processing and library preparation *Note: This work was performed by Joshua Gorham and Seong Won Kim, Harvard, Boston, USA.*
Nuclei were prepared from frozen cell pellets. 3 samples, each from a different differentiation batch, containing $>2\times10^6$ hiPSC-CM aged 40-45 days, from the control (C) and MM protocols, were processed for single nucleus RNA sequencing (RNA) together in the same *run*. 3 similar samples from the LV protocol were processed later, in a second *run*. After barcoding using Cell Plex (10X Genomics) and previously described protocols [88], snRNA-seq libraries were prepared using Chromium 3' dual index (v3.1, 10X Genomics). Sequencing data were mapped to the human reference genome (hg38) with Cell Ranger.

Analysis hiPSC-CM snRNA-seq data were analysed in R using *Seurat* (v5.1.0) [89]. Briefly, data were cleaned by *run*, by filtering genes and nuclei based on the distribution of the whole dataset, to remove doublets, poor quality droplets and low quality genes. Each parameter

relative to nuclei filtering (presented below) was $\log_2$-transformed prior outlier identification. Values were considered outliers if out of the interval [Q1−1.5×IQR , Q3+1.5×IQR] ($x \notin I$) or only above the upper bound of that interval ($x > I$).

- Filter by gene:
  - Genes expressed in less than 0.1% of the cells were excluded
- Filter by nucleus:
  - Nuclei with a number of different genes expressed (`nFeatureRNA`) $\notin I$ were excluded
  - Nuclei with a total number of counts (`nCountRNA`) $\notin I$ were excluded
  - Nuclei with a percentage of mitochondrial genes $> I$ were excluded

Then data were integrated by sample using *Harmony* (v1.2.3) [90] and scaled for RNA counts using *SCTransform* (v0.4.1) [91]. 2D UMAP projections were generated using 30 dimentions. Cells were clustered with a resolution of 0.1. Non-CMs, identified by their low expression of cardiac marker genes (TTN, MYL7, RYR2, SCN5A, etc.), were removed from the analysis and a new normalisation, dimentionality reduction, and clustering were run. Differentially expressed genes were identified with a pseudobulk analysis using *DESeq2* (v1.46.0) [92], with data aggregated by sample and cluster, with `log2(FC)` cutoff at $\log_2(1.2)$. *P*-values were adjusted for multiple testing by the Benjamini–Hochberg method. Genes with adjusted *P*-values <0.05 were used for gene ontology enrichment analysis (GO) or gene set enrichment analysis (GSEA) and differential gene expression heatmaps. GO and GSEA were performed with *clusterProfiler* (v4.14.4) [93] with biological processes terms. Heatmaps have been generated with *pheatmap* (v1.0.12). Integrated unsupervised Ward's hierarchical clustering (`ward.D2`) of both genes and cells origin was performed using the Euclidean distance method.

The adult human cardiomyocyte dataset used in this analysis was obtained from the Human Cell Atlas project "Cells of the adult human heart"

[94]. This dataset have been filtered using the associated metadata, to select healthy ventricular cardiomyocytes snRNA-seq data. Integration, normalisation, dimentionality reduction, clustering and gene enrichment analysis of the combined datasets (adult ventricular cardiomyocytes and hiPSC-CM) was performed as described above, and was followed by a pseudotime trajectory analysis and analysis of varying genes along the trajectory using *Monocle3* (v1.3.7) [95].

2.4 Specific to chapter 4

2.4.1 AAV transduction of FRET-based cAMP indicators

hiPSC-CMs were transduced with one of the FRET-based cAMP indicators AAV, 48 h prior imaging for AKAP79-CUTie and AKAP18δ-CUTie [96], and 24 h prior imaging for EPAC-S^{H187} [97]. They were all three diluted to an MOI of 25 in culture medium. Cells were incubated at 37°C, 5%CO_2. Immediately prior imaging, the cells were washed twice with warm imaging buffer and equilibrated for 5-10 min at 37°C in 2 mL of the same buffer.

2.4.2 Immunofluorescent staining and imaging

To confirm targeting of sensors, transduced cells were immunostained for $Ca_V1.2$ to confirm colocalisation with AKAP79-CuTie and SERCA2 to confirm co-localisation with AKAP18δ-CuTie (Supplementary figure 4.11). 120k cells were seeded on ethanol sterilised glass cover slips 48 h prior transduction and transduced as described above, 48 h before fixing. Cells were then washed with DPBS 3 times 5 min and fixed in 1 mL 4% paraformaldehyde for 10 min. The cells were permeabilised with 0.1% Triton in TBS for 10 min and then blocked with 2% bovine serum albu min (BSA) + 0.1% sodium azide in TBS for 30 min. They were next washed once with TBS for 5 min and incubated with primary antibody diluted at 1:200 for either $Ca_V1.2$ or SERCA2 in blocking buffer for 1-2 h at room

temperature. The cells were washed with 0.1% Triton in TBS for 3 times 5 min and incubated with secondary antibodies diluted at 1:200 in blocking buffer for 1 h at room temperature, protected from light. After washing 3 times 5 min with 0.1% Triton in TBS, they were incubated for 30 min with TO-PRO-3 Iodide diluted at 1:200, protected from light. A last wash with 0.1% Triton in TBS for 3 times 5 min was then performed, then the coverslips were inverted on 15 µL of Mowiol mounting medium on glass slides and left overnight at 4°C in a humidifed chamber, protected from light. Finally, the coverslips were sealed with nail varnish and stored at 4°C protected from light until imaged, in the following days. Imaging was performed with a Leica DM 6000 CFS confocal imaging system.

2.4.3 Live fluorescent microscopy for cAMP measurements

Live fluorescent imaging was performed on the same setup as described above, except at x10 magnification with a Nikon Plan Apo λ (Nikon, Japan). Excitation was at 435nm (mTurquoise2) and simultaneous mTurquoise/YFP emissions were split with a T495lpxr UF and filtered through an ET470/24 (mTurquoise) or ET535/30 (YFP). The cells were maintained at 37°C throughout the imaging. Time lapses were acquired at 1 frame per 5 s, with 20 ms exposure, and the image binned 4×4. Each imaging dish was used to record FRET at baseline and after the successive addition to the bath of either 10 µM PDE inhibitor or a matched volume of dimethyl sulfoxide (DMSO) after 5 min, 1nM ISO after 17 min, 0.1 mM 3-isobutyl-1-methylxanthine (IBMX) after 29 min, and finally 10 µM forskolin (FSK) after 37 min. Each experiment was stopped after 43 min.

Video analysis Data were extracted from images using a Matlab (R2023a - v9.14.0.2337262) pipeline. The two recorded channels were aligned automatically using the `imregcorr` function. Polygonal regions of interest (ROI) were manually drawn over ~10 individual cells per field of view to create a mask with the `drawpolygon` function, and mean intensities of each

ROI were recorded for each frame for both channels using the `regionprops` function.

2.4.4 Targeting of Cx43 with FluoSTEP sensors

CRISPR-Cas9 insertion of GFP fragment at the Cx43 To target FluoStep sensors to Cx43 junctions, the GFP11 fragment was tagged at the C-terminus of the Cx43 protein by genome editing using CRISPR-Cas9 on Personal Genome Project 1 (PGP1) wild type cells, as described before [98]. In brief, two batches of PGP1 wild type hiPSC were nucleofected with a Lonza nucleofector. One batch with Cas9 nuclease, HDR template, forward and reverse guides (see table below), and the second batch with a GFP plasmid to control the success of the nucleofection protocol. The guides and HDR template were designed using the Benchling software to maximise the probability of insertion and minimise the probability of off-targets [99] (See table 2.1). iPSCs were passaged twice to allow the nucleofected cells to recover, before re-plating at low density (2500 or 5000 cells per 6cm-dish) for clonal selection. Single colonies were picked from clonal selection dishes and grown in individual wells of a 96-well plate. Each clonal colony DNA was extracted, amplified by PCR and used to run DNA gels by electrophoresis to control the insertion. This resulted in 3 potential homozygous lines and 4 potential heterozygous lines observed by gel electrophoresis. To maximise the expression of the tagged Cx43, a homozygous line (D3, Cx43-GFP$^{+/+}$) was selected alongside a control line which was not inserted (E10, Cx43-GFP$^{-/-}$). Their genotypes were confirmed by Sanger sequencing (Supplementary figure A.3) and pluripotency confirmed by immunofluorescent staining (Supplementary figure A.4). Both lines were then propagated and successfully differentiated into cardiomyocytes.

2.4.4.1 PCR and gel electrophoresis

iPSC were resuspended for passaging as previously described, and 2×10^4 were transferred to PCR tubes. 20 µL of Dilution buffer with 0.5 µL of DNA

Table 2.1

	Sequence
HDR template	GACCAGCGACCTTCAAGCAGAGCCAGCAGTCGTGCCAGCA GCAGACCTCGGCCTGATGACCTGGAGATCGGCGGTAGTG GAGGACGTGACCACATGGTCCTTCATGAGTATGTAAATGCT GCTGGGATTACATAGATACAGGCTTGAAAGCATCAAGATTC CACTCAATTGTGGAGAAGAAAAAAGGTGCTGTAGAAAGT
Forward Cas9 guide	TGACCTGGAGATCTA
Reverse Cas9 guide	AAGCCTGTATCTAGA
Forward PCR primer	CAAAATCGAATGGGGCAGGC
Reverse PCR primer	TGTGCAAGTGGATGGAAAAAGAATA

release enzyme was added to each tube. They were left to incubate for 5 min at room temperature, and heated for 2 min at 98°C. Each sample was diluted with nuclease-free water to a final concentration of 100 ng/µL. The master mix containing nuclease-free water, 2x buffer, forward and reverse primers, and the Phire polymerase was prepared according to manufacturer indications, and a final volume of 40 µL per PCR tube was added to 100 ng DNA. DNA amplification was performed in a BioRad thermocycler with an initial heating phase at 98°C for 5 min, followed by 40 cycles of the following sequence [98°C for 5 s, 61°C for 5 s, 72°C for 30 s], and terminated with a final incubation at 72°C for 1 min. This PCR product was used as was for Sanger sequencing and gel electrophoresis. Gel electrophoresis was performed with 2% agarose gel containing 2 µL/100 mL GelRed stain and run in sodium borate buffer at 150 V.

2.5 Specific to chapter 5

2.5.1 Sample preparation for live fluorescent microscopy

AAV co-transduction of calcium reporter and α-actinin reporter Cells were co-transduced with calcium and α-actinin reporters, 48 h prior imaging. The calcium reporter, RGECO [100], was diluted to an MOI of 40 and GFP-α-actinin AAV was diluted to an MOI of 10 in culture medium. Cells were incubated at 37°C, 5%CO_2 for 48 h. Immediately prior imaging, the

cells were washed twice with warm imaging buffer and equilibrated for 5-10 min at 37°C in 2 mL of the same buffer.

Treatment with chemical voltage reporter FluoVolt Prior to imaging, cells were washed twice with imaging buffer and incubated for 15 min in 1 mL of the same buffer with 1 µL of FluoVolt dye and 10 µL of 100X PowerLoad. The buffer was then replaced with 2 mL of fresh buffer.

2.5.2 Live fluorescent microscopy for calcium, contractility and voltage measurements

Live fluorescent imaging was performed with a Nikon Ti-2 Eclipse inverted microscope (Nikon, Japan) at x100/1.45NA magnification with a Nikon Plan Apo λ (Nikon). Excitations at 550nm (RGECO, FluoVolt) and 470nm (GFP-α-actinin) were provided with a CooLED pE4000 (CooLED). Fluophores were imaged in pairs using dual illumination through a Quod-Filter (LED-DAPI/FITC/TRITC/Cy5). Emissions were passed through a TwinCam dual camera splitter (Cairn Research). Simultaneous RGECO/GFP emissions were split with a T565lpxr and filtered through an ET632/60 (RGECO, FluoVolt) or ET520/40 (GFP). All filters were purchased from Semrock, IDEX. Emissions were collected over dual aligned Teledyne Photometrics Kinetix sCMOS cameras (Teledyne Photometrics). Time lapses were acquired at 10 ms exposure (100 fps) for calcium and contractility measurements, and 4.9 ms exposure (200 fps) for voltage measurements. For the latter, acquisition was binned at 2×2. Cells were kept at 37°C and paced at 1 Hz for the duration of the experiment. Each imaging dish was used to record control (untreated buffer) and then incubated at 37°C for 10 min with either DMSO (dilution-matched vehicle control), 1 nM ISO, 10 nM ISO, or 100 nM ISO. Cells were imaged for no longer than 45 min and pacing was stopped during incubation to limit any effect of the pacing on the data.

Video analysis Dually acquired videos were split into contractility videos at AVI format and calcium videos as TIFF stack using a custom Matlab (R2023a - v9.14.0.2337262) script.

Calcium and voltage measurements Calcium and voltage videos were analysed using the *CalTrack* pipeline [101]. Briefly, *CalTrack* is a Matlab-based algorithm, which parametrises fluorescent calcium transients in living cardiomyocytes, including isolated single cells. 5 sec-long sequences of calcium transients (or action potentials) from single cells were extracted from fluorescent time-series. Abnormal transients (not returning to base-line, presenting arrhythmias, etc.) were both automatically and manually identified, and then removed from further analysis. For each cell sequence, individual transients were isolated and averaged. From the average traces, parameters were automatically calculated. Parameters measured include time to peak, time of decay, time decay constant (Tau), calcium transient duration, and calcium transient duration at various amplitudes.
Additional measurements of action potential duration at 10%, 40% and 80% repolarisation were performed on CalTrack output traces, with a custom R script.

Contractility measurements Contractility videos were analysed with a modified version of *SarcTrack* [102] using a Python pipeline on a supercomputation cluster. Videos were used to fine-tune sarcomere detection to the following parameters:

- Sarcomere minimun:maximum distances (in pixels) of 18:40
- Sub-window size (in pixels) of 0.2
- Morlet wavelet stretch of 1
- Morlet wavelet scale of 2
- Similarity threshold of 0.15

Sarcomeres were fitted at 8 degrees of angle variance and an angle variance filter was applied. Parametrisation of the resulting contractility trace was

performed with a hybrid sinusoid-sawtooth model. Results were manually filtered for poor fitting and parameters were converted to spatiotemporal units at a pixel size of 70 nm and timing of 10 ms per frame.

2.5.3 Statistical analyses

A custom R-based script was used to analyse the individual measurements from *CalTrack* or *SarcTrack*. These were aggregated and filtered to exclude differentiation subgroups with less than 10 data points, extreme outliers (>3 IQR from median), as well as impossible time constant (*Tau*) values (<0 or >decay time) resulting from a bad fitting of the calcium curve, and impossible contraction timings (<0 or >1sec). Then a non parametric Kruskal-Wallis test was conducted, followed by Dunn's test for post-hoc pairwise comparisons if significant, using the *rstatix* package (v0.7.2). The *P*-values were adjusted for multiple comparisons with the Holm–Bonferroni correction. All *P*-values presented were adjusted. This type of analysis was chosen because of important deviations from normality and inequality of variances of the data.

To evaluate the differences of variability between the protocols tested, a Brown-Forsythe test was also performed using the `levene_test` function from *rstatix*. Data were presented as median±IQR.

2.6 Reagents list

Product name	Purchased from	Catalogue number
mTeSR1™, basal medium and supplement	Stemcell Technologies	85850
Y-27632 (ROCK inhibitor)	Cell guidance systems	SM02-5

Product name	Purchased from	Catalogue number
Matrigel® hESC-qualified matrix	Corning	354277
DPBS	Gibco	CLS354277
EDTA	Invitrogen	15575020
CHIR99021	Tocris	4423
RPMI 1640	Gibco	21875034
B-27™ supplement minus insulin	Gibco	A1895601
B-27™ supplement plus insulin	Gibco	17504044
Glucose-free RPMI	Gibco	11879020
L-lactic acid	Sigma-Aldrich	L1750
Enzyme TrypLE™ Select 10X	Gibco	A1217701
KOSR	Gibco	10828028
Thiazovivin	SelleckChem	S1459
AGN193109	Santa Cruz Biotechnology	sc-210768
Activin A	R&D Systems	338-AC-010
BMP4	R&D Systems	314-BP-010
B-27™ supplement minus vitamin A	Gibco	12587010
RIPA buffer 10X	Cell Signalling Technologies	9806
cOmplete™ mini protease inhibitor cocktail	Roche	4693124001
PhosSTOP™ phosphatase inhibitor	Roche	4906845001
Pierce™ BCA protein assay kit	Thermo Scientific	23225
NuPAGE™ LDS sample buffer 4X	Invitrogen	NP0007

Product name	Purchased from	Catalogue number
NuPAGE™ sample reducing agent 10X	Invitrogen	NP0004
4–15% mini-PROTEAN™ TGX Stain-Free™ protein gels	BioRad	4568086
Precision Plus Protein™ prestained protein standards	BioRad	1610373
Tris Glycine SDS PAGE buffer 10X	National Diagnostics	EC-870
Anti-$Ca_V1.2$ antibody (WB & IF)	Alomone Labs	ACC-003
Anti-SERCA2 antibody (WB & IF)	Santa Cruz Biotechnology	sc-8095
Anti- MLC2a antibody	Synaptic Systems	311 011
Anti- MLC2v antibody	Proteintech	60229-1-Ig
Anti-ssTnI antibody	Santa Cruz Biotechnology	sc-514899
Anti-cTnI antibody	Abcam	ab47003
Anti-PDE3B antibody	Santa Cruz Biotechnology	sc-376823
Anti-PDE4D antibody	Proteintech	12918-1-AP
Anti-β_2-AR antibody	Invitrogen	PA5-80323
Anti-HAND1 antibody	R&D Systems	AF3168
Anti-rabbit HRP antibody	Promega	W4011
Anti-mouse HRP antibody	Promega	W4021
Anti-goat HRP antibody	Promega	V8051
Clarity™ Western Blotting ECL substrate	BioRad	1705060
Restore™ Western Blot stripping buffer	Thermo Scientific	21059

Product name	Purchased from	Catalogue number
Penicillin-Streptomycin	Gibco	15140148
Lipofectamine™ Transfection Reagent	Invitrogen	18324012
FluoVolt™ membrane potential kit	Invitrogen	F10488
Paraformaldehyde	Thermo Scientific	28908
BSA	Sigma-Aldrich	B4287-25G
Sodium azide	Sigma-Aldrich	S8032
TO-PRO™-3 Iodide	Invitrogen	T3605
Mowiol	Millipore	475904
Phire Animal Tissue Direct PCR Kit	ThermoFisher	F140WH
GelRed® Nucleic Acid Stain	Millipore	SCT122

Chapter 3

Using unbiased single nucleus RNA sequencing to compare the effects of two hiPSC-derived cardiomyocytes maturation protocols

3.1 Introduction

hiPSC-derived cardiomyocytes (hiPSC-CM) have emerged as a revolutionary model for cardiovascular research, enabling unprecedented access to patient-derived CMs for disease modelling, drug screening, and regenerative medicine. However, despite important advances in differentiation protocols, a persistent and widely acknowledged limitation of hiPSC-CM is their incomplete maturation relative to adult human CMs. This immaturity affects multiple aspects of CMs physiology, including structural, metabolic and electrophysiological properties, and represents a major limit to their translational application. These limitations are also seen at the molecular level. hiPSC-CM retain a transcriptional program reminiscent of early developmental stages.

Numerous studies have sought to promote maturation through a variety of approaches, including long-term culture, electrical or mechanical stimulation, metabolic modulation, and three-dimensional tissue engineering.

While these strategies have achieved varying degrees of success in promoting specific aspects of maturation, a comprehensive method capable to drive hiPSC-CMs to a fully adult-like state remains out of reach.

One of the principal challenges in evaluating the efficacy of maturation protocols lies in the cellular heterogeneity inherent to hiPSC-CM preparations. Bulk RNA sequencing approaches, although valuable, may mask critical information regarding cell-to-cell variability, like the presence of immature subpopulations within mature cultures. Single cell RNA sequencing has offered new insights into the transcriptional landscapes of hiPSC-CMs; however, its reliance on viable cell dissociation limits its utility in the context of highly structured or engineered tissues, where dissociation protocols may introduce technical artifacts like signs of cellular stress, or selectively bias recovery of specific cell types [103], [104].

Single nucleus RNA sequencing (snRNA-seq) has emerged as a powerful complementary approach, capable of interrogating transcriptional profiles from isolated nuclei without the need for complete cellular dissociation. This technique is particularly well-suited for mature or engineered cardiac tissues, which often resist enzymatic dissociation. Moreover, snRNA-seq enables the analysis of archived or cryopreserved samples, expanding the range of experimental designs applicable to maturation studies. snRNA-seq was therefore chosen to enable a direct comparison between adult cardiac tissues and hiPSC-CM, as adult myocardium is challenging to dissociate into viable single cells, and the majority of available transcriptomics data from human heart tissues have been generated using snRNA-seq.

Recent applications of snRNA-seq have begun to illuminate the transcriptional heterogeneity of hiPSC-CMs subjected to different maturation protocols, revealing distinct subpopulations characterized by varying degrees of metabolic, structural, and electrophysiological gene expression signatures [105], [106]. Importantly, snRNA-seq enables direct comparison of maturation efficiency across experimental conditions at single-cell resolution,

providing critical insights into the relative success of different approaches and uncovering previously unappreciated transcriptional intermediates.

As the field advances, this technique holds promise for constructing a comprehensive molecular atlas of hiPSC-CM maturation. Such efforts are likely to not only inform the optimization of maturation protocols but also advance fundamental understanding of human cardiomyocyte development and plasticity.

The work presented in this chapter is part of this approach. hiPSC-CMs from the different protocols were sent for snRNA-seq and a selection of proteins were blotted for, with the aim to determine how the two maturation protocols differ in terms of maturation efficiency and pathways involved.

3.2 Results

3.2.1 Single nucleus RNA sequencing

3 samples, each from a different differentiation batch, containing $>2\times10^6$ hiPSC-CM aged 40-45 days, from the C and MM protocols, were processed for snRNA-seq together in the same *run*. 3 similar samples from the LV protocol were processed later, in a second *run*.

3.2.1.1 Investigating cell types found in hiPSC-CM samples

After filtering, the two *runs* were merged together and the data were integrated to account for the technical variability arising from their separated processing. This was followed by normalisation, and the multi-dimensional dataset (the expression level of each gene expressed being one dimension of the dataset) was projected on two dimensions (gene sets with the highest variability across the entire dataset), where each dot is a single nucleus. This dimensionality reduction was done using the Uniform Manifold Approximation and Projection (UMAP). An unsupervised clustering

was then performed with the nuclei on this UMAP. As a result, the nuclei with a similar expression profile are represented closer on the UMAP, and cluster together.

Eight clusters arose from this analysis. The first step was to investigate the different cell types present in the dataset. Top 100 most expressed genes per cluster underwent gene ontology (GO) analysis to unbiasedly identify cell types. Pluripotency markers were also checked, but no read of either SOX2, NANOG, OCT4, TRA-1-60, or POU5F1 could be found. This confirmed that the differentiation was efficient as pluripotent cells were undetectable in this dataset. The figure 3.1 displays the GO terms associated with each cluster. These terms exhibited high redundancy across clusters and predominantly represented cardiac myocyte-associated annotations. These data revealed that all the clusters were hiPSC-CM, and no other cell-type could be identified.

The UMAP visualisation showed a clear separation between certain clusters; consequently, the relative expression levels of cardiac-specific genes were quantitatively compared across these clusters for improved characterisation. The figure 3.2 shows the different clusters identified and their expression of canonical cardiac markers. This analysis highlighted that two categories of hiPSC-CM were present in the samples, one group exhibiting higher expression of cardiac genes (clusters 0, 3, 5 and 7), compared to the other (clusters 1, 2, 4 and 6). This difference in expression was not linked to cell cycle phase. Further investigation of these 'hiPSC-CM low' and 'hiPSC-CM high' clusters was made difficult by the high complexity of the data, and it was therefore decided to focus only on the 'hiPSC-CM high' clusters for the rest of the analysis, as they were most probably better defined cardiomyocytes.

A new clustering was done on the data and revealed six different clusters (Figure 3.3). When compared to the protocol used for differentiation, it appeared that a majority of LV nuclei clustered together to form the clusters

Figure 3.1: GO analysis of top 100 most expressed genes shows only cardiomyocytes. *Top 15 GO terms associated with the top 100 most expressed genes for each clusters. These terms are highly redundant between the clusters, and are associated with cardiac myocyte function. Circles size represent the count, and colour represent adjusted P-values associated with each term. Count is the number of different genes associated with the corresponding GO term.*

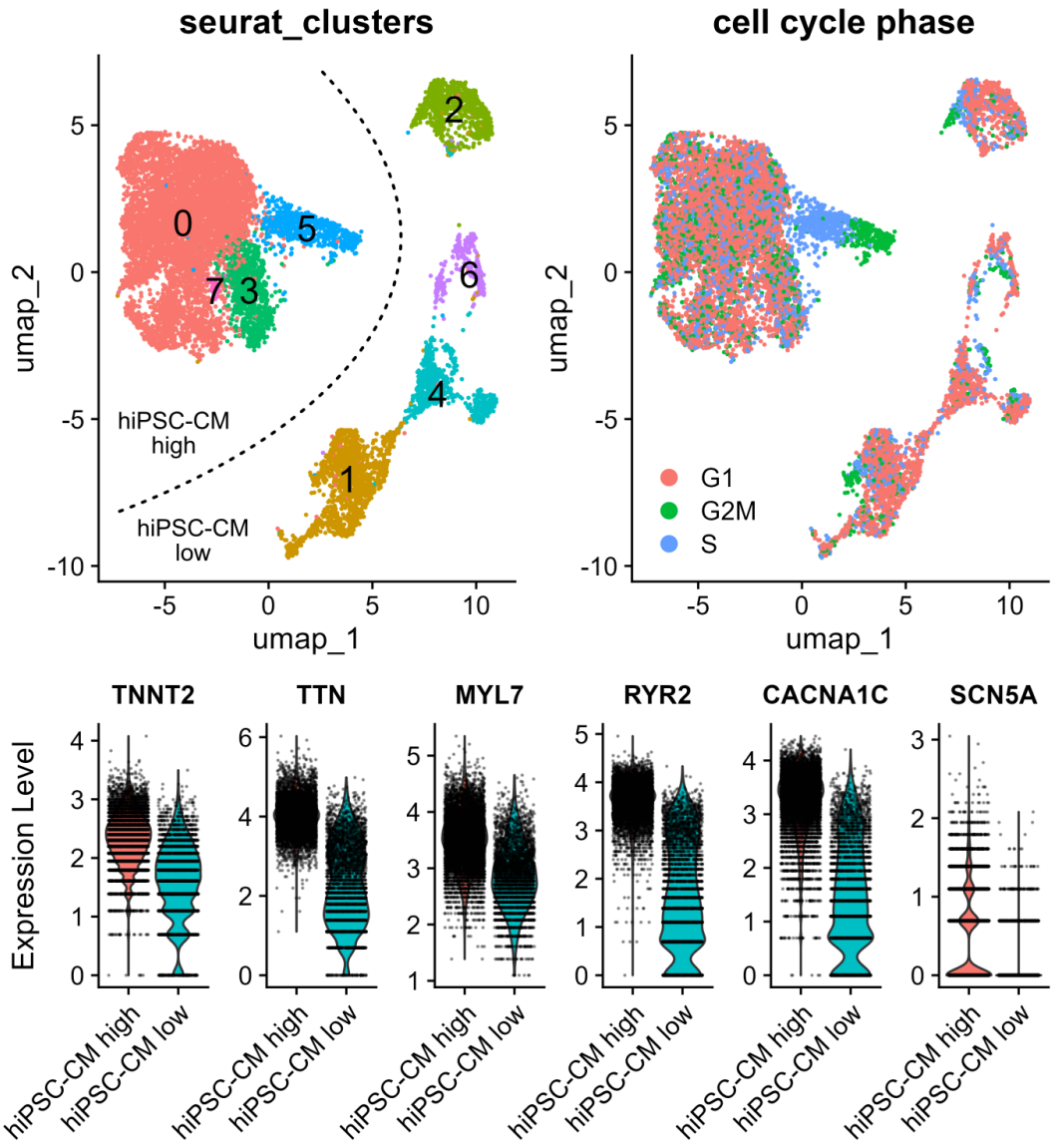

Figure 3.2: The differentiation gives rise to two groups of hiPSC-CM, separated by their expression of cardiac genes. ***Top left***: *The UMAP displays the different clusters of nuclei. Dashed line represents the separation between the two groups: hiPSC-CM high, which have a high expression of cardiac genes, and hiPSC-CM low, which have a low expression of these genes.* ***Top right***: *The UMAP displays the cell cycle phase of nuclei. All clusters have similar proportion of each phase.* ***Bottom***: *Violin plots of the relative expression of cardiac genes, in two groups. Expression level is the normalised number of corresponding reads for each nuclei. Comparison of individual clusters expression is shown in supplementary figure A.5.*

0 and 2, away from the control and MM nuclei. This suggested a relatively strong difference in the expression profile of LV nuclei, when compared to the other two.

To explore the differences between the clusters, a gene ontology analysis was done on genes enriched in each cluster, compared to all the others. As a result, it appeared that nuclei forming the small cluster 5 were characterised by terms involving some kind of virus-associated activity. While they showed this anti-virus response, they were still hiPSC-CMs and did not show immune-related terms associated with other micro-organisms. For this reason, they are hereafter referred to as 'virus-activated'.

More interestingly, nuclei from the cluster 3 expressed genes involved in cellular division (Figure 3.4). This suggested that they were proliferative cardiomyocytes, and therefore highly immature cardiomyocytes. Of note, the proportion of proliferative hiPSC-CM was the highest with the control protocol (16% in C, 10% in MM and 8% in LV), suggesting a better efficiency of the MM and LV protocols in maturing cardiomyocytes.

The GO analysis did not output significant terms that would have allowed the characterisation of the five other clusters, although cluster 0 seems to separate from the rest of the cells on the UMAP.

3.2.1.2 Comparison between the different protocols

To be able to investigate the maturing effect of the MM and LV protocols, the proliferative and 'virus-activated' cardiomyocytes identified by the previous clustering were removed from the following analysis. The nuclei were then pooled by sample to create a pseudobulk dataset, which gives better results with the differential expression analysis. In this first comparison, differentially expressed genes were identified for each protocol, as compared to the rest of the nuclei (one protocol versus the combined two others). A gene set enrichment analysis (GSEA) was then done on these differentially expressed genes by protocol. Contrary to the previous gene

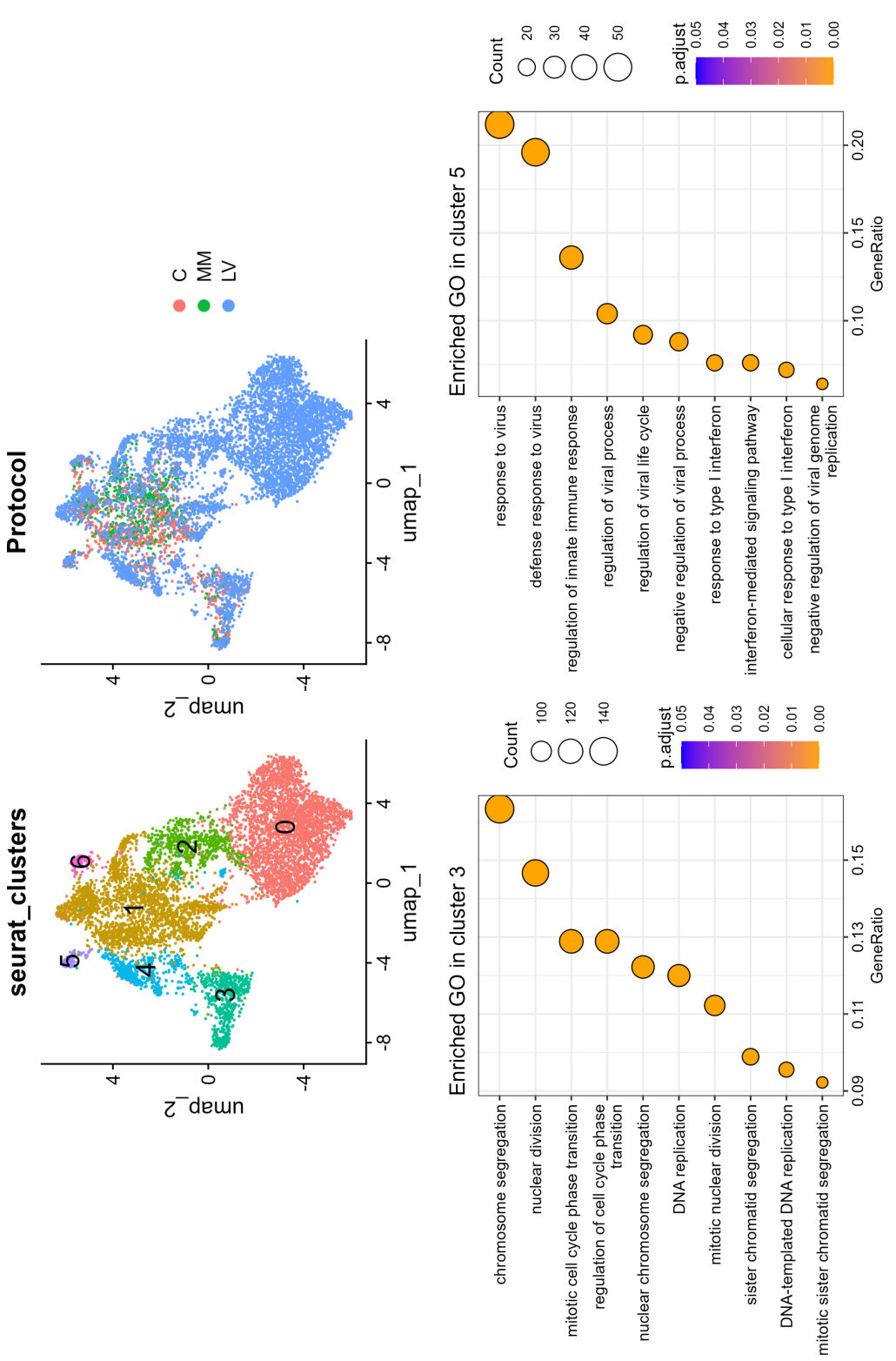

Figure 3.3: New clustering reveals a subpopulation of proliferative cardiomyocytes. ***Top**: UMAPs show the new clusters identified within the hiPSC-CM population, and from which protocol the nuclei originate. **Bottom**: the top 10 enriched GO terms are showed for the clusters 3 and 5. The GeneRatio is calculated as the number of differentially expressed genes associated with the corresponding GO term over the total number of differentially expressed genes. The count is the total number of reads of all genes associated with the corresponding GO term.*

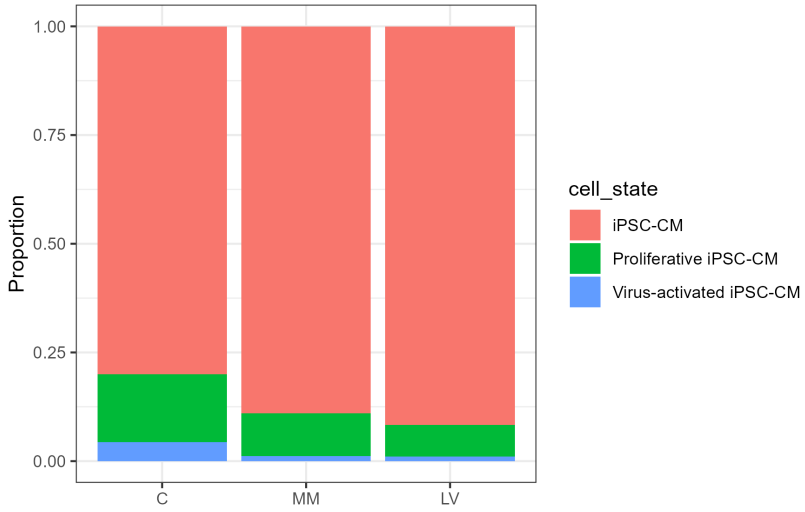

Figure 3.4: The proportion of proliferative cardiomyocytes is decreased with maturation protocols. *Proportion of the different cell states for each protocol. C=control, MM=maturation medium and LV=left-ventricle-like differentiation.*

ontology enrichment analysis, this analysis takes into account both up- and down-regulated genes and regroups them in large sets associated with the same GO terms to distinguish robust effects and their relative direction.

Considering that a majority of LV nuclei clustered together away from the control and MM nuclei, suggesting a relatively strong difference in the expression profile of LV nuclei compared to the other groups, it was expected that many GSEA terms would be significantly changed between the protocols. However, the GSEA resulted in surprisingly very few terms, and in only 2 out of 3 groups (Figure 3.5). The only meaningful result that could be seen on this analysis was the relative reduction in aerobic respiration in LV hiPSC-CMs. This weak power of the statistical analysis was attributed to the high complexity of the dataset, and it was therefore decided to compare the protocols two by two from this point on.

C versus MM When comparing C to MM hiPSC-CM, which separated nicely on the UMAP, the GSEA showed terms associated with synapse development in C hiPSC-CM and terms associated with metabolism in MM hiPSC-CM (Figure 3.6). Unsurprisingly, this suggests a better developed metabolism in hiPSC-CM from the MM group, compared to control cells.

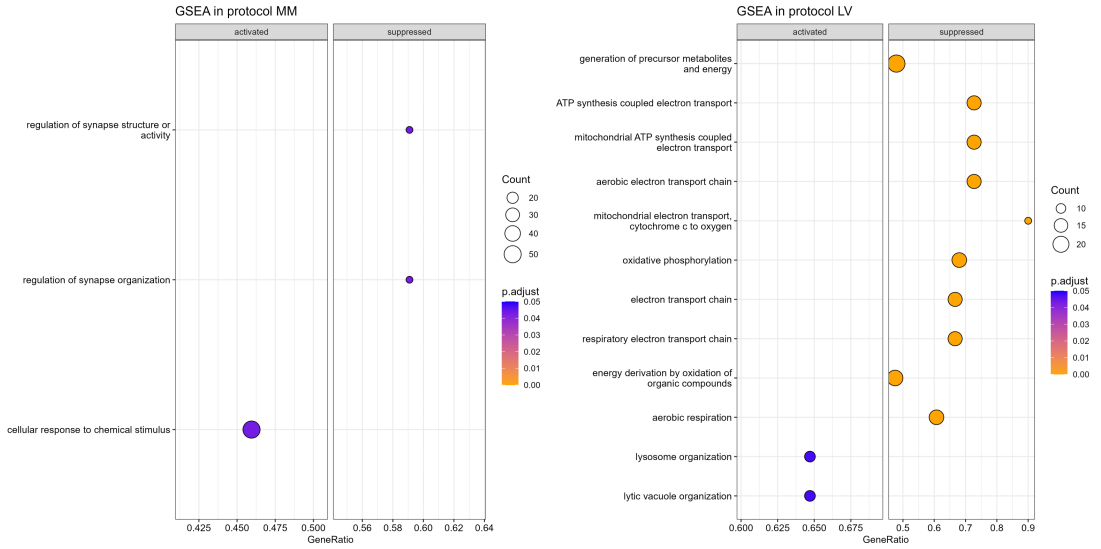

Figure 3.5: Aerobic respiration is the main driver of the separation of LV from C and MM hiPSC-CM. *Top 10 activated and top 10 suppressed gene ontology terms associated with differentially expressed gene sets between all three groups. Terms in only the MM and LV groups were significantly activated or suppressed, as compared to the other two groups. The GeneRatio is calculated as the number of differentially expressed genes associated with the corresponding GO term over the total number of differentially expressed genes. The count is the total number of reads of all genes associated with the corresponding GO term. C=control protocol, MM=maturation medium and LV=left-ventricle-like differentiation.*

C versus LV When comparing C to LV hiPSC-CM, which also separated on the UMAP, the GSEA showed terms associated with cellular respiration that were suppressed in LV hiPSC-CM (Figure 3.7).

MM versus LV When comparing the two maturation protocols, MM and LV, they separated nicely on the UMAP. The GSEA gave consistent results, with suppressed cellular respiration in LV hiPSC-CMs and activated axon development, as compared to MM (Figure 3.8). Of note, transmembrane potassium channels regulation was activated in LV hiPSC-CM as well.

All this suggested that LV hiPSC-CM had reduced cellular respiration compared to the two other groups, and MM hiPSC-CM had reduced neuronal-like activity.

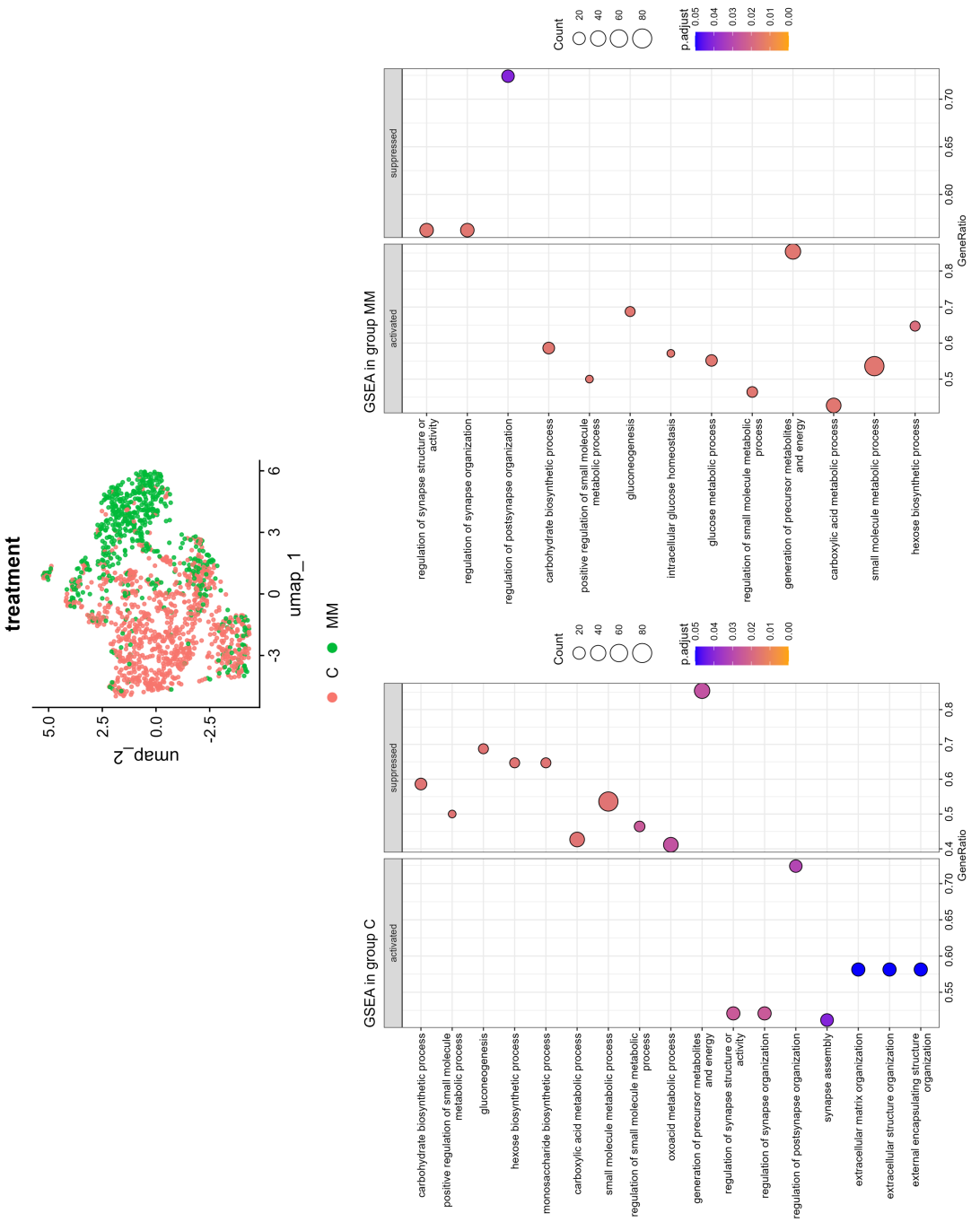

Figure 3.6: Metabolism in MM and synaptic organisation in C are the main drivers of the separation between these groups. *Top 10 activated and top 10 suppressed gene ontology terms associated with differentially expressed gene sets in the C vs MM groups. The GeneRatio is calculated as the number of differentially expressed genes associated with the corresponding GO term over the total number of differentially expressed genes. The count is the total number of reads of all genes associated with the corresponding GO term. C=control, MM=maturation medium.*

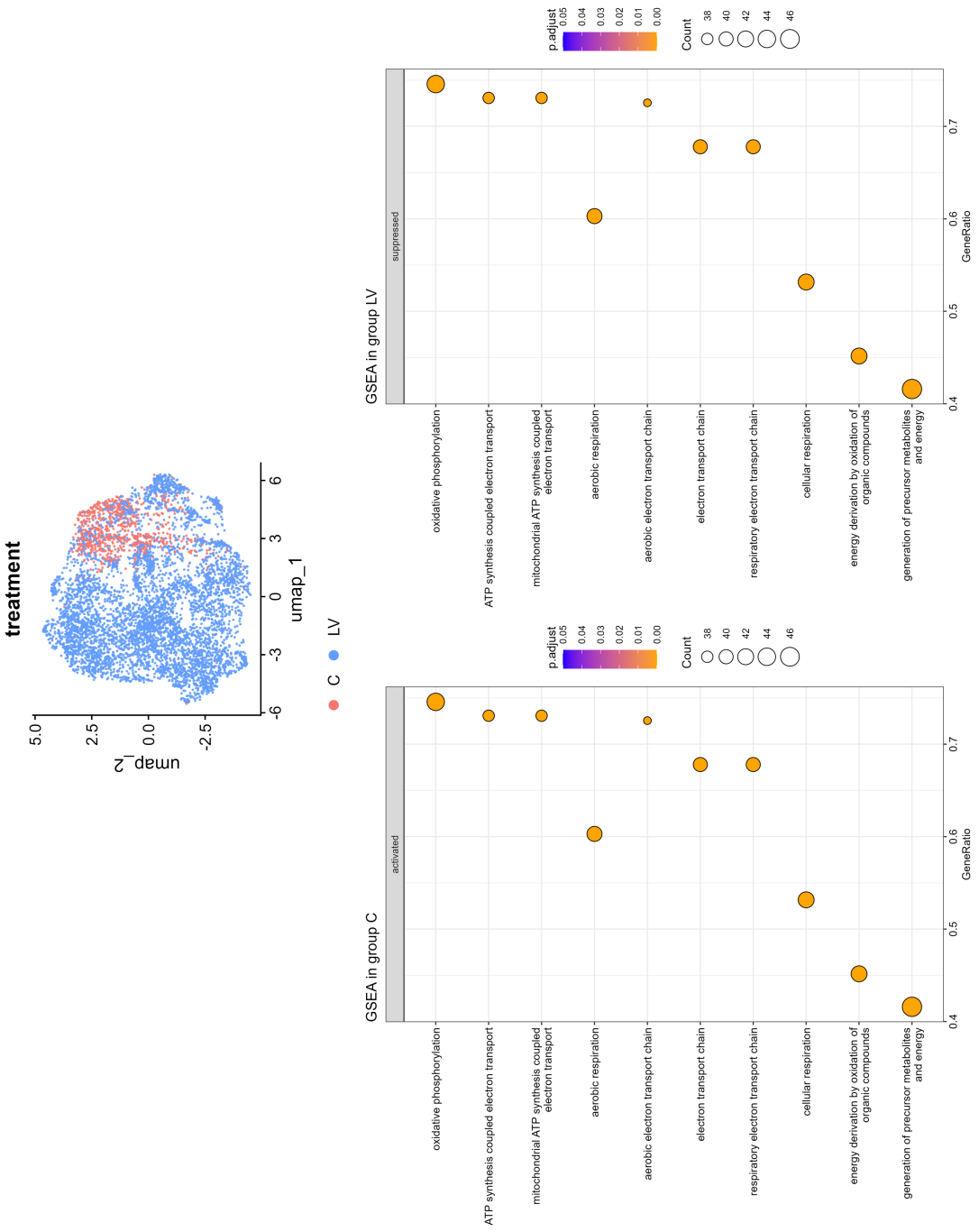

Figure 3.7: Decreased aerobic respiration in LV hiPSC-CM mainly drives their separation from C. *Top 10 activated and top 10 suppressed gene ontology terms associated with differentially expressed gene sets in the C vs LV groups. The GeneRatio is calculated as the number of differentially expressed genes associated with the corresponding GO term over the total number of differentially expressed genes. The count is the total number of reads of all genes associated with the corresponding GO term. C=control, LV=left-ventricle-like differentiation.*

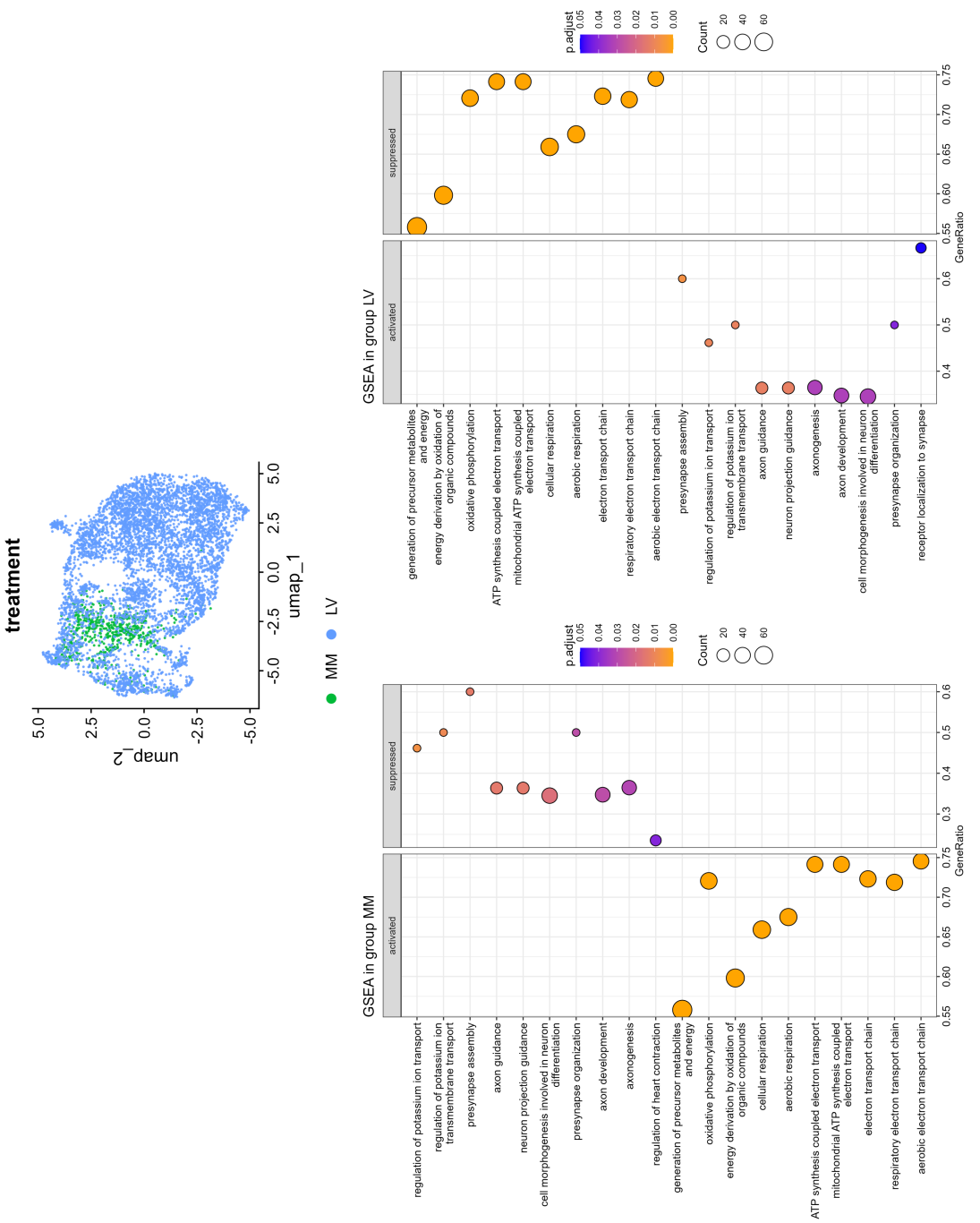

Figure 3.8: Decreased aerobic respiration and increased axon development make LV hiPSC-CM separate from MM. *Top 10 activated and top 10 suppressed gene ontology terms associated with differentially expressed gene sets in the MM vsLV groups. The GeneRatio is calculated as the number of differentially expressed genes associated with the corresponding GO term over the total number of differentially expressed genes. The count is the total number of reads of all genes associated with the corresponding GO term. MM=maturation medium and LV=left-ventricle-like differentiation.*

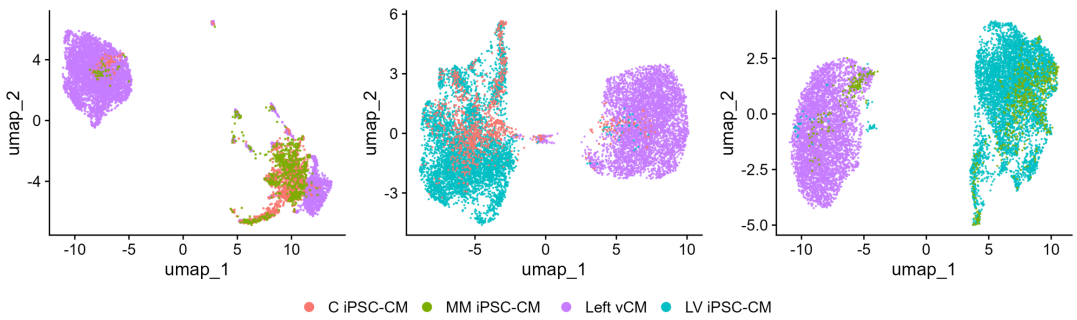

Figure 3.9: MM and LV protocols do not bring hiPSC-CMs expression profile significantly closer to adult vCMs. *UMAPs showing combined hiPSC-CM and adult vCM nuclei.* ***Left****: comparison between C, MM and vCM.* ***Middle****: comparison between C, LV and vCM.* ***Right****: comparison between MM, LV and vCM. C=control, MM=maturation medium, LV=left ventricle-like differentiation, vCM=adult ventricular CM.*

3.2.1.3 Comparison to adult ventricular cardiomyocyte

After determining what made MM and LV hiPSC-CM different from control cells, it was interesting to compare these groups to adult ventricular cardiomyocyte (vCM), to evaluate whether these changes were making hiPSC-CMs closer to adult CMs, how far they still were from this objective, and what marker genes could be identified as interesting targets to increase hiPSC-CM maturity.

To this aim, snRNA-seq data from healthy adult human left vCM were downloaded from the Human Cell Atlas project, ”Cells of the adult human heart” [94]. After integration and normalisation with the hiPSC-CM data, comparisons between the same pairs presented above and adult CMs were performed.

The UMAPs projections highlighted that while some vCM nuclei were clustering with C and MM nuclei, most of the hiPSC-CM were clustering together, completely apart from adult vCM. Moreover, no clear progression could be seen between hiPSC-CM and adult vCM with the maturation protocols, indicating that MM and LV cells are still much closer to control hiPSC-CMs than adult vCMs (Figure 3.9).

To explore more robustly and specifically the differences between hiPSC-CMs and adult vCM, the different group data (control, MM, LV and leftvCM)

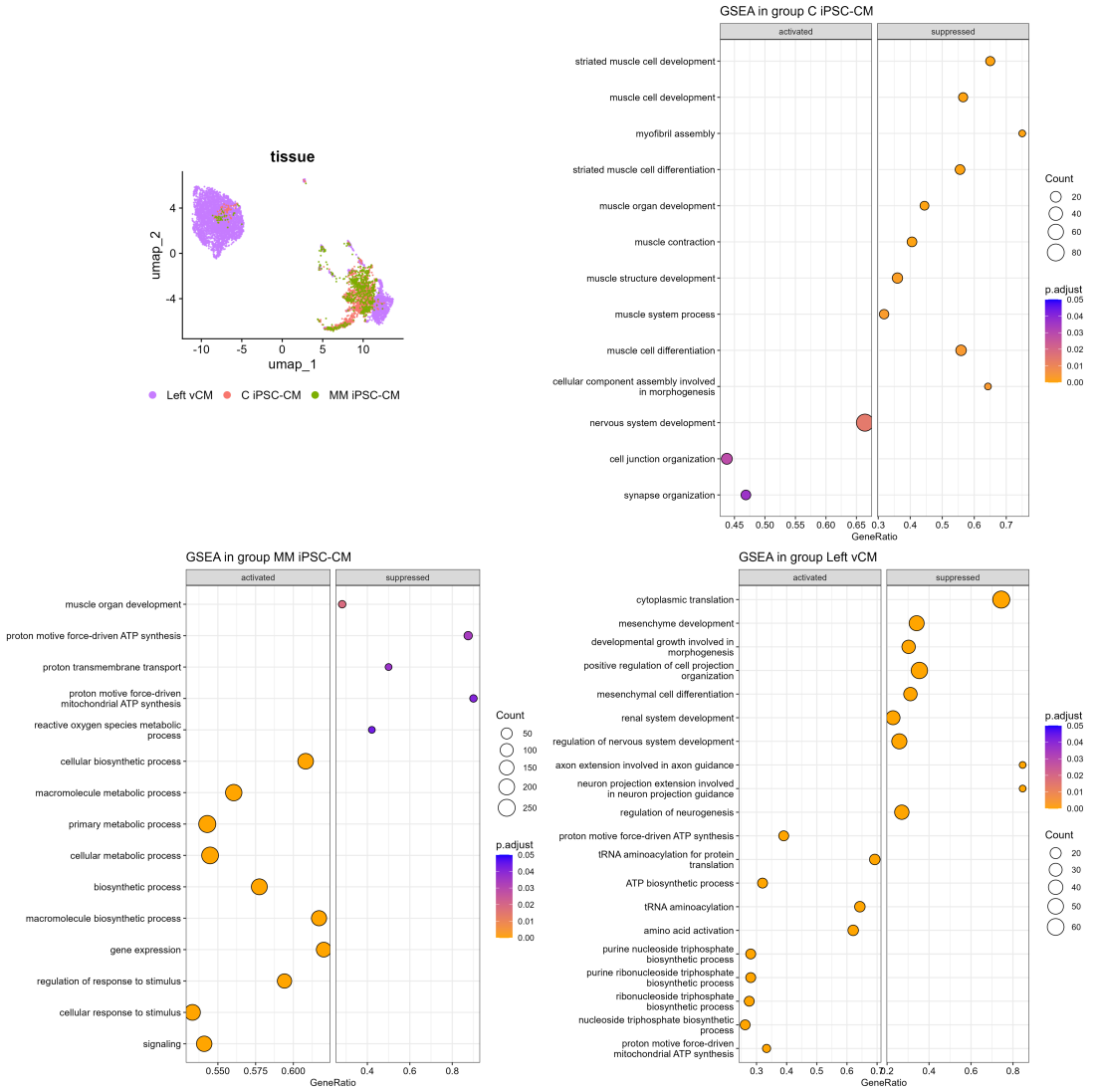

Figure 3.10: MM cells display signs of cardiac maturation and increased metabolism. *Top 20 gene ontology terms associated with differentially expressed gene sets between all cell origins (control, MM, left vCM) compared to the others. These terms are split between upregulated (activated) and downregulated terms (suppressed). C=control, MM=maturation medium and vCM=adult ventricular CM.*

were pooled by sample to perform a pseudobulk differential expression analysis by pairs against adult left vCM. Then a GSEA was run on the differentially expressed genes to study the relative specificities of each group.

vCM versus C and MM Results comparing left vCMs to C and MM hiPSC-CM are presented in the figure 3.10. Genes associated with muscle structure development and contraction were downregulated in C hiPSC-CM compared to the other groups, indicating that MM hiPSC-CMs were more mature

on this aspect. Unsurprisingly, MM cells show increased expression of genes involved in metabolic processes. Finally, results from adult left vCM highlighted that the main difference between the hiPSC-CM groups and adult vCMs lay in ATP production that was still decreased in hiPSC-CM, and mesenchymal development which was increased in hiPSC-CM.

vCM versus C and LV Results comparing left vCMs to C and LV hiPSC-CM are presented in the figure 3.11. Genes associated with muscle structure development and contraction were downregulated in C hiPSC-CM compared to the other groups, indicating that LV hiPSC-CMs were also more mature on this aspect. Additionally, it appeared that control cells still displayed terms associated with defence response against viruses, even though the cluster 5 presented in the figure 3.3 was previously removed from the analysis. To investigate more in depth, the core enrichment genes associated with these terms were extracted from the GSEA results. These genes (MX1, STAT1, EIF2AK2, TRIM5, ZC3HAV1, IFITM3, ISG15, RSAD, OAS1, OAS2, OAS3) are interferon-induced genes involved in anti-viral defence. Moreover, LV cells showed increased transcriptomic activity and reduced ATP production.

Finally, results from adult left vCM highlighted that mesenchymal development and nervous system development were increased in hiPSC-CM. The core enrichment genes associated with these nervous system development terms were extracted from the GSEA results. These genes (EPHA4, BMPR2, SEMA5A, RELN, VEGFA, NRP1, PLXNA4, BMP7, ROBO2, SLIT2, ROBO1) are also involved in the development of various other tissues, including cardiac tissue, and in cell migration. This suggested that hiPSC-CM retain developmental activity.

vCM versus MM and LV Results comparing left vCMs to MM and LV hiPSC-CM were presented in the figure 3.12. Similarly to the previous comparison, the MM group was characterised by an increased signalling and metabolism, compared to the others. Additionally, LV hiPSC-CMs displayed increased processes associated with neuronal development. In this case,

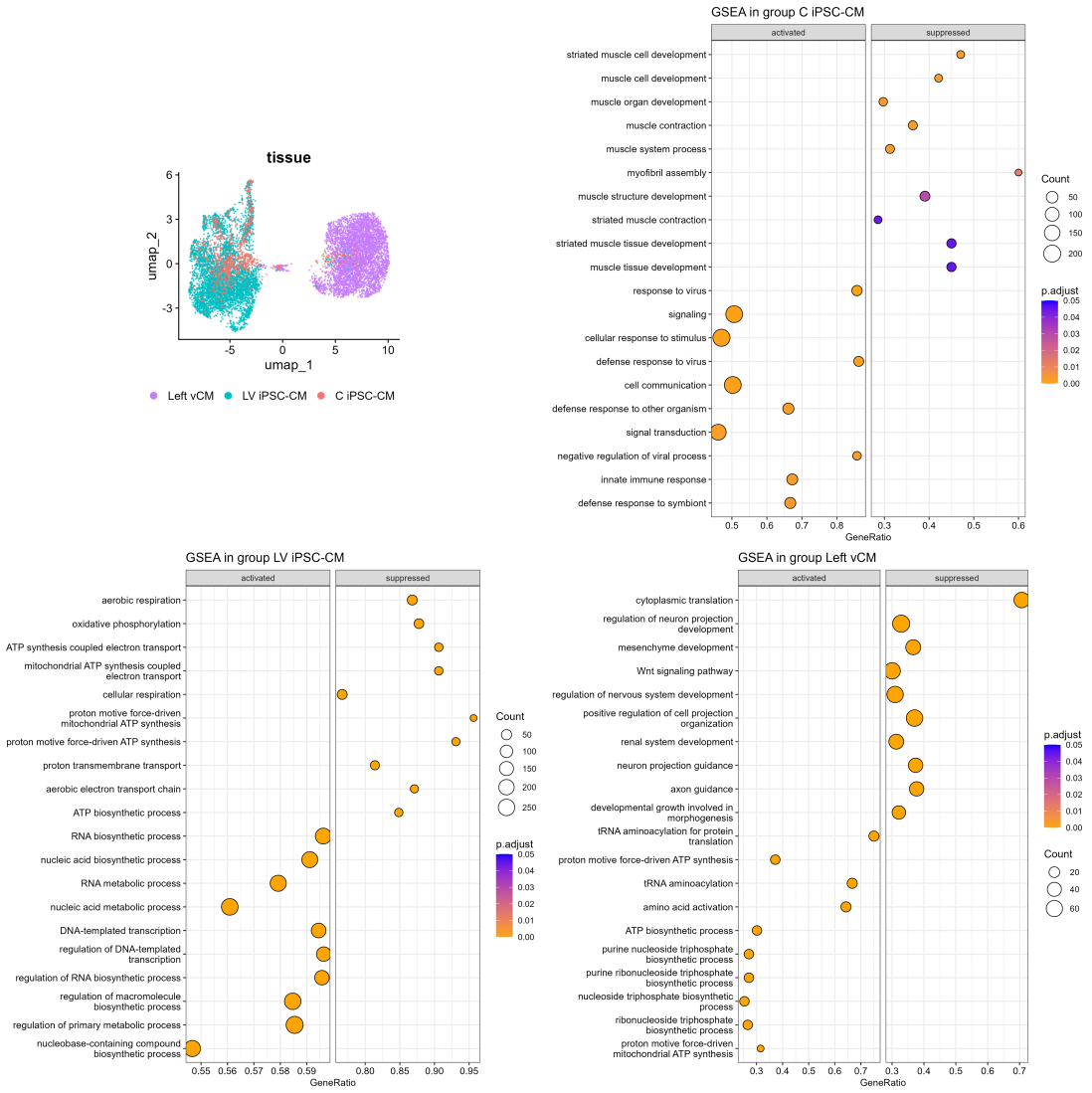

Figure 3.11: LV display signs of cardiac maturation and increased transcriptomic activity. *Top 20 gene ontology terms associated with differentially expressed gene sets between all cell origins (control, LV, left vCM) compared to the others. These terms are split between upregulated (activated) and downregulated terms (suppressed). C=control, LV=left-ventricle-like differentiation and vCM=adult ventricular CM.*

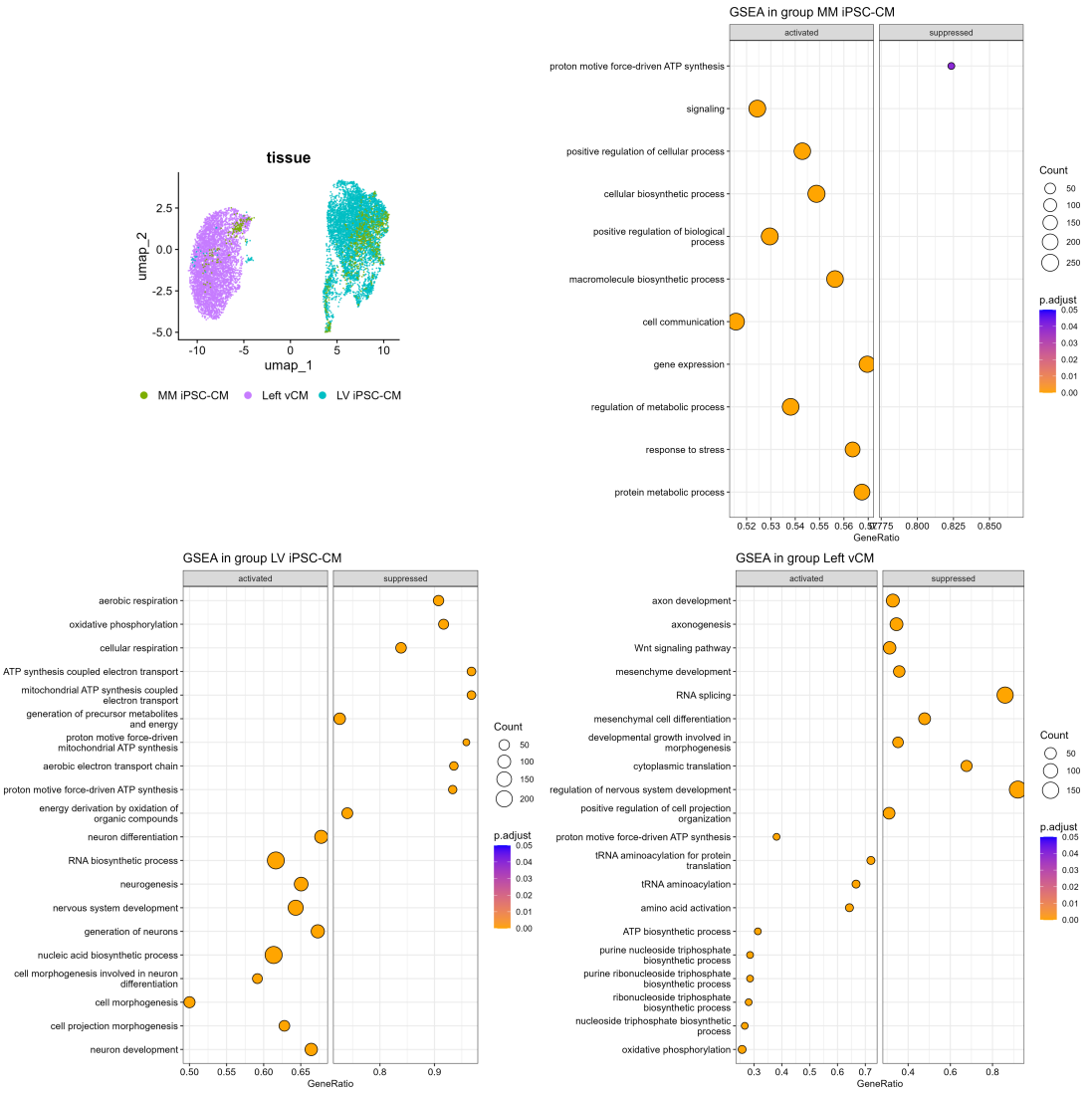

Figure 3.12: MM and LV hiPSC-CM still differ from adult left vCM mainly because of reduced cellular respiration. *Top 20 gene ontology terms associated with differentially expressed gene sets between all cell origins (MM, LV, left vCM) compared to the others. These terms are split between upregulated (activated) and downregulated terms (suppressed). MM=maturation medium, LV=left-ventricle-like differentiation and vCM=adult ventricular CM.*

the common core enrichment genes (BMPR1B, SMAD4, ETV1, FGFR2, SMO, NEO1, ADNP) are involved in cell growth, differentiation and various tissues development. This again pointed towards a general developmental activity rather than a specific neuronal specification. Finally, cellular respiration- and ATP production-related genes were activated in adult left vCMs and suppressed in hiPSC-CMs, predominantly in LV hiPSC-CMs.

3.2.1.4 Expression of genes of interest

Additionally, the differentially expressed genes determined with the pseudobulk analysis mentioned above were filtered and manually regrouped into sets corresponding to physiological functions of interest for the rest of this project. The results were gathered in the figure 3.13. The genes were clustered by similarity of expression profile across the different groups. The two biggest clusters were grouping genes that were differentially expressed between hiPSC-CMs andvCMs, which demonstrated still a high similarity between all hiPSC-CM, compared to adult vCM.

To conclude, snRNA-seq data showed a change in the expression profile of hiPSC-CM treated with the metabolic maturation medium or differentiated with the left-ventricle specification protocol. These changes were mainly related to the muscular structure and contractility of the cells, which was more developed in the MM and LV groups. Despite this, it was evident that a long way still separates the hiPSC-CM from the fully matured vCMs. Cells from the MM and LV groups still shared much more similarities with the relatively immature control hiPSC-CM than with vCMs. The main reason of this separation from vCMs was the cellular respiration and ATP production, which appeared still significantly reduced in the MM an LV groups.

3.2.2 Western Blots

As RNA does not always translate into protein, expression of a selection of proteins was investigated by western blotting. First, β_2-AR, PDE3B

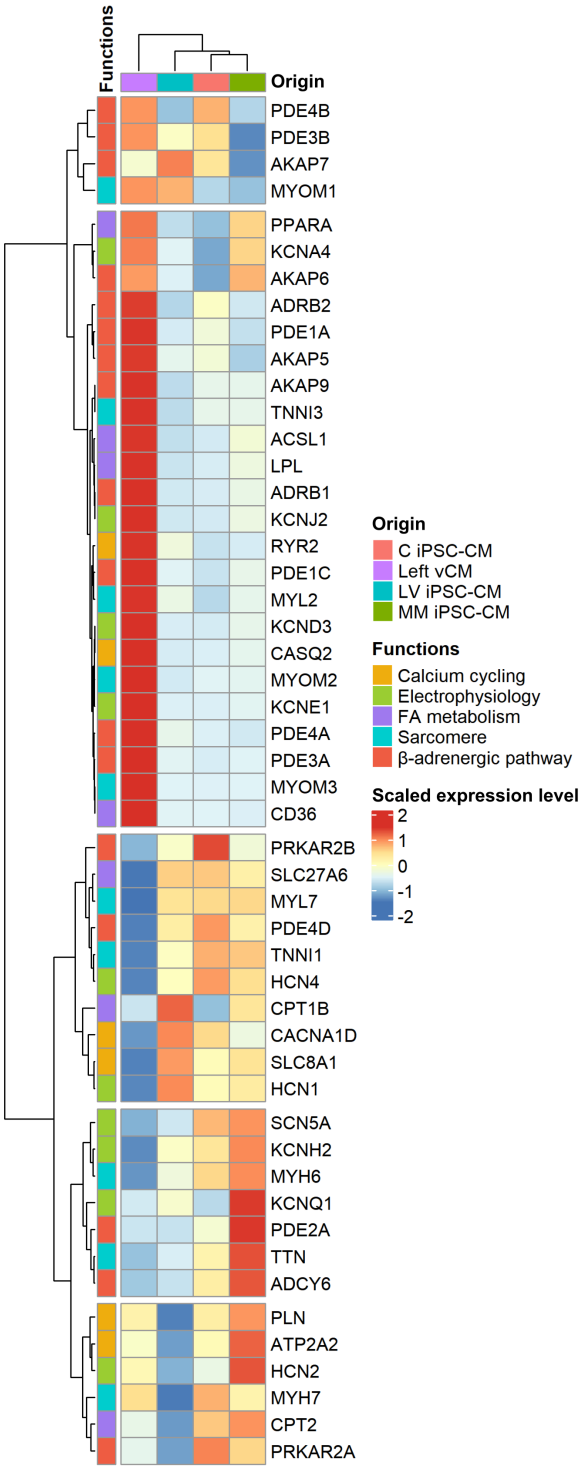

Figure 3.13: MM and LV hiPSC-CMs are still much closer to C hiPSC-CMs than adult left vCMs. *Heatmap presenting the relative expression of selected genes of interest between the four groups (Origin) C, MM and LV hiPSC-CMs, and left vCM. Genes were manually grouped into cardiac physiological functions (Functions). Columns (groups) and rows (genes) were automatically clustered (see trees on the left side and top of the heatmap), based on their relative expression profile (Scaled expression level). C=control, MM=maturation medium, LV=left-ventricle-like differentiation and vCM=adult ventricular CM.*

and PDE4D were investigated. β_2-AR and PDE4D are crucially involved in the regulation of the excitation-contraction coupling, and while PDE3B appears to have only a minor impact on CM physiology through regulation of energy metabolism, it was chosen as it is the only PDE3 isoform differentially expressed between the hiPSC-CM protocol tested (Figure 3.13). Additionally, the two pairs of sarcomeric proteins ssTnI/cTnI and MLC2a/MLC2v were also blotted for. During maturation of the sarcomeres, an isoform switch occurs from foetal to adult ventricular isoform for several proteins. In the human ventricles, ssTnI is replaced by cTnI and MLC2a is replaced by MLC2v. Finally, the SERCA and LTCC, crucial for maintaining the calcium cycling necessary to muscle contraction and relaxation were investigated.

6 samples from control and MM hiPSC-CM, and 5 from LV hiPSC-CM, each from a different differentiation batch, were harvested. A standard SDS-PAGE electrophoresis on acrylamide gels was done, followed by a dry transfer. The expression of the blotted proteins was normalised to the total protein expression observed on the corresponding gels before transfer, with the Bio-Rad Stain-Free technology, to correct for loading variability. Total protein normalisation was used because the expression of most housekeeping genes changes during maturation. The corrected values were then normalised to the control group median, for a direct comparison relative to the control group.

Blot for PDE3B gave highly variable band intensities, with variable background and no band at the expected size, around 124kDa. Similarly, LTCC showed no band at the expected size around 210-240kDa but the bands of the SERCA2 were still visible, indicating most probably that the stripping was not efficient in this case (Figure 3.14). For these reasons, PDE3B and LTCC blots were excluded from the analysis.

PDE4D blots revealed 2 main bands around 80-100kDa (Figure 3.15). The non-specific PDE4D antibody was expected to give 2 bands at 100kDa

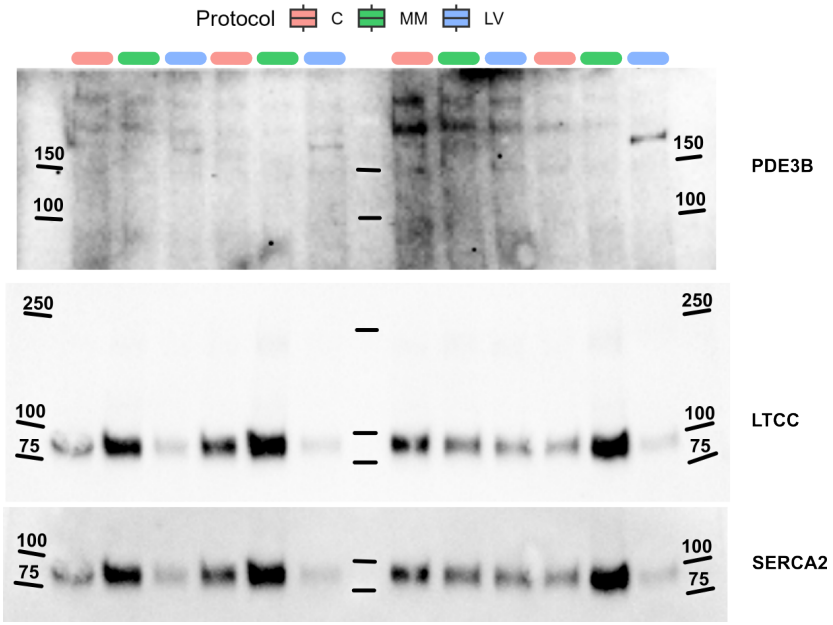

Figure 3.14: PDE3B and LTCC show no band at the expected size. *Representative blots of PDE3B, LTCC and SERCA2.*

and 85kDa for PDE4D5 and PDE4D3 isoforms. Interestingly, LV samples showed relatively high intensity for the upper band, associated with PDE4D5. The total quantification of PDE4D appeared to be down-regulated by 50% in the MM group, compared to the others, but this change was not statistically significant (1±0.6233 in C vs 0.484±0.1904 in MM and 0.9495±0.4131 in LV, P=0.476). This tendency was corroborated by the previous snRNA-seq data, where the same reduction in PDE4D expression compared to control hiPSC-CM could be observed in the MM group. With this reduction, PDE4D expression in MM hiPSC-CMs was closer to vCM expression. PDE4D is a key regulator of the calcium cycling and β-adrenergic-cAMP-PKA pathway in cardiomyocytes [16] but the main isoform regulating cAMP in human CMs switches from PDE4 to PDE3 in adult CMs.

β_2-AR blots display 3 main bands, one at the expected 46kDa, another at ~55kDa corresponding to post-translational modifications, and finally, a dimerised form at ~105kDa. The total β_2-AR expression showed a significant rise in hiPSC-CM from both maturation protocols (1±0.1587 in C vs 3.05±0.8972, P=0.020 in MM or 4.071±1.271, P=0.005 in LV). This rise is compatible with an increased maturation of the hiPSC-CM when

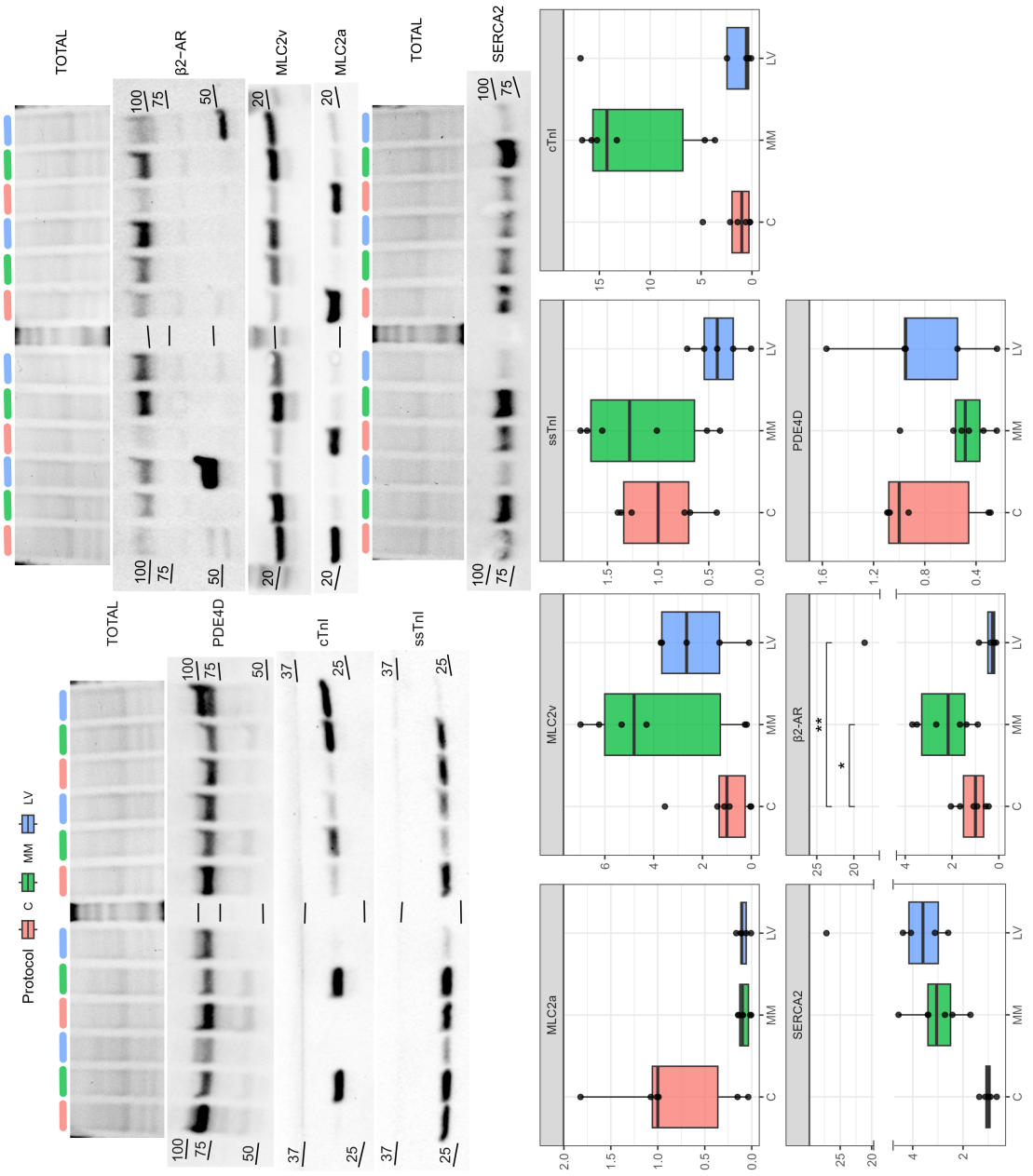

Figure 3.15: A sarcomeric maturation is induced by both the MM and LV protocols. *Representative blots and total protein expression on corresponding gels. Protein expression is normalised to total protein and to control. See detailed statistics in supplementary table B.1.*

accompanied by an increase in β_1-AR [46]. The snRNA-seq data were inconsistent with this finding, ADRB2 expression level was reduced in both LV and MM hiPSC-CM.

A single band at ~95kDa showed the relative expression of SERCA2 in the different groups. This protein expression appeared to be doubled in MM hiPSC-CM, but reduced by 2/3 in LV cells, with the exception of one outlier (1±0.861 in C vs 2.167±1.84 in MM and 0.3402±0.6455 in LV, P=0.094). Although these tendencies were not statistically significant, snRNA-seq data showed a similar pattern, with an increased expression of ATP2A2 in MM and a decrease in LV hiPSC-CM. An increase in SERCA2 expression seems to be associated with ventricular cardiomyocyte maturation [107], which would indicate that the MM protocol contributed to the hiPSC-CM calcium handling maturation, while the LV protocol did not. But calcium handling is also dependant on SERCA2 activity, and this tendency needed to be correlated to the actual calcium cycling measurements.

cTnI and ssTnI blots exhibited a single band at ~30kDa. Quantification revealed a robust increase in cTnI expression in cells treated with the MM medium (1±1.664 in C vs 14.25±8.841, P=0.057 in MM or 0.5435±2.123, P=0.777 in LV), while a reduction of >50% in expression of the foetal cardiac isoform ssTnI was observed in LV hiPSC-CM (1±0.6407 in C vs 1.282±1.022 in MM and 0.4165±0.286 in LV, P=0.064). Although this reduction was not statistically significant for the LV group, it was correlated with a reduction in TNNI1 RNA expression. If confirmed, this would indicate an increasing reliance on the adult cardiac isoform cTnI, and therefore a maturation of the sarcomeres, in both maturation protocols.

Finally, a single band at ~20kDa showed the relative expression of MLC2v and MLC2a. Although not statistically significant, a strong tendency revealed an important increase in the adult ventricular isoform MLC2v in both MM and LV hiPSC-CM (1±1.066 in C vs 4.803±4.737 in MM and 2.65±2.365 in LV, P=0.117), as well as a robust reduction in the foetal

pan-cardiac isoform MLC2a (1±0.697 in C vs 0.0994±0.0914 in MM and 0.107±0.0551 in LV, *P*=0.051). snRNA-seq data showed a similar pattern for MYL2, which is still far from the left vCM level, but not for MYL7 which expression is identical between hiPSC-CMs groups. If confirmed, this would indicate an isoform switch from the foetal to the adult isoform, as expected in matured sarcomeres, for both maturation protocols.

While only a limited number of proteins were investigated, the results presented above indicated a maturation of the sarcomeres in both MM and LV hiPSC-CM.

3.3 Discussion and perspectives

In this chapter, the objective was to determine how the two maturation protocols differ in terms of maturation efficiency and pathways involved. The results gathered from the snRNA-seq data highlighted that a subpopulation of proliferative hiPSC-CMs coexists with more mature hiPSC-CMs in all groups, but their proportion was reduced with the two maturation protocols. This information would have been lost with bulk RNA-sequencing, and implies that measurements affected by the maturity of the cells are biaised by this subpopulation. Moreover, data from both snRNA-seq and western blots were consistent with a maturation of the sarcomeric structure in both MM and LV hiPSC-CMs, as compared to control cells. Finally, snRNA-seq data suggested that the main difference between hiPSC-CMs, cultured in the conditions presented here, and human adult left vCM was the mitochondrial activity associated with cellular respiration. This was most probably due to the limiting culture conditions. Indeed, a recent study showed that long-term electrical stimulation of MM hiPSC-CM induced a significant maturation of the cells, associated with an increase in mitochondrial development and activity [84].

3.3.1 Limitations

Several limitations can affect the translatability of the results presented in this chapter. First, in terms of numbers, the LV hiPSC-CM samples sent for sequencing contained 2-3 times the amount of cells in the C and MM samples. This led to huge disparities in group sizes and probably have biaised the GSEA results, artificially inflating the importance of LV-related terms when comparing hiPSC-CM pairs to adult left vCMs. Moreover, to limit the complexity of the adult data, only left ventricular samples have been included, resulting in samples originating from only 2 donors. However, data from the 2 vCM donors clustered separately on the UMAP, even after data batch integration by sample, which indicated a significant difference between the two donors. A GSEA showed that the samples from donor D3 had reduced cardiac activity-related gene expression, in favour of pro-inflammatory genes, as compared to the donor D1 and hiPSC-CMs (Figure 3.16). The same inflammation-associated terms were enriched when comparing the left vCM samples form donor D3 to the right vCM samples of the same donor (data not shown). For this reason, as the donor D3 would not be a good comparator to the hiPSC-CM, it was removed from the analysis. As a result, samples from only one vCM donor were included, which may lead to confounding results because of genetic background differences.

Other limitations actually include the data batch integration and its impact on UMAP distances. Distances on the UMAP are theoretically proportional to the differences in expression profile: nuclei from two different cell-types have very different expression profiles and should be represented far apart on the UMAP. However, technical variability can add-up to biological variability and affect these UMAP distances, artificially separating similar cell-types. This is why the different datasets (or batches) are 'integrated'. The *Harmony* package used in this chapter for the data integration by sample works as followed: The expression profile of all cells or nuclei is used to group them by similarity of expression profile (grouping

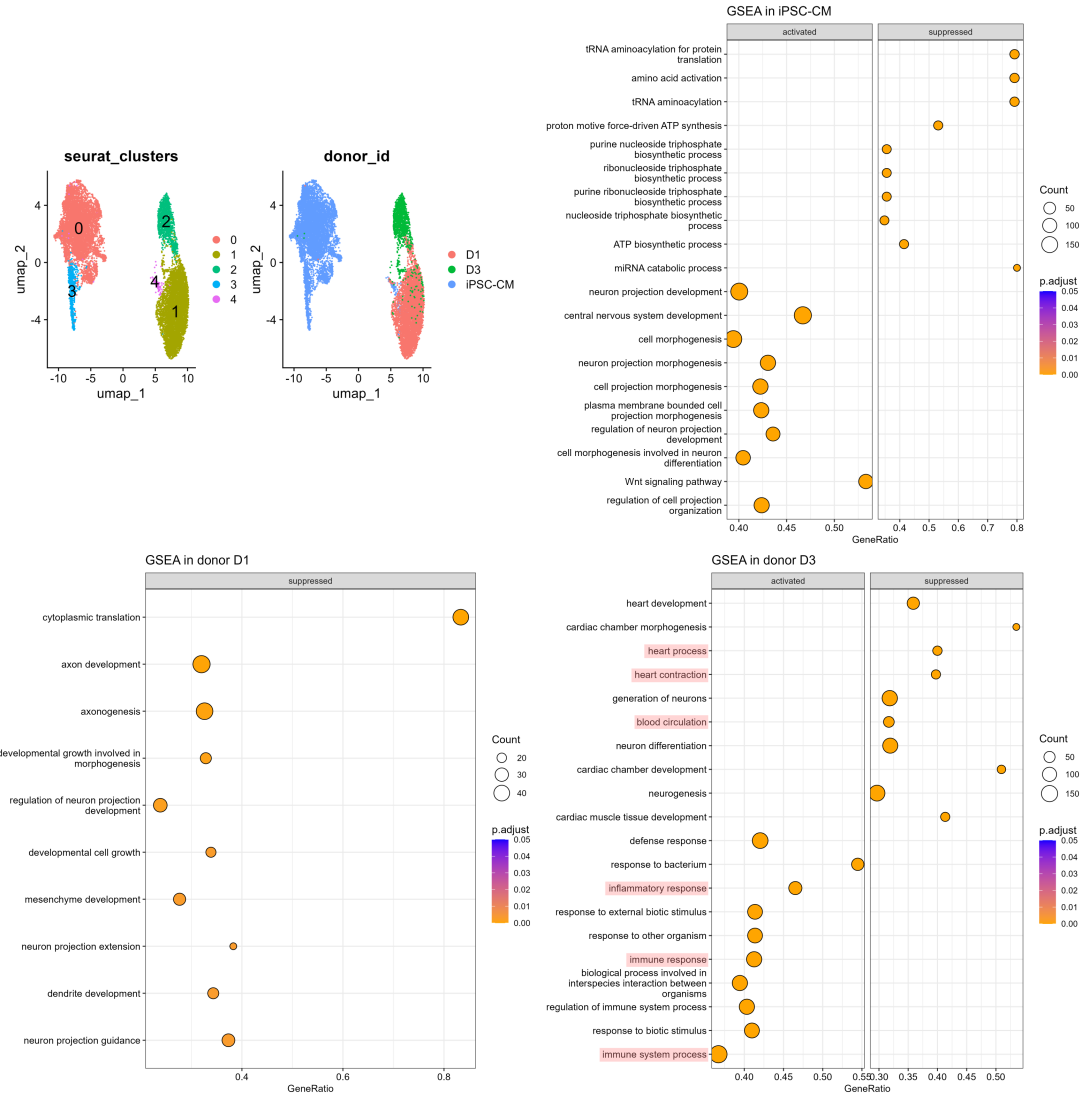

Figure 3.16: Adult vCM donor D3 shows reduced cardiac activity-related gene expression, in favour of pro-inflammatory genes. ***Top left***: *UMAPs showing the clusters and the nuclei donor origin of combined hiPSC-CM and adult vCM data with the two donors D1 and D3.* ***Top right and bottom***: *GSEA results showing the top 10 enriched and top 10 suppressed GO terms in the 3 groups (nuclei origin donor D1, donor D3, and hiPSC-CM). Highlighted terms show reduced cardiac activity-related gene expression and increased pro-inflammatory gene expression.*

together identical cell-types), favoring clusters with mixed sample origin. Based on these soft cluster memberships, the technical variability that exists between samples (or batches) is regressed-out [90]. However, this means that integrating datasets with only one cell type (at one time-point) leads to less robust results, especially on UMAPs. This fact has been tested on the data presented in this chapter. In one of the UMAPs comparing vCMs to hiPSC-CMs, a small difference in filtering of just adult vCM snRNA-seq data (from adaptive filtering to a slightly more stringent manual filtering) lead to a very different UMAP, with a subset of adult left vCM completely separating from the rest, while it was perfectly merged with the main vCM cluster before (Figure 3.17). Because of this, the biological proximity of the different groups tested in this chapter cannot be inferred by the UMAP distances. A more robust indication is the GSEA.

On the other hand, the GSEA also have limitations. It is based on manual annotations grouping genes within Gene Ontology (GO) terms, and this is not optimal on every biological process. As an example, in GO Biological Process 2023 annotation, MYL2 and TNNI3 are associated with 21 terms, MYL7 is associated with only 6 terms. Among all these terms, only 4 are common between the 3 cardiac sarcomeric genes, and they are very general terms: Blood Circulation (GO:0008015), Heart Development (GO:0007507), Heart Process (GO:0003015) and Heart Contraction (GO:0060047). The other terms are highly redundant but do not always overlap between the different genes, as terms in italics show (see Table 3.1). The most specific term grouping these 3 genes, Heart Contraction, also groups genes involved in the excitation-contraction coupling like SCN5A, KCNQ1, ATP1B1 and ATP1A2, CASQ2, RYR2 (but not CACNA1C).

Table 3.1: Example of discrepancies in GO annotations between well-known genes of similar functions.

GO Biological Process 2023 associated terms	**MYL2**	**MYL7**	**TNNI3**
Blood Circulation (GO:0008015)	X	X	X
Blood Vessel Morphogenesis (GO:0048514)			X
Calcium Ion Homeostasis (GO:0055074)			X
Calcium-Mediated Signaling (GO:0019722)			X

Table 3.1: Example of discrepancies in GO annotations between well-known genes of similar functions. (continued)

GO Biological Process 2023 associated terms	**MYL2**	**MYL7**	**TNNI3**
Cardiac Muscle Cell Development (GO:0055013)	X		
Cardiac Muscle Contraction (GO:0060048)	X		X
Cardiac Muscle Tissue Development (GO:0048738)		X	
Cardiac Muscle Tissue Morphogenesis (GO:0055008)	X		X
Cardiac Myofibril Assembly (GO:0055003)	X		
Cardiac Ventricle Morphogenesis (GO:0003208)	X		X
Circulatory System Development (GO:0072359)	X		X
Heart Contraction (GO:0060047)	X	X	X
Heart Development (GO:0007507)	X	X	X
Heart Process (GO:0003015)	X	X	X
Intracellular Calcium Ion Homeostasis (GO:0006874)			X
Intracellular Monoatomic Cation Homeostasis (GO:0030003)			X
Muscle Cell Fate Commitment (GO:0042693)	X		
Myofibril Assembly (GO:0030239)	X		
Negative Regulation Of ATP-dependent Activity (GO:0032780)			X
Negative Regulation Of Cell Growth (GO:0030308)	X		
Negative Regulation Of Cellular Process (GO:0048523)	X		
Negative Regulation Of Growth (GO:0045926)	X		
Regulation Of Cardiac Muscle Contraction (GO:0055117)			X
Regulation Of Cardiac Muscle Contraction By Calcium Ion Signaling (GO:0010882)			X
Regulation Of Cell Growth (GO:0001558)	X		
Regulation Of Muscle Contraction (GO:0006937)	X		
Regulation Of Striated Muscle Contraction (GO:0006942)	X		
Skeletal Muscle Contraction (GO:0003009)			X
Striated Muscle Contraction (GO:0006941)	X		X
Striated Muscle Tissue Development (GO:0014706)		X	

Table 3.1: Example of discrepancies in GO annotations between well-known genes of similar functions. (continued)

GO Biological Process 2023 associated terms	**MYL2**	**MYL7**	**TNNI3**
Vasculogenesis (GO:0001570)			X
Ventricular Cardiac Muscle Tissue Development (GO:0003229)	X		X
Ventricular Cardiac Muscle Tissue Morphogenesis (GO:0055010)	X		X

Similarly, neurodevelopmental processes were highlighted in hiPSC-CMs, and especially in control cells, as compared to adult vCMs. While it has been suggested from single-cell proteomics studies that there might be a novel neuro-cardiac hybrid cell-type in hiPSC-CM cultures [108], it is an early finding and remains debatable, especially whether it is a characteristic of *in vivo* developing human CMs, or if it is indicative of hiPSC-CMs culture conditions. Furthermore, when individually investigated, most genes found under the neurodevelopmental terms were also involved in more general cell growth and cardiac development [109]–[113]. This is in line with other findings from single cell transcriptomics which found an interaction between certain neurogenesis genes and cardiogenesis transcription factors during hiPSC-CM differentiation [114]. This suggests a bias toward neuronal development in GO annotations, obscuring these genes role in cardiogenesis and falsely implying a hybrid cell type. Future work should focus on this important aspect of hiPSC-CMs.

Taken together, these observations constitute a limit to the use of GSEA and prevents unbiased and meaningful analysis of global physiological system changes, and forces the manual exploration of a limited number of genes.

A lot of discrepancies were seen between RNA and protein expression: ADRB2/β2-AR, TNNI3/cTnI, MYL7/MLC2a showed opposite patterns of expression between RNA and protein levels, in the LV and MM groups

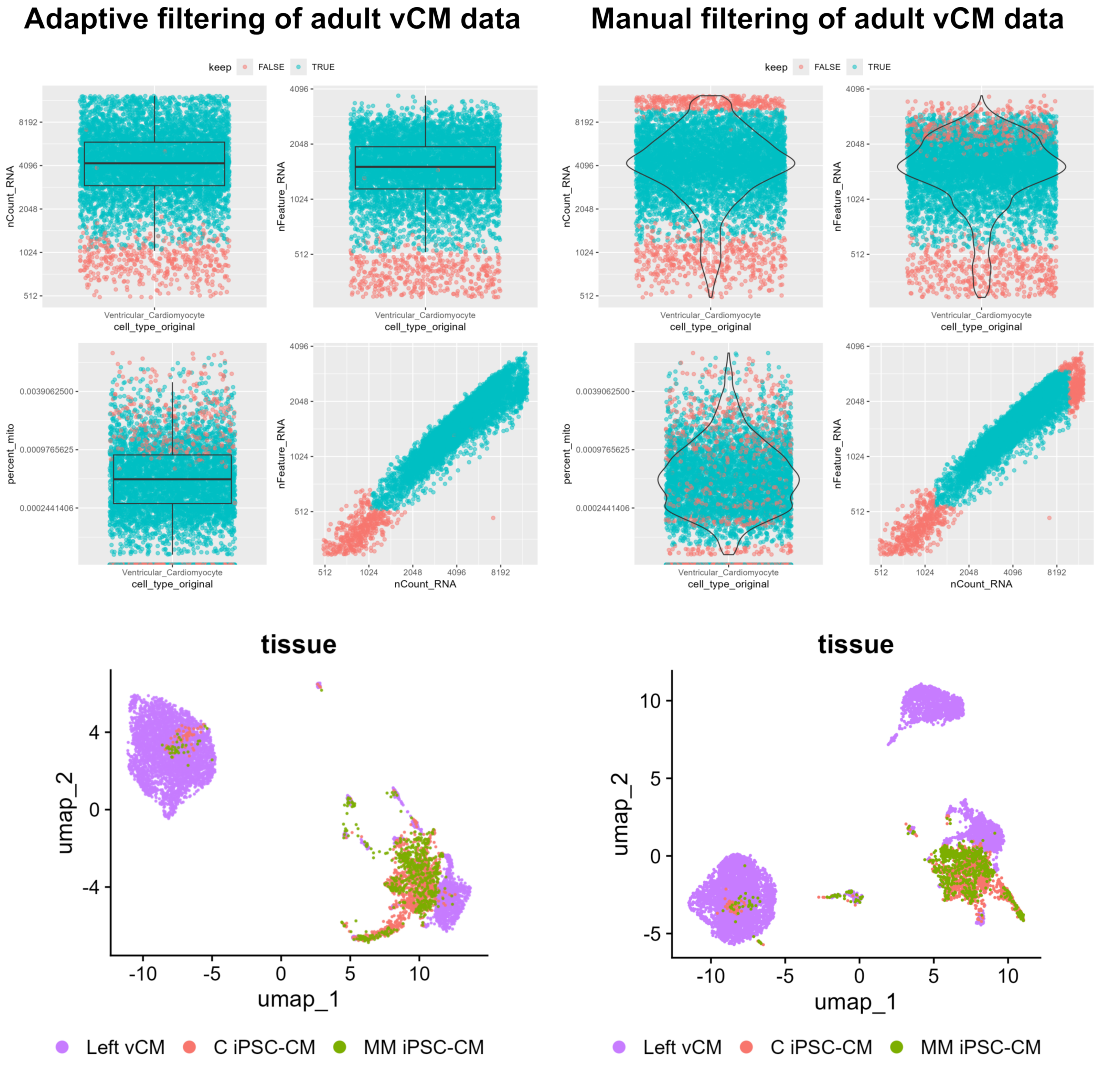

Figure 3.17: UMAP distances are not robust, a small change in data filtering can completely separate a cluster in two. ***Left***: *Dot plots and box plots show data distribution for three important measurements (nCount_RNA, nFeature_RNA and percent_mitochondria). Colors indicate which nuclei were excluded by the filtering. The filtering was adaptive to each measurement distribution, extreme outliers (>3 IQR from median) were excluded. The UMAP below was generated after the corresponding filtering.* ***Right***: *Dot plots and violin plots show data distribution for three important measurements (nCount_RNA, nFeature_RNA and percent_mitochondria). Colors indicate which nuclei were excluded by the filtering. The filtering was manually determined based on each measurement density. The UMAP below was generated after the corresponding filtering.*

compared to the control group. This highlights the importance of focusing on global transcriptomic analyses — such as GSEA, which assesses patterns across sets of related genes — rather than relying on individual gene analysis to draw meaningful conclusions. Beyond translation regulations that occur in cells, this problem might have been intensified by the use of single *nucleus* RNA-sequencing instead of single *cell*-RNA sequencing. snRNA-seq does not rely on viable cell dissociation, which is particularly useful for adult cardiac tissue since it is resistant to enzymatic digestion, which leads to technical artifacts. Additionally, snRNA-seq can be used with fixed and frozen samples, making it well-suited for many experimental designs. To be able to compare hiPSC-CM samples to adult human cardiac samples, snRNA-seq was chosen for this project. The drawback however, is that snRNA-seq only gives access to nuclear RNA. Some genes have been shown to be depleted in nuclei compared to the cytoplasm, which might explain part of the discrepancies between transcriptomics data and protein expression [115].

Additionally, different antibodies were used for blotting adult and foetal ventricular sarcomeric protein isoforms (MLC2v & MLC2a and cTnI & ssTnI). As the antibodies affinity for the proteins is probably different, the proper adult/foetal ratio could not be calculated, and only tendencies could be stated. Moreover, loading normalisation was performed with total protein quantification. This was chosen to avoid the problems associated with variations in many proteins expression (including numerous housekeeping genes) during hiPSC-CM maturation, but total protein quantification was performed on gels. This introduced possible bias associated with inhomogeneous transfer of proteins on the membrane. To be able to draw robust conclusions on protein expression, future work will include proteomics. This future analysis will include 6 samples from different differentiation batches from the three protocols, similar to the samples presented in this chapter, as well as 6 human adult cardiac samples. This work is ongoing as the samples have been sent for processing and mass spectrometry in early April 2025.

Finally, while the focus has been made on hiPSC-CM highly expressing cardiac genes to reduce the complexity of the data and increase the power of further analyses, a deeper investigation of the different 'hiPSC-CM low' clusters would also give an interesting perspective on the effects of the maturation protocols. Interestingly, most 'hiPSC-CM low' clusters were solely LV hiPSC-CM, with C and MM nuclei appearing in mostly one 'hiPSC-CM low' cluster (Figure 3.18). Of note, along with differences in the composition of these clusters, the total proportion of 'hiPSC-CM low' nuclei was increased with the LV protocol but remained unchanged with the MM protocol, ranging from 20% in C and MM groups, to 35% in LV. This suggested that this proportion was not changed due to the maturation of the cells, but rather due to the type of differentiation they originated from.

Differences in canonical cardiac genes expression with a population characterised by a higher expression of these genes compared to the other, was also reported in a single-cell proteomics study published earlier this year [108]. These 'hiPSC-CM low' cells could be hybrid or intermediate cell-types as they were found to co-express some features of other cell-types, such as smooth muscle cell proteins in this study. Future work on snRNA-seq data will include further investigation of these clusters.

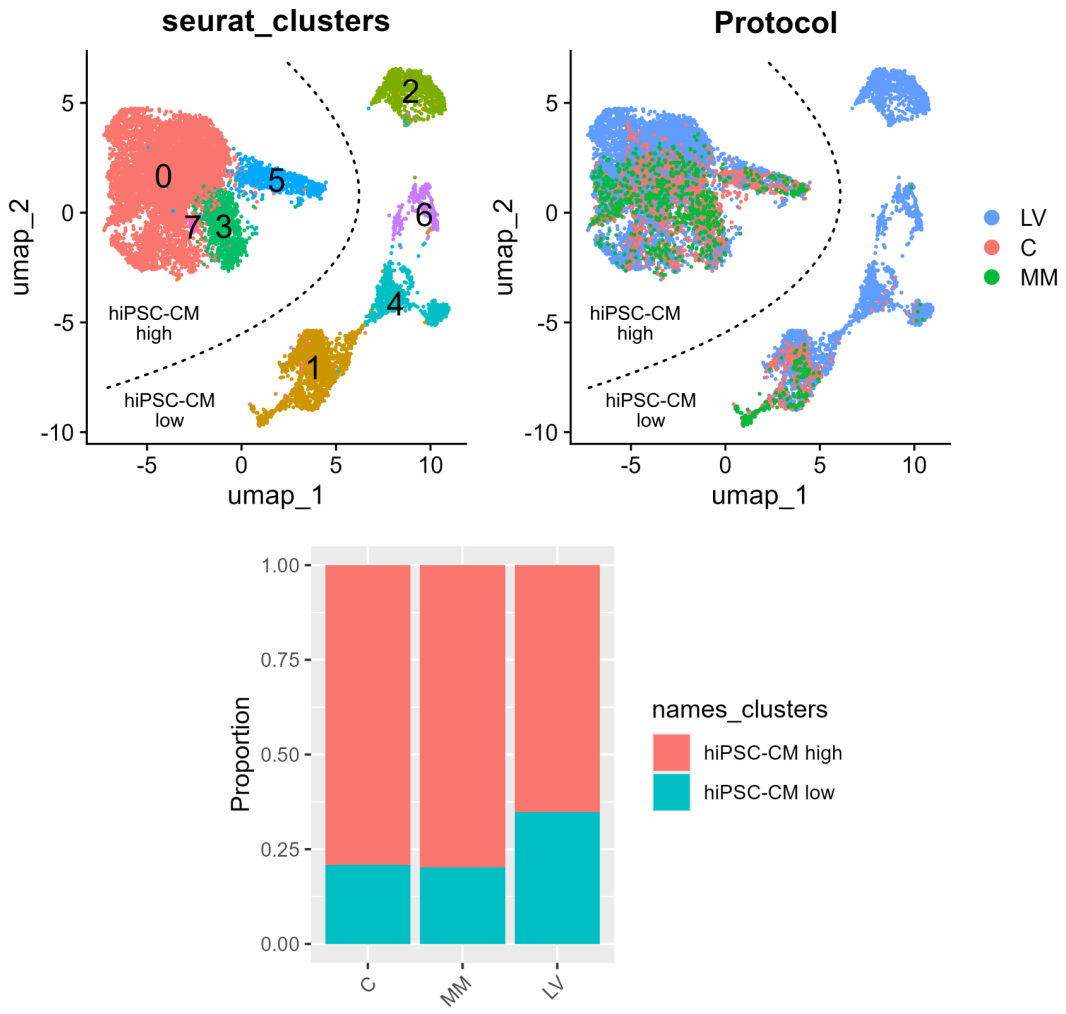

Figure 3.18: Most 'hiPSC-CM low' clusters are solely LV hiPSC-CM, with C and MM nuclei appearing in only one cluster. ***Top left**: The UMAP displays the different clusters of nuclei. Dashed line represents the separation between the two groups: hiPSC-CM high, which have a high expression of cardiac genes, and hiPSC-CM low, which have a low expression of these genes. **Top right**: The UMAP displays the protocol of origin of the nuclei. **Bottom**: Proportion of hiPSC-CM high versus hiPSC-CM low from the different protocols. This proportion is increased in the LV group but unchanged in the MM.*

Chapter 4

Using FRET-based cAMP sensors to explore the impact of maturation on β-adrenergic pathway in hiPSC-derived cardiomyocytes

4.1 Introduction

β-adrenergic stimulation is a key regulatory mechanism in cardiac physiology, enabling the heart to adapt to increased peripheral metabolic demands through enhanced force development (inotropy), heart rate (chronotropy), and relaxation (lusitropy). Catecholamines signal through binding to β-ARs, leading to an increase in AC activity and subsequent cAMP production. cAMP serves as an intracellular second messenger, activating PKA, the central effector of β-adrenergic signalling. However, cAMP is a ubiquitous second messenger that orchestrates, in addition to excitation-contraction coupling, a myriad of other cellular processes in CMs, including gene expression and metabolism, among others. The coordination of the multiplicity of cAMP/PKA dependent effects is therefore of primordial importance. For example, when sympathetic stimulation enhances cAMP signalling as we walk up a flight of stairs, it must do so without simultaneously triggering gene transcription. Such coordination is achieved via spatial and temporal confinement of both PKA and cAMP, within subcellular compartments where PKA is anchored in proximity of specific phosphorylation targets and is activated by spatially confined pools of cAMP. These functional localised gradients of cAMP are

called nanodomains, as their size has been measured to be in the range of 30-60 nM [14], [15]. Current evidence suggests that four phenomena may contribute to generate these cAMP gradients: localized cAMP production, localised breakdown by PDEs, restricted diffusion and buffering of cAMP. One of the main actors of this confinement are AKAPs, scaffold proteins that bind together β-AR, AC, PKA, PKA phosphorylation targets, phosphatases (PP) and PDEs. Individual AKAPs preferentially bind specific isoforms of β-AR, AC, PDE as well as specific target proteins. This leads to the formation of various functional combinations called signalosomes. The adrenergic pathway is highly responsive through the localised production of cAMP, which occurs in close proximity to PKA and its targets. However, to ensure specificity of its effects, cAMP diffusion must also be strictly controlled, as evidenced by experiments using FRET sensors [20]. FRET sensors allow the precise assessment of cAMP levels and PKA activity throughout the cell with sub-cellular resolution [116]. Indeed, when used in intact living cells, they allow for the real-time measurement of cAMP levels and PKA activity variations in a physiological state where intracellular organisation is preserved. FRET consists of an energy transfer from a donor fluorophore to a suitable acceptor that is proximity dependent (effective when the distance between the fluorophores is <10 nM). cAMP FRET sensors are usually made of a cAMP binding site from the PKA regulatory subunit, or the exchange protein directly activated by cAMP (EPAC), sandwiched between a donor and an acceptor fluorophore. Upon cAMP binding to the sensor cAMP binding site, the sensor conformation changes and therefore the distance between the fluorophores changes, which alters the efficiency of energy transfer. This change in FRET efficiency can then be measured by live cell imaging. Importantly, FRET sensors can be genetically fused to target protein domains, allowing accurate subcellular localisation of the sensor, and a very precise spatiotemporal measurement of cAMP across diverse nanodomains [20]. cAMP diffusion is thought to be shaped by PDEs, which act as ”sinks” by degrading cAMP from specific locations [21].

The cAMP pathway is also involved in the differentiation and maturation

processes of different cell lineages, including CMs, and most differentiation protocols include treatment with cAMP-elevating agents [82], [117]–[119]. When treated with ISO, a β-adrenergic agonist, hiPSC-CMs aged 90 days produce significantly more cAMP than cells aged 30 days. This stimulation by ISO is associated with a significant increase in β-AR and ACs expression, and increased PKA-mediated phosphorylation of Troponin I and Phospholamban in older hiPSC-CMs. Moreover, no specificity of β-AR subtype for activation of downstream mediators was shown in early hiPSC-CMs. In more mature (from day 90) hiPSC-CMs, the expression of caveolin3, a protein implicated in the formation of caveolae as well as T-tubules increases. As a consequence, caveolar nanodomains develop, allowing β_2-AR compartmentation. And with the establishment of the PDE ”sinks”, localisation of associated cAMP signals is possible [45], [46].

Recently, Giacomelli and collaborators co-cultured cardiac fibroblasts (CFs), endothelial cells (ECs) and CMs, in 3D microtissues. Their results suggest that cAMP and the downstream β-adrenergic pathway could be involved in CM maturation [82]. After 21 days, the CMs from these microtissues show an enhanced maturity when compared to CMs cultured in 2D or in the presence of only ECs or CFs. As a marker of maturity, CMs display a more rectangular shape with an increased sarcomere alig nMent, which is associated with enhanced contraction. These co-cultured CMs also have a more negative resting membrane potential and a prolonged action potential duration, closer to adult ventricular electrophysiology. Moreover, these cells display a more mature metabolic profile, as they primarily use fatty acid oxidation and produce more ATP. The authors found that this maturation was associated with the upregulation of adrenergic signalling proteins such as ADCY5, a cardiac specific adenylyl cyclase. Consistently, they found a higher concentration of cAMP in co-cultured CMs as compared to CMs cultured alone in 2D. This was correlated with the upregulation of the soluble guanylyl cyclase isoform GUCY1A3, as well as a higher expression of connexin 43 (Cx43) in both CMs and CFs from the microtissues. Silencing GJA1 (coding for Cx43) in CFs prior to microtissue formation impaired CM

maturation. Conversely, treatment of 2D cultured CMs with a membrane permeant form of cAMP enhanced maturity. The suggested mechanism of maturation in the co-cultured system is a close coupling between CFs and CMs from these microtissues, involving Cx43, which can act as a bridge to allow the diffusion of cyclic guanosine monophosphate (cGMP) from the CFs to the CMs in co-culture. There, cGMP is thought to enhance cAMP levels via the inhibitory effects of cGMP on PDE3 that degrade cAMP.

Despite interesting advances, research on cAMP nanodomains in hiPSC-CMs remains limited, and their mechanisms of formation and regulation are still not well understood. Addressing this knowledge gap is crucial for gaining deeper insights into embryonic and fetal cardiac development. Moreover, it could lead to the identification of novel targets to enhance the maturation of hiPSC-CMs, ultimately improving their utility for disease modelling and regenerative medicine. The work presented in this chapter aligns with this perspective: The specific aim is to use real-time FRET imaging to compare the contributions of PDE3 and PDE4 — two phosphodiesterases whose relative expression marks the transition from embryonic to mature cardiac myocytes — in regulating the cAMP-PKA pathway in hiPSC-CMs subjected to different maturation protocols.

4.2 Results

As an attempt to assess more directly cAMP signalling, both cytosolic and targeted FRET-based cAMP sensors were transduced (via AAV vector) in hiPSC-CMs aged 40-45 days, either treated with the maturation protocols presented before, or grown with the regular protocol. The cytosolic sensor, named EPAC-S^{H187} differs from the targeted CUTie sensors, as it is made with a pair of acceptor fluorophores, which greatly increases its brightness (Figure 4.1). Two targeted CUTie sensors were used, one linked to the AKAP79 anchoring protein, localised at the plasma membrane ; and the other linked to AKAP18, an anchoring protein localised at the SR

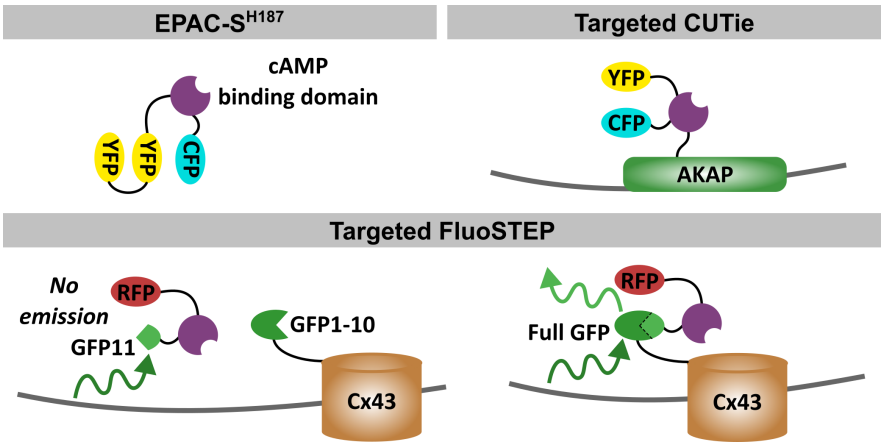

Figure 4.1: Schematic presenting the different FRET-based cAMP sensors used.

membrane (Figure 4.1). For each sensor, PDE-specific inhibitors were used to investigate the relative contribution of PDE3 and PDE4 at these sites, where known cAMP nanodomains relevant to the β-adrenergic signalling are maintained in CMs.

In addition to these known nanodomains, the presence and maturity of a novel nanodomain localised at the gap junction Cx43 was investigated, where Giacomelli *et al*. [82] suggest that cAMP diffuses from CFs to CMs. To this aim, CRISPR-Cas9 was used to insert the 11th β strand of the super-folder GFP (GFP11) at the C-terminus of the human gene GJA1 (coding for Cx43) in hiPSCs. This genetically modified hiPSC line (Cx43-GFP11) have been used in combination with specific FRET sensors (FluoSTEP ICUE) designed by our collaborators from the University of California, San Diego. In the FluoSTEP sensors, the donor fluorophore is the complementary fragment of the super-folder GFP (GFP1-10) [24]. Neither of the GFP fragments (GFP1-10 and GFP11) are fluorescent by themselves. However, when expressed in the same cell, the two fragments associate to form a fully functional fluorescent GFP. This allowed to investigate cAMP gradients specifically at Cx43 where the FRET sensor's donor fluorophore was functional (Figure 4.1). This approach also has the advantage of preserving endogenous levels of the targeted protein (here, Cx43) and avoid mistargeting of the sensor.

4.2.1 EPAC-S^{H187}

The principle of the FRET experiments presented in this chapter is as follows, with the example of the EPAC-S^{H187} sensor: This sensor is composed of a cAMP binding domain derived for the EPAC protein. This binding domain is sandwiched between a cyan fluorescent protein (CFP) and a couple of yellow fluorescent proteins (YFPs) (Figure 4.2). In the absence of cAMP, upon excitation of the CFP, a fluorescence resonance energy transfer (FRET) occurs and the CFP emission excites the pair of YFP. The main emission of the sensor is therefore the YFP wavelength. Upon treatments that induce a rise in cAMP concentration, cAMP has better chances to bind to the sensor. This induces a conformational change in the cAMP binding domain which results in the donor CFP and acceptor YFP to move away from each other. As a result, the FRET cannot occur as effectively and the main emission of the sensor is the CFP wavelength. The two emission wavelengths are recorded separately and the ratio CFP/YFP is used as a direct readout of cAMP concentration variations. Experiments were performed on live cells, maintained at 37°C. The measurements were carried out on individual cells, by manually drawing regions of interest before extracting the data for each cell (Figure 4.3). The results presented below were calculated as the percentage of change in fluorescent ratio normalised to baseline (R/R_0), or the maximum absolute R/R_0 (R_{max}).

4.2.1.1 Specific phosphodiesterase inhibition

After 5min of recording baseline fluorescence, a selective PDE inhibitor was added to the bath. Two different inhibitors were tested: rolipram (ROLI) (10 µM), a selective PDE4 inhibitor and cilostamide (CILO) (10 µM), a PDE3 inhibitor. DMSO was used as a control, as it is the solvent of both selective inhibitors. Addition of DMSO alone induced a transitory increase in cAMP in all hiPSC-CM groups, but this response was increased in LV and especially MM cells, and more sustained in MM (Figure 4.4). This response to the control treatment was unexpected but seemed to be due to an increase in

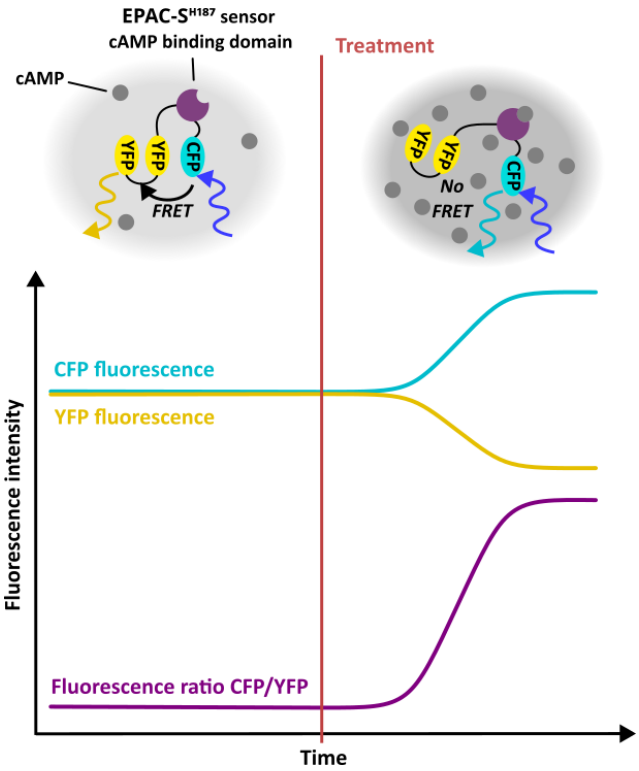

Figure 4.2: Schematic presenting the principles of the FRET experiments, with the example of the cAMP sensor, EPAC-S^{H187}.

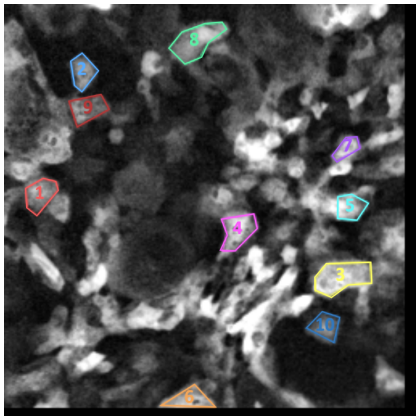

Figure 4.3: Example of ROIs drawn over hiPSC-CM transduced with EPAC-S^{H187} AAV.

cAMP concentration as both fluorescence traces (CFP and YFP) evolved in opposite direction, whereas an artefactual response due to changes in the optical properties of the bath would most likely have induced asymmetrical variations of the curves (Supplementary figure A.6).

ROLI induced a much higher and sustained rise in cAMP compared to DMSO alone, and this was even enough to saturate the sensor in the MM group, as the curve stayed flat, even with the addition of the other treatments. This saturation of the signal while other traces reached a higher amplitude strongly suggested these cells had a higher basal concentration of cAMP, thereby starting closer to the sensors saturation point and limiting the maximal amplitude. Traces from one biological replicate (1/3) exhibited a decrease in cAMP after the peak response, in C and LV hiPSC-CM (Figure 4.5), which suggested an increase in activity of other PDEs, in response to the rise in cAMP and subsequent PKA activity [120].

CILO however, induced an almost immediate but transitory decrease in

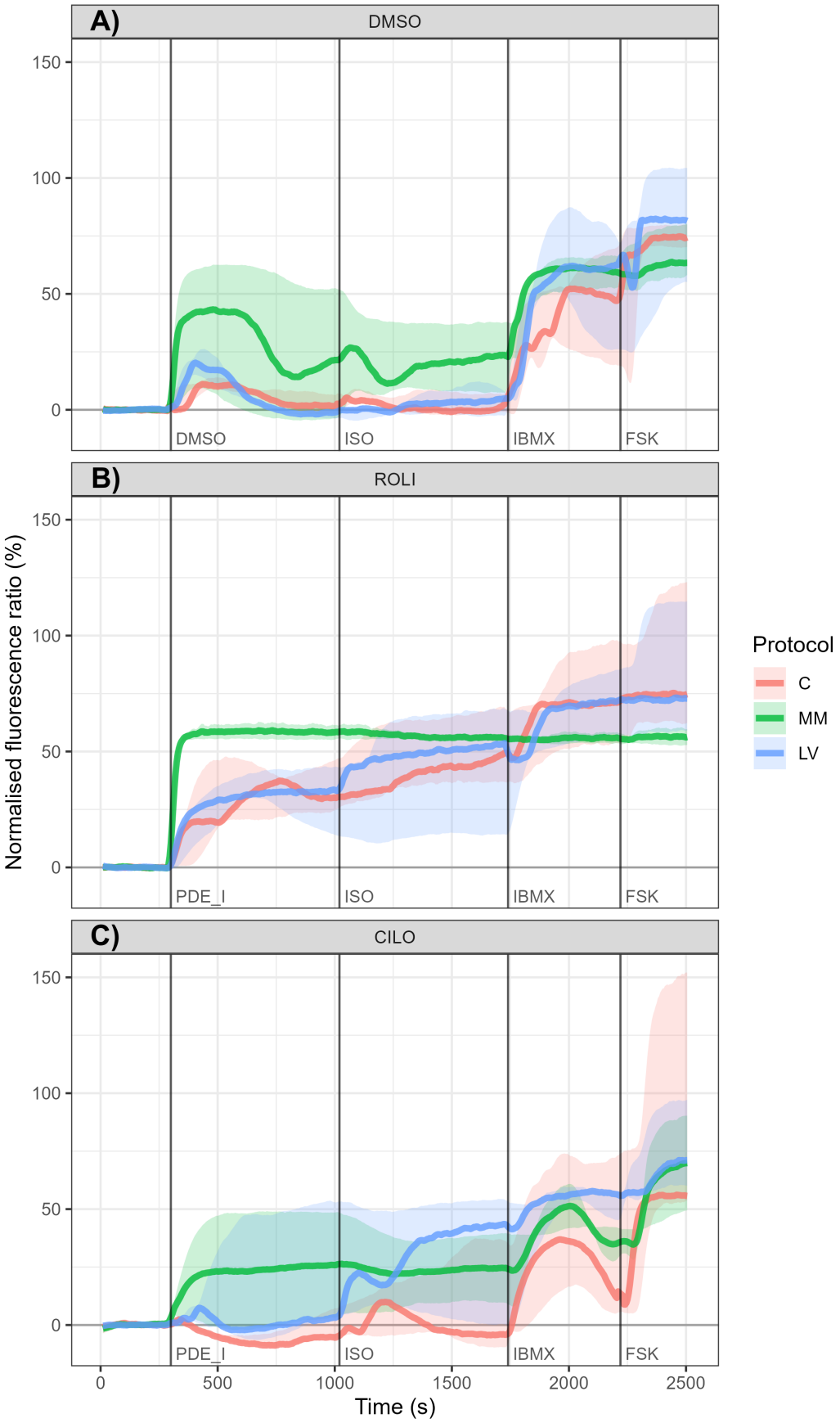

Figure 4.4: PDE4 remains the main regulator of β-AR stimulation in hiPSC-CM. *(Legend on next page.)*

Figure 4.4: PDE4 remains the main regulator of β-AR stimulation in hiPSC-CM. *Curves are rolling median (5-points average, centred) of cAMP sensor normalised fluorescence ratio, and coloured areas are corresponding 95% confidence interval. The curves are normalised to baseline ([Fluorescence/Baseline fluorescence]×100-100). Vertical dark lines indicate timings of each treatment successive addition to the bath.* ***A)*** *The first treatment is a DMSO control at volume matched to PDE inhibitors.* ***B)*** *The first treatment is the PDE4 inhibitor rolipram (ROLI) at 10 µM.* ***C)*** *The first treatment is the PDE3 inhibitor cilostamide (CILO) at 10 µM. DMSO/PDE_I = DMSO or selective PDE inhibitor, as indicated above each plot. isoproterenol (ISO) at 1 nM, 3-isobutyl-1-methylxanthine (IBMX) at 0.1 mM, forskolin (FSK) at 10 µM. C = control protocol, MM = metabolic maturation protocol, LV = left ventricle-like differentiation protocol. n=30 for DMSO, n=28 for rolipram (ROLI), n=29 for cilostamide (CILO), from 2-3 differentiations in C; n=28 for DMSO, n=18 for ROLI, n=20 for CILO, from 2-3 differentiations in MM; n=28 for DMSO, n=30 for ROLI, n=29 for CILO, from 2-3 differentiations in LV. See individual fluorescence channels in supplementary figure A.6.*

cytoplasmic cAMP in all C hiPSC-CM and some MM (cells from replicate 1, 50% of the cells with a negative R_{max}) and LV cells (cells from replicates 2 and 3, 67% of the cells with a negative R_{max}) (Figure 4.6). This counter-intuitive result could be explained by the increased activation of other, more prominent PDE isoforms in response to a local increase in cAMP. But interestingly, the cells that responded to CILO with an increase in cAMP, were nearly already saturated by this treatment. Of note however, it is difficult to distinguish this response of MM hiPSC-CM to CILO and the response of these cells to DMSO alone, as it induced a similar and sustained increase in one biological replicate (1/3).

Taken together, these results indicated that PDE4 was the main isoform responsible for cytoplasmic cAMP regulation at baseline in hiPSC-CM but to a lesser extent in C and LV, compared to MM. This was expected in immature human cardiomyocytes, where this isoform remains the principal regulator of cAMP, before PDE3 becomes the main isoform in adult human cardiomyocytes [121]. Interestingly, a subset of hiPSC-CM from both maturation protocols exhibited an increased reliance on PDE3, indicating a maturation of the β-adrenergic-cAMP-PKA pathway in progress.

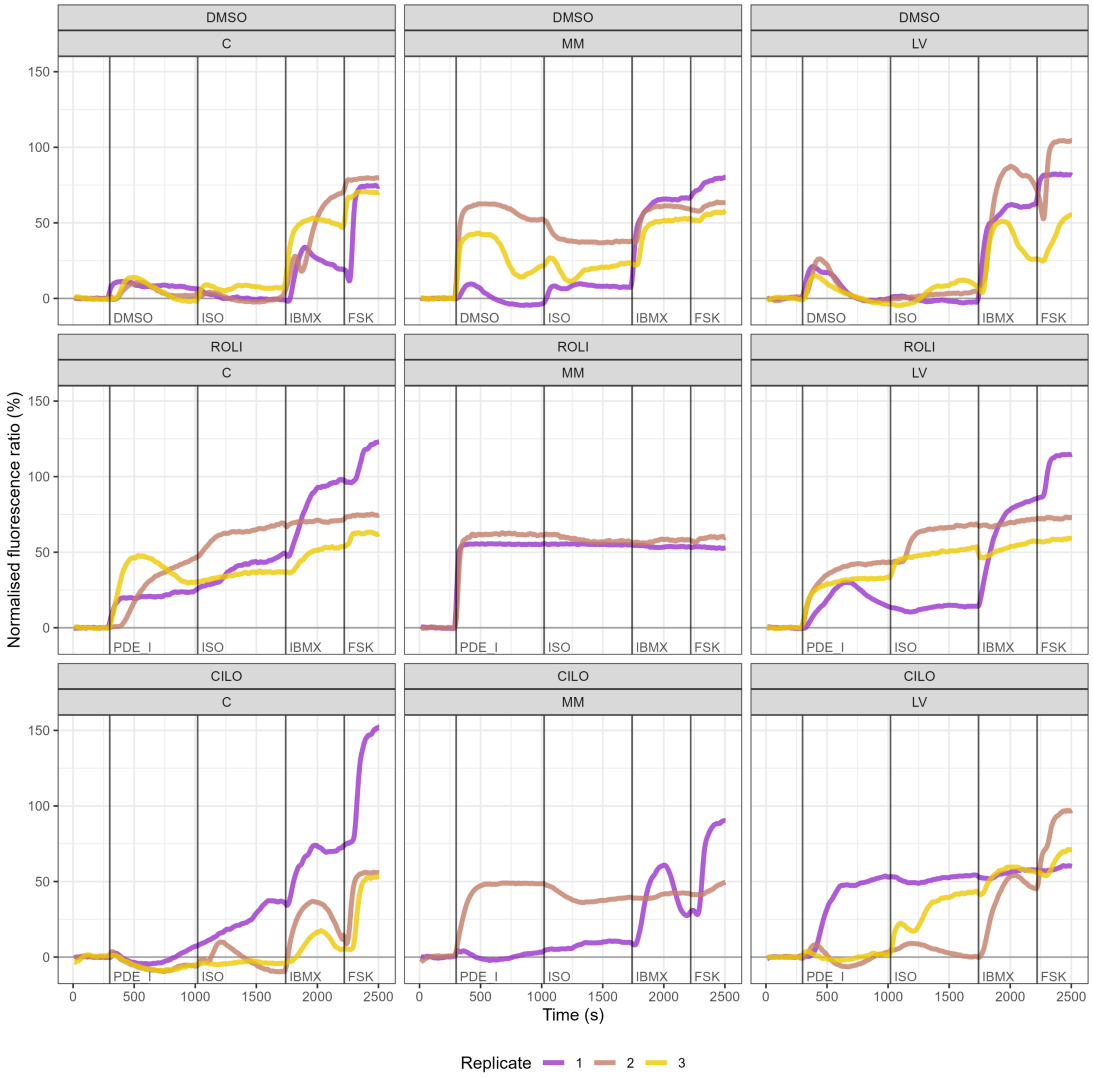

Figure 4.5: Traces of individual biological replicates show the diversity of responses to the successive treatments. *Curves are rolling median (5-points average, centred) of cAMP sensor fluorescence ratio, averaged by biological replicate for each experimental condition. The curves are normalised to baseline ([Fluorescence/Baseline fluorescence]×100-100). Vertical dark lines indicate timings of each treatment successive addition to the bath. The first row shows responses to treatments in presence of the DMSO control ; The second row shows responses to treatments in presence of the PDE4 inhibitor ROLI ; The third row shows responses to treatments in presence of the PDE3 inhibitor CILO. The first column shows responses of C hiPSC-CM ; The second column shows responses of MM hiPSC-CM ; The third column shows responses of LV hiPSC-CM. DMSO/PDE_I = DMSO or selective PDE inhibitor, as indicated above each plot. C = control protocol, MM = metabolic maturation protocol, LV = left ventricle-like differentiation protocol.*

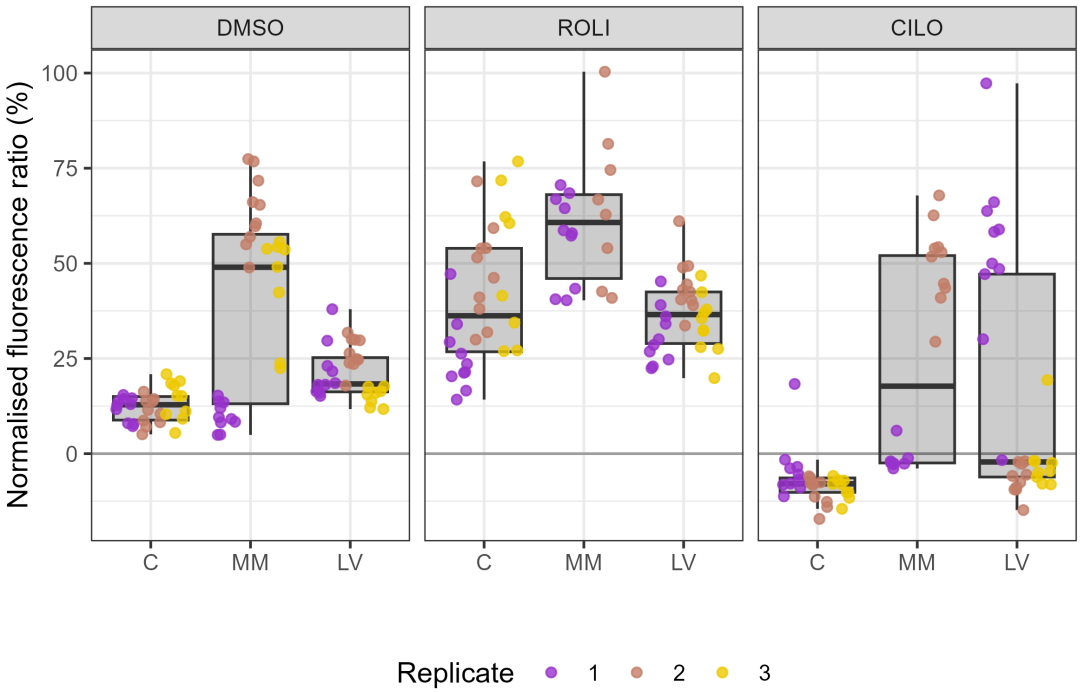

Figure 4.6: An increased reliance on PDE3 is seen in some MM and LV hiPSC-CM in basal conditions. *R_{max} in response to PDE inhibitor or DMSO, as indicated above each plot. Colors indicate the biological replicate (differentiation batch) of origin for individual cells.*

4.2.1.2 β-adrenergic stimulation

The response to β-adrenergic stimulation and its potentiation by selective PDE inhibition was then tested by the addition of 1 nM isoproterenol (ISO). The figure 4.5 showed that, following the DMSO control, a small sustained cytoplasmic response to ISO was observed only in one out of three replicates (replicate 3 for C and LV, replicate 1 for MM). However, The MM replicates unresponsive to ISO showed strong DMSO responses, which might have masked any small ISO response. The observed lack of response to β-adrenergic stimulation was attributable to either insufficient cAMP synthesis (because of reduced β-AR expression, activity, coupling, reduced AC expression or activity, etc.), or enhanced PDE-mediated degradation of cAMP, counteracting its accumulation at the cytoplasmic level. Specific inhibition of PDEs provided insight on this matter.

In the case of PDE4 inhibition by ROLI, β-adrenergic stimulation induced a further increase in cAMP production in both C and LV hiPSC-CM but not

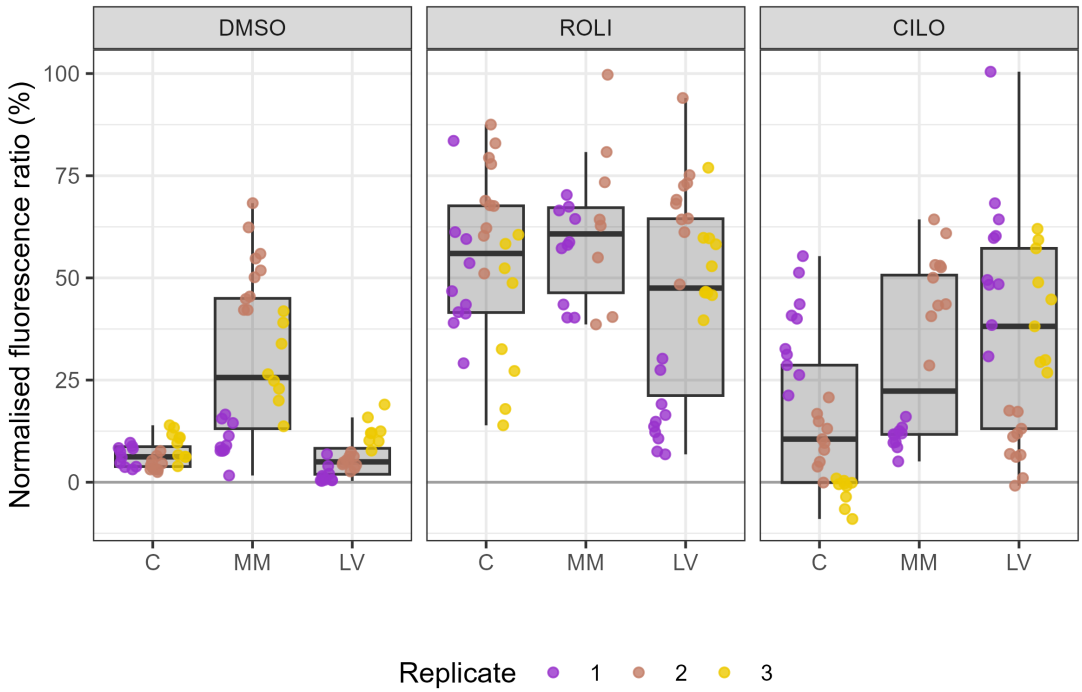

Figure 4.7: The response to low ISO dose is mainly restricted by PDE4, with an increased importance of PDE3 in matured hiPSC-CM. *R_{max} in response to ISO with or without selective PDE inhibitor, as indicated above each plot. Colors indicate the biological replicate (differentiation batch) of origin for individual cells.*

MM, compared to PDE4 inhibition alone. This increase indicated that these cells were sensitive to ISO stimulation and were able to increase cAMP production in response. As the PDE4 inhibitor ROLI allowed this ISO-induced increase to become visible at the cytoplasmic level (which was not the case in control conditions), it indicated that PDE4 was, at least in part, responsible for the adaptive degradation of cAMP generated by β-ARs stimulation, preventing its rise in control conditions (DMSO+ISO). As indicated before, PDE4 inhibition alone was enough to saturate MM cells, completely masking any ISO-induced rise in cAMP. But interestingly, a subset of LV hiPSC-CM demonstrated a degradation of cAMP despite PDE4 inhibition (cells from replicate 1, <25% R_{max}), that was barely counter-balanced by the increased production of cAMP in response to ISO (Figure 4.7).

Similarly, PDE3 inhibition potentiated hiPSC-CM response to β-adrenergic stimulation. This effect was minor and mainly transitory in most C hiPSC-

CM (except in cells from replicate 1, >25% R_{max}) but more significant on MM (cells from replicate 2, >25% R_{max}) and especially LV cells (cells from replicates 1 and 3, >25% R_{max}). Some LV cells did follow the same transitory pattern observed in C (cells from replicate 2) but most of them displayed a strong increase in cytosolic cAMP, almost as high as what was observed under PDE4 inhibition. This indicated that PDE3 was of almost equivalent importance in ISO-induced cAMP homeostasis in LV hiPSC-CM, which was consistent with a switch in the relative role of PDE isoforms towards mature regulation of the β-adrenergic stimulation. On the other hand, the results in MM hiPSC-CM were more difficult to interpret as the response pattern was highly similar to what was seen with DMSO alone. But it was undeniable that PDE3 was of less importance compared to PDE4, in regulating the response to β-adrenergic stimulation.

These results indicated a strong inhibition of the β-adrenergic response to ISO stimulation in hiPSC-CM. This inhibition was primarily due to the PDE4 isoform, but a vast proportion of LV cells (2/3) seemed to rely on PDE3, to the same extent. This was again consistent with a maturation of the β-adrenergic pathway.

4.2.1.3 Non-selective PDE inhibition

To investigate the role of other PDE isoforms in regulating cAMP, 100 µM of the non-selective PDE inhibitor 3-isobutyl-1-methylxanthine (IBMX) was then added to the bath. The results are also presented in the figure 4.4. Unsurprisingly this induced a strong rise in cytoplasmic cAMP, of an even larger amplitude in LV hiPSC-CM in DMSO control. Interestingly, this rise appeared to be transitory in some C (replicates 1 and 3) and LV (replicates 2 and 3), but not MM hiPSC-CM.

Following combined PDE4 and non-selective inhibition, a further increase in cAMP was also observed in a similar way in C and LV hiPSC-CM, although replicates 2 were almost already saturated with the combined PDE4 inhibition and ISO stimulation for both protocols (Figures 4.5). As

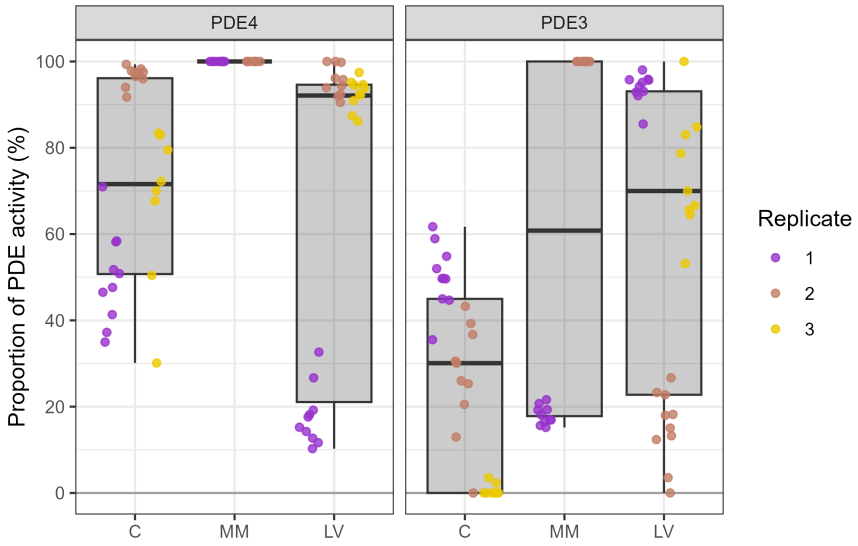

Figure 4.8: An increased reliance on PDE3 over PDE4 for cAMP regulation in the context of β-adrenergic stimulation is observed in hiPSC-CM from maturation protocols. *The proportion of PDE4 or PDE3 activity in response to ISO, is calculated as* Max_{ISO}/Max_{IBMX}, *where* Max_{ISO} *is the* R_{max} *following ISO treatment, and* Max_{IBMX} *is the same following IBMX, after PDE4 or PDE3 inhibition respectively.*

mentionned before, all MM cells were already saturated. PDE4 accounted for 71.58±45.39% of the measurable cAMP hydrolytic activity following β-adrenergic stimulation in C hiPSC-CM, 100% in MM and 92.11±73.54% in LV (Figure 4.8). Noteworthy, two distinct subpopulations were identified in the LV group: one group of cells from the replicates 2 and 3, 67% of cells with PDE4 accounting for around 90% of total measurable PDE hydrolytic activity and the other group around 20% of the total measurable activity.

In the case of PDE3 inhibition, the increase in cytoplasmic cAMP following IBMX treatment was lower in the LV group, where a great proportion of cells were already saturated (cells from replicate 1) or nearly saturated (cells from replicate 3) by the combination of CILO and ISO. However, the total amplitude of the response was higher in the LV group, compared to C, where the variability was substantial. The proportion of PDE3 activity in regard to the total measurable PDE activity, in response to β-adrenergic stimulation, was much lower in C hiPSC-CM, compared to both maturation protocols: 30.08±45.23% in C, 63.74±93.83% in MM, and 69.98±70.32%

in LV. Again, two subpopulations could be observed in the LV group, one around 10-20% (cells from replicate 2) and the other around 80-90% (cells from the replicates 1 and 3). This was also seen in MM hiPSC-CM, one population of cells being grouped at 100% (replicate 2), and the other at 20% (replicate 1).

Overall, these results indicated a predominance of PDE4 over PDE3 in the regulation of the β-adrenergic signalling pathway. PDE4 accounted for >70% and PDE3 <30% of the measurable cAMP hydrolytic activity, in response to ISO. However, a proportion of cells exhibited a switch in this dynamic. This switch was gradual and not as advanced in C hiPSC-CM but more pronounced in both MM and LV groups. Replicate 1 of the LV group being the perfect example of matured hiPSC-CM, with an inverted reliance, where PDE4:PDE3 is ~15%:95%. The internal variability of the maturation protocols was mostly due to the differentiation batches, indicating that events related to the differentiation process can prevent proper maturation of the hiPSC-CM.

4.2.1.4 Adenylyl cyclase direct activation

Lastly, the adenylyl cyclase (AC) activator forskolin (FSK) was added to the cells (10 µM). To investigate the intrinsic activity of β-ARs in response to ISO, the R_{max} after β stimulation and in the absence of PDE control (just *before* FSK addition to the bath) was compared to the R_{max} after total AC activation (maximum measurable cAMP production, just *after* FSK addition). The results displayed in the figure 4.9, highlighted that β-ARs in C hiPSC-CM were significantly less active in response to ISO, compared to the cells from maturation protocols (75.17±38.48% in C ; 92.54±15.73%, *P*=3.69e-10 in MM ; 87.09±19.37%, *P*=4.57e-06 in LV).

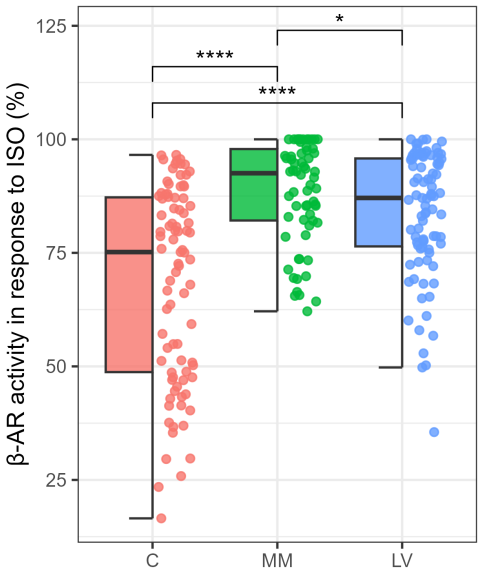

Figure 4.9: Maturation protocols induce an enhanced β-AR activity in response to ISO. *The percentage of β-AR activity in response to 1 nM ISO (in absence of PDE control) is calculated as* Max_{IBMX}/Max_{FSK}, *where* Max_{IBMX} *is the maximum CFP/YFP ratio change following IBMX treatment, and* Max_{FSK} *is the same following FSK.*

4.2.2 Targeted sensors

4.2.2.1 CUTie sensors

The previous results indicate a significant maturation of the β-adrenergic-cAMP-PKA pathway in hiPSC-CM from the MM and LV protocols. However, to ensure specificity of the β-adrenergic signal, cAMP is mainly confined in specific pools around PKA and its targets. The use of targeted FRET-based cAMP sensors allows the investigation of these nanoscale pools of cAMP and the proteins involved in the associated signalosomes. A variety of targeted sensors have been developed to this aim and among them, the targeted CUTie sensors have been tested in hiPSC-CM for this project [96]. Among them, only two were properly expressed and localised in hiPSC-CM: AKAP79-CUTie, targeted at AKAP79 which anchors LTCC, PKA and PDE4 together ; and AKAP18δ-CUTie, targeted at AKAP18δ which anchors SERCA, PKA and PDE3 [122] (Figure 4.10).

The expression of the cAMP sensors was good, the localisation could

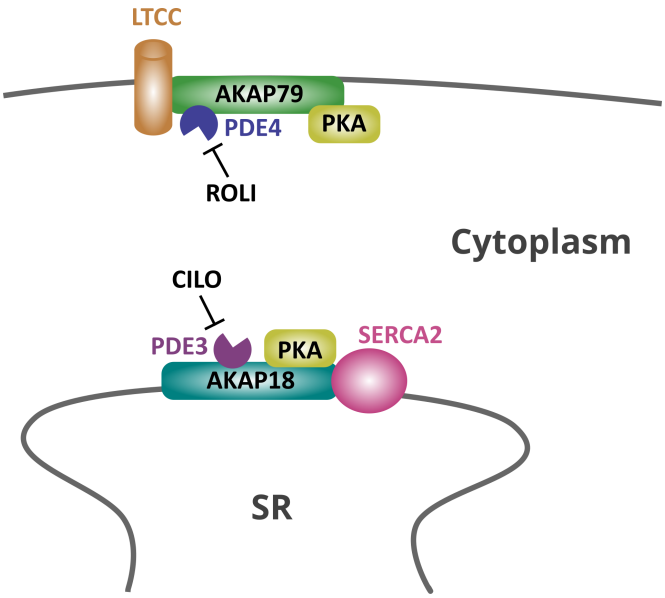

Figure 4.10: AKAP79- and AKAP18-associated signalosomes in human cardiomyocytes.

be confirmed for each sensor (cell membrane for AKAP79-CUTie and SR membrane for AKAP18-CUTie, see figure 4.11). During the test experiments with a quick analysis, a decent R_{max} was observed at maximum stimulation, which indicated the correct function of the sensors. However, following a more thorough analysis, it has become obvious that the poor signal to noise ratio was making the measurements difficult and not reliable. This noise induces a random variability of the fluorescence intensity of individual pixels, which masks the ”real” signal as its amplitude is close to the measured ”real” signal amplitude. To minimise the noise impact, a single region of interest (ROI) over the whole field of view was used, instead of much smaller ROIs over individual cells. This slightly ameliorated the signal to noise ratio but also reduced the number of different measurements that could be done for each experiment.

Additionally, a recurring drift in the signal could be identified in recording from both targeted CUTie sensors. This drift is a non-cAMP dependent constant increase (or decrease) of the measured fluorescence. As showed in the Figure 4.12, the R_{max} displayed a constant increase following the CILO, ISO and IBMX treatments but this drift is also seen in the individual fluorescence channels, both going in the same direction and at the same

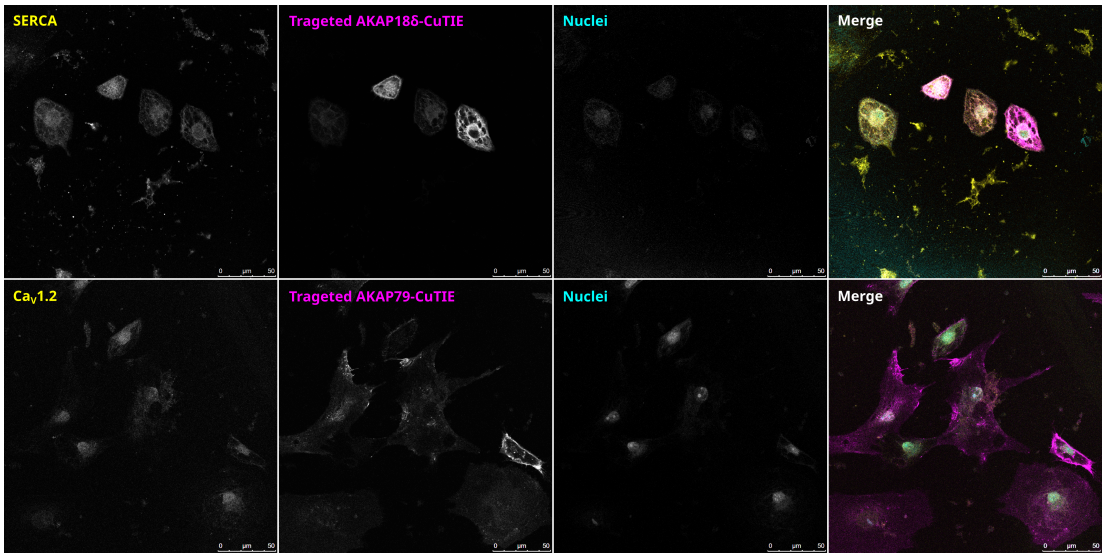

Figure 4.11: Immunofluorescence confirms AKAP79- and AKAP18-CUTie sensors correct targeting in hiPSC-CM. ***Top line**: Fluorescent images of AKAP18-CUTie and its signalosome partner in adult CM, SERCA. Co-localisation of both protein and sensor indicates proper sensor targeting.* ***Bottom line**: Fluorescent images of AKAP79-CUTie and its signalosome partner in adult CM, $Ca_V1.2$. No co-localisation, but $Ca_V1.2$ does not appear at the cell membrane, while AKAP79-CUTie does, which indicates proper sensor targeting.*

rate, compared to the baseline. A cAMP-dependent response would induce a change in fluorescence intensity in opposite directions depending on the channel.

Moreover, as seen following the FSK treatment, CUTie sensors displayed prolonged kinetics as compared as what was measured in the cytoplasm with the EPAC-S^{H187} sensor. This resulted in the end of the recording before the fluorescence change could reach a plateau, indicative of the maximum measurable cAMP production.

For all these reasons, no reliable measurement of cAMP variations at targeted sites could be performed, and it was decided to stop further analyses.

4.2.2.2 FluoSTEP sensors

To study cAMP levels in a specific nanodomain, the FRET-based biosensor is typically fused to a protein that localizes to that domain. The biosensor is then delivered to CMs, which express the construct in large quantity. This is

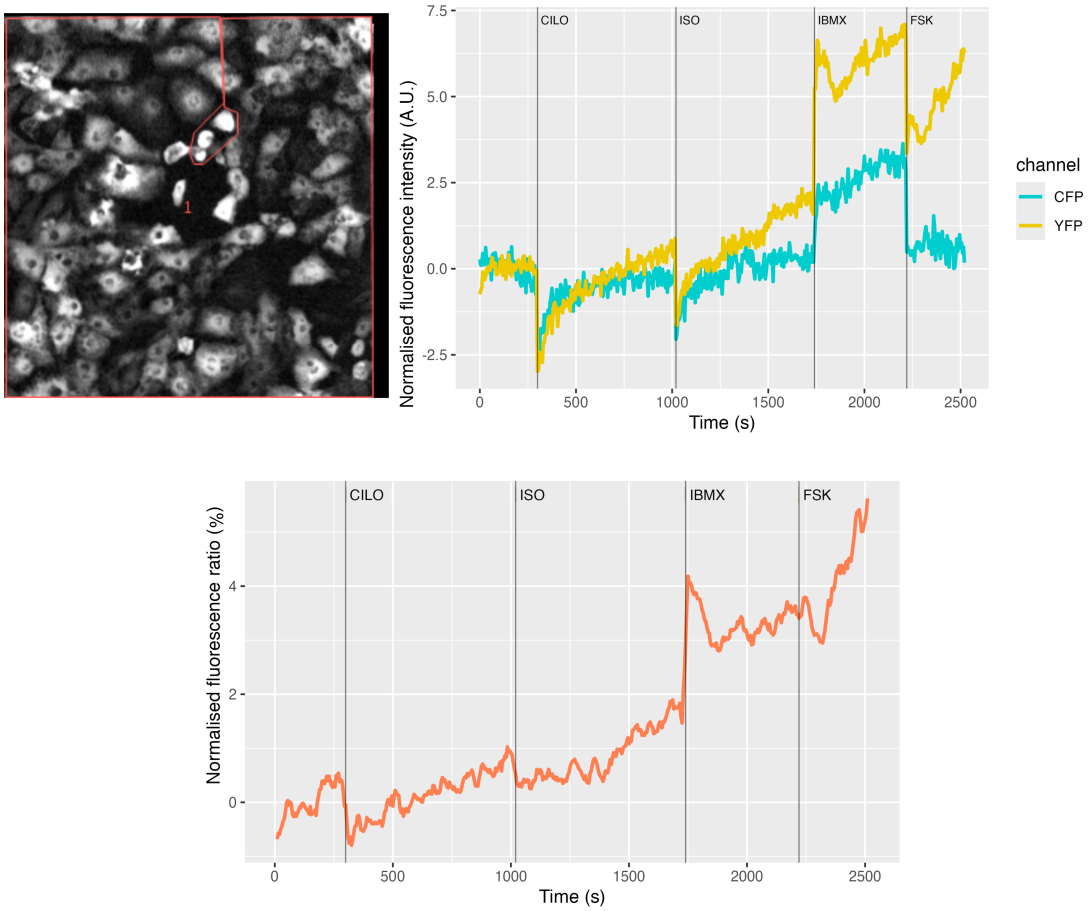

Figure 4.12: Targeted CUTie signal analysis faces important obstacles. ***Top left****: example of ROI covering the entire field of view, except saturated areas.* ***Top right****: representative traces of CUTie cAMP sensor individual channels normalised fluorescence from the example ROI.* ***Bottom****: rolling median (5-points average, centred) of cAMP sensor normalised fluorescence ratio from the example ROI. Vertical dark lines indicate timings of each treatment addition to the bath.*

typically the case with the targeted CUTie sensors presented in the previous section. However, because of the high level of expression, the sensor can also end up in locations other than the intended nanodomain, thereby confounding the analysis. To overcome this problem, a new FRET-based cAMP biosensor was developed, taking advantage of a split GFP system: FluoSTEP [24]. In FluoSTEP, the donor GFP is missing a small fragment that is tagged to the targeting protein of interest using CRISPR-Cas9 genome editing. Neither part of the split GFP fluoresces by itself, so only when FluoSTEP is introduced in the edited cells, the two parts assemble at the target protein to form a complete GFP donor, resulting in a functional sensor (Figure 4.1). This technique enables live cell imaging of cAMP nanodomains with high resolution at endogenous expression levels of the target protein. To understand the role of the gap junction-associated cAMP nanodomain in hiPSC-CM, endogenous levels of protein expression must be maintained to avoid interference with the hiPSC-CM maturation process. This technique was therefore used in hiPSC-CMs to study how the maturation of these cells is affected by a newly identified cAMP nanodomain found at gap junctions, which regulates communication between adjacent CMs [82].

To do so, the missing GFP fragment (the 11^{th} β strand of the GFP super folder, GFP11) was added to the C-terminus of the Cx43 protein using CRISPR-Cas9 on the same PGP1 hiPSC cell line used throughout this thesis. The successfully edited clones are noted Cx43-GFP$11^{+/+}$. Once differentiated into CMs, the Cx43-GFP$11^{+/+}$ cells were transduced with the FluoSTEP ICUE sensor, which GFP complementary fragment (GFP1-10) could associate with GFP11 at Cx43.

The FRET imaging was performed similarly as presented in the previous sections, with the exception of the PDE selective inhibition, which was not done, and the concentration of ISO was increased to 1 μM. The localisation of the sensor was confirmed as cell membranes were brighter, and especially cell-cell junctions where clusters of sensor were visible, which corresponded to the Cx43 localisation pattern 4.13.

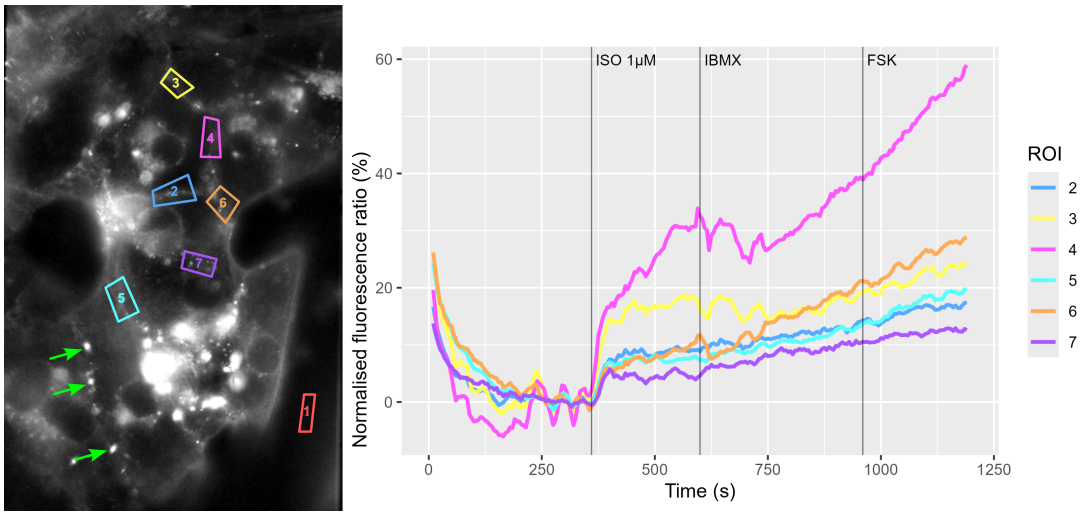

Figure 4.13: FluoSTEP sensors can be used to target endogenous proteins. ***Left**: example of ROIs drawn over cell junctions. The cells are Cx43-GFP11$^{+/+}$ hiPSC-CMs transduced with FluoSTEP ICUE sensor. Green arrows indicate bright clusters of the sensor, at a cell-cell junction. **Right**: Curves are FluoSTEP cAMP sensor normalised fluorescence ratio from individual ROIs showed on the left. The curves are normalised to baseline ([Fluorescence/Baseline fluorescence]×100-100). Vertical dark lines indicate timings of each treatment addition to the bath.*

A R_{max} of 8-20% was observed at cell-cell junctions following the ISO treatment, which indicated a nice and sustained response of the cells to β-adrenergic stimulation, visible around Cx43 gap-junctions. This also confirmed that the localisation did not affect the sensor function. Further treatments with IBMX and FSK showed a much slower but sustained increase in cAMP measurable concentration around Cx43.

The Cx43-GFP11$^{+/+}$ iPSC started to differentiate spontaneously in culture shortly after the first experiments, leading to undirected non-specific differentiations which prevented further directed differentiations into CMs. This challenge could not be resolved within the timeframe of my PhD, preventing the repetition and expansion of these experiments to investigate the Cx43 nanodomain. Nevertheless, these experiments serve as proof-of-principle studies, demonstrating a promising approach for future research aimed at targeting FRET-based cAMP sensors at endogenous protein expression levels.

4.3 Discussion and perspectives

This chapter focused on the evaluation of PDE3 and PDE4 hydrolytic activity and their relative importance in regulating the cAMP-PKA pathway in hiPSC-CMs subjected to different maturation protocols. The results indicated that PDE3 and PDE4 are both important isoforms in hiPSC-CM, as they are in primary CMs, but PDE4 is the main isoform responsible for cytoplasmic cAMP regulation in hiPSC-CM. This was expected in immature human CMs, where this isoform remains the principal regulator of cAMP, before PDE3 becomes the main isoform in adult human CMs [121].

Interestingly, a proportion around ~50% of hiPSC-CM from both maturation protocols exhibited an increased reliance on PDE3, indicating a maturation of the β-adrenergic-cAMP-PKA pathway in progress.

An increased β-AR activity in response to ISO stimulation in matured hiPSC-CM could also be observed. This is probably due to an increased expression of β-ARs and/or ACs, as seen in the western-blots from the previous chapter (Figure 3.15) an expected in more mature hiPSC-CM [45], [46].

A surprising observation is the transitory aspect of the response to IBMX in both DMSO and CILO conditions. This cAMP degradation despite a non-selective inhibition of PDEs is most probably due to PDE8, a PDE isoform that is insensitive to IBMX, and usually plays a minor role in cardiac cAMP regulation [16], [123]. However, this cAMP hydrolytic activity seems to disappear with the ROLI treatment, and PDE8 is also insensitive to ROLI. PDE4 has a IC_{50} of 26 µM for IBMX so, by using 100 µM, PDE4 activity should be completely blocked. But as most traces reach saturation already after the ISO treatment in the case of ROLI pre-treatment, this could mask the variations induced by PDE8. This potential involvement of PDE8 in regulating cAMP in hiPSC-CM would require further investigation as it is

not seen - to this extent - in adult CMs, nor in rodent neonatal CMs, and could indicate a specificity of early human cardiomyocytes.

These findings advance our knowledge on the mechanisms of formation and regulation of cAMP nanodomains in hiPSC-CMs. This will help gaining deeper insights into embryonic and fetal cardiac development. Moreover, it creates new leads for the identification of novel targets to enhance the maturation of hiPSC-CMs, ultimately improving their utility for disease modelling and regenerative medicine.

4.3.1 Limitations

While these results provide new insight in the regulation of the cAMP-PKA pathway in hiPSC-CM, there are limitations that need to be accounted for. Firstly, the control treatment DMSO induced a rise in cytoplasmic cAMP, particularly in MM hiPSC-CM. While this effect is minimal and transitory in most groups, it is strong and sustained in replicates 2 and 3 of MM hiPSC-CM. The concentration used was matched to the one from PDE selective inhibitors: 1µL of pure DMSO in 2.2mL of buffer (0.0045%). DMSO is a known solvent, widely used in comparable conditions as the ones presented in this chapter, and such effect on cAMP has never been described. This points to a possible chemical contamination of the DMSO used for control in MM hiPSC-CM, with one of the other drugs used to elevate cAMP concentration. This experiment should therefore be replicated with care, to ensure no contamination of the DMSO control would limit the interpretability of the data.

The second limitation lies with the high variability between differentiation batches seen throughout the experiments and is a known pitfall of the use of hiPSC-CM. This probably depends on the efficiency of the differentiation, which leads to the generation of more or less mature hiPSC-CM. Rather than increasing the number of cells for each measurement, future work should focus on including cells from more differentiation batches. But

understanding the technical origin of this important variability would be of utmost importance to increase the robustness and reproducibility of the data obtained with these cells. This problem has remained understudied for over a decade and guidelines published for neurology sciences in 2023 still point out important unknowns on the influence of various culture parameters on this variability [124]. But a recent paper suggests that more defined culture conditions of iPSCs could reduce the variability between batches [125], which is something to consider for future work involving iPSC-derived cells.

Finally, the technical obstacles faced during the experiments involving the targeted cAMP sensors limits the applicability of these findings. Indeed, in terms of cellular signalling, functionally relevant cAMP dynamics are not the global ones, but rather the localized events within specific nanodomains [13]. Developing targeted sensors from EPAC-S^{H187} would increase the signal to noise ratio, and therefore increase the robustness of the data. In this biologically highly variable model, reduce the technical variability is of higher importance, and should be considered for future work involving hiPSC-CM.

Chapter 5

Investigating maturation-induced physiological changes in hiPSC-derived CMs

5.1 Introduction

The immature phenotype of hiPSC-CM is manifested across multiple biological domains, including electrophysiology, calcium handling, metabolism, and contractile function. Morphologically, hiPSC-CM retain a fetal-like round or polygonal shape, lack well-organized sarcomeres, and exhibit no T-tubules that are hallmarks of adult vCM. Electrophysiologically, hiPSC-CM display unstable resting membrane potentials, leading to spontaneous depolarisations, and prolonged action potential durations, reflecting an underdeveloped ion channel organisation. Similarly, their calcium handling machinery is characterized by reduced SR calcium storage, impaired excitation-contraction coupling, and blunted responsiveness to β-adrenergic stimulation [72].

Given these limitations, considerable efforts have been directed towards designing maturation protocols to recapitulate the structural and functional properties of adult CMs. Strategies have encompassed long-term culture, mechanical and electrical stimulation, metabolic conditioning, three-dimensional tissue engineering, and co-culture with non-myocytes. As these approaches variably enhance specific aspects of CM maturation, a point of central importance remains the quantitative and functional assessment of their efficacy.

Physiological measurements — particularly those probing contractile performance, calcium handling dynamics, and electrophysiological properties — are therefore indispensable tools in benchmarking iPSC-CM maturation. High-resolution video microscopy easily provide metrics of contractile properties, while fluorescent optical methods readily quantify action potential kinetics and calcium transient features. Importantly, the responsiveness of hiPSC-CM to neurohormonal stimulation, particularly via the β-adrenergic signalling pathway, offers a critical functional readout of maturation status, and the relevance of hiPSC-CMs to model specific conditions.

In the adult heart, β-adrenergic stimulation via catecholamines such as ISO elicits well-characterized enhancements in contractility, relaxation kinetics, and calcium cycling through PKA-mediated phosphorylation of key targets including PLN, RyR2 and LTCC. However, in immature hiPSC-CM, the β-adrenergic pathway is often underdeveloped or dysregulated, exhibiting attenuated chronotropic, inotropic, and lusitropic responses [46], [126]. This deficiency may reflect incomplete expression of β-AR, impaired G-protein coupling or AC activity, or an imbalance in PDEs expression and localisation. Therefore, evaluating the amplitude and kinetics of β-adrenergic responses in hiPSC-CM serves both as an additional diagnostic measure of the β-adrenergic pathway maturation and as a functional endpoint to assess the efficacy of maturation protocols. Ultimately, integrating physiological measurements with omics-level and FRET-based characterisation holds promise not only for refining maturation strategies but also for elucidating the developmental assembly of β-adrenergic signalling networks in human CMs.

Using high-resolution fluorescent microscopy, this chapter explores the functional maturity of hiPSC-CMs and investigates the relative efficiency of the maturation protocols with regards to the actual physiology of the cells, but also assesses more directly the β-adrenergic development of hiPSC-CM cultured with the two protocols, MM and LV.

5.2 Results

Definition In this chapter, *basal conditions* refers to *no treatment conditions*.

5.2.1 Calcium handling

To investigate the extent of calcium handling maturity, the RGECO fluorescent calcium reporter was used to record calcium transients of hiPSC-CM aged 40-45 days, maintained at 37°C and paced at 1Hz. The image stacks were analysed using CalTrack [101]. To further explore the magnitude of the changes observed, data have been compared to simulated adult CM physiological measurements. These simulated measurements have been generated with the published model [127], by Alfonso Bueno-Orovio, University of Oxford.

5.2.1.1 Basal conditions

Under basal conditions, only subtle differences in calcium handling could be observed between the protocols tested (Figures 5.1, 5.2). hiPSC-CM generated with the LV protocol exhibited a shorter CTD40 than what was observed in C or MM. This shortening was due to a faster calcium reuptake, in the early part of the calcium decay. Indeed, the CTD90 was not significantly decreased. In the case of MM, a delayed time to peak was observed, with a shorter decay time, maintaining a similar CTD.

When compared to simulated adult CM calcium transients, the time to peak calcium was significantly prolonged in all hiPSC-CMs (~45ms in adult vCMs, ~200ms in hiPSC-CMs), resulting in a prolonged transient (~550ms in adult vCMs, ~770ms in hiPSC-CMs) despite similar decay times (~500ms in adult vCMs, ~550ms in hiPSC-CMs). This demonstrated efficient calcium reuptake/extrusion, as opposed to the calcium release/entry in hiPSC-CMs.

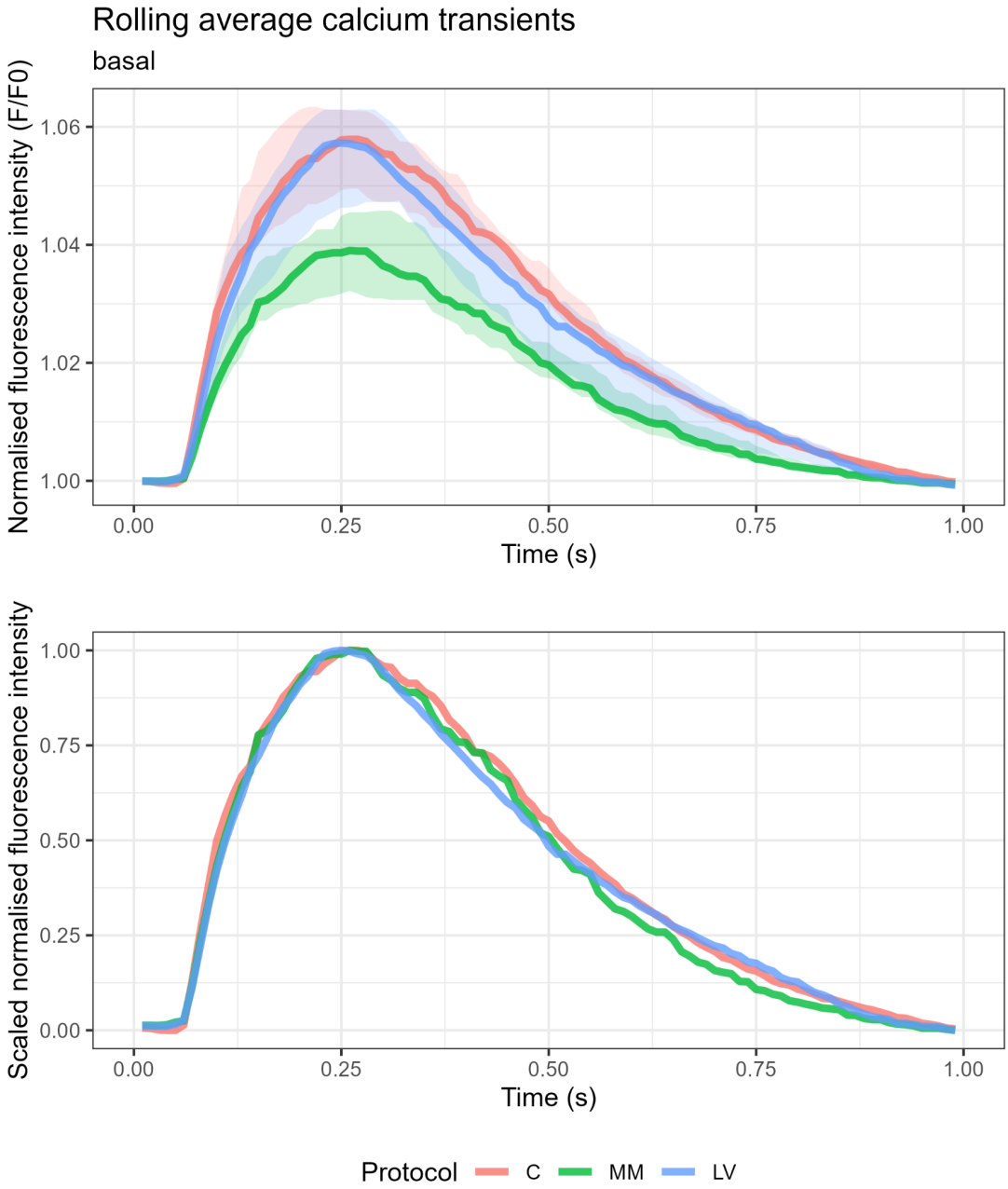

Figure 5.1: The maturation protocols tested do not induce a calcium handling maturation in basal conditions. *Calcium transients from hiPSC-CMs maintained at 37°C and paced at 1Hz. Curves are rolling median (3-points average, centred) of calcium transients and coloured ribbons are 95% confidence intervals.* ***Top****: The curves are normalised to baseline (Fluorescence/Baseline fluorescence).* ***Bottom****: The normalised curved are scaled between 0 and 1. n=80, from 4 differentiation batches in C ; n=66, from 4 differentiation batches in MM ; n=66, from 3 differentiation batches in LV.*

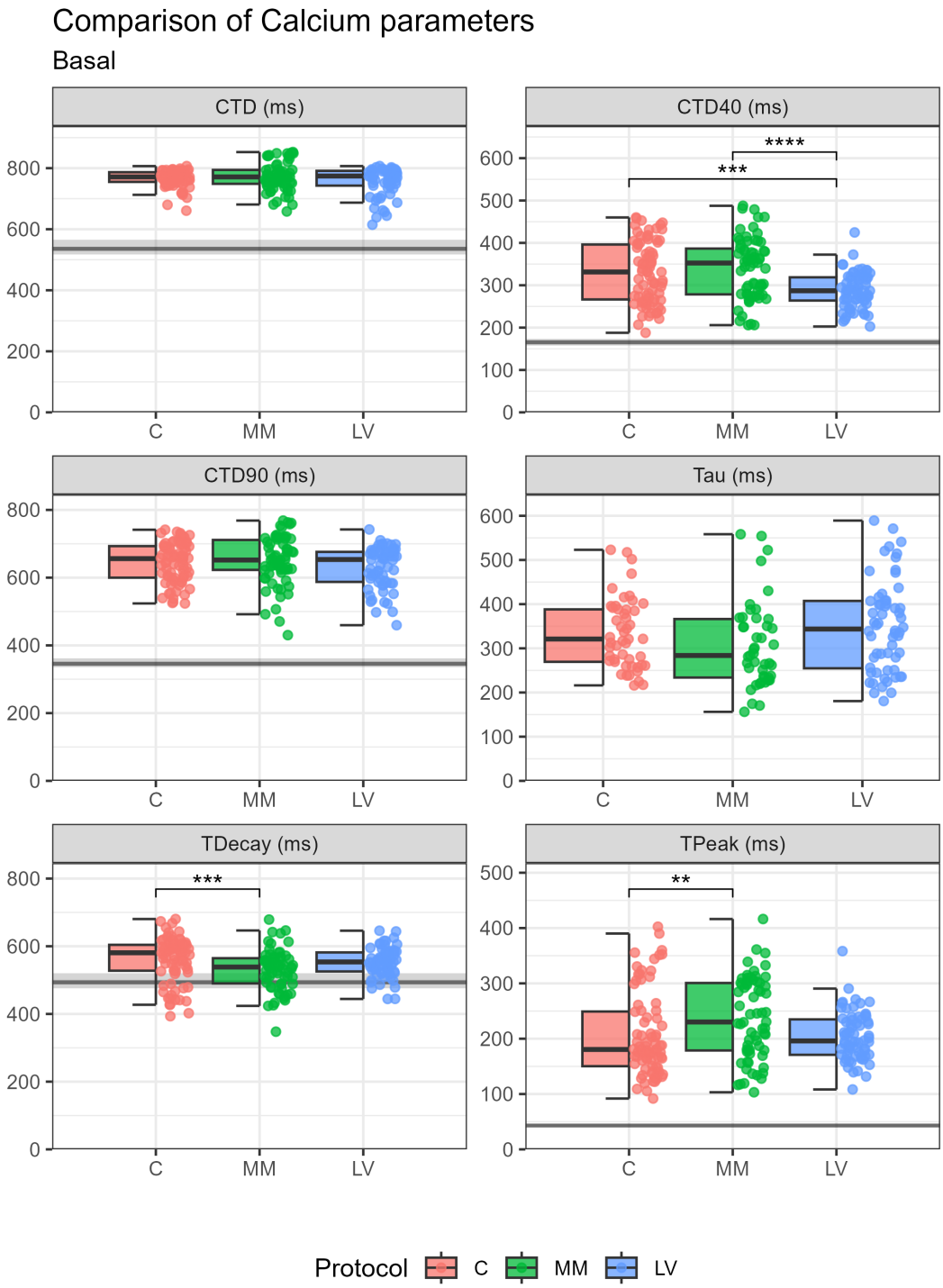

Figure 5.2: The LV protocol gives rise to more homogeneous hiPSC-CM populations in terms of calcium handling. *Dark grey lines and shaded areas are the median and interquartile range of corresponding measurement on simulated adult CM calcium transients (Sim). CTD = calcium transient duration, CTD40|CTD90 = calcium transient duration at 40|90% of peak, Tau = decay time constant (from fitted double exponential curve), TDecay = decay time, TPeak = time to peak. n=80, from 4 differentiation batches in C ; n=66, from 4 differentiation batches in MM ; n=66, from 3 differentiation batches in LV ; n=83 in Sim. See detailed statistics in supplementary table B.2.*

Of note however, the LV protocol produced more homogeneous hiPSC-CMs, exhibiting less variable calcium transient shapes, as evidenced by the reduced variability in CTD40 (IQR 129.7ms in C and 108.1ms in MM, compared to 54.87ms in LV, *P*=1.04e-06), time to peak (IQR 98.86ms in C and 122ms in MM, compared to 64.05ms in LV, *P*=4.5e-04) and decay time (IQR 76.50ms in C and 74.51ms in MM, compared to 56.26ms in LV, *P*=2.45e-02).

5.2.1.2 β-adrenergic stimulation

To explore the extent of β-adrenergic development, hiPSC-CMss were treated with increasing doses of the β_2-adrenergic receptor agonist iso-proterenol (ISO), before recording calcium transients. The control cells responded to ISO in a dose-dependent manner with a significant shortening of the time of decay, resulting in a faster calcium transient ; with the exception however of the highest dose (0.1μM), which didn't induce a further shortening of the time of decay compared to the previous dose, but on the contrary induced a prolonged time to peak (Figure 5.3). This showed that control hiPSC-CM had an efficient calcium reuptake/extrusion, that was adaptable to β-adrenergic stimulation whereas the calcium entry/release from the sarcoplasmic reticulum was not. Conversely, in LV hiPSC-CMs, a dose-dependant shortening of the transient at 40% and 90% of the peak was seen, in relation to faster time to peak. Similarly, the MM hiPSC-CM responded to the highest dose of ISO with a reduction of the calcium transient duration, mainly due to a faster time to peak. However, the high variability of the C and MM data (especially the CTD40 and TPeak measurements) demonstrated that this effect was not robust, contrary to what was seen in the LV cells.

Overall, these data suggested no significant maturation of the calcium handling induced by either protocol, but the LV protocol lead to more homogeneous hiPSC-CM populations, more mature calcium transient shape and more robust responses to β-adrenergic stimulation.

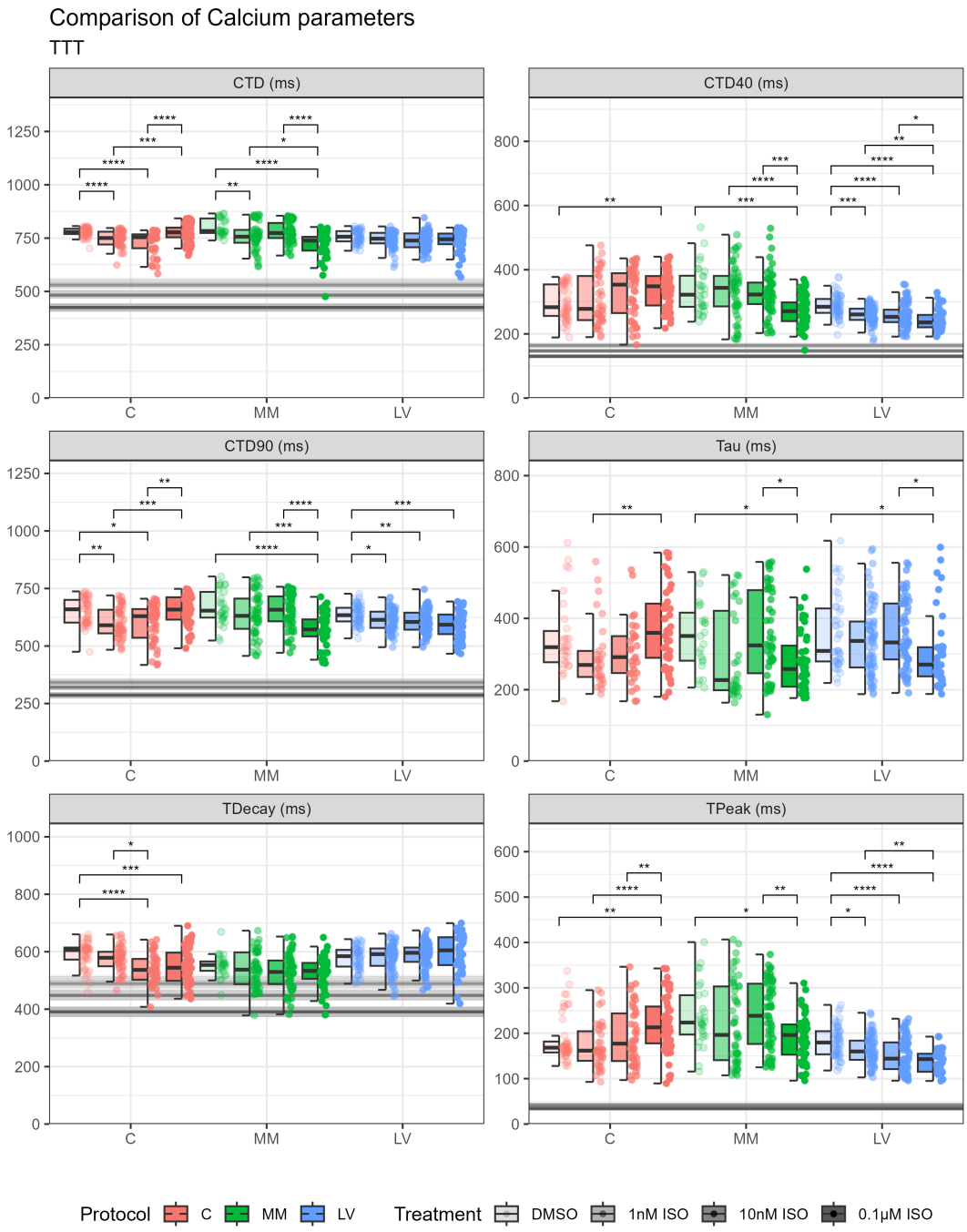

Figure 5.3: β-adrenergic stimulation induces a shortening of calcium transient decay time in control but a shortening of time to peak in "matured" hiPSC-CM. *Dark grey lines and shaded areas are the median and interquartile range of corresponding measurement on simulated adult CM calcium transients (Sim). CTD = calcium transient duration, CTD40|CTD90 = calcium transient duration at 40|90% of peak, Tau = decay time constant (from fitted double exponential curve), TDecay = decay time, TPeak = time to peak. n=51 for DMSO, n=42 for 1nM ISO, n=42 for 10nM ISO, n=68 for 0.1µM ISO, from 2-4 differentiation batches in C ; n=27 for DMSO, n=50 for 1nM ISO, n=50 for 10nM ISO, n=48 for 0.1µM ISO, from 2-3 differentiation batches in MM ; n=58 for DMSO, n=70 for 1nM ISO, n=69 for 10nM ISO, n=45 for 0.1µM ISO, from 2-3 differentiation batches in LV ; n=83 in Sim. See corresponding traces in supplementary figure A.7, and detailed statistics in supplementary table B.3.*

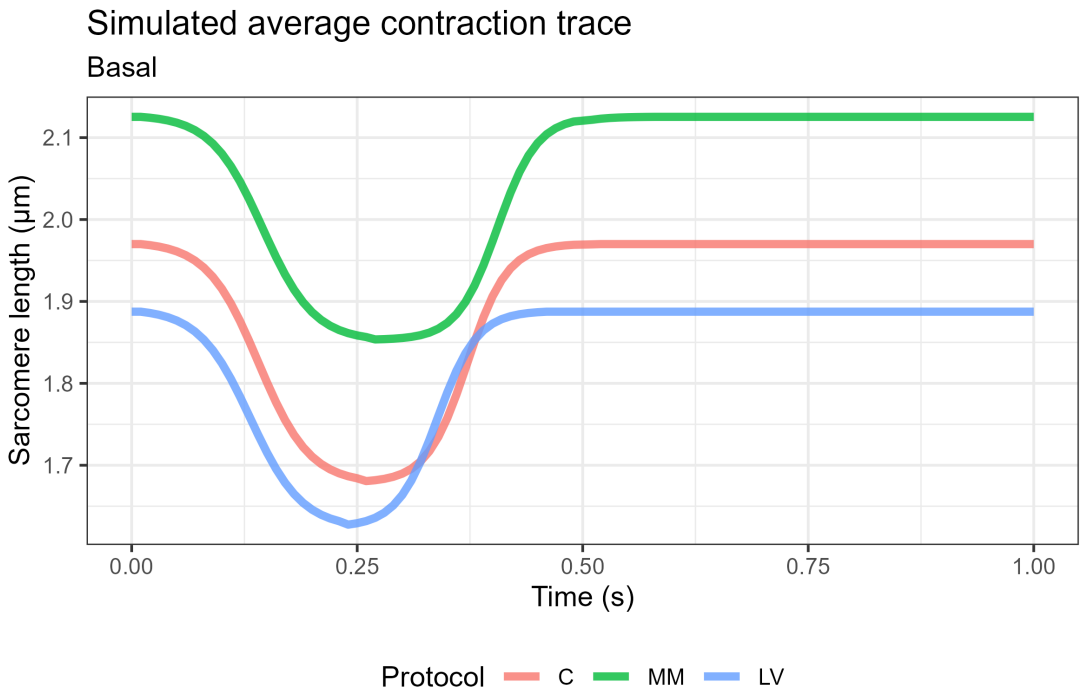

Figure 5.4: MM and LV maturation protocols have mixed effects on contractility. *Contraction curves from hiPSC-CMs maintained at 37°C and paced at 1Hz. Curves are simulated average contraction traces generated from median contraction parameters extracted with SarcTrack. n=89, from 4 differentiation batches in C ; n=77, from 4 differentiation batches in MM ; n=101, from 4 differentiation batches in LV.*

5.2.2 Contractility

To investigate the impact of maturation on hiPSC-CM contractility — which is closely linked to calcium handling — a GFP-tagged α-actinin protein was overexpressed in hiPSC-CMs and fluorescent sarcomeres were recorded simultaneously with calcium. hiPSC-CMs were aged 40-45 days, maintained at 37°C and paced at 1Hz. Image stacks were analysed using SarcTrack [102].

5.2.2.1 Basal conditions

Under basal conditions, the MM protocol induced a lengthening of the sarcomere length to physiological adult length (2-2.2µm). But it also impaired the contractile function, reducing the fractional shortening and increasing the relaxation time (Figures 5.4, 5.5). Conversely, the LV

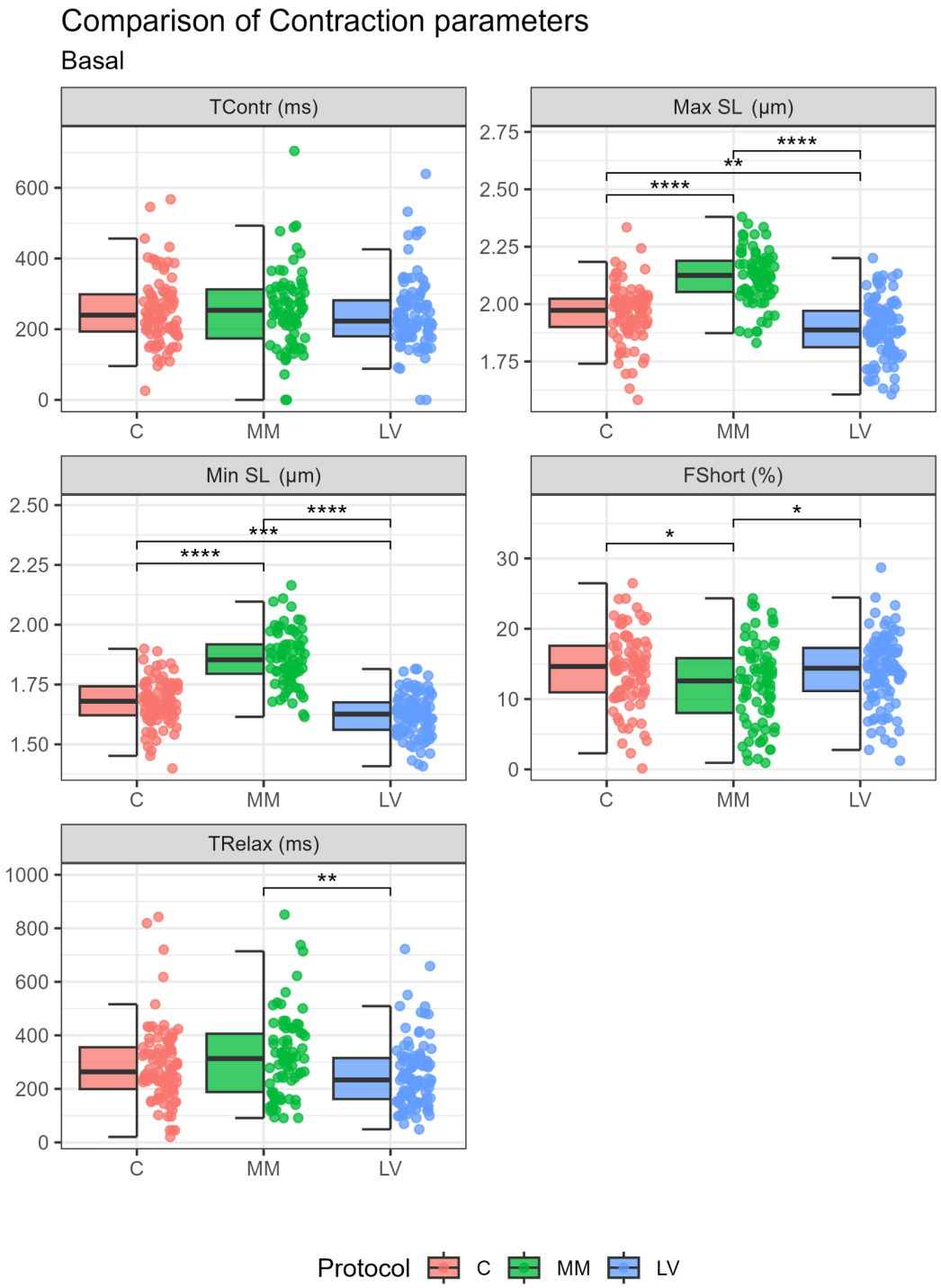

Figure 5.5: Maturation protocols mainly impact sarcomere length. *Max SL = maximal sarcomere length, Min SL = minimal sarcomere length, FShort = fractional shortening, TContr = time to contraction peak, TRelax = relaxation time. n=89, from 4 differentiation batches in C ; n=77, from 4 differentiation batches in MM ; n=101, from 4 differentiation batches in LV. See detailed statistics in supplementary table B.4.*

protocol induced a shortening of the sarcomere length along with a slight reduction of relaxation times.

These two maturation protocols induced opposite effects on hiPSC-CM contractility. Sarcomere length was at the expected adult size in MM hiPSC-CMs, but this protocol also impaired contractility, by inducing a reduction in fractional shortening and increasing relaxation time. The opposite was found in LV hiPSC-CMs. In both cases, the overall contraction-relaxation times were directly following the tendencies of calcium transient duration at 90% off peak.

5.2.2.2 β-adrenergic stimulation

To explore further the functional adaptability of hiPSC-CMs to β-adrenergic stimulation, they were treated with increasing doses of the β-AR agonist isoproterenol (ISO) and their fluorescent sarcomeres were tracked over time. Overall, ISO had no effect on control cells contractility and only minor effects on cells from other protocols (Figure 5.6). Low ISO treatment induced a shortening of time to contraction peak in MM cells, with no further increase at higher doses. It also induced a similar decrease in relaxation time. The LV protocol only induced a reduction in relaxation time following low β-adrenergic stimulation, with no further increase at higher doses.

In all cases, β-adrenergic stimulation dramatically increased data variability, which indicated that this response was far from robust.

Overall, these data suggested an incomplete and subtle maturation of hiPSC-CM contractility with the protocols tested. The LV protocol gave more promising results in basal conditions, compared to MM. However, while β-adrenergic stimulation did have a coherent effect in both MM and LV hiPSC-CM, the response was neither dose-dependent nor robust, as the treatment led to increased variability in the data. This contrasts with the results observed for calcium handling in LV hiPSC-CM, suggesting that β-adrenergic maturation at the level of the sarcomere is less developed compared to calcium handling mechanisms.

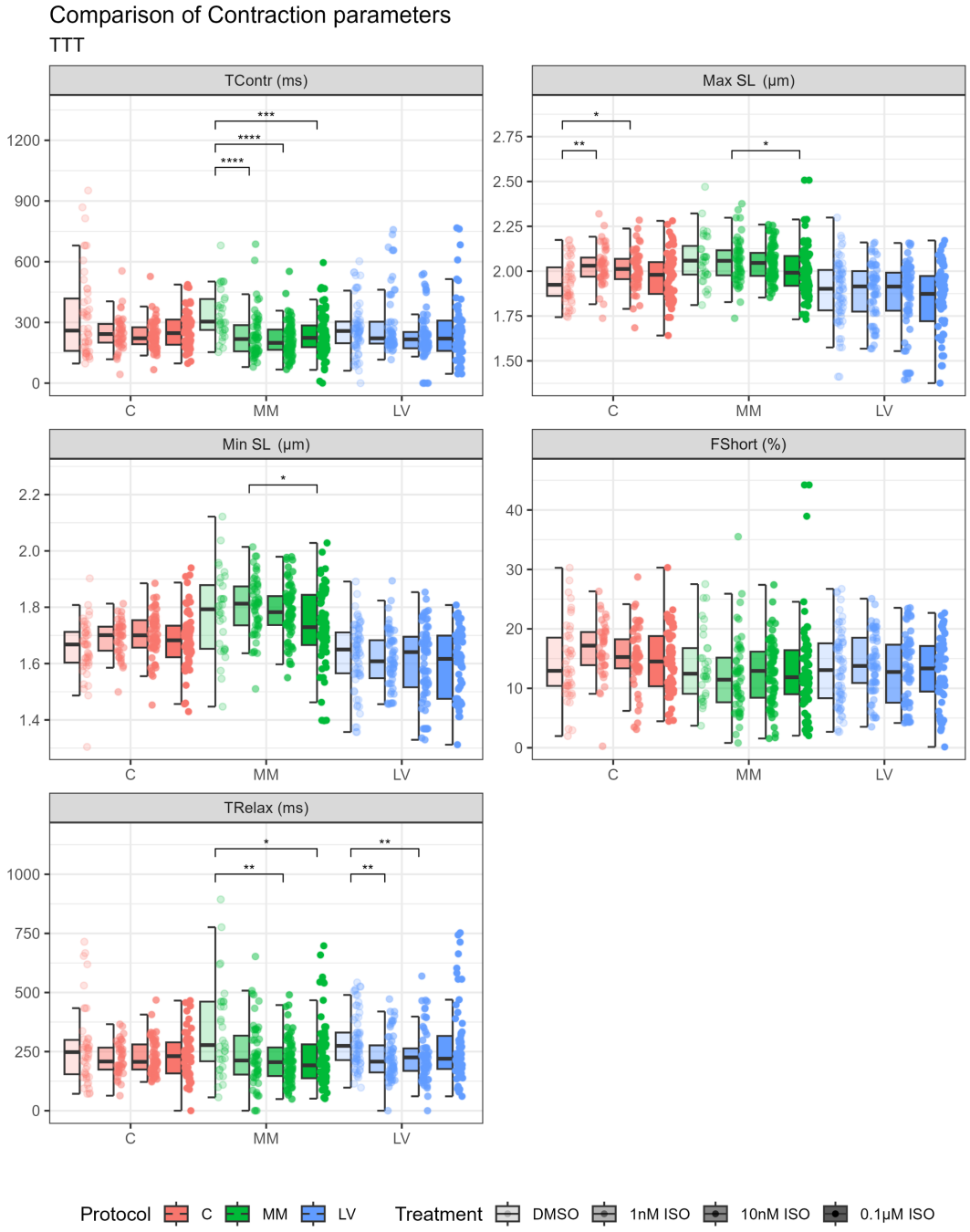

Figure 5.6: β-adrenergic stimulation induces a shortening of contraction times in MM and LV hiPSC-CMs. *Max SL = maximal sarcomere length, Min SL = minimal sarcomere length, FShort = fractional shortening, TContr = time to contraction peak, TRelax = relaxation time. n=48 for DMSO, n=42 for 1nM ISO, n=54 for 10nM ISO, n=62 for 0.1µM ISO, from 2-3 differentiation batches in C ; n=32 for DMSO, n=54 for 1nM ISO, n=71 for 10nM ISO, n=75 for 0.1µM ISO, from 2-4 differentiation batches in MM ; n=75 for DMSO, n=58 for 1nM ISO, n=68 for 10nM ISO, n=64 for 0.1µM ISO, from 2-3 differentiation batches in LV. See corresponding traces in supplementary figure A.8, and detailed statistics in supplementary table B.5.*

5.2.3 Action potentials

Finally, to determine the impact of maturation protocols on hiPSC-CM eletrophysiology, action potentials were investigated using the fluorescent reporter dye FluoVolt on cells maintained at 37°C and paced at 1Hz. Image analysis was performed using CalTrack.

5.2.3.1 Basal conditions

The LV protocol gave rise to hiPSC-CMs with more rectangular and therefore more ventricular-shaped action potentials. Surprisingly, this was not accompanied by a significant rise in triangulation score. MM cells, however, displayed a significantly higher score compared to the control, confirming that MM cells had more rectangular action potentials compared to control hiPSC-CMs (Figures 5.7, 5.8). Moreover, LV cell population was highly homogeneous compared to C and MM hiPSC-CMs, as showed by a much lower IQR (0.1927 in C and 0.2257 in MM versus 0.1041 in LV, *P*=5.43E-05). Additionally, action potential duration was robustly reduced in the LV group, in relation to both a reduction in time to peak and much shorter repolarisation time. Impressively, action potential duration at 50% of repolarisation was exactly the expected measurement for adult CMs. Conversely, MM hiPSC-CMs displayed a very high variability (for the APD measurement, IQR=297.62ms in MM versus 136.49ms in C and 138.51ms in LV, *P*=3.30E-07 ; and for TRepol, IQR=321.31ms in MM vs 130.72ms in C and 140.07ms in LV, *P*=1.07E-09) leading to seemingly two sub-populations of hiPSC-CM with different repolarisation times and action potential shapes. The majority of the cells however display a prolonged action potential induced by both an increase in time to peak, and a slower repolarisation time, compared to both the other protocols.

Action potential shape was also specifically studied, grouping the traces between ventricular-like and non-ventricular action potentials. The ventricular-like action potentials were defined by APD40/APD10 > 1.75 (characteristic

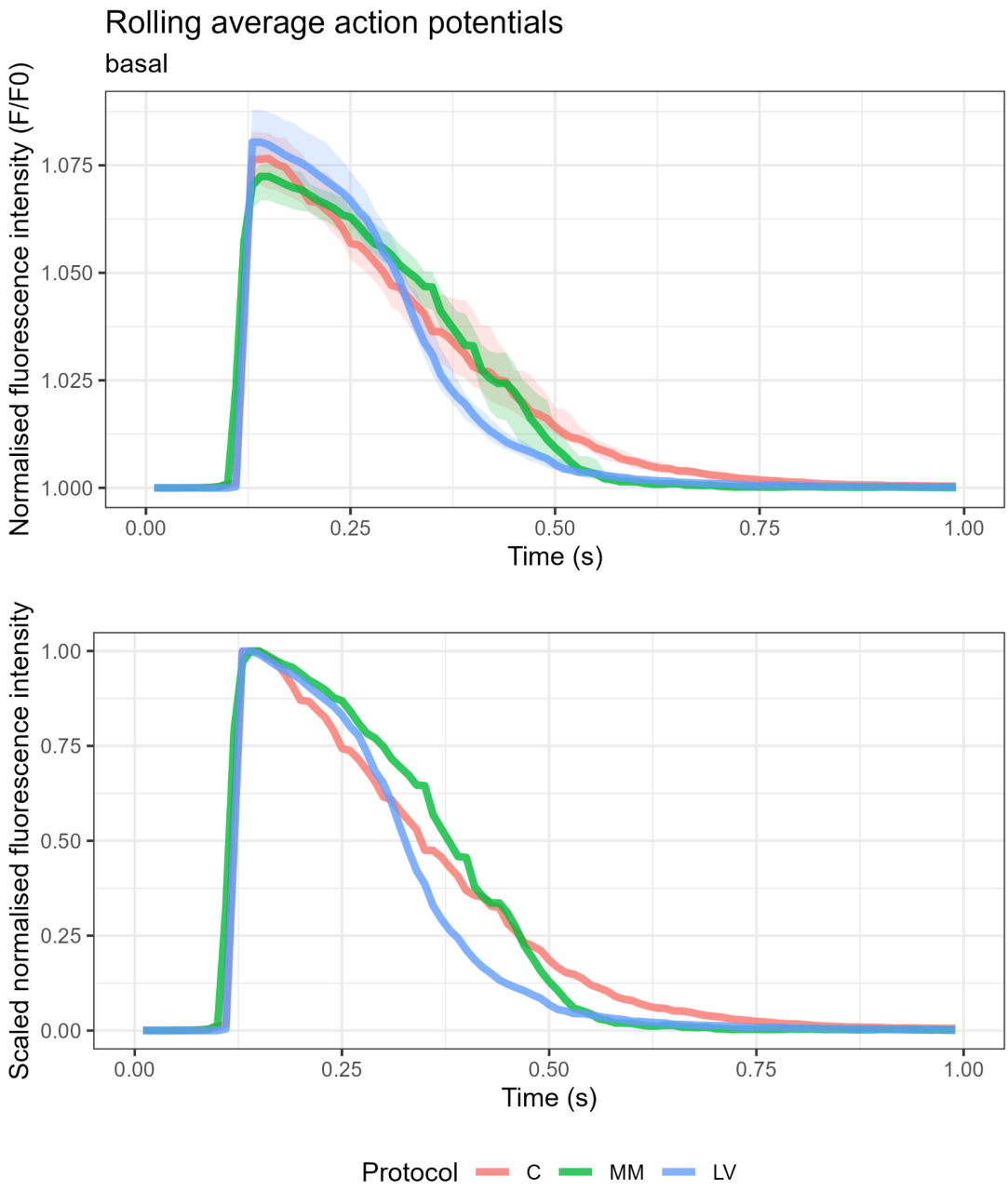

Figure 5.7: LV action potentials are shorter and more rectangular. *Action potentials from hiPSC-CMs maintained at 37°C and paced at 1Hz. Curves are rolling median (3-points average, centred) of action potentials and coloured areas are 95% confidence intervals.* ***Top****: The curves are normalised to baseline (Fluorescence/Baseline fluorescence).* ***Bottom****: The normalised curves are scaled between 0 and 1. n=81, from 4 differentiation batches in C ; n=81, from 4 differentiation batches in MM ; n=79, from 4 differentiation batches in LV.*

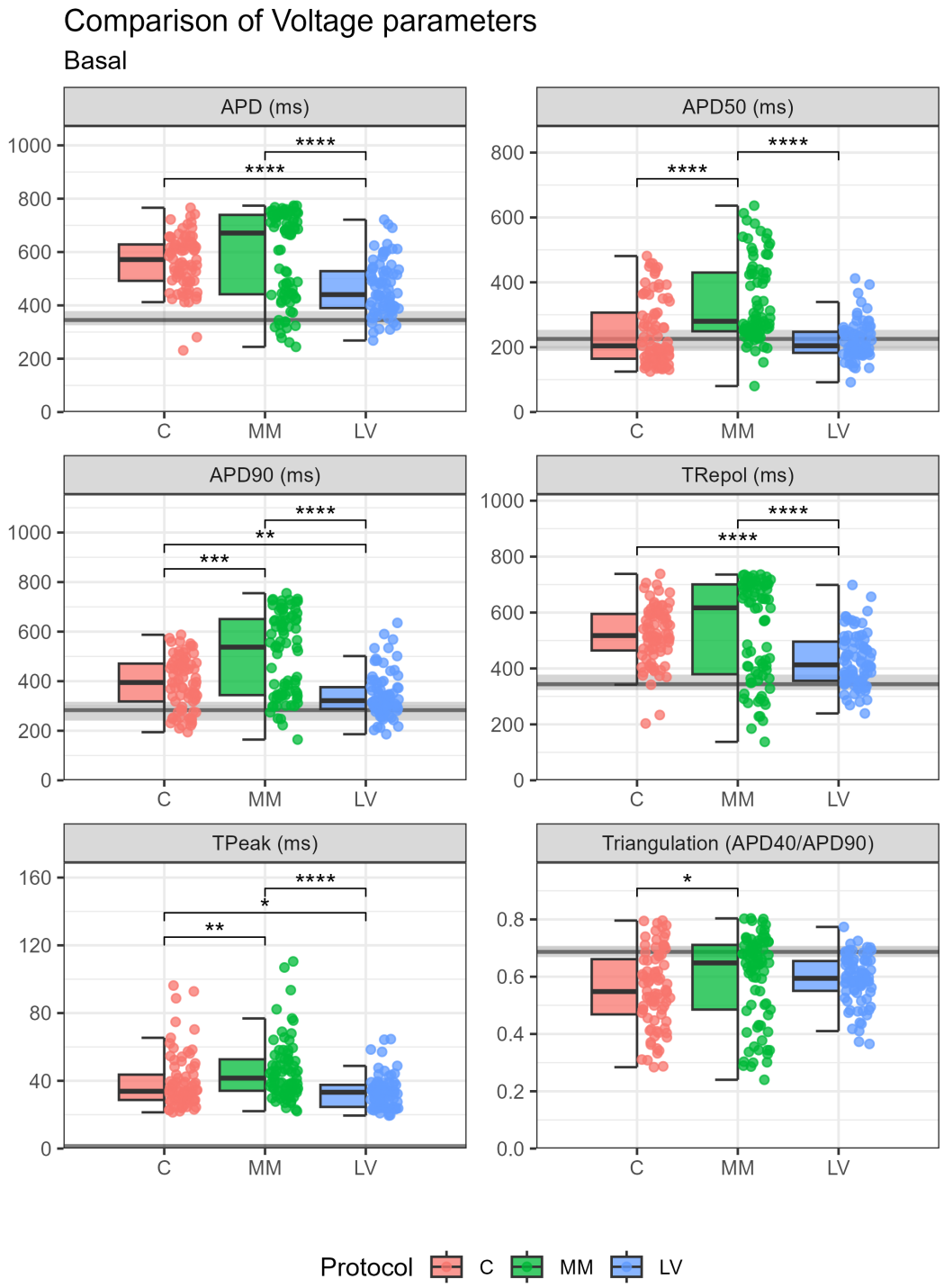

Figure 5.8: LV hiPSC-CMs electrophysiology is much closer to adult ventricular electrophysiology. *Dark grey lines and shaded areas are the median and interquartile range of corresponding measurement on simulated adult CM calcium transients (Sim). APD = action potential duration, APD50|APD90 = action potential duration at 50|90% repolarisation, TRepol = repolarisation time, TPeak = time to peak, Triangulation = APD40/APD90 score (closer to 1 is more rectangular versus triangular). n=81, from 4 differentiation batches in C ; n=81, from 4 differentiation batches in MM ; n=79, from 4 differentiation batches in LV ; n=83 in Sim. See detailed statistics in supplementary table B.6.*

of the prolonged plateau phase) and APD80/APD40 < 1.5 (characteristic of the faster repolarisation after plateau) based on empirical observations of the data. The figure 5.9 highlighted a rise in the proportion of ventricular-like action potentials with both maturation protocols, but more importantly the LV protocol (~45% in C, ~55% in MM, ~65% in LV). It is important to note that these proportions were solely indicative, as the parameters selected for AP shape characterisation were non-standard and might have under-estimated the real proportions. Additionally, the average control ventricular AP was unexpectedly triangular, due to greater variability in individual durations compared to MM and LV, though individual APs remained ventricular-like with a distinct plateau and rapid repolarisation.

Overall, the LV protocol gave rise to more mature action potentials, closer to adult ventricular action potentials. On the contrary, the MM protocol increased the variability of the dataset and induced delayed and prolonged action potential, characteristic of an immature electrophysiology, despite more rectangular action potentials in majority. Compared to adult ventricular action potentials, as observed with calcium handling, the time to peak was significantly delayed (~35ms in hiPSC-CM vs <5ms in mature CMs). Repolarisation time was also delayed, although the LV group was getting significantly closer.

5.2.3.2 β-adrenergic stimulation

Finally, to investigate whether basal maturation of hiPSC-CM action potential would ensure a robust β-adrenergic adaptability, hiPSC-CM were also treated with increasing doses of ISO prior action potential recording. Surprisingly, the ISO treatment induced a prolonged APD50 in control cells, opposite of the expected effect in mature CMs. In the LV group, a non-significant tendency to faster time to peak, in a dose-dependent manner was observed (Figure 5.10). Additionally, a reduction in APD50 was observed in response to the highest doses but this effect was not seen in

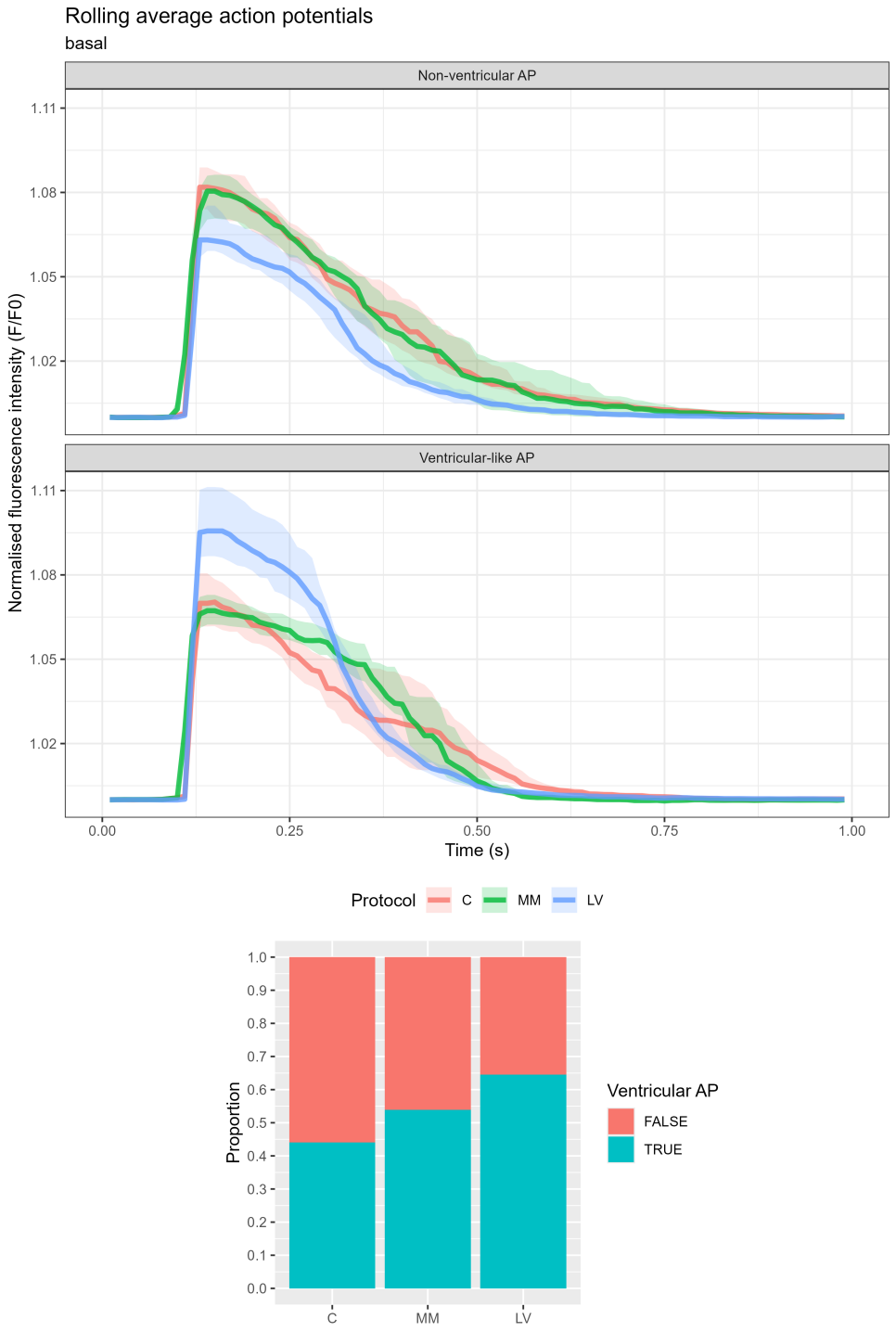

Figure 5.9: The proportion of ventricular-like action potentials is elevated in MM and further increased in LV hiPSC-CMs. ***Top**: Action potentials grouped between ventricular-like and non-ventricular action potentials (AP). Curves are rolling median (3-points average, centred) of action potentials and coloured areas are 95% confidence intervals. The curves are normalised to baseline (Fluorescence/Baseline fluorescence). **Bottom**: Proportion of ventricular-like versus non-ventricular AP. n=81, from 4 differentiation batches in C ; n=81, from 4 differentiation batches in MM ; n=79, from 4 differentiation batches in LV.*

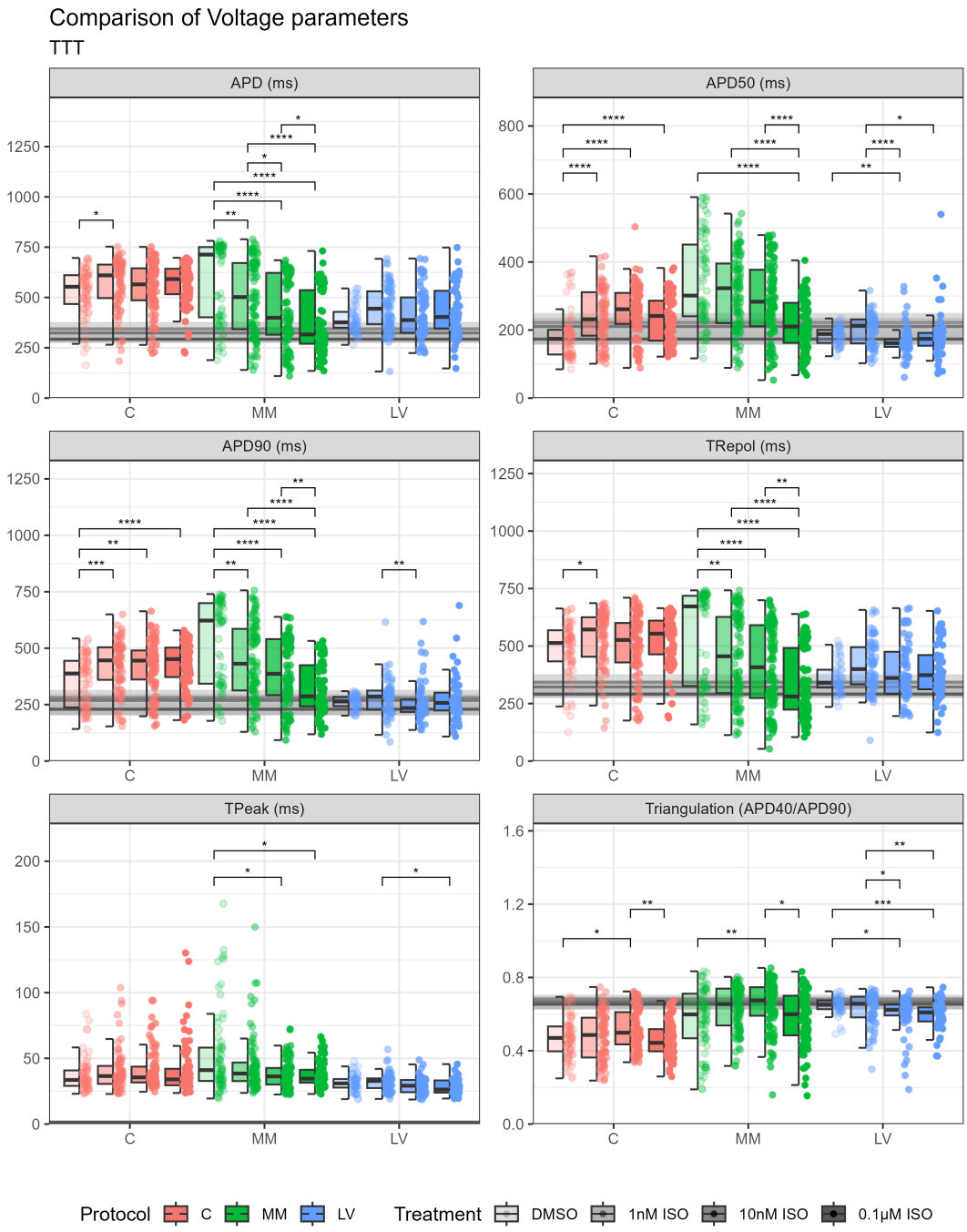

Figure 5.10: MM hiPSC-CM react to ISO with a dose-dependant shortening of action potentials duration. *Dark grey lines are the median of corresponding measurement on simulated adult CM action potentials (Sim), and shaded areas are interquartile range. CTD = calcium transient duration, CTD40|CTD90 = calcium transient duration at 40|90% of peak, Tau = decay time constant (from fitted double exponential curve), TRepol = repolarisation time, TPeak = time to peak. n=72 for DMSO, n=75 for 1nM ISO, n=86 for 10nM ISO, n=88 for 0.1µM ISO, from 4 differentiation batches in C ; n=70 for DMSO, n=96 for 1nM ISO, n=89 for 10nM ISO, n=89 for 0.1µM ISO, from 4 differentiation batches in MM ; n=51 for DMSO, n=71 for 1nM ISO, n=66 for 10nM ISO, n=57 for 0.1µM ISO, from 2-3 differentiation batches in LV ; n=83 in Sim. See corresponding traces in supplementary figure A.9,and detailed statistics in supplementary table B.7.*

ADP90 measurements. Finally, the MM protocol induced a dose-dependant reduction in time to peak and especially repolarisation time, leading to a robust reduction in action potential duration. This suggested a subtle and non-robust effect of the β-adrenergic stimulation on action potentials in LV hiPSC-CMs, while MM hiPSC-CM treated with ISO had a robust shortening of action potential kinetics, as expected in mature CMs.

Overall, it appears that both maturation protocols helped mature hiPSC-CM electrophysiology in a different way. LV cells exhibited shorter and more rectangular, ventricle-like action potentials, much closer to adult ventricular action potentials, and with homogeneous action potential shapes. β-adrenergic stimulation induced a subtle shortening of the action potential duration at 50% of repolarisation, thereby correcting the reverse effect the drug had on control hiPSC-CM. MM cells also showed more rectangular action potentials, although this protocol exacerbated population heterogeneity (especially the electrophysiology), inducing a very high variability in the data. MM hiPSC-CMs reacted to ISO with a robust dose-dependant shortening of action potentials duration, with response amplitudes exceeding the effect observed in adult ventricular CMs.

5.3 Discussion and perspectives

The objective of this chapter was to establish how differentiation and maturation protocols influence the functional maturity of CMs produced in 2D culture, and assess the maturity of the cAMP signalling pathway by assaying how β-adrenergic stimulation alters cellular function.

When compared to adult vCMs, all hiPSC-CMs still demonstrated a significant immaturity.

In terms of calcium handling, all hiPSC-CMs showed a slightly prolonged decay time compared to what was observed in adult ventricular CMs, with a significantly prolonged time to peak. This highlighted a robust immaturity

of the calcium release, while calcium reuptake/extrusion was more efficient. This delay could be explained by an extended reliance on extracellular calcium rather than SR stocks in hiPSC-CM subpopulations [128]. But more importantly — as the delay was asymetrical between release and reuptake — this was probably due to spacially uncoupled LTCC and RyR, induced by the lack of T-tubules in hiPSC-CM, which delays the opening of RyRs as the calcium must diffuse on longer distances to activate them [129].

Similarly, action potential depolarisation time was still significantly increased in all hiPSC-CM compared to adult vCMs. This is usually explained by the depolarised resting membrane potential in hiPSC-CMs, which reduces the driving force and therefore slows down sodium influx [130], combined with slower kinetics of the $Na_V1.5e$ channel (neonatal) isoform [131].

Interestingly, hiPSC-CM dose-dependent responses to β-adrenergic stimulation were progressing linearly with increasing doses, while adult vCM showed an exponential evolution. Additionally, hiPSC-CMs were more sensitive to low ISO dose than adult vCMs, which illustrates the persistent immaturity of β-adrenergic responses in hiPSC-CMs, despite maturation protocols.

Comparing the relative functional maturation status of hiPSC-CMs revealed that the functional impact of both maturation protocols was different depending on the cellular function examined. The MM protocol induced improvements in electrophysiology compared to control hiPSC-CM, with more ventricular-like action potentials and a robust adaptation to β-adrenergic stimulation only for action potentials and not for calcium handling. On the other hand, the LV protocol increased further the proportion of ventricular-like action potentials, but only demonstrated a robust adaptation of calcium handling to ISO.

Calcium transients were not robustly matured by either maturation protocol at basal state, but the contractile function of hiPSC-CM was differentially affected by the two protocols. The MM protocol induced

longer sarcomeres, to the expected length in mature CMs, but at the same time impaired the contractile function by reducing the fractional shortening and increasing relaxation times, although calcium reuptake had close to mature kinetics. In contrast, LV differentiation gave rise to hiPSC-CMs with shorter, less mature sarcomere length, but decreased relaxation times. Electrophysiology, however, was dramatically improved by the LV protocol. Although both protocols promoted the generation of rectangular, ventricle-like action potentials, only LV hiPSC-CMs exhibited a robust reduction of action potentials depolarisation and repolarisation times, leading to close to mature action potential duration.

LV maturation protocol induced an interesting change in calcium handling in response to β-adrenergic stimulation. While control hiPSC-CM demonstrated a shortening of calcium transient duration due to a shorter decay time, LV hiPSC-CM responded to ISO with a reduction in the time to peak. MM cells demonstrated an intermediate response, with a non-significant shortening of decay time, alongside a shortening of time to peak at high ISO dose. Moreover, both MM and LV hiPSC-CM tolerated the highest dose of ISO, which induced the greatest amplitude of response, while it induced an opposite effect in control cells. Taken together, these results suggested significant changes in cAMP dynamics around NCX1 or SERCA/PLN complexes, and LTCC as well as RYR channels, by maturation protocols ; thereby limiting increasing activity of proteins involved in calcium reuptake/extrusion and increasing the speed and probability of opening of calcium channels, in response to β-adrenergic stimulation. A further investigation of this phenomenon would be required to elucidate the exact mechanism involved. Phospho-protein quantification and targeted cAMP sensors would have been of great help on this matter. Additionally, specific inhibitors of these ATPase, exchanger and ion channels (such as ryanodine and dihydropyridine for example) could be used to delineate the respective roles of these proteins in calcium handling and β-adrenergic adaptation within these cells.

The β-adrenergic stimulation induced a dose-independent shortening of the relaxation time in a similar way in both MM and LV hiPSC-CMs. Contraction time however, was only reduced in MM cells. These results were not correlated to ISO-induced calcium kinetics changes, and therefore suggested a subtle maturation of the sarcomeric cAMP nanodomain.

Looking at action potentials, β-adrenergic stimulation induced a dose-dependent shortening of the action potential duration at 50% and 90% in cells from both maturation protocols, but with more robust results in MM hiPSC-CMs ; whereas ISO had a surprising reverse effect on control cells. This demonstrated an increased maturation of β-adrenergic processes associated with action potential modulation, induced by both maturation protocols, and especially MM medium.

Overall, the functional impact of both maturation protocols was different, demonstrating that these maturation protocols do not induce an homogeneous global maturation, and that care must be taken when selecting maturation protocols, to ensure it gives the best results on studied functions or pathways. But it also questions how maturity is usually evaluated in these cells, with often restricted focus on one or two functions, and calls for clearly defined standards that still lack in this field.

Independently from the maturation status, the LV protocol gave rise to impressively homogeneous population of hiPSC-CMs, as opposed to the MM protocol which often inflated data variability from control cells. This alone indicated that the LV protocol would be a preferable choice, especially because high data variability is already a known hurdle of this model, thus reducing reproducibility and applicability of the results.

This variability could come from either mixed or heterogeneous populations of CMs that emerge from the differentiation process, or from non-CMs (endothelial cells, cardiac fibroblasts, etc.) that arise in different proportions depending on the protocol used. These other cell types can induce variability when they are included in the dataset and also have a

direct impact on the CMs physiology through cell-to-cell communication [82], [132]–[134]. In terms of mixed populations, analysis of action potentials shape demonstrated an increased proportion of ventricular-like AP in the MM group, and a further increase in the LV group. These CM subtypes differences might explain part of this increased variability in the MM group, as more mature atrial or ventricular hiPSC-CMs would have increasingly robust differences in terms of function. This hypothesis will be further explored in the next chapter.

5.3.1 Limitations

Several limitations can affect the translatability of the results found in this chapter.

First, similar to FRET measurements, the high data variability and low number of differentiation batches per condition, coupled with the use of a single cell line, limit the robustness of the results presented in this chapter.

Another limitation of this work was the use of fluorescent reporters. This choice was motivated by the ease of use, as all facilities and expertise were already on site, as opposed to gold standard procedure such as patch clamp. Moreover, only global function was investigated while specific currents or activity of ion channels or pumps could have brought in-depth knowledge of hiPSC-CM maturity and underlying mechanisms.

Additionally, the use of the calcium reporter RGECO instead of a ratiometric chemical dye, such as Fura-2 for example, was preferable in this experimental design, as our group showed that chemical dyes alter contractility in CMs [135], and contractility measurements were performed simultaneously to calcium measurements. Future work will develop an integrated pipeline combining CalTrack and SarcTrack to directly correlate calcium handling with contractility at the single-cell level, to complete this analysis.

However, the fluorescent reporters used in this chapter limit the functional investigation to kinetics and do not give access to actual voltage, calcium concentration, nor force generation, which prevent these data from being generalised. Future work will complete this dataset with contractility measurements — including contraction force — with the use of engineered heart tissues. The results presented here are therefore preliminary, and indicative of effects to investigate further with more robust and costly methods.

Chapter 6

Discussion

hiPSC-CMs have emerged as an innovative tool in cardiovascular research as they represent a convenient source of human CMs, can be genetically modified to create new cell lines, or even reflect the genetic background of individual patients when derived directly from patient cells. hiPSC-CM therefore offer unprecedented opportunities to model human cardiac disease mechanisms at the cellular level, improve predictability of preclinical studies in drug testing, and explore regenerative medicine.

But despite their promise, hiPSC-CMs resemble fetal CMs in terms of structure and function, rather than adult CMs. This relative immaturity limit their applicability in adult-onset diseases. Despite the proliferation of methods since the 2010s to improve hiPSC-CM maturation, no strategy so far has achieved a fully mature CM phenotype.

Several studies have suggested a role for the β-adrenergic pathway in hiPSC-CM maturation. However, at present it is unknown how cAMP nanodomains are established and regulated during maturation. This is why this thesis aimed to explore the dynamics between maturation and organisation of the cAMP signalling pathway in hiPSC-CMs.

The first objective was to establish how differentiation and maturation protocols influence the proportion and maturity of CMs produced in 2D culture.

Results from snRNA-seq, highlighted that while all protocols gave rise to a heterogeneous population of hiPSC-CMs, with highly immature and proliferative CMs alongside more mature CMs, the proportion of immature cells was reduced with the MM medium treatment, and even more with the

LV protocol. Compared to regular age-matched hiPSC-CM, cells treated with the MM medium showed increased maturation as developmental processes were suppressed. The principal influence of the MM protocol was unsurprisingly the development of metabolic processes. hiPSC-CMs from the LV protocol, however, only robustly exhibited a reduction in cellular respiration, compared to both control and MM cells. LV hiPSC-CMs also had increased developmental processes compared to MM cells. Reduced cellular respiration and increased developmental processes tend to indicate a relative immaturity of LV hiPSC-CMs compared to those from the MM protocol.

However, at the functional level, LV hiPSC-CMs appeared to be significantly closer to the adult phenotype than control cells, and often than MM cells. Moreover, this lineage specification induced a significantly greater homogeneity of the hiPSC-CM physiology.

The second objective investigated the relative contribution of PDE3 and PDE4, as an in-depth investigation of the β-adrenergic-cAMP pathway development in the context of hiPSC-CM maturation.

Results from the FRET-based cAMP measurements highlighted a persistent predominance of PDE4 in regulating cAMP levels, in basal conditions or in response to ISO stimulation. However, both LV and MM protocols gave rise to hiPSC-CMs with an increased reliance on the principal adult isoform, PDE3; an indication of progressed β-adrenergic-cAMP pathway maturation.

The final objective was to assess the maturity of the cAMP signalling pathway by assaying how β-adrenergic stimulation alters cellular function, and how this correlates with changes in PDE3 and PDE4 activity.

At the functional level, β-adrenergic stimulation demonstrated an ongoing maturation of this pathway in hiPSC-CM from both protocols, with more robust alterations of cellular function compared to control cells. MM cells had a more robust response to β-adrenergic stimulation of action potentials compared to LV hiPSC-CM, while conversely calcium transient were more robustly altered by ISO treatment in LV cells. This corroborated the previous

finding, with an increasing predominance of the mature isoform PDE3 in these cells.

6.1 The predictive power of snRNA-seq on hiPSC-CM function

To evaluate the predictive power of snRNA-seq on hiPSC-CM function, this section will integrate the findings of the different chapters.

Comparative expression of sarcomeric protein isoforms showed a strong tendency toward sarcomeric maturation with both maturation protocols, with a reduction in the expression of foetal cardiac ventricular isoforms and and/or an increase in adult isoforms. This was not consistent with the corresponding genes expression in half of the investigated proteins.

Gene expression coding for key proteins involved in calcium cycling revealed several changes between the protocols (Figure 6.1). SLC8A1 and CACNA1D, both found to be overexpressed in immature CMs are still highly expressed in all hiPSC-CM groups, compared to adult left vCMs. RYR2 and CASQ2 expression was significantly reduced in all hiPSC-CM compared to adult vCMs, and this could be correlated with a prolonged time to peak calcium. PLN and ATP2A2 were up-regulated in MM hiPSC-CM, compared to C and LV cells and this was correlated with a reduction in calcium transient decay time in these cells. However, LV hiPSC-CMs show a reduction in these genes expression, with no effect on calcium decay.

The highest impact of maturation protocols was seen on action potentials. MM and LV action potentials were more rectangular, ventricle-like, with a sustained calcium plateau and faster repolarisation. Gene expression of key proteins involved in action potentials also revealed important changes induced by the MM maturation protocol (Figure 6.2). But although SCN5A (I_{Na}) and KCNA4 (I_{To}), KCNQ1 (I_{Ks}), KCNH2 (I_{Kr}) are highly expressed in MM hiPSC-CM, depolarisation (sodium current) and repolarisation (potassium

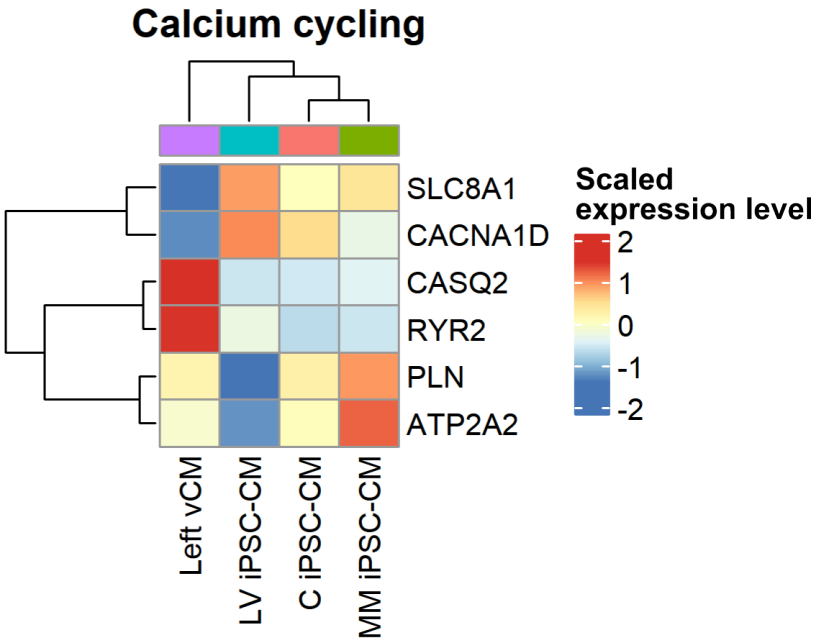

Figure 6.1: Comparison of the expression of genes involved in calcium cycling.*Heatmap presenting the relative expression of selected differentially expressed genes involved in calcium cycling between the four groups C, MM and LV hiPSC-CMs, and left vCM. Columns (groups) and rows (genes) were automatically clustered (see trees on the left side and top of the heatmap), based on their relative expression profile (Scaled expression level).*

current) were on the contrary prolonged compared to LV hiPSC-CM. The lack of significant change in ion channels gene expression in LV cells was not consistent with the observed advanced maturity of measured LV action potentials.

snRNA-seq revealed a decrease in PDE4D and PDE4B genes expression, in both MM and LV hiPSC-CM compared to control cells, while PDE4A did not show a significant change (Figure 6.3). PDE3B gene expression was massively reduced in MM cells, while the main PDE3 isoform, PDE3A, did not show any significnt change between hiPSC-CM groups. Overall, this shows a global reduction in all PDEs gene expression in MM cells, but only a reduction in PDE4 isoforms in LV cells, compared to C. But at the protein level, PDE4D expression was only reduced (not significantly) in MM cells. Additionally, FRET-based experiments revealed that, while PDE4 remained the main isoform regulating global cAMP variations, an increased reliance on PDE3 was observed in half of the MM and LV batches. This change was not

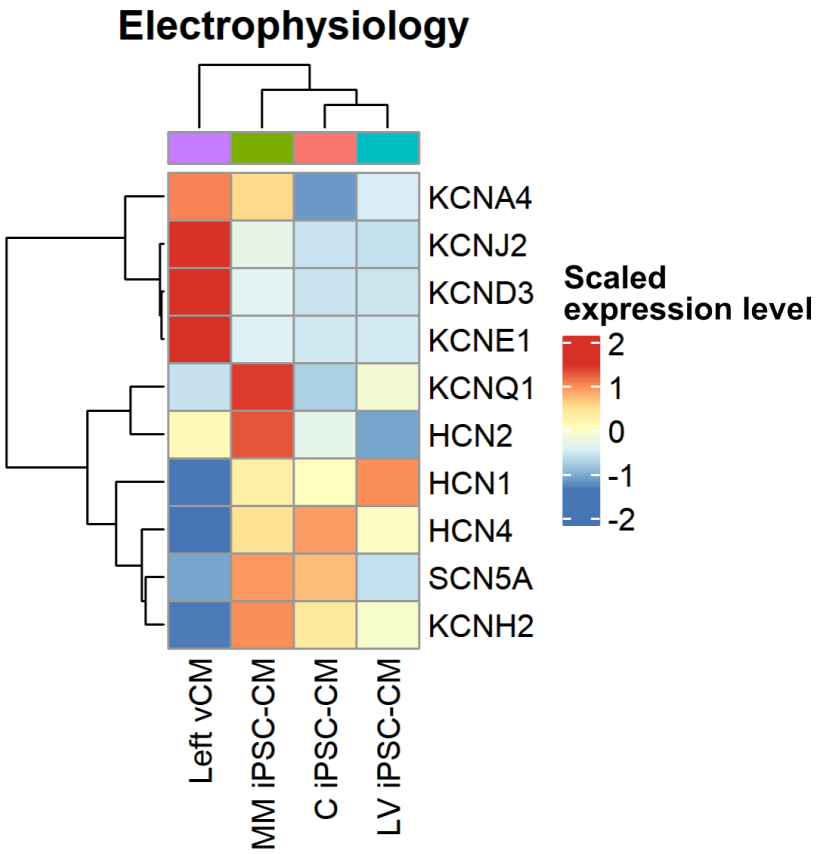

Figure 6.2: Comparison of the expression of genes involved in action potential.*Heatmap presenting the relative expression of selected differentially expressed genes involved in action potentials between the four groups C, MM and LV hiPSC-CMs, and left vCM. Columns (groups) and rows (genes) were automatically clustered (see trees on the left side and top of the heatmap), based on their relative expression profile (Scaled expression level).*

robust across differentiation batches but suggested a progression induced by both maturation protocols towards a more mature β-adrenergic pathway.

Finally, while no significant change in gene expression of either β_1-AR or β_2-AR could be seen, protein expression of the latter was significantly increased in both MM and LV hiPSC-CMs compared to control cells. This finding was linked to an increased β-AR activity in response to ISO in both groups, highlighting a higher maturity induced by both MM and LV protocols. AKAP7 gene expression was reduced in MM hiPSC-CMs and increased in LV hiPSC-CM as compared to C. Another alias for AKAP7 is AKAP18, the anchoring protein found at SERCA-associated cAMP nanodomain. However,

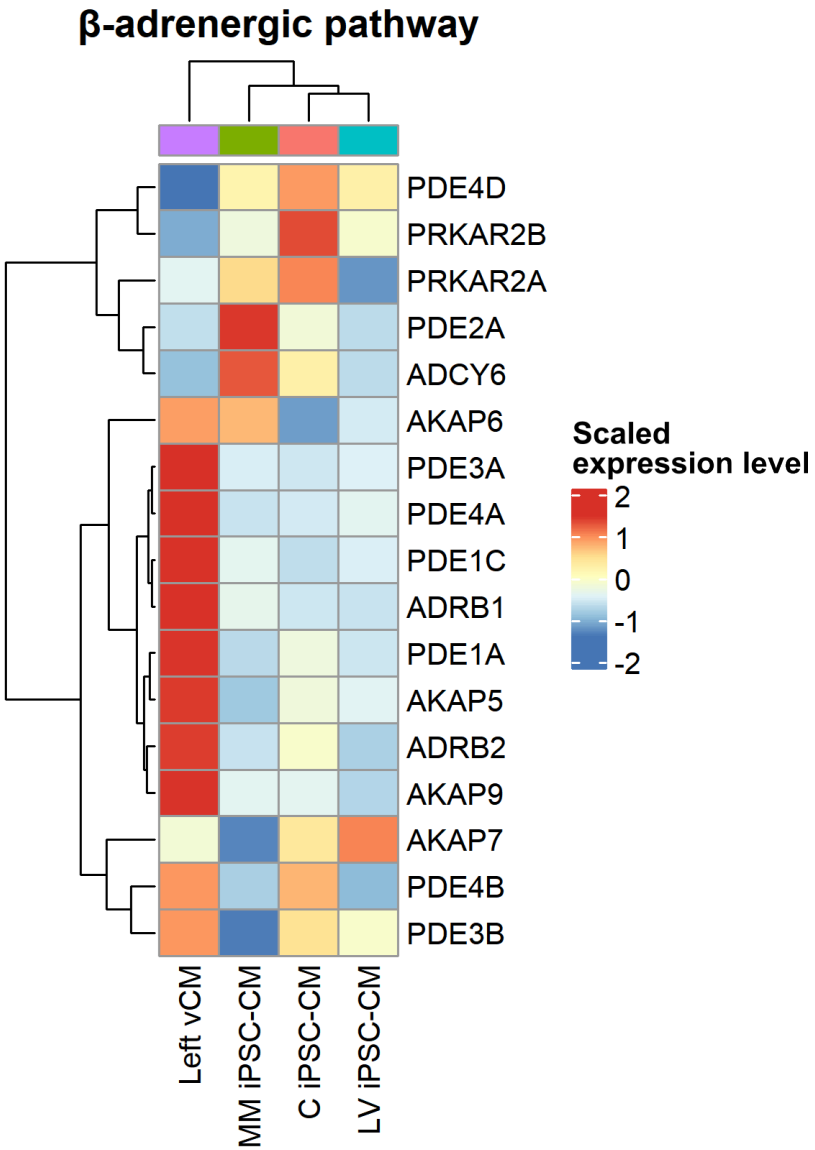

Figure 6.3: Comparison of the expression of genes involved in β-adrenergic pathway.*Heatmap presenting the relative expression of selected differentially expressed genes involved in β-adrenergic pathway between the four groups C, MM and LV hiPSC-CMs, and left vCM. Columns (groups) and rows (genes) were automatically clustered (see trees on the left side and top of the heatmap), based on their relative expression profile (Scaled expression level).*

at the functional level, β-adrenergic stimulation induced no change in calcium decay time, in both MM and LV hiPSC-CM, contrary to what was seen in control cells. On the whole, more robust responses to β-adrenergic stimulation were seen in both MM and LV hiPSC-CMs, while no such tendency could be deduced from the snRNA-seq data.

Besides functional maturity, LV cells displayed a significantly reduced variability in calcium transients and action potentials, highlighting the advantage of this protocol, which gives rise to a functionally homogeneous hiPSC-CM population. As this hurdle is known to reduce significantly the reliability of hiPSC-CMs as a model, such benefit is non negligible.
This is in relation to a significantly reduced proportion of immature hiPSC-CM in the LV group, as shown by snRNA-seq; although MM hiPSC-CMs also had a reduced proportion of immature hiPSC-CMs but showed a significant global increase in functional variability, compared to both control and LV cells. This suggests that this observed functional variability comes from heterogeneity within the mature hiPSC-CM population.
Other cell-types emerging from the differentiation could induce variability when they are included in the dataset and also have a direct impact on the CMs physiology through cell-to-cell communication [82], [132]–[134]. In this study however, snRNA-seq analysis demonstrated that no other cell types were detectable in either protocol, thereby ruling out their contribution as a significant factor affecting data variability. Taken together, these results suggested that the population of cardiomyocytes itself was therefore probably heterogeneous.

snRNA-seq analysis revealed the existence of two populations, one with lower cardiac genes expression (’hiPSC-CM low’) compared to the other (’hiPSC-CM high’), which could have been the reason of this increased variability in MM data. But, on the contrary, the proportion of ’hiPSC-CM low’ was only increased in LV hiPSC-CM.
One other explanation investigated was the proportion of atrial versus ventricular CMs in culture. These CM subtypes differences might explain

part of this increased variability in the MM group, as more mature atrial and ventricular hiPSC-CMs would have increasingly robust differences in terms of function. The proportion of ventricle-like action potentials was shown to be increased in LV hiPSC-CMs, which could explain the robust decrease in variability in this group, compared to the other two. This analysis also showed more ventricular-like action potentials in the MM group than in C; but the proportion of ventricular CM was still lower than in LV samples, and it is possible that the MM medium matures atrial CMs better than the LV differentiation, thereby exacerbating subtype functional specificities, and inflating global variability.

The expression of specific atrial and ventricular markers was additionally compared across all three protocols using snRNA-seq data, but no definitive trends could be identified (Figure 6.4). Of note, differentiation at the time of physiology measurements was increasingly challenging (for both differentiation protocols), with most differentiations yielding no cardiomyocytes. The few successful cases showed reduced purity, with only scattered patches of beating cells, compared to the higher purity obtained for snRNA-seq samples. This might explain the discrepancy between functional measurements and snRNA-seq data on atrial versus ventricular CMs proportion differences.

Nevertheless, one of the main sources of variability identified was the differentiation itself. The figure 6.5 shows that the variability between differentiation batches was often higher than the variability within each batch, and therefore represents the main driver of the global data variability. One extreme example was action potential measurements in MM hiPSC-CMs, where two distinct subpopulations were visible, that were in fact coming from different differentiation batches (Figure 6.6). This also contradicts the idea that differentiation batches contained varying proportions of atrial and ventricular CMs both matured by the MM protocol, as such variability should be evident within batches, not just between them.

In conclusion, snRNA-seq data were not predictive of the changes

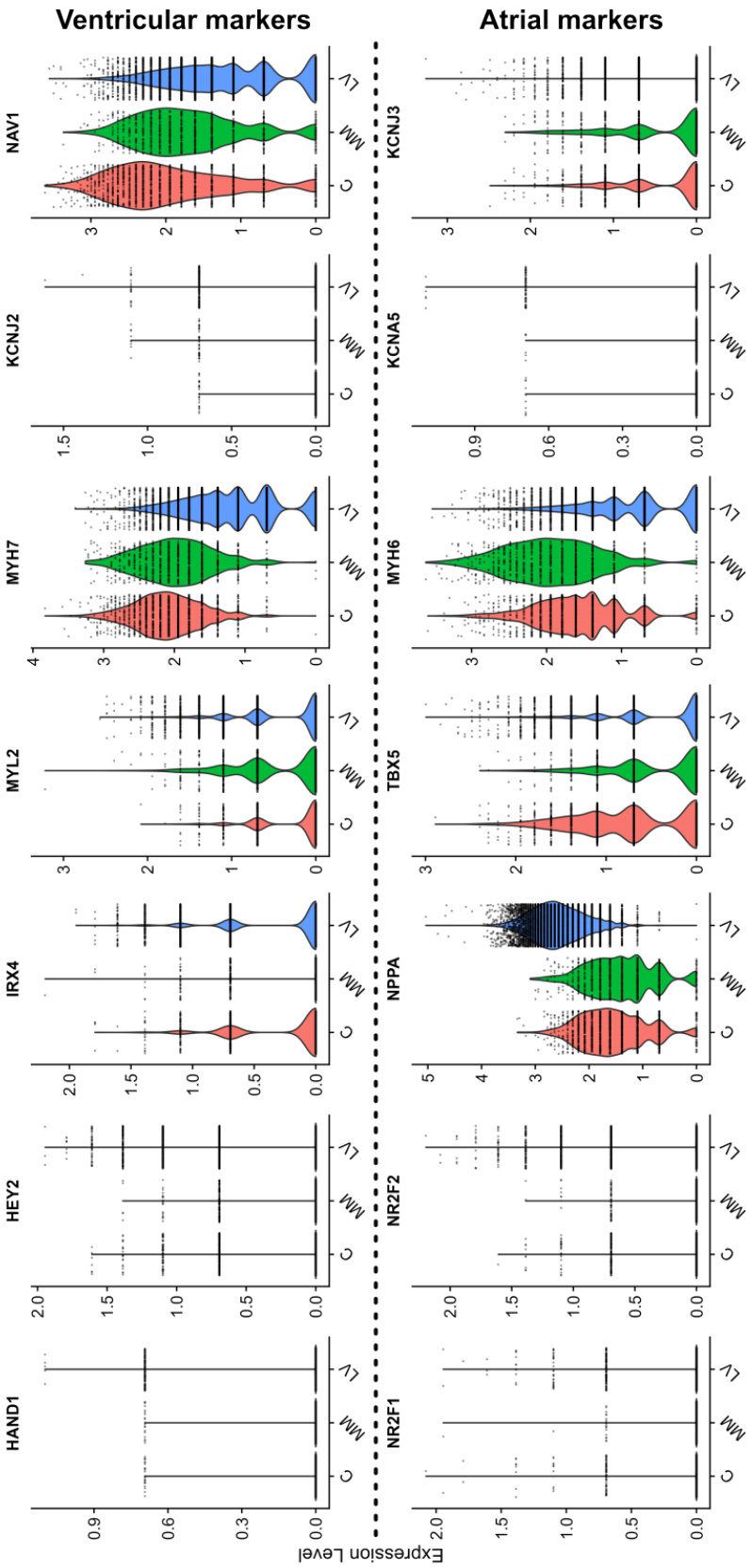

Figure 6.4: Marker gene expression shows no difference in ventricular versus atrial hiPSC-CM proportions across protocols. *Violin plots of ventricular or atrial marker genes expression in the different protocols. The whole dataset is presented here (including both 'hiPSC-CM low' and 'hiPSC-CM high').* ***Top line****: Ventricular markers.* ***Bottom line****: Atrial markers.*

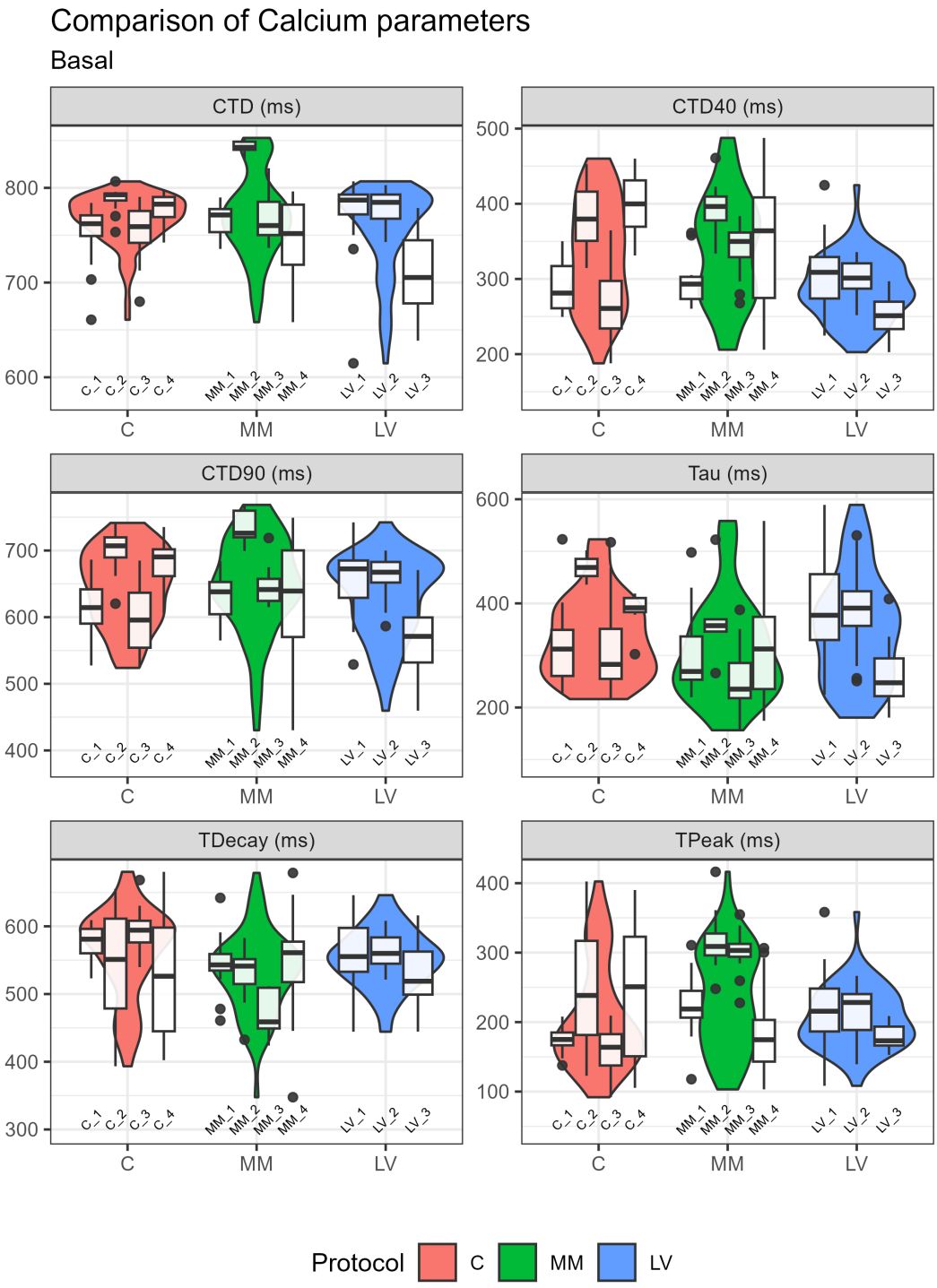

Figure 6.5: The variability between differentiation batches is the main driver of global variability. *Violin plots represent the global distribution of the data per protocol. The superimposed boxplots represent the distribution of each differentiation batches that form the dataset, per protocol. Of note, the control hiPSC-CMs and MM hiPSC-CMs showed here come from the same differentiation batches that have been split between the two protocols from day 20.*

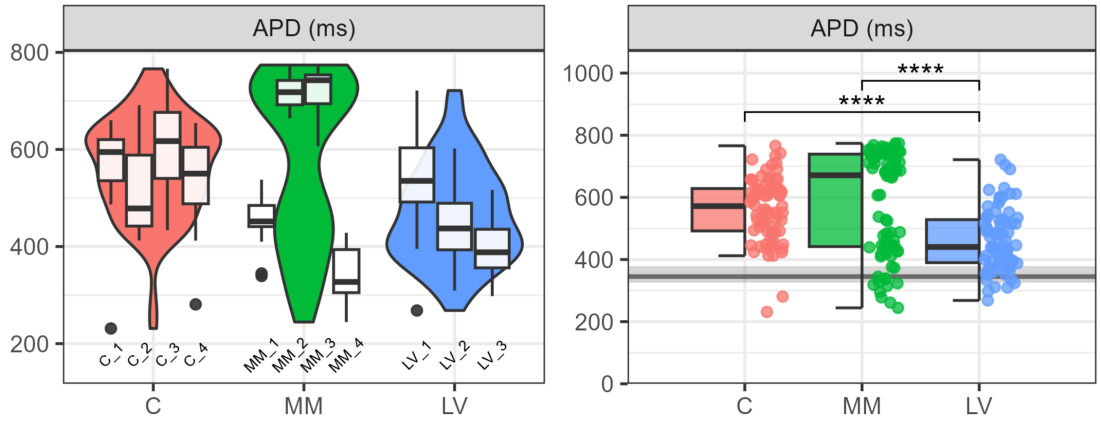

Figure 6.6: Differentiation variability creates functionally distinct subpopulations. ***Left:*** *Violin plots represent the global distribution of the data per protocol. The superimposed boxplots represent the distribution of each differentiation batches that form the dataset, per protocol. Of note, the control hiPSC-CMs and MM hiPSC-CMs showed here come from the same differentiation batches that have been split between the two protocols from day 20.* ***Right:*** *Dots represent single cells from the whole dataset, per protocol. Two distinct subpopulations are visible in MM.*

observed at the protein, nor at the functional level. This could be confounded by the fact that differentiation batches between chapters were unmatched; but nonetheless questions the use of this technique as a robust predictor of cells physiology, especially in the context of bottom-up analyses, which focus on a small number of genes to infer more global and robust changes. This is especially true for hiPSC-CMs, which are subjected to broad changes involved in maturation processes. Robust and various functional measurements are therefore of utmost importance in evaluating hiPSC-CMs maturity.

6.2 The replication of maturation protocols

Although significant improvements in hiPSC-CM maturity were found with the use of both MM and LV protocols (See table 6.1), the results from the corresponding papers could not be entirely replicated.

Consequently to MM treatment, Feyen and colleagues [85] found significant and global increase in the RNA expression of genes involved

	MM protocol	**LV protocol**
Transcriptomics	↓ Proliferative CM, ↑ Metabolism	↓↓ Proliferative CM, ↓ Aerobic respiration
Protein expression	↑ MLC2v, ↑ cTnI, ↓ MLC2a, = ssTnI, ↑↑ β_2-AR	↑ MLC2v, = cTnI, ↓ MLC2a, ↓ ssTnI, ↑↑ β_2-AR
β-adrenergic pathway	↑ PDE3 reliance, ↑ β-AR activity	↑ PDE3 reliance, ↑ β-AR activity
Calcium, no stimulation	=	=
Calcium, β stimulation	↓ (No robust adaptation)	↑ (Dose-dependent shortening)
Contractility	Longer SL, ↓ fractional shortening	Shorter SL, = fractional shortening
Action potentials, no stimulation	↑ Ventricular AP	↑↑ Ventricular AP
Action potentials, β stimulation	↑ (Dose-dependent shortening)	= (No robust adaptation)
Global	↑↑ data variability	↓↓ data variability

Table 6.1: Summary of the relative efficiency of MM and LV protocols on hiPSC-CMs. *Based on this study measurements. β stimulation, β-adrenergic stimulation; ↓, decreased or worse compared to control protocol; ↑, increased or better compared to control protocol; =, equivalent to control protocol.*

adult CMs processes (metabolism, calcium cycling, sarcomeres and ion channels). This was only partially consistent with this study snRNA-seq data. Consistently, they found that metabolic activity was increased in these cells. Metabolic function was not assessed in this study, leaving a significant gap, especially since the MM protocol targets metabolism. Additionally, snRNA-seq data indicated metabolism as the primary differentiator between LV and other protocols, as well as between adult vCMs and hiPSC-CMs. Given the limited predictive power of snRNA-seq data on hiPSC-CM function, evaluating metabolic function would have provided valuable insight into the relative impact of both protocols. Additionally, I_{Na} and I_{K1} densities were significantly increased, with faster depolarisation times, in the original paper. Although specific currents densities were not evaluated here, MM action potentials demonstrated a higher proportion of ventricular CM. Feyen and colleagues also showed that calcium transient duration was reduced,

with faster time to peak and decay, consistent with an increased reliance on SR calcium stocks; and associated with increased contraction rate. However, none of this could be replicated.

According to Dark and colleagues, the LV specification induced a higher proximity with adult LV CMs at the transcriptomic level. Although difficult to evaluate, it was not robustly demonstrated in the present work. At the phenotypic level, higher mitochondrial content correlated with increased metabolic activity and ATP production in the original paper, important data which are missing from this thesis. Intriguingly, transmission electron micrographs (TEM) showed longer sarcomere length in LV hiPSC-CMs, reaching adult CM length. The opposite was measured on fluorescent-tagged sarcomeres using SarTrack. A likely explanation is the difficulty in transducing mature CMs compared to immature ones. Experiments with AAV-transduced fluorescent reporters showed significantly reduced expression in LV cells compared to MM and C hiPSC-CMs, though not quantified. Since mature CMs are harder to transduce, many mature LV CMs may have been excluded from live measurements due to low fluorescence, biasing results toward more immature CMs with shorter sarcomeres. Finally, as calcium and action potential measurements were performed in engineered heart tissues (EHT) in the original paper, the results are not directly comparable to this study, as the three dimensional culture itself has an impact on hiPSC-CMs maturity. Nevertheless, a predominance of the LV protocol in terms of data homogeneity and increased ventricular CM proportion was evident already in 2D culture.

In this thesis, although functional measurements were matured under the effects of both protocols, the maturation level was mostly not as advanced as expected, with the exception of LV action potentials. Several reasons could explain these discrepancies. First, the cell line used was different from the ones in the published papers. In the case of LV hiPSC-CM, culture conditions were different from the published paper, optimised to

better correspond to the PGP1 cell line physiology. But time in culture was also different, while most measurements were done at Day 20 in the original paper, it was prolonged to Day 40-45 in this thesis to match the other groups time in culture. Additionally, important measurements presented by Dark and colleagues were performed in EHTs (calcium, action potentials), and measurements performed with different techniques (TEM versus AAV-transduced fluorescent tag). In addition, for the generation of MM hiPSC-CM, the differentiation protocol was slightly different from the published paper.

Excessive variability exhibited within the differentiated products, including batch-to-batch variabilities, is a wide-spread challenge in the reproducibility of results obtained with hiPSC-CM [136]. Beyond line-to-line variability, known sources of variability that can explain batch-to-batch variability can be intrinsic to the cells used or acquired. For example, the dynamic transcriptional state of cells at the start of differentiation induces heterogeneity in pluripotency [137]; iPSC culture conditions can significantly imprint their behaviour [138] (mechanical stress, cell-to-cell contact, oxygen levels, genetic drift, cryopreservation); subtle differences at the start or within differentiation protocols (cell density or cell cycle phase at start of differentiation, small changes in various components concentration) [77].

However, despite this knowledge, the use of commercial media with graded formulation and efforts made to standardise iPSC culture, there are still significant changes in differentiation efficiency over time. During the course of this work, it happened several times that differentiations would suddenly stop working for months in a row before starting to work again, without notable changes in iPSC culture or differentiation conditions. More work is required to identify the sources of variability, and properly address this problem.

6.3 How far are we still from adult CMs ?

When comparing snRNA-seq data of hiPSC-CMs to adult CMs, it appeared that all hiPSC-CMs, regardless of their protocol of origin, demonstrated a higher proximity between themselves than with adult vCMs. This difference was mainly due to reduced processes involved in mitochondrial ATP production, in all hiPSC-CM groups compared to adult vCM. This was expected as increased mitochondrial density and activity seems to be mainly linked to long-term electrical stimulation in 2D monocultures. In a study combining MM medium with nanopatterning and long-term electrical stimulation, a key finding was that mitochondrial ATP production was also the main difference between hiPSC-CMs cultured with MM medium alone and highly mature hiPSC-CM cultured with the combined three techniques [84]. However, it is difficult to know if this is a robust finding, as few studies using electrical stimulation assessed mitochondrial activity, and even fewer studies directly compared the respective efficiency of the different techniques on hiPSC-CM maturity.

Overall the results of this thesis demonstrated that both maturation protocols, despite their different design and some specificities, induced a similar maturation of the β-adrenergic pathway and global physiology of hiPSC-CMs. However, the LV protocol led to the generation of homogeneous hiPSC-CMs, while the MM protocol seemed to even have the opposite effect, as dramatically visible at the functional level. These findings underscore the importance of selecting effective differentiation protocols and optimal culture conditions to generate iPSC-CMs that are more homogeneous, and will therefore robustly recapitulate the adult human CM phenotype when matured.

This study represents an introduction to the systematic study of the β-adrenergic pathway development, in relation to hiPSC-CM global maturity. These advances contribute to bridging the gap in knowledge around β-adrenergic pathway development through the nanodomains structure and the relative importance of associated PDE isoforms.

Importantly, it also highlights that functional maturation must be evaluated in an integrative context, rather than relying on single-parameter improvements. For instance, enhanced maturation of action potentials do not necessarily indicate mature β-adrenergic responses or enhanced calcium handling. Standardization of maturation metrics is needed to enable cross-study comparisons and meta-analyses.

Despite the fact that hiPSC-CMs still do not reach full maturity in vitro, the continued improvement in differentiation and maturation protocols brings hope to see this outcome in future work. Specific-lineage differentiation [86], 3D culture conditions, inclusion of the appropriate stromal cells [82], as well as 'Organ-on-a-chip' microfluidic devices [139] have emerged as robust techniques to improve hiPSC-CM functional maturity. Moreover, combined electrical and mechanical stimulation play important roles in the emergence of adult-like phenotypes from hiPSC-CMs [84].

Although bottom-up analyses involving RNA sequencing have shown important predictive limitations, transcriptional profiling of both hiPSC-CM and human organ samples provide robust benchmarks for cellular identity, and differentiation and maturation processes.

To compare human iPSC-CMs to primary rat neonatal CMs, with a focus on G-protein-coupled receptor signalling components, Bourque and colleagues [140] used integrated single-cell signalling and bulk RNA sequencing. Their data revealed species-specific GPCR landscapes: differential expression of β-adrenergic, α-adrenergic, and endothelin receptors that influence electrophysiological and contractile properties. These differences were mainly attributed to cross-species transcriptomic differences, rather than maturity-induced, suggesting that hiPSC-CMs are still superior for human disease modelling than rat models.

When investigating cardiac differentiation process *in vitro*, single-cell trajectory using transcriptomics at multiple differentiation time points has proven to be very informative. Li and colleagues [105] generated a high-resolution map of cardiac differentiation by sequencing 32,365 single cells from two human iPSC lines at four key time points. They found discrete

populations corresponding to several pluripotent progenitors, mesodermal intermediates, early cardiomyocytes, and more mature iPSC-CMs. Additionally, reconstruction of a differentiation trajectory and single-cell regulatory network interference highlighted CREG and NR2F2 as putative master regulators of CM lineage commitment. This work provides a transcriptomic benchmark of stage-specific gene expression programs, against which new differentiation protocols can be quantitatively evaluated.

Ai and colleagues [108] applied label-free, single-cell proteomics to over 1,600 individual cells, encompassing undifferentiated iPSCs, iPSC-CMs at multiple differentiation time points, and adult human CMs. They quantified >700 proteins per cell, revealing distinct metabolic subtypes: one iPSC-CM population enriched in glycolytic enzymes versus an adult CM population dominated by fatty acid–oxidation machinery. They also reported a rare hybrid phenotype: single cells co-expressing cardiac and neuronal markers, that was also seen in the chapter 3 of this thesis, although many of the involved gene 'markers' were in fact broader developmental-associated genes. Finally, and very interestingly, spatial heterogeneity in iPSCs was found. Cells at colony edges expressed high Lin28a and Tra-1-60, underscoring microenvironment influences on pluripotency, and adding a new hint to variablity in differenciation efficiency and hiPSC-CM heterogeneity.

Recognizing that neither proteomics nor transcriptomics alone capture the full complexity of the human heart, Tang and colleagues [141] reviewed the integration of scRNA-seq with spatial transcriptomics, proteomics, and epigenomics to map cellular heterogeneity in situ. They highlight advances in data-integration algorithms, advocate for multi-layered human cardiac atlases (healthy and diseased) to avoid current limitations in aligning disparate omic datasets and the need for robust computational frameworks. Such integrative atlases will provide the ultimate external benchmarks to validate the fidelity of iPSC-CM models across molecular, spatial, and functional dimensions.

These studies underscore that rigorous characterization of iPSC-CMs,

and the advancement of maturation protocols, also depends on parallel transcriptomic and proteomic profiling, anchored by direct comparisons to human cardiac tissue. By codifying protein and RNA level signatures of cellular identity, signalling maturity, and lineage commitment, the field will move closer to establishing quantitative, multi-omic benchmarks that will guide the development of iPSC-CMs for research, drug screening, and ultimately, regenerative therapies.

References

[1] K. Y. Bogdanov, T. M. Vinogradova, and E. G. Lakatta, "Sinoatrial Nodal Cell Ryanodine Receptor and Na+-Ca2+ Exchanger," *Circulation Research*, Jun. 2001, Publisher: American Heart Association, DOI: 10.1161/hh1201.092095.

[2] V. A. Maltsev and E. G. Lakatta, "Synergism of coupled subsarcolemmal Ca2+ clocks and sarcolemmal voltage clocks confers robust and flexible pacemaker function in a novel pacemaker cell model," *American Journal of Physiology - Heart and Circulatory Physiology*, Mar. 2009, DOI: 10.1152/ajpheart.01118.2008.

[3] S. Kurtenbach, S. Kurtenbach, and G. Zoidl, "Gap junction modulation and its implications for heart function," *Frontiers in Physiology*, Feb. 2014, DOI: 10.3389/fphys.2014.00082.

[4] A. O. Grant, "Cardiac Ion Channels," *Circulation: Arrhythmia and Electrophysiology*, Apr. 2009, DOI: 10.1161/CIRCEP.108.789081.

[5] I. E. Setterberg, C. Le, M. Frisk, H. Perdreau-Dahl, J. Li, and W. E. Louch, "The Physiology and Pathophysiology of T-Tubules in the Heart," *Frontiers in Physiology*, Sep. 2021, Publisher: Frontiers, DOI: 10.3389/fphys.2021.718404.

[6] C. M. Loescher, A. J. Hobbach, and W. A. Linke, "Titin (TTN): From molecule to modifications, mechanics, and medical significance," *Cardiovascular Research*, Oct. 2021, DOI: 10.1093/cvr/cvab328.

[7] C. Crocini and M. Gotthardt, "Cardiac sarcomere mechanics in health and disease," *Biophysical Reviews*, Oct. 2021, DOI: 10.1007/s12551-021-00840-7.

[8] M. V. Razumova, A. E. Bukatina, and K. B. Campbell, "Different Myofilament Nearest-Neighbor Interactions Have Distinctive Effects on Contractile Behavior," *Biophysical Journal*, Jun. 2000, Publisher: Elsevier, DOI: 10.1016/S0006-3495(00)76849-4.

[9] A. M. Gordon, A. F. Huxley, and F. J. Julian, "The variation in isometric tension with sarcomere length in vertebrate muscle fibres," *The Journal of Physiology*, 1966, DOI: 10.1113/jphysiol.1966.sp007909.

[10] H. Hsu, Y. A. Mou, T. C. Irving, and P. P. d. Tombe, "Structural Changes in Both the Troponin Complex and the Thick Filament May Underlie Myofilament Length Dependent Activation," *Biophysical Journal*, Jan. 2012, Publisher: Elsevier, DOI: 10.1016/j.bpj.2011.11.116.

[11] D. M. Bers, "Cardiac excitation–contraction coupling," *Nature*, Jan. 2002, Publisher: Nature Publishing Group, DOI: 10.1038/415198a.

[12] J. S. Hayes, L. L. Brunton, J. H. Brown, J. B. Reese, and S. E. Mayer, "Hormonally specific expression of cardiac protein kinase activity," *Proceedings of the National Academy of Sciences*, Apr. 1979, Publisher: Proceedings of the National Academy of Sciences, DOI: 10.1073/pnas.76.4.1570.

[13] D. M. Bers, Y. K. Xiang, and M. Zaccolo, "Whole-Cell cAMP and PKA Activity are Epiphenomena, Nanodomain Signaling Matters," *Physiology*, Jul. 2019, DOI: 10.1152/physiol.00002.2019.

[14] A. Bock, P. Annibale, C. Konrad, *et al.*, "Optical Mapping of cAMP Signaling at the Nanometer Scale," *Cell*, Sep. 2020, Publisher: Elsevier, DOI: 10.1016/j.cell.2020.07.035.

[15] S. E. Anton, C. Kayser, I. Maiellaro, *et al.*, "Receptor-associated independent cAMP nanodomains mediate spatiotemporal specificity of GPCR signaling," *Cell*, Mar. 2022, Publisher: Elsevier, DOI: 10.1016/j.cell.2022.02.011.

[16] R. Kamel, J. Leroy, G. Vandecasteele, and R. Fischmeister, "Cyclic nucleotide phosphodiesterases as therapeutic targets in cardiac hypertrophy and heart failure," *Nature Reviews. Cardiology*, Feb. 2023, DOI: 10.1038/s41569-022-00756-z.

[17] F. Ahmad, W. Shen, F. Vandeput, *et al.*, "Regulation of Sarcoplasmic Reticulum Ca2+ ATPase 2 (SERCA2) Activity by Phosphodiesterase 3A (PDE3A) in Human Myocardium: PHOSPHORYLATION-DEPENDENT INTERACTION OF PDE3A1 WITH SERCA2*," *Journal of Biological Chemistry*, Mar. 2015, DOI: 10.1074/jbc.M115.638585.

[18] C. B. Nichols, C. F. Rossow, M. F. Navedo, *et al.*, "Sympathetic Stimulation of Adult Cardiomyocytes Requires Association of AKAP5 With a Subpopulation of L-Type Calcium Channels," *Circulation Research*, Sep. 2010, DOI: 10.1161/CIRCRESAHA.109.216127.

[19] J. Leroy, A. Abi-Gerges, V. O. Nikolaev, *et al.*, "Spatiotemporal Dynamics of β-Adrenergic cAMP Signals and L-Type Ca2+ Channel Regulation in Adult Rat Ventricular Myocytes," *Circulation Research*, May 2008, Publisher: American Heart Association, DOI: 10.1161/CIRCRESAHA.107.167817.

[20] K. Schleicher and M. Zaccolo, "Using cAMP Sensors to Study Cardiac Nanodomains," *Journal of Cardiovascular Development and Disease*, Mar. 2018, DOI: 10.3390/jcdd5010017.

[21] G. S. Baillie, "Compartmentalized signalling: Spatial regulation of cAMP by the action of compartmentalized phosphodiesterases," *The FEBS Journal*, 2009, DOI: 10.1111/j.1742-4658.2009.06926.x.

[22] F. Rochais, G. Vandecasteele, F. Lefebvre, *et al.*, "Negative Feedback Exerted by cAMP-dependent Protein Kinase and cAMP Phosphodiesterase on Subsarcolemmal cAMP Signals in Intact Cardiac Myocytes: AN IN VIVO STUDY USING ADENOVIRUS-MEDIATED EXPRESSION OF CNG CHANNELS *," *Journal of Biological Chemistry*, Dec. 2004, DOI: 10.1074/jbc.M405697200.

[23] J. J. Saucerman, E. C. Greenwald, and R. Polanowska-Grabowska, "Mechanisms of cyclic AMP compartmentation revealed by computational models," *Journal of General Physiology*, Dec. 2013, DOI: 10.1085/jgp.201311044.

[24] J. Z. Zhang, T.-W. Lu, L. M. Stolerman, *et al.*, "Phase Separation of a PKA Regulatory Subunit Controls cAMP Compartmentation and Oncogenic Signaling," *Cell*, Sep. 2020, Publisher: Elsevier, DOI: 10.1016/j.cell.2020.07.043.

[25] M. Movsesian, F. Ahmad, and E. Hirsch, "Functions of PDE3 Isoforms in Cardiac Muscle," *Journal of Cardiovascular Development and Disease*, Feb. 2018, DOI: 10.3390/jcdd5010010.

[26] W. Richter, M. Xie, C. Scheitrum, J. Krall, M. A. Movsesian, and M. Conti, "Conserved expression and functions of PDE4 in rodent and human heart," *Basic Research in Cardiology*, Mar. 2011, DOI: 10.1007/s00395-010-0138-8.

[27] L. Puertas-Umbert, J. Alonso, L. Hove-Madsen, J. Martínez-González, and C. Rodríguez, "PDE4 Phosphodiesterases in Cardiovascular Diseases: Key Pathophysiological Players and Potential Therapeutic Targets," *International Journal of Molecular Sciences*, Nov. 2023, DOI: 10.3390/ijms242317017.

[28] V. O. Nikolaev, A. Moshkov, A. R. Lyon, *et al.*, "B2-Adrenergic Receptor Redistribution in Heart Failure Changes cAMP Compartmentation," *Science*, Mar. 2010, Publisher: American Association for the Advancement of Science, DOI: 10.1126/science.1185988.

[29] D. R. Zakhary, C. S. Moravec, and M. Bond, "Regulation of PKA Binding to AKAPs in the Heart," *Circulation*, Mar. 2000, Publisher: American Heart Association, DOI: 10.1161/01.CIR.101.12.1459.

[30] T.-T. Aye, S. Soni, T. A. B. v. Veen, *et al.*, "Reorganized PKA-AKAP associations in the failing human heart," *Journal of Molecular and Cellular Cardiology*, Feb. 2012, Publisher: Elsevier, DOI: 10.1016/j.yjmcc.2011.06.003.

[31] L. Li, J. Li, B. M. Drum, *et al.*, "Loss of AKAP150 promotes pathological remodelling and heart failure propensity by disrupting calcium cycling and contractile reserve," *Cardiovascular Research*, Feb. 2017, DOI: 10.1093/cvr/cvw221.

[32] R. Dash, K. F. Frank, A. N. Carr, C. S. Moravec, and E. G. Kranias, "Gender Influences on Sarcoplasmic Reticulum Ca2+-handling in Failing Human Myocardium," *Journal of Molecular and Cellular Cardiology*, Jul. 2001, Publisher: Elsevier, DOI: 10.1006/jmcc.2001.1394.

[33] Y. S. Han, J. Arroyo, and O. Ogut, "Human heart failure is accompanied by altered protein kinase A subunit expression and post-translational state," *Archives of Biochemistry and Biophysics*, Oct. 2013, DOI: 10.1016/j.abb.2013.08.002.

[34] S. E. Lehnart, X. H. T. Wehrens, S. Reiken, *et al.*, "Phosphodiesterase 4D Deficiency in the Ryanodine-Receptor Complex Promotes Heart Failure and Arrhythmias," *Cell*, Oct. 2005, Publisher: Elsevier, DOI: 10.1016/j.cell.2005.07.030.

[35] B. Ding, J.-i. Abe, H. Wei, *et al.*, "Functional Role of Phosphodiesterase 3 in Cardiomyocyte Apoptosis," *Circulation*, May 2005, Publisher: American Heart Association, DOI: 10.1161/01.CIR.0000165128.39715.87.

[36] W. E. Knight, S. Chen, Y. Zhang, *et al.*, "PDE1C deficiency antagonizes pathological cardiac remodeling and dysfunction," *Proceedings of the National Academy of Sciences*, Nov. 2016, Publisher: Proceedings of the National Academy of Sciences, DOI: 10.1073/pnas.1607728113.

[37] H. Mehel, J. Emons, C. Vettel, *et al.*, "Phosphodiesterase-2 Is Up-Regulated in Human Failing Hearts and Blunts β-Adrenergic Responses in Cardiomyocytes," *JACC*, Oct. 2013, Publisher: American College of Cardiology Foundation, DOI: 10.1016/j.jacc.2013.05.057.

[38] N. K. Bhogal, A. Hasan, and J. Gorelik, "The Development of Compartmentation of cAMP Signaling in Cardiomyocytes: The Role of T-Tubules and Caveolae Microdomains," *Journal of Cardiovascular Development and Disease*, Jun. 2018, DOI: 10.3390/jcdd5020025.

[39] A. Najafi, M. Schuldt, T. V. Pham, *et al.*, "PKA's favorite son: Prioritizing phosphorylation of phospholamban over cardiac troponin I contributes to diastolic dysfunction in hypertrophic cardiomyopathy," *Journal of Molecular and Cellular Cardiology*, Jul. 2018, Publisher: Elsevier, DOI: 10.1016/j.yjmcc.2018.05.120.

[40] Q. Wang, Y. Liu, Q. Fu, *et al.*, "Inhibiting Insulin-Mediated β2-Adrenergic Receptor Activation Prevents Diabetes-Associated Cardiac Dysfunction," *Circulation*, Jan. 2017, Publisher: American Heart Association, DOI: 10.1161/CIRCULATIONAHA.116.022281.

[41] S. Mangmool, T. Denkaew, S. Phosri, *et al.*, "Sustained βAR Stimulation Mediates Cardiac Insulin Resistance in a PKA-Dependent Manner," *Molecular Endocrinology*, Jan. 2016, DOI: 10.1210/me.2015-1201.

[42] J.-C. Fernández-Morales and M. Morad, "Regulation of Ca2+ signaling by acute hypoxia and acidosis in rat neonatal cardiomyocytes," *Journal of Molecular and Cellular Cardiology*, Jan. 2018, Publisher: Elsevier, DOI: 10.1016/j.yjmcc.2017.10.004.

[43] R. S. Decker, A. K. Rines, S. Nakamura, T. J. Naik, J. A. Wassertsrom, and H. Ardehali, "Phosphorylation of contractile proteins in response to α- and β-adrenergic stimulation in neonatal cardiomyocytes," *Translational Research*, Jan. 2010, Publisher: Elsevier, DOI: 10.1016/j.trsl.2009.09.007.

[44] H. Tanaka and K. Shigenobu, "Role of beta-adrenoceptor-adenylate cyclase system in the developmental decrease in sensitivity to isoprenaline in foetal and neonatal rat heart.," *British Journal of Pharmacology*, May 1990, DOI: 10.1111/j.1476-5381.1990.tb12065.x.

[45] A. Hasan, N. Mohammadi, A. Nawaz, *et al.*, "Age-Dependent Maturation of iPSC-CMs Leads to the Enhanced Compartmentation of β2AR-cAMP Signalling," *Cells*, Oct. 2020, DOI: 10.3390/cells9102275.

[46] G. Jung, G. Fajardo, A. J. S. Ribeiro, *et al.*, "Time-dependent evolution of functional vs. remodeling signaling in induced pluripotent stem cell-derived cardiomyocytes and induced maturation with biomechanical stimulation," *FASEB journal: official publication of the Federation of American Societies for Experimental Biology*, Apr. 2016, DOI: 10.1096/fj.15-280982.

[47] K. Takahashi and S. Yamanaka, "Induction of Pluripotent Stem Cells from Mouse Embryonic and Adult Fibroblast Cultures by Defined Factors," *Cell*, Aug. 2006, Publisher: Elsevier, DOI: 10.1016/j.cell.2006.07.024.

[48] I.-H. Park, N. Arora, H. Huo, *et al.*, "Disease-Specific Induced Pluripotent Stem Cells," *Cell*, Sep. 2008, Publisher: Elsevier, DOI: 10.1016/j.cell.2008.07.041.

[49] P. Karagiannis, K. Takahashi, M. Saito, *et al.*, "Induced Pluripotent Stem Cells and Their Use in Human Models of Disease and Development," *Physiological Reviews*, Jan. 2019, DOI: 10.1152/physrev.00039.2017.

[50] M. A. M. Aboul-Soud, A. J. Alzahrani, and A. Mahmoud, "Induced Pluripotent Stem Cells (iPSCs)—Roles in Regenerative Therapies, Disease Modelling and Drug Screening," *Cells*, Sep. 2021, DOI: 10.3390/cells10092319.

[51] L. Santini, C. Palandri, C. Nediani, E. Cerbai, and R. Coppini, "Modelling genetic diseases for drug development: Hypertrophic cardiomyopathy," *Pharmacological Research*, Oct. 2020, DOI: 10.1016/j.phrs.2020.105176.

[52] D. Shah, L. Virtanen, C. Prajapati, *et al.*, "Modeling of LMNA-Related Dilated Cardiomyopathy Using Human Induced Pluripotent Stem Cells," *Cells*, Jun. 2019, DOI: 10.3390/cells8060594.

[53] E. Wallace, L. Howard, M. Liu, *et al.*, "Long QT Syndrome: Genetics and Future Perspective," *Pediatric Cardiology*, 2019, DOI: 10.1007/s00246-019-02151-x.

[54] P. Liang, K. Sallam, H. Wu, *et al.*, "Patient-Specific and Genome-Edited Induced Pluripotent Stem Cell-Derived Cardiomyocytes Elucidate Single-Cell Phenotype of Brugada Syndrome," *Journal of the American College of Cardiology*, Nov. 2016, DOI: 10.1016/j.jacc.2016.07.779.

[55] T. Zimmer, V. Haufe, and S. Blechschmidt, "Voltage-gated sodium channels in the mammalian heart," *Global Cardiology Science & Practice*, Dec. 2014, DOI: 10.5339/gcsp.2014.58.

[56] L. Yang, M. H. Soonpaa, E. D. Adler, *et al.*, "Human cardiovascular progenitor cells develop from a KDR+ embryonic-stem-cell-derived population," *Nature*, May 2008, Publisher: Nature Publishing Group, DOI: 10.1038/nature06894.

[57] T. C. Doetschman, H. Eistetter, M. Katz, W. Schmidt, and R. Kemler, "The in vitro development of blastocyst-derived embryonic stem cell lines: Formation of visceral yolk sac, blood islands and myocardium," *Journal of Embryology and Experimental Morphology*, Jun. 1985.

[58] K. Osafune, L. Caron, M. Borowiak, *et al.*, "Marked differences in differentiation propensity among human embryonic stem cell lines," *Nature Biotechnology*, Mar. 2008, Publisher: Nature Publishing Group, DOI: 10.1038/nbt1383.

[59] P. W. Burridge, D. Anderson, H. Priddle, *et al.*, "Improved Human Embryonic Stem Cell Embryoid Body Homogeneity and Cardiomyocyte Differentiation from a Novel V-96 Plate Aggregation System Highlights Interline Variability," *Stem Cells*, Apr. 2007, DOI: 10.1634/stemcells.2006-0598.

[60] M. A. Laflamme, K. Y. Chen, A. V. Naumova, *et al.*, "Cardiomyocytes derived from human embryonic stem cells in pro-survival factors enhance function of infarcted rat hearts," *Nature Biotechnology*,

Sep. 2007, Publisher: Nature Publishing Group, DOI: 10.1038/nbt1327.

[61] S. J. Kattman, A. D. Witty, M. Gagliardi, *et al.*, "Stage-Specific Optimization of Activin/Nodal and BMP Signaling Promotes Cardiac Differentiation of Mouse and Human Pluripotent Stem Cell Lines," *Cell Stem Cell*, Feb. 2011, Publisher: Elsevier, DOI: 10.1016/j.stem.2010.12.008.

[62] D. M. Lyra-Leite, Ó. Gutiérrez-Gutiérrez, M. Wang, Y. Zhou, L. Cyganek, and P. W. Burridge, "A review of protocols for human iPSC culture, cardiac differentiation, subtype-specification, maturation, and direct reprogramming," *STAR Protocols*, Aug. 2022, DOI: 10.1016/j.xpro.2022.101560.

[63] J. H. Lee, S. I. Protze, Z. Laksman, P. H. Backx, and G. M. Keller, "Human Pluripotent Stem Cell-Derived Atrial and Ventricular Cardiomyocytes Develop from Distinct Mesoderm Populations," *Cell Stem Cell*, Aug. 2017, Publisher: Elsevier, DOI: 10.1016/j.stem.2017.07.003.

[64] E. I. Parrotta, V. Lucchino, L. Scaramuzzino, S. Scalise, and G. Cuda, "Modeling Cardiac Disease Mechanisms Using Induced Pluripotent Stem Cell-Derived Cardiomyocytes: Progress, Promises and Challenges," *International Journal of Molecular Sciences*, Jun. 2020, DOI: 10.3390/ijms21124354.

[65] C. W. van den Berg, S. Okawa, S. M. Chuva de Sousa Lopes, *et al.*, "Transcriptome of human foetal heart compared with cardiomyocytes from pluripotent stem cells," *Development*, Sep. 2015, DOI: 10.1242/dev.123810.

[66] I. Karakikes, M. Ameen, V. Termglinchan, and J. C. Wu, "Human Induced Pluripotent Stem Cell–Derived Cardiomyocytes," *Circulation Research*, Jun. 2015, DOI: 10.1161/CIRCRESAHA.117.305365.

[67] D. Ottaviani, M. ter Huurne, D. A. Elliott, M. Bellin, and C. L. Mummery, "Maturing differentiated human pluripotent stem cells

in vitro: Methods and challenges," *Development*, Jun. 2023, DOI: 10.1242/dev.201103.

[68] T. Hong and R. M. Shaw, "Cardiac T-Tubule Microanatomy and Function," *Physiological Reviews*, Jan. 2017, DOI: 10.1152/physrev.00037.2015.

[69] F. B. Bedada, S. S.-K. Chan, S. K. Metzger, *et al.*, "Acquisition of a Quantitative, Stoichiometrically Conserved Ratiometric Marker of Maturation Status in Stem Cell-Derived Cardiac Myocytes," *Stem Cell Reports*, Sep. 2014, DOI: 10.1016/j.stemcr.2014.07.012.

[70] Z. Yin, J. Ren, and W. Guo, "Sarcomeric protein isoform transitions in cardiac muscle: A journey to heart failure," *Biochimica et Biophysica Acta (BBA) - Molecular Basis of Disease*, Jan. 2015, DOI: 10.1016/j.bbadis.2014.11.003.

[71] P. Ernst, P. A. Bidwell, M. Dora, D. D. Thomas, and F. Kamdar, "Cardiac calcium regulation in human induced pluripotent stem cell cardiomyocytes: Implications for disease modeling and maturation," *Frontiers in Cell and Developmental Biology*, Jan. 2023, DOI: 10.3389/fcell.2022.986107.

[72] C. C. Veerman, G. Kosmidis, C. L. Mummery, S. Casini, A. O. Verkerk, and M. Bellin, "Immaturity of Human Stem-Cell-Derived Cardiomyocytes in Culture: Fatal Flaw or Soluble Problem?" *Stem Cells and Development*, May 2015, DOI: 10.1089/scd.2014.0533.

[73] G. D. Lopaschuk and J. S. Jaswal, "Energy Metabolic Phenotype of the Cardiomyocyte During Development, Differentiation, and Postnatal Maturation," *Journal of Cardiovascular Pharmacology*, Aug. 2010, DOI: 10.1097/FJC.0b013e3181e74a14.

[74] J. A. Gaspar, M. X. Doss, J. G. Hengstler, C. Cadenas, J. Hescheler, and A. Sachinidis, "Unique Metabolic Features of Stem Cells, Cardiomyocytes, and Their Progenitors," *Circulation Research*, Apr. 2014, DOI: 10.1161/CIRCRESAHA.113.302021.

[75] T. D. CHANG and G. R. CUMMING, "Chronotropic Responses of Human Heart Tissue Cultures," *Circulation Research*, Jun. 1972, Publisher: American Heart Association, DOI: 10.1161/01.RES.30.6.628.

[76] M. Brito-Martins, S. E. Harding, and N. N. Ali, "B1- and β2-adrenoceptor responses in cardiomyocytes derived from human embryonic stem cells: Comparison with failing and non-failing adult human heart," *British Journal of Pharmacology*, 2008, DOI: 10.1038/sj.bjp.0707619.

[77] S. M. Biendarra-Tiegs, F. J. Secreto, and T. J. Nelson, "Addressing Variability and Heterogeneity of Induced Pluripotent Stem Cell-Derived Cardiomyocytes," in *Cell Biology and Translational Medicine, Volume 6: Stem Cells: Their Heterogeneity, Niche and Regenerative Potential*, K. Turksen, Ed., Cham, 2020, DOI: 10.1007/5584_2019_350.

[78] L. Sartiani, E. Bettiol, F. Stillitano, A. Mugelli, E. Cerbai, and M. E. Jaconi, "Developmental Changes in Cardiomyocytes Differentiated from Human Embryonic Stem Cells: A Molecular and Electrophysiological Approach," *Stem Cells*, May 2007, DOI: 10.1634/stemcells.2006-0466.

[79] C. Y. Ivashchenko, G. C. Pipes, I. M. Lozinskaya, *et al.*, "Human-induced pluripotent stem cell-derived cardiomyocytes exhibit temporal changes in phenotype," *American Journal of Physiology-Heart and Circulatory Physiology*, Sep. 2013, DOI: 10.1152/ajpheart.00819.2012.

[80] S. D. Lundy, W.-Z. Zhu, M. Regnier, and M. A. Laflamme, "Structural and Functional Maturation of Cardiomyocytes Derived from Human Pluripotent Stem Cells," *Stem Cells and Development*, Jul. 2013, DOI: 10.1089/scd.2012.0490.

[81] C. C. Veerman, I. Mengarelli, E. M. Lodder, *et al.*, "Switch From Fetal to Adult SCN5A Isoform in Human Induced Pluripotent Stem

Cell–Derived Cardiomyocytes Unmasks the Cellular Phenotype of a Conduction Disease–Causing Mutation," *Journal of the American Heart Association*, Jul. 2017, Publisher: Wiley, DOI: 10.1161/JAHA.116.005135.

[82] E. Giacomelli, V. Meraviglia, G. Campostrini, *et al.*, "Human-iPSC-Derived Cardiac Stromal Cells Enhance Maturation in 3D Cardiac Microtissues and Reveal Non-cardiomyocyte Contributions to Heart Disease," *Cell Stem Cell*, Jun. 2020, DOI: 10.1016/j.stem.2020.05.004.

[83] K. Kroll, M. Chabria, K. Wang, F. Häusermann, F. Schuler, and L. Polonchuk, "Electro-mechanical conditioning of human iPSC-derived cardiomyocytes for translational research," *Progress in Biophysics and Molecular Biology*, Cardiac Mechanics and Electrics: it takes two to tango, Nov. 2017, DOI: 10.1016/j.pbiomolbio.2017.07.003.

[84] W. Li, X. Luo, A. Strano, *et al.*, "Comprehensive promotion of iPSC-CM maturation by integrating metabolic medium with nanopatterning and electrostimulation," *Nature Communications*, Mar. 2025, DOI: 10.1038/s41467-025-58044-6.

[85] D. A. M. Feyen, W. L. McKeithan, A. A. N. Bruyneel, *et al.*, "Metabolic Maturation Media Improve Physiological Function of Human iPSC-Derived Cardiomyocytes," *Cell Reports*, Jul. 2020, DOI: 10.1016/j.celrep.2020.107925.

[86] N. Dark, M.-V. Cosson, L. I. Tsansizi, *et al.*, "Generation of left ventricle-like cardiomyocytes with improved structural, functional, and metabolic maturity from human pluripotent stem cells," *Cell Reports Methods*, Apr. 2023, DOI: 10.1016/j.crmeth.2023.100456.

[87] C. Lei, J. Yang, J. Hu, and X. Sun, "On the Calculation of TCID50 for Quantitation of Virus Infectivity," *Virologica Sinica*, May 2020, DOI: 10.1007/s12250-020-00230-5.

[88] E. R. Nadelmann, J. M. Gorham, D. Reichart, *et al.*, "Isolation of Nuclei from Mammalian Cells and Tissues for Single-Nucleus Molecular Profiling," *Current protocols*, May 2021, DOI: 10.1002/cpz1.132.

[89] Y. Hao, T. Stuart, M. H. Kowalski, *et al.*, "Dictionary learning for integrative, multimodal and scalable single-cell analysis," *Nature Biotechnology*, Feb. 2024, Publisher: Nature Publishing Group, DOI: 10.1038/s41587-023-01767-y.

[90] I. Korsunsky, N. Millard, J. Fan, *et al.*, "Fast, sensitive and accurate integration of single-cell data with Harmony," *Nature Methods*, Dec. 2019, Publisher: Nature Publishing Group, DOI: 10.1038/s41592-019-0619-0.

[91] S. Choudhary and R. Satija, "Comparison and evaluation of statistical error models for scRNA-seq," *Genome Biology*, Jan. 2022, DOI: 10.1186/s13059-021-02584-9.

[92] M. I. Love, W. Huber, and S. Anders, "Moderated estimation of fold change and dispersion for RNA-seq data with DESeq2," *Genome Biology*, Dec. 2014, DOI: 10.1186/s13059-014-0550-8.

[93] T. Wu, E. Hu, S. Xu, *et al.*, "clusterProfiler 4.0: A universal enrichment tool for interpreting omics data," *The Innovation*, Aug. 2021, Publisher: Elsevier, DOI: 10.1016/j.xinn.2021.100141.

[94] M. Litviňuková, C. Talavera-López, H. Maatz, *et al.*, "Cells of the adult human heart," *Nature*, Dec. 2020, Publisher: Nature Publishing Group, DOI: 10.1038/s41586-020-2797-4.

[95] J. Cao, M. Spielmann, X. Qiu, *et al.*, "The single-cell transcriptional landscape of mammalian organogenesis," *Nature*, Feb. 2019, Publisher: Nature Publishing Group, DOI: 10.1038/s41586-019-0969-x.

[96] N. C. Surdo, M. Berrera, A. Koschinski, *et al.*, "FRET biosensor uncovers cAMP nano-domains at β-adrenergic targets that dictate precise tuning of cardiac contractility," *Nature Communications*, Apr.

2017, Number: 1 Publisher: Nature Publishing Group, DOI: 10.1038/ncomms15031.

[97] J. Klarenbeek, J. Goedhart, A. v. Batenburg, D. Groenewald, and K. Jalink, "Fourth-Generation Epac-Based FRET Sensors for cAMP Feature Exceptional Brightness, Photostability and Dynamic Range: Characterization of Dedicated Sensors for FLIM, for Ratiometry and with High Affinity," *PLOS ONE*, 2015, Publisher: Public Library of Science, DOI: 10.1371/journal.pone.0122513.

[98] A. Sharma, C. N. Toepfer, T. Ward, *et al.*, "CRISPR/Cas9-Mediated Fluorescent Tagging of Endogenous Proteins in Human Pluripotent Stem Cells," *Current Protocols in Human Genetics*, 2018, DOI: 10.1002/cphg.52.

[99] C. D. Richardson, G. J. Ray, M. A. DeWitt, G. L. Curie, and J. E. Corn, "Enhancing homology-directed genome editing by catalytically active and inactive CRISPR-Cas9 using asymmetric donor DNA," *Nature Biotechnology*, Mar. 2016, Number: 3 Publisher: Nature Publishing Group, DOI: 10.1038/nbt.3481.

[100] A. J. Sparrow, K. Sievert, S. Patel, *et al.*, "Measurement of Myofilament-Localized Calcium Dynamics in Adult Cardiomyocytes and the Effect of Hypertrophic Cardiomyopathy Mutations," *Circulation Research*, Apr. 2019, DOI: 10.1161/CIRCRESAHA.118.314600.

[101] Y. Psaras, F. Margara, M. Cicconet, *et al.*, "CalTrack: High-Throughput Automated Calcium Transient Analysis in Cardiomyocytes," *Circulation Research*, Jul. 2021, DOI: 10.1161/CIRCRESAHA.121.318868.

[102] C. N. Toepfer, A. Sharma, M. Cicconet, *et al.*, "SarcTrack," *Circulation Research*, Apr. 2019, DOI: 10.1161/CIRCRESAHA.118.314505.

[103] F. Wen, X. Tang, L. Xu, and H. Qu, "Comparison of single□nucleus and single□cell transcriptomes in hepatocellular carcinoma tissue," *Molecular Medicine Reports*, Nov. 2022, Publisher: Spandidos Publications, DOI: 10.3892/mmr.2022.12855.

[104] M. Wolfien, A.-M. Galow, P. Müller, *et al.*, "Single-Nucleus Sequencing of an Entire Mammalian Heart: Cell Type Composition and Velocity," *Cells*, Feb. 2020, Number: 2 Publisher: Multidisciplinary Digital Publishing Institute, DOI: 10.3390/cells9020318.

[105] L. Li, D. Li, J. Wang, and Y. Dai, "Single-cell RNA sequencing reveals key regulators and differentiation trajectory of iPSC-derived cardiomyocytes," *Scientific Reports*, Nov. 2024, Publisher: Nature Publishing Group, DOI: 10.1038/s41598-024-79488-8.

[106] T. Grancharova, K. A. Gerbin, A. B. Rosenberg, *et al.*, "A comprehensive analysis of gene expression changes in a high replicate and open-source dataset of differentiating hiPSC-derived cardiomyocytes," *Scientific Reports*, Aug. 2021, Publisher: Nature Publishing Group, DOI: 10.1038/s41598-021-94732-1.

[107] W. Liu, K. Yasui, T. Opthof, *et al.*, "Developmental changes of Ca(2+) handling in mouse ventricular cells from early embryo to adulthood," *Life Sciences*, Aug. 2002, DOI: 10.1016/s0024-3205(02)01826-x.

[108] L. Ai, A. Binek, V. Zhemkov, *et al.*, "Single Cell Proteomics Reveals Specific Cellular Subtypes in Cardiomyocytes Derived from Human iPSCs and Adult Hearts," *Molecular & Cellular Proteomics*, Jan. 2025, DOI: 10.1016/j.mcpro.2025.100910.

[109] J. Li, W. Dong, X. Gao, *et al.*, "EphA4 is highly expressed in the atria of heart and its deletion leads to atrial hypertrophy and electrocardiographic abnormalities in rats," *Life Sciences*, Aug. 2021, DOI: 10.1016/j.lfs.2021.119595.

[110] Q. Sun, S. Liu, K. Liu, and K. Jiao, "Role of Semaphorin Signaling During Cardiovascular Development," *Journal of the American Heart Association*, Jun. 2018, Publisher: Wiley, DOI: 10.1161/JAHA.118.008853.

[111] X. Liu, E. De la Cruz, X. Gu, *et al.*, "Lymphoangiocrine signals promote cardiac growth and repair," *Nature*, Dec. 2020, Publisher: Nature Publishing Group, DOI: 10.1038/s41586-020-2998-x.

[112] J. A. Epstein, H. Aghajanian, and M. K. Singh, "Semaphorin Signaling in Cardiovascular Development," *Cell Metabolism*, Feb. 2015, DOI: 10.1016/j.cmet.2014.12.015.

[113] J. Zhao, S. Bruche, H. G. Potts, B. Davies, and M. T. M. Mommersteeg, "Tissue□Specific Roles for the Slit–Robo Pathway During Heart, Caval Vein, and Diaphragm Development," *Journal of the American Heart Association*, Apr. 2022, Publisher: Wiley, DOI: 10.1161/JAHA.121.023348.

[114] J. M. Churko, P. Garg, B. Treutlein, *et al.*, "Defining human cardiac transcription factor hierarchies using integrated single-cell heterogeneity analysis," *Nature Communications*, Nov. 2018, Publisher: Nature Publishing Group, DOI: 10.1038/s41467-018-07333-4.

[115] N. Thrupp, C. S. Frigerio, L. Wolfs, *et al.*, "Single-Nucleus RNA-Seq Is Not Suitable for Detection of Microglial Activation Genes in Humans," *Cell Reports*, Sep. 2020, Publisher: Elsevier, DOI: 10.1016/j.celrep.2020.108189.

[116] M. Zaccolo and T. Pozzan, "Discrete Microdomains with High Concentration of cAMP in Stimulated Rat Neonatal Cardiac Myocytes," *Science*, Mar. 2002, Publisher: American Association for the Advancement of Science, DOI: 10.1126/science.1069982.

[117] G. Lepski, C. E. Jannes, G. Nikkhah, and J. Bischofberger, "cAMP promotes the differentiation of neural progenitor cells in vitro via modulation of voltage-gated calcium channels," *Frontiers in Cellular Neuroscience*, Sep. 2013, Publisher: Frontiers, DOI: 10.3389/fncel.2013.00155.

[118] K. Bacallao and P. V. Monje, "Requirement of cAMP Signaling for Schwann Cell Differentiation Restricts the Onset of Myelination," *PLOS ONE*, 2015, Publisher: Public Library of Science, DOI: 10.1371/journal.pone.0116948.

[119] S. Ogawa, J. Surapisitchat, C. Virtanen, *et al.*, "Three-dimensional culture and cAMP signaling promote the maturation of human

pluripotent stem cell-derived hepatocytes," *Development*, Aug. 2013, DOI: 10.1242/dev.090266.

[120] K. Omori and J. Kotera, "Overview of PDEs and Their Regulation," *Circulation Research*, Feb. 2007, DOI: 10.1161/01.RES.0000256354.95791.f1.

[121] U. Saleem, D. Ismaili, I. Mannhardt, *et al.*, "Regulation of ICa,L and force by PDEs in human-induced pluripotent stem cell-derived cardiomyocytes," *British Journal of Pharmacology*, 2020, DOI: 10.1111/bph.15032.

[122] Q. Fu, Y. Wang, C. Yan, and Y. K. Xiang, "Phosphodiesterase in heart and vessels: From physiology to diseases," *Physiological Reviews*, Apr. 2024, DOI: 10.1152/physrev.00015.2023.

[123] D. A. Fisher, J. F. Smith, J. S. Pillar, S. H. St. Denis, and J. B. Cheng, "Isolation and Characterization of PDE8A, a Novel Human cAMP-Specific Phosphodiesterase," *Biochemical and Biophysical Research Communications*, May 1998, DOI: 10.1006/bbrc.1998.8684.

[124] L. Dutan Polit, I. Eidhof, R. V. McNeill, *et al.*, "Recommendations, guidelines, and best practice for the use of human induced pluripotent stem cells for neuropharmacological studies of neuropsychiatric disorders," *Neuroscience Applied*, Jan. 2023, DOI: 10.1016/j.nsa.2023.101125.

[125] I. Eidhof, B. Ulfenborg, M. Kele, *et al.*, "Defined culture conditions robustly maintain human stem cell pluripotency, highlighting a role for Ca2+ signaling," *Communications Biology*, Feb. 2025, Publisher: Nature Publishing Group, DOI: 10.1038/s42003-025-07658-z.

[126] I. Germanguz, O. Sedan, N. Zeevi-Levin, *et al.*, "Molecular characterization and functional properties of cardiomyocytes derived from human inducible pluripotent stem cells," *Journal of Cellular and Molecular Medicine*, Jan. 2011, DOI: 10.1111/j.1582-4934.2009.00996.x.

[127] R. Doste, R. Coppini, and A. Bueno-Orovio, "Remodelling of potassium currents underlies arrhythmic action potential prolongation under beta-adrenergic stimulation in hypertrophic cardiomyopathy," *Journal of Molecular and Cellular Cardiology*, Nov. 2022, Publisher: Elsevier, DOI: 10.1016/j.yjmcc.2022.08.361.

[128] X. Yang, L. Pabon, and C. E. Murry, "Engineering adolescence: Maturation of human pluripotent stem cell-derived cardiomyocytes," *Circulation Research*, Jan. 2014, DOI: 10.1161/CIRCRESAHA.114.300558.

[129] L. Yee-Ki and S. Chung-Wah, "Calcium Handling in hiPSC-Derived Cardiomyocytes," in *Calcium Handling in hiPSC-Derived Cardiomyocytes*, L. Yee-Ki and S. Chung-Wah, Eds., New York, NY, 2012, DOI: 10.1007/978-1-4614-4093-2_1.

[130] J. Ma, L. Guo, S. J. Fiene, *et al.*, "High purity human-induced pluripotent stem cell-derived cardiomyocytes: Electrophysiological properties of action potentials and ionic currents," *American Journal of Physiology - Heart and Circulatory Physiology*, Nov. 2011, DOI: 10.1152/ajpheart.00694.2011.

[131] R. Onkal, J. H. Mattis, S. P. Fraser, *et al.*, "Alternative splicing of Nav1.5: An electrophysiological comparison of 'neonatal' and 'adult' isoforms and critical involvement of a lysine residue," *Journal of Cellular Physiology*, Sep. 2008, DOI: 10.1002/jcp.21451.

[132] M. Ieda, T. Tsuchihashi, K. N. Ivey, *et al.*, "Cardiac Fibroblasts Regulate Myocardial Proliferation through β1 Integrin Signaling," *Developmental Cell*, Feb. 2009, Publisher: Elsevier, DOI: 10.1016/j.devcel.2008.12.007.

[133] A. Pointon, J. Pilling, T. Dorval, Y. Wang, C. Archer, and C. Pollard, "From the Cover: High-Throughput Imaging of Cardiac Microtissues for the Assessment of Cardiac Contraction during Drug Discovery," *Toxicological Sciences*, Feb. 2017, DOI: 10.1093/toxsci/kfw227.

[134] E. Ongstad and P. Kohl, "Fibroblast–myocyte coupling in the heart: Potential relevance for therapeutic interventions," *Journal of Molecular and Cellular Cardiology*, Feb. 2016, Publisher: Elsevier, DOI: 10.1016/j.yjmcc.2016.01.010.

[135] P. Robinson, A. J. Sparrow, Y. Psaras, *et al.*, "Comparing the effects of chemical Ca2+ dyes and R-GECO on contractility and Ca2+ transients in adult and human iPSC cardiomyocytes," *Journal of Molecular and Cellular Cardiology*, Jul. 2023, Publisher: Elsevier, DOI: 10.1016/j.yjmcc.2023.04.008.

[136] J. M. Osterloh and K. Mullane, "Manipulating cell fate while confronting reproducibility concerns," *Biochemical Pharmacology*, May 2018, DOI: 10.1016/j.bcp.2018.01.016.

[137] L. Yu, J. Li, J. Hong, *et al.*, "Low Cell-Matrix Adhesion Reveals Two Subtypes of Human Pluripotent Stem Cells," *Stem Cell Reports*, Jul. 2018, Publisher: Elsevier, DOI: 10.1016/j.stemcr.2018.06.003.

[138] A. M. Newman and J. B. Cooper, "Lab-Specific Gene Expression Signatures in Pluripotent Stem Cells," *Cell Stem Cell*, Aug. 2010, Publisher: Elsevier, DOI: 10.1016/j.stem.2010.06.016.

[139] D. E. Ingber, "Human organs-on-chips for disease modelling, drug development and personalized medicine," *Nature Reviews Genetics*, Aug. 2022, Publisher: Nature Publishing Group, DOI: 10.1038/s41576-022-00466-9.

[140] K. Bourque, J. Jones-Tabah, D. Pétrin, R. D. Martin, J. C. Tanny, and T. E. Hébert, "Comparing the signaling and transcriptome profiling landscapes of human iPSC-derived and primary rat neonatal cardiomyocytes," *Scientific Reports*, Jul. 2023, Publisher: Nature Publishing Group, DOI: 10.1038/s41598-023-39525-4.

[141] Z. Tang, F. Alrumaihi, W. M. Alwanian, *et al.*, "The future of cardiology: Integrating single-cell transcriptomics with multi-omics for enhanced cardiac disease insights," *Current Problems in Cardiology*, Apr. 2025, DOI: 10.1016/j.cpcardiol.2025.103005.

Appendix A

Supplementary figures

Chapter 2

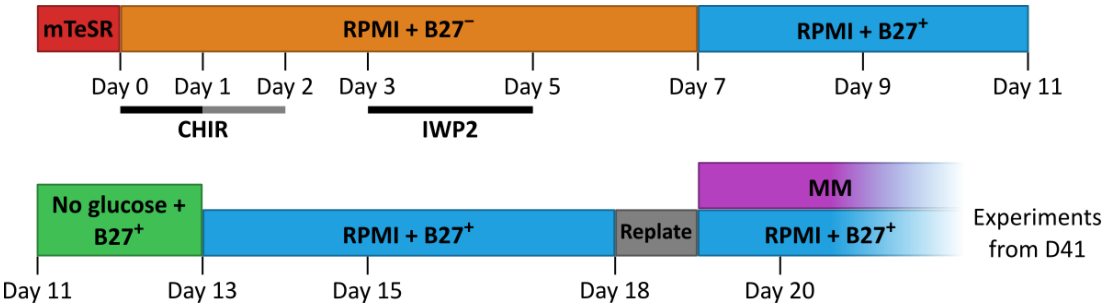

Figure A.1: Regular hiPSC-CM differentiation protocol and metabolic maturation.

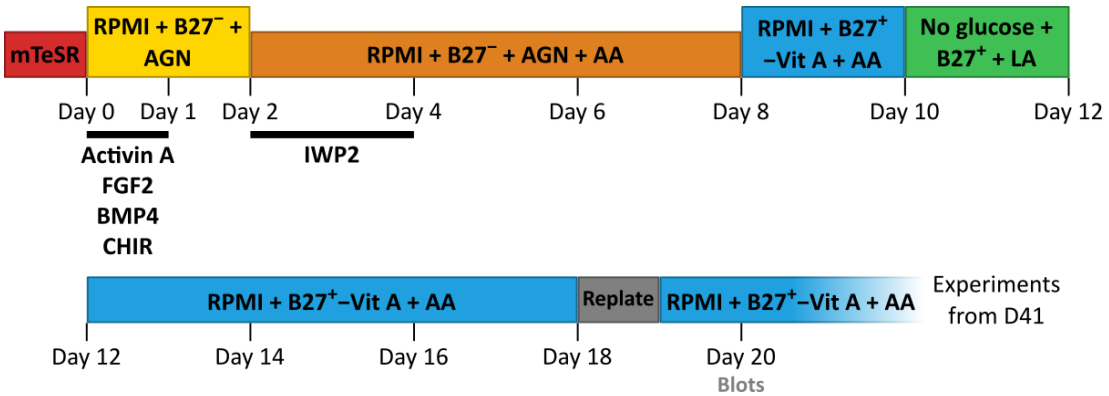

Figure A.2: Left-ventricle like hiPSC-CM differentiation protocol.

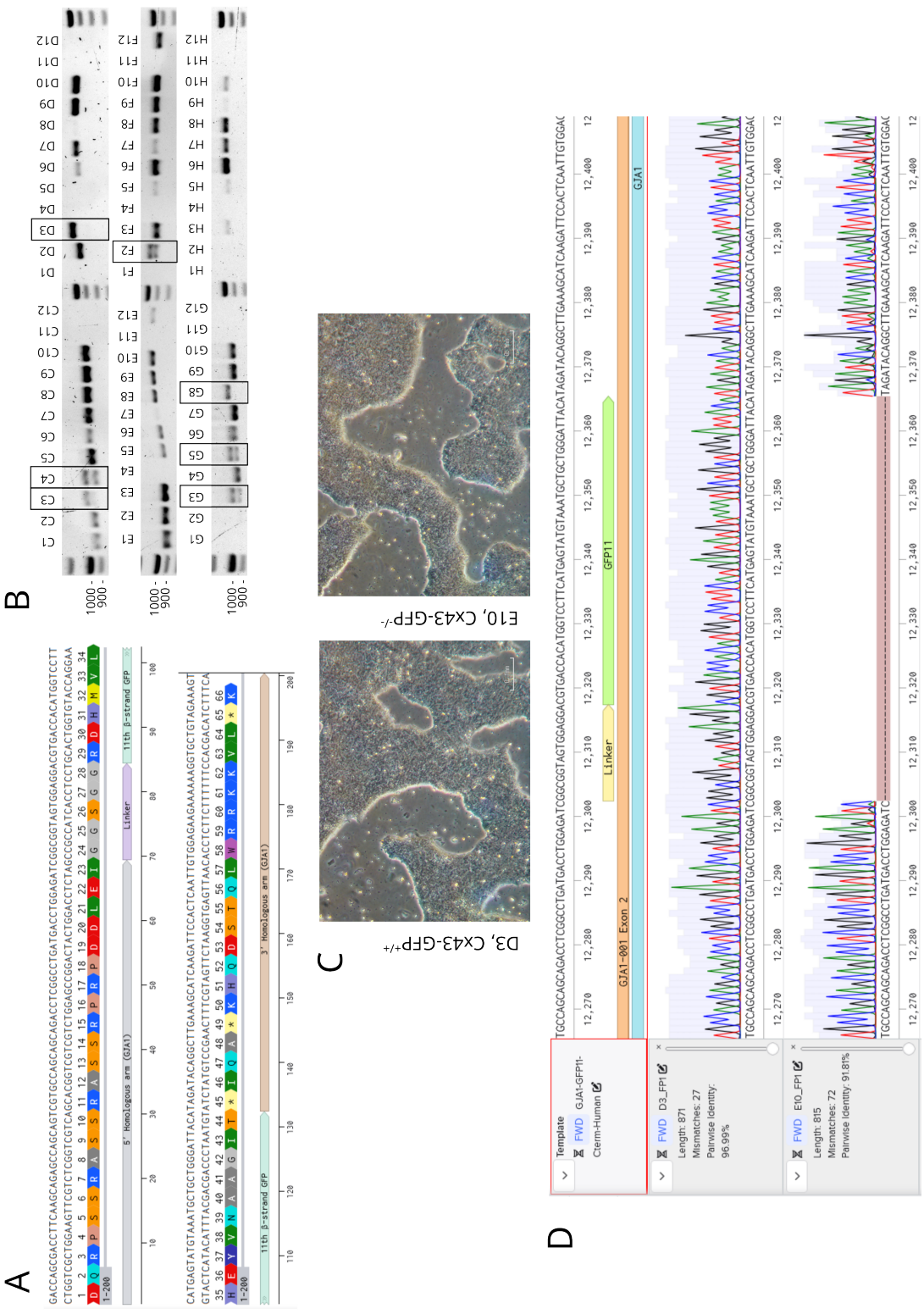

Figure A.3: Insertion of the GFP11 fragment at the C-terminus of Cx43 using Cas9 genome editing. ***A**: Homology directed repair template sequence and labels stating its structure.* ***B**: Electrophoresis gel showing DNA amplified from insertion region. Rectangles highlight edited lines.* ***C**: Pictures from bright field microscopy of iPSCs in culture from selected clones, after genome editing. D3 is a homozygous edited clone and E10 is a non-inserted clone used as a technical control.* ***D**: Sequencing from the two selected lines: the homozygous edited line D3 and non-inserted line E10.*

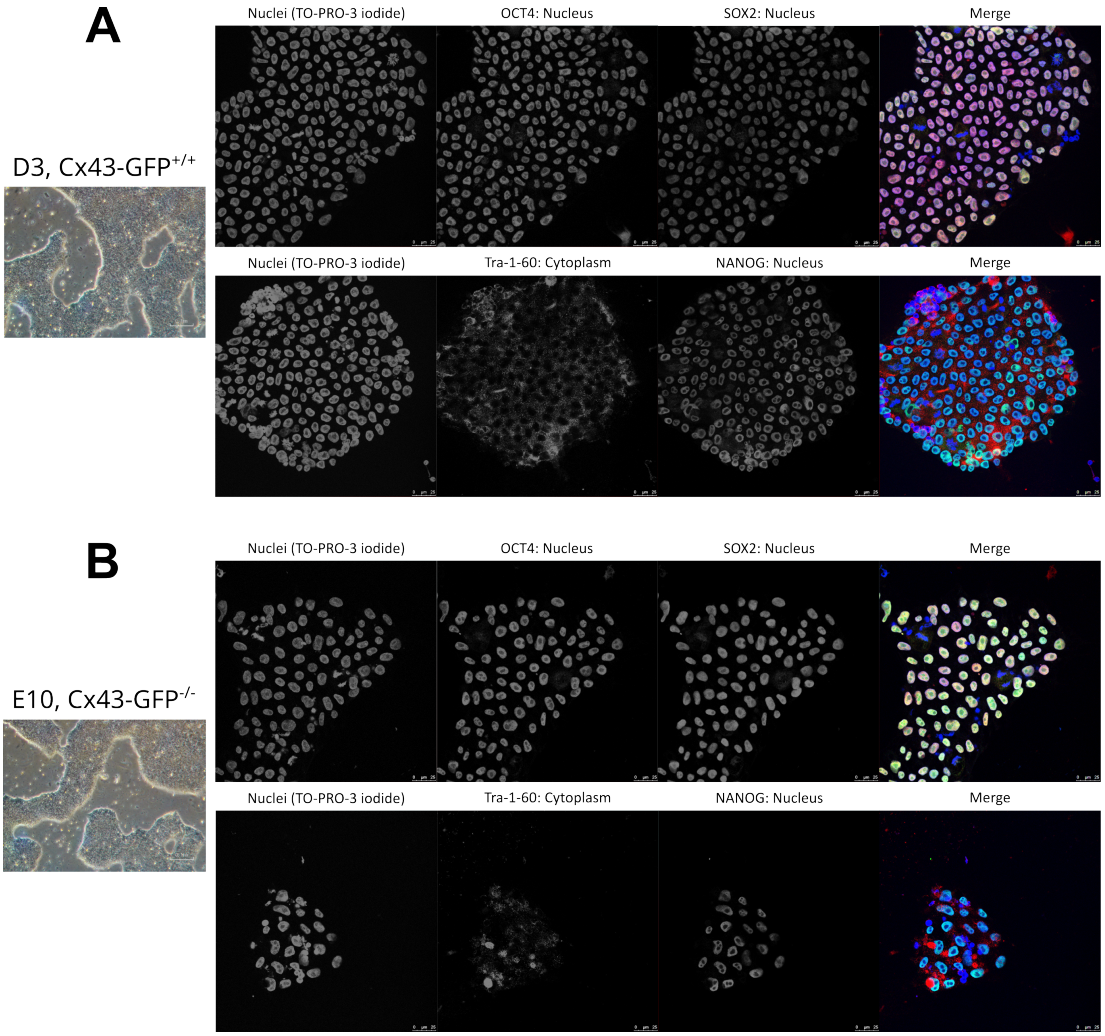

Figure A.4: Immunostaining confirmed pluripotency of edited Cx43-GFP cells. ***A**: Bright field view of newly edited cell-line Cx43-GFP$^{+/+}$ iPSCs in culture, and corresponding immunofluorescent staining of four pluripotency markers. **B**: Bright field view of newly edited cell-line Cx43-GFP$^{-/-}$ iPSCs in culture, and corresponding immunofluorescent staining of four pluripotency markers.*

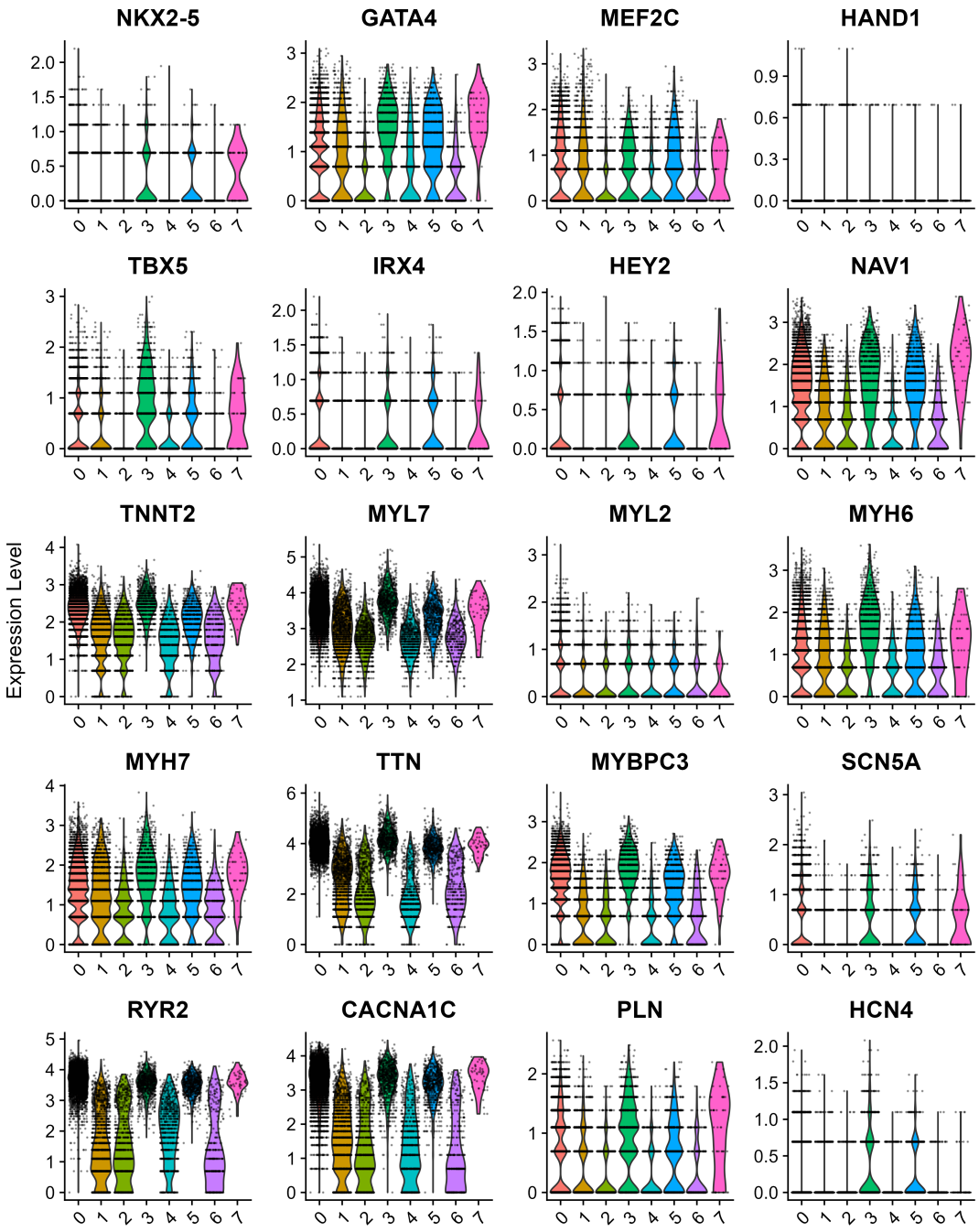

Figure A.5: The relative expression of early and late cardiac genes by clusters reveals clusters with either high or low expression. *Violin plots of the relative expression of cardiac genes, in the different clusters. Expression level is the normalised number of corresponding reads for each nuclei. Clusters 0, 3, 5 and 7 show higher expression in most late cardiac genes investigated.*

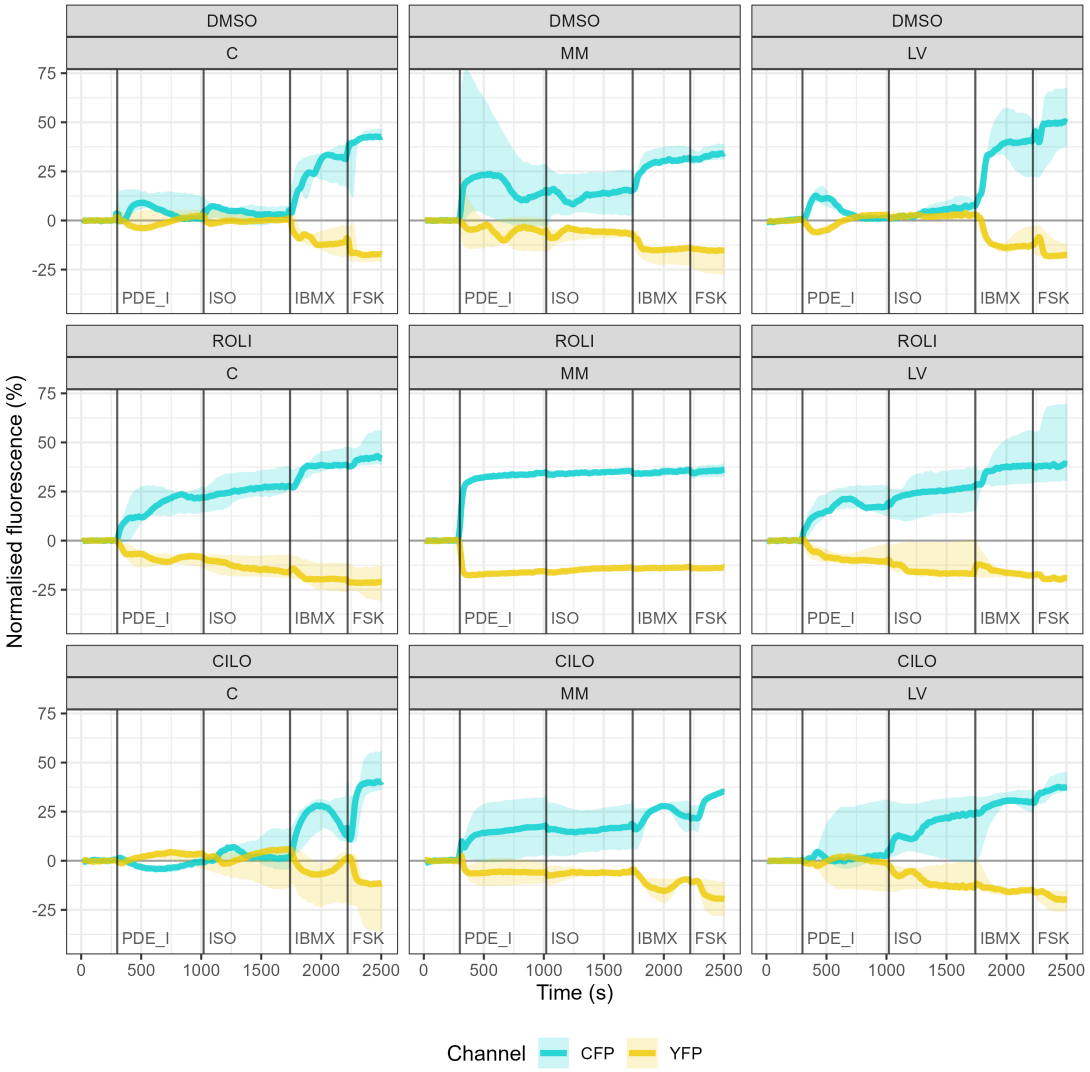

Figure A.6: Average traces of cAMP sensor individual channels. *Curves are rolling median (5-points average, centred) of each cAMP sensor channel fluorescence, and coloured areas are corresponding 95% confidence interval. The curves are normalised to baseline ([Fluorescence/Baseline fluorescence]×100-100). Vertical dark lines indicate timings of each treatment addition to the bath. PDE_I=PDE inhibitor (ROLI or CILO, as indicated above each plot). n=30 for DMSO, n=28 for ROLI, n=29 for CILO, from 2-3 differentiations in C, n=28 for DMSO, n=18 for ROLI, n=20 for CILO, from 2-3 differentiations in MM, n=28 for DMSO, n=30 for ROLI, n=29 for CILO, from 2-3 differentiations in LV.*

Chapter 5

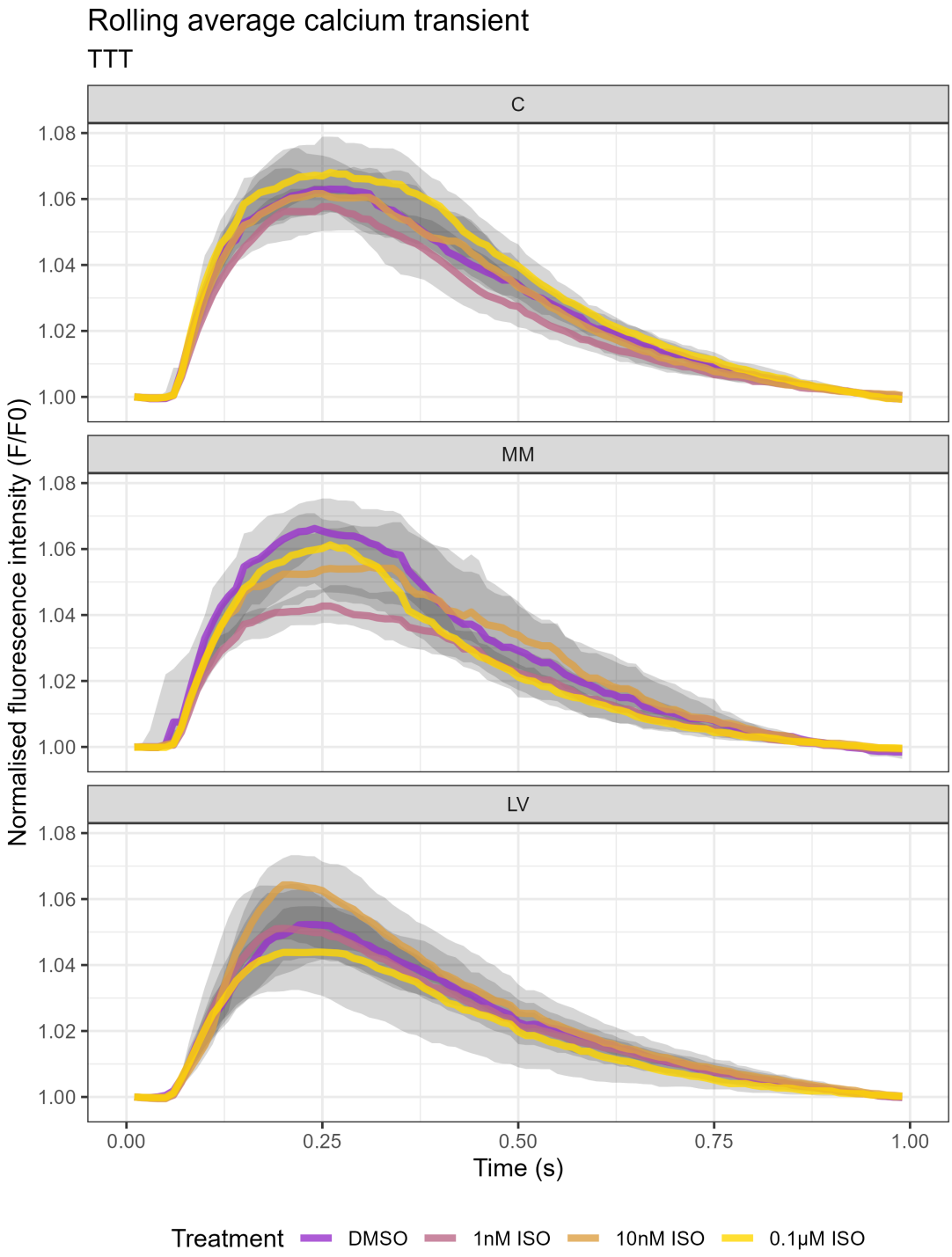

Figure A.7: β-adrenergic stimulation have no robust effect on hiPSC-CM calcium transient. *Curves are rolling median (3-points average, centred) of calcium transients and shaded areas are 95% confidence intervals. The curves are normalised to baseline (Fluorescence/Baseline fluorescence). n=51 for DMSO, n=42 for 1nM ISO, n=42 for 10nM ISO, n=68 for 0.1µM ISO, from 2-4 differentiation batches in C ; n=27 for DMSO, n=50 for 1nM ISO, n=50 for 10nM ISO, n=48 for 0.1µM ISO, from 2-3 differentiation batches in MM ; n=58 for DMSO, n=70 for 1nM ISO, n=69 for 10nM ISO, n=45 for 0.1µM ISO, from 2-3 differentiation batches in LV.*

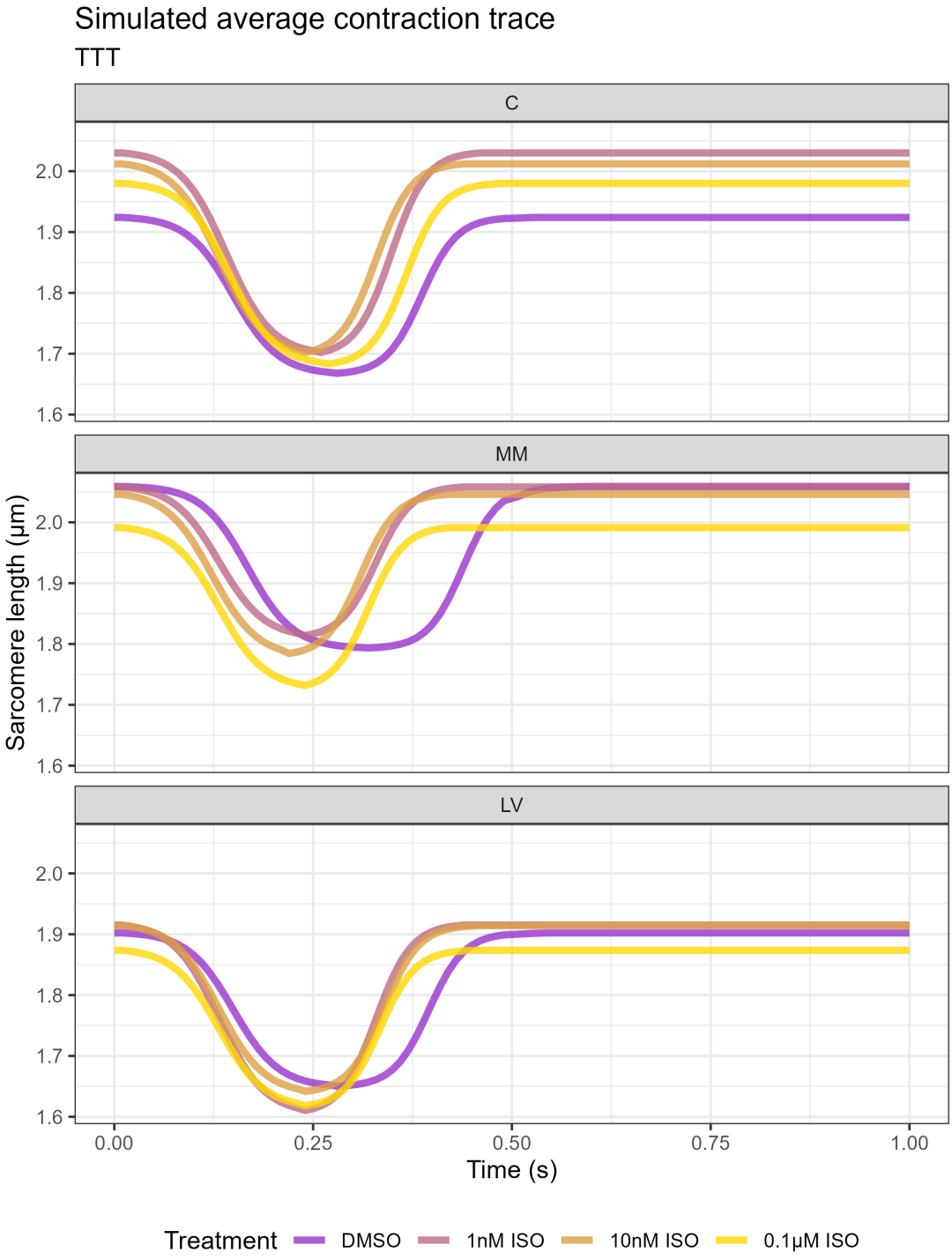

Figure A.8: β-adrenergic stimulation induces a shortening of contraction times in MM and LV hiPSC-CMs. *Curves are simulated contraction traces from median measured parameters. n=48 for DMSO, n=42 for 1nM ISO, n=54 for 10nM ISO, n=62 for 0.1µM ISO, from 2-3 differentiation batches in C ; n=32 for DMSO, n=54 for 1nM ISO, n=71 for 10nM ISO, n=75 for 0.1µM ISO, from 2-4 differentiation batches in MM ; n=75 for DMSO, n=58 for 1nM ISO, n=68 for 10nM ISO, n=64 for 0.1µM ISO, from 2-3 differentiation batches in LV.*

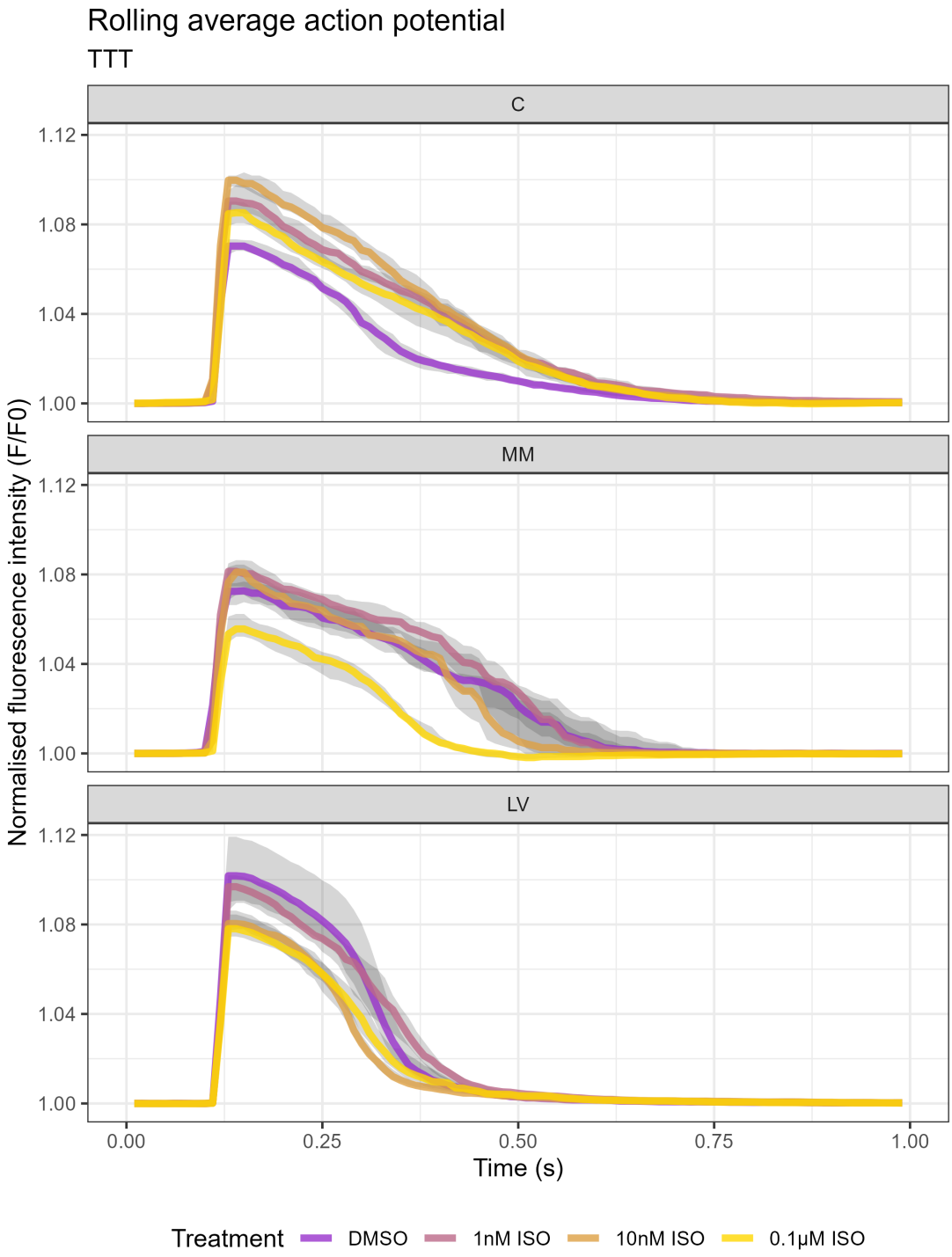

Figure A.9: β-adrenergic stimulation induces a prolongation of action potentials in control cells but not in cells from the maturation protocols. *Curves are rolling median (3-points average, centred) of action potentials and shaded areas are 95% confidence intervals. The curves are normalised to baseline (Fluorescence/Baseline fluorescence). n=72 for DMSO, n=75 for 1nM ISO, n=86 for 10nM ISO, n=88 for 0.1µM ISO, from 4 differentiation batches in C ; n=70 for DMSO, n=96 for 1nM ISO, n=89 for 10nM ISO, n=89 for 0.1µM ISO, from 4 differentiation batches in MM ; n=51 for DMSO, n=71 for 1nM ISO, n=66 for 10nM ISO, n=57 for 0.1µM ISO, from 2-3 differentiation batches in LV.*

Appendix B

Supplementary tables

Chapter 3

Table B.1: Statistical comparison of protein expression

Prot	Group 1	Size	Median±IQR	Group 2	P-value Signif
MLC2a	C	6	1±0.697	NA	0.0513 ns
	MM	6	0.09941±0.091		
	LV	5	0.107±0.055		
MLC2v	C	6	1±1.066	NA	0.117 ns
	MM	6	4.803±4.737		
	LV	5	2.65±2.365		
ssTnI	C	6	1±0.641	NA	0.0641 ns
	MM	6	1.282±1.022		
	LV	5	0.4165±0.286		
cTnI	C	6	1±1.664	MM	0.05726 ns
				LV	0.7768 ns
	MM	6	14.25±8.841	LV	0.102 ns
	LV	5	0.5435±2.123	NA	NA
SERCA2	C	6	1±0.861	NA	0.0941 ns
	MM	6	2.167±1.84		
	LV	5	0.3402±0.645		
β2-AR	C	6	1±0.159	MM	0.02019 *
	C	6	1±0.159	LV	0.004538 **
	MM	6	3.05±0.897	LV	0.4718 ns
	LV	5	4.071±1.271	NA	NA
PDE4D	C	6	1±0.623	NA	0.476 ns
	MM	6	0.4840±0.19		

Table B.1: Statistical comparison of protein expression (continued)

Prot	Group 1	Size	Median±IQR	Group 2	P-value Signif
	LV	5	0.9495±0.413		

Chapter 5

Table B.2: Statistical comparison of calcium transient parameters

Param	Group 1	Size	Median±IQR	Group 2	P-value Signif
CTD	C	80	771.4±31.78	MM	1e+00 ns
				LV	1e+00 ns
	MM	65	771.4±45.52	LV	1e+00 ns
	LV	65	774.3±48.41	NA	NA
CTD40	C	80	331.4±129.7	MM	3.77e-01 ns
				LV	4.09e-04 ***
	MM	66	352.5±108.1	LV	3.38e-05 ****
	LV	66	287±54.87	NA	NA
CTD90	C	80	656.2±93.22	MM	5.09e-01 ns
				LV	4.55e-01 ns
	MM	66	652±88.45	LV	2.23e-01 ns
	LV	66	653.6±88.64	NA	NA
Tau	C	80	321.1±118.8	MM	1.79e-01 ns
				LV	5.52e-01 ns
	MM	66	283.8±132.5	LV	5.51e-02 ns
	LV	66	343.7±152.5	NA	NA
TDecay	C	80	580.7±76.5	MM	5.29e-04 ***
				LV	1.04e-01 ns
	MM	66	538.6±74.51	LV	1.04e-01 ns
	LV	65	553.7±56.26	NA	NA
TPeak	C	80	180.5±98.86	MM	9.22e-03 **
				LV	3.87e-01 ns
	MM	66	230.2±122	LV	9.09e-02 ns
	LV	66	196±64.05	NA	NA

Table B.3: Statistical comparison of calcium transient parameters in response to β-adrenergic stimulation

Param, Protocol	Group 1	Size	Median±IQR	Group 2	P-value Signif
CTD, C	DMSO	51	778.1±24.87	1nM ISO	4.63e-05 ****
				10nM ISO	7.99e-06 ****
				0.1μM ISO	9.62e-01 ns
	1nM ISO	42	750.5±59.99	10nM ISO	9.62e-01 ns
				0.1μM ISO	1.97e-04 ***
	10nM ISO	42	754.1±65.14	0.1μM ISO	3.95e-05 ****
	0.1μM ISO	68	777.1±45.42	NA	NA
CTD, MM	DMSO	27	783.3±68.04	1nM ISO	2.47e-03 **
				10nM ISO	7.38e-02 ns
				0.1μM ISO	4.51e-08 ****
	1nM ISO	50	756.8±60.22	10nM ISO	1.10e-01 ns
				0.1μM ISO	1.38e-02 *
	10nM ISO	50	773.8±70.76	0.1μM ISO	5.09e-05 ****
	0.1μM ISO	48	738±64.85	NA	NA
CTD, LV	DMSO	58	756.7±47.9	1nM ISO	3.37e-01 ns
				10nM ISO	7.23e-02 ns
				0.1μM ISO	3.37e-01 ns
	1nM ISO	70	747.3±49.38	10nM ISO	1.00e+00 ns
				0.1μM ISO	1.00e+00 ns
	10nM ISO	69	738.4±64.9	0.1μM ISO	1.00e+00 ns
	0.1μM ISO	45	744.6±50.05	NA	NA
CTD40, C	DMSO	49	283.2±98.28	1nM ISO	1.00e+00 ns
				10nM ISO	6.01e-02 ns
				0.1μM ISO	4.36e-03 **
	1nM ISO	42	278±137.4	10nM ISO	2.45e-01 ns
				0.1μM ISO	6.01e-02 ns
	10nM ISO	42	353.4±124.2	0.1μM ISO	1.00e+00 ns
	0.1μM ISO	69	348.3±91.86	NA	NA
CTD40, MM	DMSO	29	322.2±96.82	1nM ISO	1.00e+00 ns
				10nM ISO	1.00e+00 ns
				0.1μM ISO	6.98e-04 ***

Table B.3: Statistical comparison of calcium transient parameters in response to β-adrenergic stimulation (continued)

Param, Protocol	Group 1	Size	Median±IQR	Group 2	P-value Signif
	1nM ISO	52	343.5±94.95	10nM ISO	1.00e+00 ns
				0.1μM ISO	6.26e-05 ****
	10nM ISO	53	322.7±66.98	0.1μM ISO	1.99e-04 ***
	0.1μM ISO	48	270.7±58.43	NA	NA
CTD40, LV	DMSO	59	284.5±43.29	1nM ISO	3.03e-04 ***
				10nM ISO	1.31e-05 ****
				0.1μM ISO	5.73e-10 ****
	1nM ISO	71	260.6±35.03	10nM ISO	4.21e-01 ns
				0.1μM ISO	5.62e-03 **
	10nM ISO	69	253.2±38.87	0.1μM ISO	3.34e-02 *
	0.1μM ISO	43	235.8±38.7	NA	NA
CTD90, C	DMSO	51	659.5±98.78	1nM ISO	2.80e-03 **
				10nM ISO	1.30e-02 *
				0.1μM ISO	1.00e+00 ns
	1nM ISO	42	590.2±102.6	10nM ISO	1.00e+00 ns
				0.1μM ISO	2.99e-04 ***
	10nM ISO	43	629.7±124.8	0.1μM ISO	2.39e-03 **
	0.1μM ISO	68	658.5±97.14	NA	NA
CTD90, MM	DMSO	29	653.6±111.7	1nM ISO	4.73e-01 ns
				10nM ISO	8.30e-01 ns
				0.1μM ISO	2.14e-05 ****
	1nM ISO	51	631.1±131.5	10nM ISO	8.30e-01 ns
				0.1μM ISO	6.12e-04 ***
	10nM ISO	52	657.7±108.4	0.1μM ISO	3.36e-05 ****
	0.1μM ISO	48	572.1±74.12	NA	NA
CTD90, LV	DMSO	59	634±59.05	1nM ISO	2.85e-02 *
				10nM ISO	5.37e-03 **
				0.1μM ISO	2.82e-04 ***
	1nM ISO	69	613.7±70.63	10nM ISO	5.46e-01 ns
				0.1μM ISO	2.60e-01 ns
	10nM ISO	69	604.7±73.85	0.1μM ISO	4.77e-01 ns

Table B.3: Statistical comparison of calcium transient parameters in response to β-adrenergic stimulation (continued)

Param, Protocol	Group 1	Size	Median±IQR	Group 2	P-value Signif
	0.1μM ISO	45	592.6±85.12	NA	NA
Tau, C	DMSO	50	319.2±87.55	1nM ISO	1.04e-01 ns
				10nM ISO	4.85e-01 ns
				0.1μM ISO	7.91e-01 ns
	1nM ISO	41	269.4±72.99	10nM ISO	7.91e-01 ns
				0.1μM ISO	6.80e-03 **
	10nM ISO	43	291.3±103.5	0.1μM ISO	1.04e-01 ns
	0.1μM ISO	69	359.5±151.9	NA	NA
Tau, MM	DMSO	29	350.6±134.7	1nM ISO	7.58e-02 ns
				10nM ISO	1.00e+00 ns
				0.1μM ISO	2.42e-02 *
	1nM ISO	50	227.1±222.7	10nM ISO	7.58e-02 ns
				0.1μM ISO	1.00e+00 ns
	10nM ISO	53	324.2±233	0.1μM ISO	1.63e-02 *
	0.1μM ISO	48	257.9±115.2	NA	NA
Tau, LV	DMSO	56	308.8±148.6	1nM ISO	8.49e-01 ns
				10nM ISO	9.86e-01 ns
				0.1μM ISO	2.52e-02 *
	1nM ISO	70	336.7±128.8	10nM ISO	8.49e-01 ns
				0.1μM ISO	1.39e-01 ns
	10nM ISO	69	332.5±156.9	0.1μM ISO	1.67e-02 *
	0.1μM ISO	43	270.4±81.7	NA	NA
TDecay, C	DMSO	48	605.7±42.02	1nM ISO	2.30e-01 ns
				10nM ISO	2.45e-05 ****
				0.1μM ISO	5.21e-04 ***
	1nM ISO	42	578.8±50.36	10nM ISO	1.38e-02 *
				0.1μM ISO	1.27e-01 ns
	10nM ISO	43	536.7±72.56	0.1μM ISO	2.30e-01 ns
	0.1μM ISO	68	544.2±98.31	NA	NA
TDecay, MM	DMSO	28	554±32.67	1nM ISO	1.00e+00 ns
				10nM ISO	6.13e-01 ns

Table B.3: Statistical comparison of calcium transient parameters in response to β-adrenergic stimulation (continued)

Param, Protocol	Group 1	Size	Median±IQR	Group 2	P-value Signif
				0.1μM ISO	6.13e-01 ns
	1nM ISO	51	537.6±110.4	10nM ISO	1.00e+00 ns
				0.1μM ISO	1.00e+00 ns
	10nM ISO	53	529.4±81.85	0.1μM ISO	1.00e+00 ns
	0.1μM ISO	48	533.2±55.47	NA	NA
TDecay, LV	DMSO	58	584.4±58.05	1nM ISO	9.92e-01 ns
				10nM ISO	4.67e-01 ns
				0.1μM ISO	1.17e-01 ns
	1nM ISO	70	591.4±60.61	10nM ISO	9.92e-01 ns
				0.1μM ISO	3.94e-01 ns
	10nM ISO	69	596.1±49.89	0.1μM ISO	9.92e-01 ns
	0.1μM ISO	44	604.8±97.03	NA	NA
TPeak, C	DMSO	49	168.2±24.06	1nM ISO	3.62e-01 ns
				10nM ISO	7.61e-01 ns
				0.1μM ISO	2.27e-03 **
	1nM ISO	42	161.7±65.07	10nM ISO	3.36e-01 ns
				0.1μM ISO	1.03e-05 ****
	10nM ISO	43	177.2±105	0.1μM ISO	9.32e-03 **
	0.1μM ISO	69	213±81.07	NA	NA
TPeak, MM	DMSO	29	223.6±86.72	1nM ISO	3.90e-01 ns
				10nM ISO	9.84e-01 ns
				0.1μM ISO	2.58e-02 *
	1nM ISO	51	196.2±162.4	10nM ISO	3.90e-01 ns
				0.1μM ISO	3.90e-01 ns
	10nM ISO	53	238.4±132.8	0.1μM ISO	6.29e-03 **
	0.1μM ISO	48	196.1±66.51	NA	NA
TPeak, LV	DMSO	59	179.6±50.91	1nM ISO	1.57e-02 *
				10nM ISO	2.19e-05 ****
				0.1μM ISO	1.98e-08 ****
	1nM ISO	70	159.9±42.33	10nM ISO	1.11e-01 ns
				0.1μM ISO	1.40e-03 **

Table B.3: Statistical comparison of calcium transient parameters in response to β-adrenergic stimulation (continued)

Param, Protocol	Group 1	Size	Median±IQR	Group 2	P-value Signif
	10nM ISO	69	144.1±58.84	0.1μM ISO	1.11e-01 ns
	0.1μM ISO	43	143±39.74	NA	NA

Table B.4: Statistical comparison of contraction parameters

Param	Group 1	Size	Median±IQR	Group 2	P-value Signif
Max SL	C	89	1.973±0.1229	MM	6.13e-11 ****
				LV	1.55e-03 **
	MM	77	2.125±0.136	LV	1.58e-22 ****
	LV	101	1.887±0.1585	NA	NA
Min SL	C	89	1.68±0.1214	MM	8.41e-15 ****
				LV	9.96e-04 ***
	MM	77	1.853±0.1229	LV	8.00e-29 ****
	LV	101	1.626±0.1148	NA	NA
FShort	C	89	14.63±6.628	MM	3.83e-02 *
				LV	8.66e-01 ns
	MM	77	12.58±7.801	LV	3.83e-02 *
	LV	101	14.39±6.134	NA	NA
TContr	C	88	239.7±105.4	MM	7.82e-01 ns
				LV	5.62e-01 ns
	MM	75	253.5±138.8	LV	5.62e-01 ns
	LV	97	222.9±101.7	NA	NA
TRelax	C	89	263.8±156.3	MM	1.73e-01 ns
				LV	1.03e-01 ns
	MM	77	313.4±218	LV	3.25e-03 **
	LV	99	233.5±153.2	NA	NA

Table B.5: Statistical comparison of contraction parameters in response to β-adrenergic stimulation

Param, Protocol	Group 1	Size	Median±IQR	Group 2	P-value Signif
Max SL, C	DMSO	48	1.924±0.1592	1nM ISO	1.61e-03 **
				10nM ISO	1.13e-02 *
				0.1μM ISO	3.25e-01 ns
	1nM ISO	42	2.031±0.1064	10nM ISO	4.25e-01 ns
				0.1μM ISO	8.20e-02 ns
	10nM ISO	54	2.012±0.113	0.1μM ISO	3.25e-01 ns
	0.1μM ISO	62	1.98±0.1774	NA	NA
Max SL, MM	DMSO	32	2.059±0.1594	1nM ISO	1.00e+00 ns
				10nM ISO	1.00e+00 ns
				0.1μM ISO	5.22e-02 ns
	1nM ISO	54	2.058±0.1396	10nM ISO	1.00e+00 ns
				0.1μM ISO	4.77e-02 *
	10nM ISO	71	2.046±0.1282	0.1μM ISO	5.22e-02 ns
	0.1μM ISO	75	1.991±0.166	NA	NA
Max SL, LV	DMSO	75	1.902±0.2253	1nM ISO	1e+00 ns
				10nM ISO	1e+00 ns
				0.1μM ISO	1e+00 ns
	1nM ISO	58	1.915±0.2259	10nM ISO	1e+00 ns
				0.1μM ISO	1e+00 ns
	10nM ISO	68	1.914±0.212	0.1μM ISO	1e+00 ns
	0.1μM ISO	64	1.874±0.2519	NA	NA
Min SL, C	DMSO	48	1.668±0.109	1nM ISO	2.97e-01 ns
				10nM ISO	6.96e-02 ns
				0.1μM ISO	7.02e-01 ns
	1nM ISO	42	1.701±0.0853	10nM ISO	9.07e-01 ns
				0.1μM ISO	9.07e-01 ns
	10nM ISO	54	1.7±0.0974	0.1μM ISO	7.02e-01 ns
	0.1μM ISO	62	1.683±0.1118	NA	NA
Min SL, MM	DMSO	32	1.793±0.2261	1nM ISO	1.00e+00 ns
				10nM ISO	1.00e+00 ns
				0.1μM ISO	3.91e-01 ns

Table B.5: Statistical comparison of contraction parameters in response to β-adrenergic stimulation (continued)

Param, Protocol	Group 1	Size	Median±IQR	Group 2	P-value Signif
	1nM ISO	54	1.813±0.1382	10nM ISO	1.00e+00 ns
				0.1μM ISO	1.05e-02 *
	10nM ISO	71	1.783±0.1027	0.1μM ISO	6.02e-02 ns
	0.1μM ISO	75	1.729±0.1781	NA	NA
Min SL, LV	DMSO	75	1.65±0.1452	1nM ISO	1.00e+00 ns
				10nM ISO	1.00e+00 ns
				0.1μM ISO	9.81e-01 ns
	1nM ISO	58	1.608±0.1348	10nM ISO	1.00e+00 ns
				0.1μM ISO	1.00e+00 ns
	10nM ISO	68	1.641±0.1793	0.1μM ISO	1.00e+00 ns
	0.1μM ISO	64	1.617±0.2245	NA	NA
FShort, C	DMSO	48	12.94±8.123	1nM ISO	7.69e-02 ns
				10nM ISO	7.27e-01 ns
				0.1μM ISO	8.18e-01 ns
	1nM ISO	42	17.17±5.567	10nM ISO	7.27e-01 ns
				0.1μM ISO	1.60e-01 ns
	10nM ISO	54	15.26±4.897	0.1μM ISO	8.18e-01 ns
	0.1μM ISO	62	14.52±8.452	NA	NA
FShort, MM	DMSO	32	12.45±7.689	1nM ISO	1e+00 ns
				10nM ISO	1e+00 ns
				0.1μM ISO	1e+00 ns
	1nM ISO	54	11.45±7.509	10nM ISO	1e+00 ns
				0.1μM ISO	1e+00 ns
	10nM ISO	71	12.93±7.758	0.1μM ISO	1e+00 ns
	0.1μM ISO	75	11.86±7.415	NA	NA
FShort, LV	DMSO	75	13.07±9.233	1nM ISO	1e+00 ns
				10nM ISO	1e+00 ns
				0.1μM ISO	1e+00 ns
	1nM ISO	58	13.76±7.615	10nM ISO	1e+00 ns
				0.1μM ISO	1e+00 ns
	10nM ISO	68	12.75±9.76	0.1μM ISO	1e+00 ns

Table B.5: Statistical comparison of contraction parameters in response to β-adrenergic stimulation (continued)

Param, Protocol	Group 1	Size	Median±IQR	Group 2	P-value Signif
	0.1μM ISO	64	13.34±7.662	NA	NA
TContr, C	DMSO	48	259.8±258.8	1nM ISO	1.00e+00 ns
				10nM ISO	5.41e-01 ns
				0.1μM ISO	1.00e+00 ns
	1nM ISO	42	242.4±92.41	10nM ISO	1.00e+00 ns
				0.1μM ISO	1.00e+00 ns
	10nM ISO	52	221.9±83.69	0.1μM ISO	1.00e+00 ns
	0.1μM ISO	61	247.3±124.4	NA	NA
TContr, MM	DMSO	32	304.2±152.9	1nM ISO	7.15e-05 ****
				10nM ISO	3.08e-06 ****
				0.1μM ISO	3.23e-04 ***
	1nM ISO	53	217.7±129.2	10nM ISO	9.19e-01 ns
				0.1μM ISO	9.19e-01 ns
	10nM ISO	69	198.8±100.3	0.1μM ISO	4.82e-01 ns
	0.1μM ISO	72	223.6±107.4	NA	NA
TContr, LV	DMSO	71	257.7±107.1	1nM ISO	1.00e+00 ns
				10nM ISO	8.66e-02 ns
				0.1μM ISO	2.39e-01 ns
	1nM ISO	57	221.7±108	10nM ISO	1.99e-01 ns
				0.1μM ISO	3.76e-01 ns
	10nM ISO	66	216.4±80.58	0.1μM ISO	1.00e+00 ns
	0.1μM ISO	60	220.3±149.7	NA	NA
TRelax, C	DMSO	46	247.9±145.3	1nM ISO	1e+00 ns
				10nM ISO	1e+00 ns
				0.1μM ISO	1e+00 ns
	1nM ISO	42	208.1±92.71	10nM ISO	1e+00 ns
				0.1μM ISO	1e+00 ns
	10nM ISO	52	206.6±106	0.1μM ISO	1e+00 ns
	0.1μM ISO	61	230.9±131.3	NA	NA
TRelax, MM	DMSO	32	277.4±252.2	1nM ISO	5.55e-02 ns
				10nM ISO	6.85e-03 **

Table B.5: Statistical comparison of contraction parameters in response to β-adrenergic stimulation (continued)

Param, Protocol	Group 1	Size	Median±IQR	Group 2	P-value Signif
				0.1μM ISO	1.08e-02 *
	1nM ISO	54	212.2±164.7	10nM ISO	1.00e+00 ns
				0.1μM ISO	1.00e+00 ns
	10nM ISO	71	205.4±121	0.1μM ISO	1.00e+00 ns
	0.1μM ISO	74	191.8±143.3	NA	NA
TRelax, LV	DMSO	73	274.4±116.4	1nM ISO	5.39e-03 **
				10nM ISO	6.87e-03 **
				0.1μM ISO	1.65e-01 ns
	1nM ISO	58	207.6±114.4	10nM ISO	8.32e-01 ns
				0.1μM ISO	6.14e-01 ns
	10nM ISO	65	225.6±95.19	0.1μM ISO	6.14e-01 ns
	0.1μM ISO	62	220.1±139.9	NA	NA

Table B.6: Statistical comparison of action potential parameters

Param	Group 1	Size	Median±IQR	Group 2	P-value Signif
APD	C	81	571.8±136.5	MM	4.39e-01 ns
				LV	1.36e-06 ****
	MM	81	671.2±297.6	LV	2.90e-08 ****
	LV	79	440.4±138.5	NA	NA
APD50	C	81	204.1±142.2	MM	2.59e-08 ****
				LV	3.56e-01 ns
	MM	81	279.9±181	LV	1.67e-10 ****
	LV	78	204.4±64.73	NA	NA
APD90	C	81	394.9±152.8	MM	1.43e-04 ***
				LV	7.44e-03 **
	MM	81	537.5±306.8	LV	1.06e-10 ****
	LV	79	321.5±87.96	NA	NA
TRepol	C	81	517.6±130.7	MM	5.89e-01 ns
				LV	9.54e-06 ****

Table B.6: Statistical comparison of action potential parameters (continued)

Param	Group 1	Size	Median±IQR	Group 2	P-value Signif
	MM	81	616.9±321.3	LV	9.61e-07 ****
	LV	79	412.9±140.1	NA	NA
TPeak	C	79	33.83±14.95	MM	2.59e-03 **
				LV	2.96e-02 *
	MM	78	41.61±18.56	LV	2.43e-07 ****
	LV	77	33.24±13	NA	NA
Triang	C	81	0.5481±0.1927	MM	1.34e-02 *
				LV	2.30e-01 ns
	MM	81	0.6481±0.2257	LV	2.09e-01 ns
	LV	79	0.5944±0.1041	NA	NA

Table B.7: Statistical comparison of action potential parameters in response to β-adrenergic stimulation

Param, Protocol	Group 1	Size	Median±IQR	Group 2	P-value Signif
APD, C	DMSO	72	553.3±143.3	1nM ISO	4.46e-02 *
				10nM ISO	4.90e-01 ns
				0.1µM ISO	1.86e-01 ns
	1nM ISO	75	609.9±166.6	10nM ISO	6.51e-01 ns
				0.1µM ISO	9.64e-01 ns
	10nM ISO	86	565.3±159.2	0.1µM ISO	9.64e-01 ns
	0.1µM ISO	88	591.4±126.6	NA	NA
APD, MM	DMSO	70	713.2±349	1nM ISO	7.34e-03 **
				10nM ISO	4.23e-07 ****
				0.1µM ISO	9.86e-14 ****
	1nM ISO	96	502±329.1	10nM ISO	1.98e-02 *
				0.1µM ISO	1.38e-06 ****
	10nM ISO	89	399.1±307.3	0.1µM ISO	1.98e-02 *
	0.1µM ISO	89	316.2±266.2	NA	NA
APD, LV	DMSO	51	376.3±79.01	1nM ISO	1.07e-01 ns
				10nM ISO	9.18e-01 ns

Table B.7: Statistical comparison of action potential parameters in response to β-adrenergic stimulation (continued)

Param, Protocol	Group 1	Size	Median±IQR	Group 2	P-value Signif
				0.1μM ISO	7.57e-01 ns
	1nM ISO	71	444.2±163.7	10nM ISO	5.04e-01 ns
				0.1μM ISO	9.18e-01 ns
	10nM ISO	66	387.7±175.8	0.1μM ISO	9.18e-01 ns
	0.1μM ISO	57	403.2±187	NA	NA
APD50, C	DMSO	70	174.1±72.63	1nM ISO	2.21e-05 ****
				10nM ISO	6.01e-09 ****
				0.1μM ISO	3.47e-06 ****
	1nM ISO	77	231.7±127.9	10nM ISO	4.22e-01 ns
				0.1μM ISO	7.75e-01 ns
	10nM ISO	87	261.1±91.26	0.1μM ISO	4.37e-01 ns
	0.1μM ISO	88	241.4±117.3	NA	NA
APD50, MM	DMSO	74	301.3±210.9	1nM ISO	3.33e-01 ns
				10nM ISO	6.60e-02 ns
				0.1μM ISO	6.55e-10 ****
	1nM ISO	96	323.1±175.3	10nM ISO	3.14e-01 ns
				0.1μM ISO	2.02e-08 ****
	10nM ISO	97	283.3±166.2	0.1μM ISO	2.61e-05 ****
	0.1μM ISO	89	210.2±117.8	NA	NA
APD50, LV	DMSO	51	188.5±38.52	1nM ISO	2.33e-01 ns
				10nM ISO	9.31e-03 **
				0.1μM ISO	2.33e-01 ns
	1nM ISO	65	212.4±70.22	10nM ISO	3.58e-06 ****
				0.1μM ISO	1.10e-02 *
	10nM ISO	65	161.3±22	0.1μM ISO	2.01e-01 ns
	0.1μM ISO	57	174.1±37.75	NA	NA
APD90, C	DMSO	72	387.7±206.7	1nM ISO	3.44e-04 ***
				10nM ISO	1.25e-03 **
				0.1μM ISO	7.14e-05 ****
	1nM ISO	77	446.1±144.3	10nM ISO	1.00e+00 ns
				0.1μM ISO	1.00e+00 ns

Table B.7: Statistical comparison of action potential parameters in response to β-adrenergic stimulation (continued)

Param, Protocol	Group 1	Size	Median±IQR	Group 2	P-value Signif
	10nM ISO	87	445±128.7	0.1μM ISO	1.00e+00 ns
	0.1μM ISO	88	451.7±130.7	NA	NA
APD90, MM	DMSO	69	622.4±357	1nM ISO	4.46e-03 **
				10nM ISO	9.14e-06 ****
				0.1μM ISO	4.39e-14 ****
	1nM ISO	96	431.1±273	10nM ISO	7.10e-02 ns
				0.1μM ISO	9.99e-07 ****
	10nM ISO	99	386.5±248.3	0.1μM ISO	1.58e-03 **
	0.1μM ISO	89	286.5±182.6	NA	NA
APD90, LV	DMSO	51	264±41.07	1nM ISO	4.19e-01 ns
				10nM ISO	4.19e-01 ns
				0.1μM ISO	9.04e-01 ns
	1nM ISO	65	285.9±84.7	10nM ISO	4.49e-03 **
				0.1μM ISO	4.19e-01 ns
	10nM ISO	64	234.7±55.32	0.1μM ISO	4.19e-01 ns
	0.1μM ISO	56	257.8±78.88	NA	NA
TRepol, C	DMSO	72	513.4±135.1	1nM ISO	3.12e-02 *
				10nM ISO	5.14e-01 ns
				0.1μM ISO	1.47e-01 ns
	1nM ISO	73	571.9±171.7	10nM ISO	4.83e-01 ns
				0.1μM ISO	7.92e-01 ns
	10nM ISO	87	526.5±171.6	0.1μM ISO	7.92e-01 ns
	0.1μM ISO	88	553.9±146.7	NA	NA
TRepol, MM	DMSO	70	672.3±392.1	1nM ISO	5.38e-03 **
				10nM ISO	1.94e-05 ****
				0.1μM ISO	1.19e-12 ****
	1nM ISO	96	455.4±331.4	10nM ISO	9.10e-02 ns
				0.1μM ISO	9.02e-06 ****
	10nM ISO	99	407.7±316.7	0.1μM ISO	4.87e-03 **
	0.1μM ISO	89	280.9±268.1	NA	NA
TRepol, LV	DMSO	51	340.3±77.55	1nM ISO	1.62e-01 ns

Table B.7: Statistical comparison of action potential parameters in response to β-adrenergic stimulation (continued)

Param, Protocol	Group 1	Size	Median±IQR	Group 2	P-value Signif
				10nM ISO	1.00e+00 ns
				0.1μM ISO	7.68e-01 ns
	1nM ISO	70	400±161.4	10nM ISO	7.68e-01 ns
				0.1μM ISO	1.00e+00 ns
	10nM ISO	66	361.1±181.9	0.1μM ISO	1.00e+00 ns
	0.1μM ISO	57	373.7±148.7	NA	NA
TPeak, C	DMSO	69	33.54±11.78	1nM ISO	5.85e-01 ns
				10nM ISO	2.55e-01 ns
				0.1μM ISO	1.00e+00 ns
	1nM ISO	75	36.52±13.67	10nM ISO	1.00e+00 ns
				0.1μM ISO	7.71e-01 ns
	10nM ISO	85	35.53±12.05	0.1μM ISO	4.12e-01 ns
	0.1μM ISO	87	33.99±12.57	NA	NA
TPeak, MM	DMSO	72	41.06±25.37	1nM ISO	8.84e-01 ns
				10nM ISO	2.19e-02 *
				0.1μM ISO	2.19e-02 *
	1nM ISO	86	38.45±14.13	10nM ISO	9.85e-02 ns
				0.1μM ISO	9.85e-02 ns
	10nM ISO	92	36.28±12.58	0.1μM ISO	9.04e-01 ns
	0.1μM ISO	81	34.58±9.789	NA	NA
TPeak, LV	DMSO	51	30.96±6.481	1nM ISO	8.19e-01 ns
				10nM ISO	4.77e-01 ns
				0.1μM ISO	1.31e-01 ns
	1nM ISO	69	32.8±7.363	10nM ISO	1.30e-01 ns
				0.1μM ISO	1.82e-02 *
	10nM ISO	64	29.18±9.312	0.1μM ISO	8.19e-01 ns
	0.1μM ISO	54	26.29±9.284	NA	NA
Triang, C	DMSO	72	0.4699±0.1357	1nM ISO	9.66e-01 ns
				10nM ISO	4.03e-02 *
				0.1μM ISO	9.66e-01 ns
	1nM ISO	77	0.4861±0.2173	10nM ISO	9.94e-02 ns

Table B.7: Statistical comparison of action potential parameters in response to β-adrenergic stimulation (continued)

Param, Protocol	Group 1	Size	Median±IQR	Group 2	P-value Signif
				0.1μM ISO	7.26e-01 ns
	10nM ISO	87	0.4984±0.176	0.1μM ISO	2.50e-03 **
	0.1μM ISO	88	0.4432±0.121	NA	NA
Triang, MM	DMSO	73	0.5984±0.2435	1nM ISO	5.78e-02 ns
				10nM ISO	5.65e-03 **
				0.1μM ISO	7.31e-01 ns
	1nM ISO	94	0.6546±0.2013	10nM ISO	7.31e-01 ns
				0.1μM ISO	8.94e-02 ns
	10nM ISO	97	0.6746±0.1558	0.1μM ISO	1.03e-02 *
	0.1μM ISO	89	0.599±0.2164	NA	NA
Triang, LV	DMSO	51	0.6509±0.0483	1nM ISO	4.56e-01 ns
				10nM ISO	1.11e-02 *
				0.1μM ISO	2.11e-04 ***
	1nM ISO	71	0.6564±0.1127	10nM ISO	4.13e-02 *
				0.1μM ISO	1.02e-03 **
	10nM ISO	65	0.6235±0.0601	0.1μM ISO	3.81e-01 ns
	0.1μM ISO	57	0.6089±0.0769	NA	NA